Amorphous and nanocrystalline phase formation in highly-driven Al-based binary alloys

by

Yunus Eren Kalay

A dissertation submitted to the graduate faculty

in partial fulfillment of the requirements for the degree of

DOCTOR OF PHILOSOPHY

Major: Materials Science and Engineering

Program of Study Committee:
L. Scott Chumbley, Co-major Professor
Iver E. Anderson, Co-major Professor
Ralph E. Napolitano
Rohit Trivedi
Frank E. Peters

Iowa State University

Ames, Iowa

2009

INFORMATION TO USERS

The quality of this reproduction is dependent upon the quality of the copy submitted. Broken or indistinct print, colored or poor quality illustrations and photographs, print bleed-through, substandard margins, and improper alignment can adversely affect reproduction.
In the unlikely event that the author did not send a complete manuscript and there are missing pages, these will be noted. Also, if unauthorized copyright material had to be removed, a note will indicate the deletion.

ProQuest LLC
789 East Eisenhower Parkway
P.O. Box 1346
Ann Arbor, MI 48106-1346

TABLE OF CONTENTS

ABSTRACT

Remarkable advances have been made since rapid solidification was first introduced to the field of materials science and technology. New types of materials such as amorphous alloys and nanostructure materials have been developed as a result of rapid solidification techniques. While these advances are, in many respects, ground breaking, much remains to be discerned concerning the fundamental relationships that exist between a liquid and a rapidly solidified solid.

The scope of the current dissertation involves an extensive set of experimental, analytical, and computational studies designed to increase the overall understanding of morphological selection, phase competition, and structural hierarchy that occurs under far-from equilibrium conditions. High pressure gas atomization and Cu-block melt-spinning are the two different rapid solidification techniques applied in this study. The research is mainly focused on Al-Si and Al-Sm alloy systems. Silicon and samarium produce different, yet favorable, systems for exploration when alloyed with aluminum under far-from equilibrium conditions. One of the main differences comes from the positions of their respective T_0 curves, which makes Al-Si a good candidate for solubility extension while the plunging T_0 line in Al-Sm promotes glass formation.

The rapidly solidified gas-atomized Al-Si powders within a composition range of 15 to 50 wt% Si are examined using scanning and transmission electron microscopy. The non-equilibrium partitioning and morphological selection observed by examining powders at different size classes are described via a microstructure map. The interface velocities and the amount of undercooling present in the powders are estimated from measured eutectic spacings based on Jackson-Hunt (JH) and Trivedi-Magnin-Kurz (TMK) models, which permit a direct comparison of theoretical predictions. For an average particle size of 10 μm with a Péclet number of ~0.2, JH and TMK deviate from each other. This deviation indicates

an adiabatic type solidification path where heat of fusion is reabsorbed. It is interesting that this particle size range is also consistent with the appearance of a microcellular growth. While no glass formation is observed within this system, the smallest size powders appear to consist of a mixture of nanocrystalline Si and Al.

Al-Sm alloys have been investigated within a composition range of 34 to 42 wt% Sm. Gas atomized powders of Al-Sm are investigated to explore the morphological and structural hierarchy that correlates with different degrees of departure from full equilibrium conditions. The resultant powders show a variety of structural selection with respect to amount of undercooling, with an amorphous structure appearing at the highest cooling rates. Because of the chaotic nature of gas atomization, Cu-block melt-spinning is used to produce a homogeneous amorphous structure. The as-quenched structure within Al-34 to 42 wt% Sm consists of nanocrystalline fcc-Al (on the order of 5 nm) embedded in an amorphous matrix. The nucleation density of fcc-Al after initial crystallization is on the order of 10^{22}-10^{23} m^{-3}, which is 10^{5}-10^{6} orders of magnitude higher than what classical nucleation theory predicts. Detailed analysis of liquid and as-quenched structures using high energy synchrotron X-ray diffraction, high energy transmission electron microscopy, and atom probe tomography techniques revealed an Al-Sm network similar in appearance to a medium range order (MRO) structure. A model whereby these MRO clusters promote the observed high nucleation density of fcc-Al nanocrystals is proposed. The devitrification path was identified using high temperature, in-situ, high energy synchrotron X-ray diffraction techniques and the crystallization kinetics were described using an analytical Johnson-Mehl-Avrami (JMA) approach.

CHAPTER 1: OVERVIEW

General Introduction

Thermodynamics and Kinetics of Rapid Solidification

One of earliest studies on rapid solidification of alloys was initiated by Falkenhagen and Hoffmann [1], who first determined the nucleation, undercoolings and cooling rates (up to 10^5 K/S) for a number of metal alloys. Following this work, Pol Duwez [1] and co-workers invented a practical process of quenching hot molten alloys from their liquid states onto the chilled surface of a rotating copper wheel, which introduced a new path to produce intriguing, novel materials such as super saturated solid solutions, metallic glasses, and nanostructured alloys under non-equilibrium conditions [2] . Since then, rapid solidification processing (RSP) has become one of the most important topics in solidification research.

The general understanding of the term RSP involves production of a high solidification rate (typically V>1 cm/s where V = solidification front velocity) by larger undercooling values from suppression of active nucleants or from effective melt quenching, which breaks down many assumptions of conventional solidification. In other words under rapid solidification conditions diffusion distance is shorter than the scale of the microstructure (i.e., low Péclet number) [3]. Although local interfacial equilibrium is lost at higher solidification rates, the free-energy functions of the solid and liquid phases can be used to estimate the range of compositions that can exist at the interface at various temperatures [4-6]. Therefore, the free energies of the different competing phases in a given system can be calculated at various temperatures (at fixed pressures) and the stability of the phases can be determined. In this sense, non-equilibrium conditions can be understood to mean that different degrees of departure from full equilibrium may occur, with the

differences constituting a hierarchy of stability which is followed with increasing solidification rate [7].

In Fig.1 the common tangent between A and B shows the most stable state for a compositional interval of A to B at a temperature of T_A. For any pair of solid and liquid compositions, there exists one temperature where the free energies of the solid and liquid phases are equal to each other. This thermodynamic temperature is expressed as T_0 curve in the phase diagram and it can be estimated by connecting the midpoints between the liquidus and solidus lines at a given temperature. The relative positions of the liquidus, solidus and T_0 lines are schematically shown in a hypothetical free energy curve and phase diagram in Fig. 1. Any undercooling from the liquid state that corresponds to temperatures below the T_0 curve may cause a diffusionless transformation of the liquid alloy to a solid solution. Therefore, the position and curvature extension of T_0 is important in determining the minimum degree of undercooling for partitionless solidification [8]. For example, if the T_0 curve plunges to very low temperatures, a single phase (α or β) crystal cannot be formed from the melt. In this case, deep undercooling may result in a depression of the solidification temperature to a point where it approaches the glass transition temperature, where the viscosity of the undercooled liquid prevents crystallization [8]. Eutectic systems with plunging T_0 curves are good candidates for easy metallic glass formation [9]. In contrast, alloys with T_0 curves which are only slightly depressed below the stable liquidus curves make good candidates for solubility extension and are unlikely ones for glass formation [8]. These conditions are schematically illustrated in Fig.2 (a) and (b).

According to the thermodynamic point of view, at a given undercooling there is a possibility of formation of both stable and competing metastable phases. Therefore, thermodynamics is not sufficient to determine the hierarchy of phases during nucleation by itself; the kinetics of the process must be taken into account. Nucleation of a crystalline phase from a melt is classified in two types, namely, homogeneous and heterogeneous nucleation

[11-13]. Homogeneous nucleation is rarely seen in practice in solidification. In both types of nucleation, there is a barrier of energy to be considered when a small, spherical (assumed) solid crystal is created. Eq. 1 shows the change in free energy during the nucleation of solid crystal where, ΔG_v is free energy per volume due to the liquid to solid phase transformation, γ_{SL} is the solid-liquid interfacial free energy, and r is the radius of the nucleus. S(θ) is the wetting factor that must be considered for heterogeneous nucleation (given by Eq. 2) and θ is the wetting angle [14]. The relationship between these various factors is shown schematically in Fig. 3.

The change in free energy (ΔG_r) is initially increasing due to the increased in interfacial energy and reaches a maximum r^* and $\Delta G,^*$ after which it becomes negatives. This means that r^* represents a critical nucleus size and clusters with diameters larger than the critical value decrease their free energy if the solid grows in the liquid. The critical nucleus size and energy barrier are given in Eq. 3 and 4 respectively.

$$\Delta G_r = \left\{ -\frac{4}{3}\pi r^3 \Delta G_v + 4\pi r^2 \gamma_{SL} \right\} S(\theta) \qquad \text{Equation 1}$$

$$S(\theta) = 0.25(2+\cos\theta)(1-\cos\theta)^2 \qquad \text{Equation 2}$$

$$r^* = -\frac{2\gamma_{SL}}{\Delta G_v} \qquad \text{Equation 3}$$

$$\Delta G^* = -\frac{16\pi\gamma_{SL}^3}{3(\Delta G_v)^2}.S(\theta) \qquad \text{Equation 4}$$

The free energy barrier, ΔG^* is inversely proportional to ΔG_v which is given in Eq.5 where L_v is the latent heat of fusion. At the melting point T_m, the free energies of the solid and the liquid phases are equal to each other and the free energy ΔG^* is infinite, indicating that a solid would never form under this conditions. In theory, a liquid can easily be undercooled to temperatures below T_m without nucleation for a certain amount of time that in needed to build a cluster of the critical size. At low undercooling levels, although the atomic mobility necessary to facilitate interatomic diffusion is high, the amount of time required for a liquid to freeze into a solid can be long due to the fact that the energy barrier that must be

overcome to initiate nucleation is high. Nucleation time initially decreases with an increasing degree of undercooling since ΔG^* is inversely proportional to ΔT (Eq.1.5) [14]. Interestingly, atomic mobility also deceases so that at high undercooling, nucleation time again increases. These competing processes mean that the amount of time required for a liquid to freeze into a solid is variable and is function of temperature [8], which is plotted as a T-T-T (Time-Temperature-Transformation) curves.

$$\Delta G_v = -\frac{L_v \Delta T}{T_m} \qquad \text{Equation 5}$$

Predictions of growth morphology, segregation patterns and the rate of phase growth are particularly complex in a rapid solidification processes. Both heat and solute equations need to be solved under non-equilibrium conditions at the liquid-solid interface [8]. Baker and Cahn [6] described conditions for a binary alloy in terms of interface temperature (T_I), and the composition C_S^*. These relationships are given in Eq. 6 and 7:

$$T_I = T^*(V, C_L^*) - T_M \Gamma K_M \qquad \text{Equation 6}$$

$$C_S^* = C_L^* k^*(V, C_L^*) \qquad \text{Equation 7}$$

where V is the local interface velocity, C_L* is the composition of the liquid at the interface, Γ is the capillary constant, KM is the mean curvature of the solid-liquid interface, T* and k* are the interface temperature and partition coefficient functions, respectively, which are dependent on velocity and composition of the liquid at the interface. The values of T* and k* can be easily determined from phase diagrams at zero interface velocities. Several models have been proposed [16-18] at higher solidification rates in order to calculate T* and k*. The distribution of the solute plays the major role in forming the microstructure as compared to heat distribution since solute diffusivities are much smaller than thermal diffusivities. The dimensionless solute Péclet number (P_c = Vl / 2D), where V is the interface velocity, l is the characteristic length, and D is the liquid diffusion coefficient), is almost always considered for analysis of solute redistribution [3]. For slow solidification rates the diffusion length is much longer than the system size, producing a solute Péclet number much smaller than unity.

Under rapid solidification conditions the solute Péclet number can approach unity. The effect of P_c is discussed in [8] for eutectic [16, 17, 19-25], dendritic [26-33], and cellular [8, 24-36] growth morphologies, and summarized in Table 1.

Amorphous Structure

If the nucleation and growth of any crystalline phases are suppressed upon cooling, a liquid will eventually "freeze" due to the continuous increase in viscosity into a metastable solid state. Although structurally similar to a liquid, the metastable solid is called the glassy state [8]. The temperature at which the glass ceases to flow like a liquid (an amorphous solid is usually believed to have a viscosity of higher than 10^{12} Pa s) is usually called the glass transition temperature (T_g) [37-39]. As discussed earlier, alloy systems with plunging T_0 curves are good candidates for easy metallic glass formation depending on the glass transition temperature. It should be noted that T_g is not a material constant, but changes with cooling rate and thermal history of the material [40, 41]. Some materials, such as polymers, are easy to form in an amorphous state, whereas in others (such as metals) an amorphous phase is not easily produced. Many theories have been postulated in order to predict the glass forming ability (GFA) of metallic materials [13, 42] based on the number of alloying elements (confusion principle), the atomic size effect, heats of mixing of constituent elements, and atomic elasticity [13, 43-49]. Among these theories, the Turnbull criterion is still the most popular for predicting GFA [13, 42]. According to Turnbull, a compound with high GFA will have a so-called reduced glass transition temperature ($T_{rg} = T_g/T_m$) which is equal or higher than 2/3. Bulk metallic glasses (BMG) posses values of T_{rg} that exceed 0.6 and can be easily solidified to an amorphous state with relatively low cooling rates, on the order of 10^2 K/s [50]. In contrast, marginal glass forming alloys do not easily form disordered glassy structures, i.e., a higher cooling rates (on the order of 10^5 K/s) are required as compared to BMGs [51]. Because of the difficulty in fully transforming to a glass,

nanocrystalline phase formation is often observed in highly undercooled marginal glass forming alloys. Examples of bulk metallic glasses and marginal glass former alloys are given in Table 2.

The atomic structures of disordered phases are quite different than crystalline phases as the former do not posses any long-range atomic order. X-ray, neutron and electron scattering techniques are often used to characterize non-crystalline systems, however, in most of the time conventional methods for using these scattering techniques are not sufficient individually to resolve the details of disordered structures, requiring more specialized instrumental and analysis techniques [52]. For example, Cu-K_α radiation is the most commonly used standard diffraction technique to resolve crystal structures, and it can be also used to differentiate amorphous and crystalline materials. However, this technique is not capable of resolving structural details in non-crystalline materials, mostly because of its low value of Q_{max} and the low brilliance of the source. In such cases high energy synchrotron X-ray radiation or a pulsed neutron source may be more helpful to collect data of high sensitivity.

Another example of a specialized characterization technique used for amorphous materials is advanced transmission electron microscopy. Although conventional bright-field (BF) and selected area diffraction (SAD) techniques are useful to determine whether or not the structure is crystalline, these methods fail to give information about the atomic structure. However, with the help of an intensity recording device (e.g. image plates or slow scan CCD) and energy-filtering systems it is possible to conduct comprehensive studies on the atomic structure of non-crystalline materials using a transmission and/or scanning transmission electron microscope (TEM / STEM).

Three different types of order are considered when describing the atomic arrangement of a compound, namely, short, medium and long range order structures. Crystalline materials posses long-range order structure as the atoms occupy the positions in a regular three-

dimensional lattice that can be extended to infinity. The size of long range correlations, which are on the order of 3nm and longer, are easily detected using conventional diffraction and imaging techniques.

Correlations within the 0.5 – 3 nm are called medium range order. It is particularly elusive to detect any correlations within a 1-2 nm range because of the low signal-to-noise ratio and the weakness of the coherent diffraction signal that is typical using conventional diffraction and imaging techniques. Fluctuation electron microscopy (FEM) is a new tool to detect structure within the medium range order (MRO) scale [53-59]. FEM uses the spatial fluctuations in diffraction due to Bragg-like diffraction from nanoscale regions to resolve the MRO in disordered materials. High resolution electron microscopy (HRTEM) and nano-diffraction techniques using a nano-electron probe in a field-emission TEM or STEM are also helpful to detect MRO structures.

Correlations with a size of less than 0.5 nm can still have order up to some degree since any two atoms can not be closer than specific bonding distance. This type of order is considered to be short range order (SRO) and it is studied using X-ray, neutron and electron diffraction techniques.

Analysis of diffraction data from a non-crystalline material is quite different than that for a crystalline materials because the entire reciprocal space of scattering intensity has to be carefully examined [52, 60]. The total intensity function of a scattered X-ray experiment is given by

$$I_{total}(Q) = I_{el}(Q) + I_{Inel}(Q) + I_{mult}(Q) + I_{air}(Q) + I_{back}(Q) \qquad \text{Equation 8}$$

where

$I_{el}(Q)$ = intensity of elastically scattered x rays,

$I_{inel}(Q)$ = intensity of Compton scattering,

$I_{mut}(Q)$ = multiple scattering intensity,

$I_{air}(Q)$ = air scattering intensity,

$I_{back}(Q)$ = Background intensity from sample holder

Structural information is really contained in the first term of Eq. 8, i.e., the elastic component of the total scattering. Therefore, other components have to be calculated or measured and subtracted from the total scattering function in order to evaluate the structure of non-crystalline material. This is explained in detail in [60]. After $I_{el}(Q)$ is calculated the total structure factor, S(Q) can be calculated by:

$$S(Q) = \frac{I(Q)}{< f(Q) >^2} + 1 - \frac{< f(Q)^2 >}{< f(Q) >^2} \qquad \text{Equation 9}$$

where f(Q) is the atomic scattering factor. The most useful pieces of information that can be derived from the total structure factor is Fourier-transform S(Q), to obtain the pair distribution function ρ(r), as given by

$$\rho(r) = \rho_0 + \frac{1}{2\pi^2 r} \int_{Q_{\min}}^{Q_{\max}} Q[S(Q) - 1] \sin(Qr) dQ \qquad \text{Equation 10}$$

where ρ_0 is the average atomic density. Another important function to be considered is the radial distribution function (RDF) which is given by $4\pi r^2\rho(r)$. The area under the first peak in the RDF gives the atomic coordination number. The atomic pair distribution function is given by $G(r)=4\pi r[\rho(r)-\rho_0]$. S(Q) and G(r) functions contain valuable structural information for non-crystalline samples in reciprocal and real spaces, respectively. The total structural factor function can be calculated from data obtained using different methods such as high energy synchrotron X-ray radiation [61-65], energy-dispersive X-ray diffraction (EDXD) , extended X-ray absorption edge fine structure (EXAFS) [66, 67], differential anomalous scattering measurements [68], neutron scattering [69-73], and electron diffraction with energy-filtering techniques [74-76].

One of the major issues in analyzing non-crystalline systems is to produce structural models that agree with experimental data. The two common methods used to simulate disordered systems are Metropolis Monte Carlo (MMC) and Molecular Dynamics (MD) simulations. Both of these simulations are based on interatomic potentials which are

particularly difficult to derive for metallic alloys. Another simulation technique which does not rely on the interatomic potentials is the Reverse Monte Carlo (RMC) method [73, 77-83]. RMC can produce three dimensional models of disordered structures using either individual or combined diffraction data (from neutron, X-rays, and EXAFS). RMC simulation is usually started with an initial configuration (e.g. a random or crystal structure) with periodic boundary conditions. The difference in the experimental total structure factor and the one determined from the configuration is calculated according to Eq.11 with an experimental error of $\sigma(Q_i)$. Atoms are moved and if χ_n^2 is less than χ_0^2, the atomic move is accepted. If χ_n^2 is more than χ_0^2, the move is accepted with a probability $\exp(-(\chi_n^2 - \chi_0^2)/2)$.

$$\chi_o^2 = \sum_{i=1}^{n} \frac{[S_0(Q_i) - S_0^C(Q_i)]^2}{\sigma(Q_i)^2} \qquad \text{Equation 11}$$

Although RMC is a practical and useful technique, it should be noted that the three dimensional structures produced by RMC are not unique but just provide simple models that agree with the diffraction data. In the absence of any other supporting information, there is no way of determining the "absolutely correct" structure. The other disadvantage of RMC is that the configurational entropy is always maximized. However, this effect can be minimized by using additional constraints [77, 78].

The local atomic environment of the structures simulated by RMC can be described by several characteristics such as coordination number, or bond angle determination. One well known method is the Voronoi polyhedron analyses [84-86]. In this method, the bonds between any atom and its closest neighbors are bisected with planes and the intersections of these planes form a Voronoi polyhedron. The distribution of different Voronoi polyhedrons are indexed by Schläfli notation [85], where a polyhedron is expressed by an eight number set of indices $n_3, n_4, \ldots, n_8$ where n_i is the number of faces with i vertices. The Voronoi index of a truncated tetrahedron is given as an example in Fig. 4.

Devitrification

Devitrification can be defined as the controlled crystallization of a partially or fully amorphous material under isothermal or isochronal heating conditions. Thermal and structural changes during devitrification are usually monitored using thermal calorimetry and in-situ diffraction techniques. Fig. 5 shows typical specific temperatures observed during an isochronal thermal analysis of bulk metallic amorphous and marginal glass forming alloys.

Upon heating of an amorphous alloy, an initial relaxation occurs in the structure due to annihilation of the free volume created during rapid solidification, followed by a change from amorphous to super cooled liquid state which is denoted as the glass transition (T_g). In amorphous alloys the glass transition temperature can be monitored in a DSC as a step-like shift in the baseline, but is often hindered for marginal glass forming alloys, because in these alloys, an irreversible crystallization reaction starts at temperatures close to T_g. Using special techniques such as modulated differential scanning calorimetry (MDSC) it is sometime possible to resolve the glass transition in a marginal glass forming alloy during isochronal heating [87] of marginal glass formers. Further heating of both bulk amorphous and marginal glass formers causes crystallization by an exothermic reaction with an onset temperature of T_x.

Crystallization of an amorphous structure has been observed to proceed in three inter-related steps: nucleation, growth, and impingement of growing particles [14, 88, 89]. Nucleation can be homogeneous or heterogeneous. It is heterogeneous if the nucleation starts at sites such as interfaces, inclusions or defects in the as-quenched material. Once a nucleus is formed and starts to grow, different growth patterns can be observed in the system. Different growth mechanisms can result in different transformations, commonly being, primary crystallization, eutectic, and polymorphic transformations [89]. Primary crystallization is a diffusion controlled process where there is a homogenization of the concentration gradient between the growing crystal and the surrounding matrix. Eutectic

transformation requires diffusion as well, but it is a coupled growth that depends on the interparticle spacing of the growing crystal. In polymorphic transformation (i.e.interface controlled growth [88]), the matrix and the growing crystals have the same composition and growth proceeds by movement of atoms through the interface. Growth can also occur via a mixed mode or change in characteristics during crystallization as well. As nucleated crystals grow larger in size a point can be reached where it is possible for their diffusion fields to start to interfere with each other. This effect is known as impingement and can result in a slowing of the growth rate.

In order to model the kinetics of amorphous to crystalline phase transformation, nucleation, growth and impingement should be taken into consideration. Under special conditions the transformation kinetics of the amorphous alloy can be described by the well-known JMA (Johnson, Mehl and Avrami) analytical expression [90-93] . According JMA the transformed volume fraction X is given by

$$X(t) = 1 - \exp\{-[K_T (t - t_0)]^n\} \qquad \text{Equation 12}$$

where K_T is the temperature dependent reaction constant, t_0 is the incubation time, and n is the Avrami exponent. The reaction constant K_T can be calculated from the intercept of the JMA plot [90-92]. The Avrami exponent, n, contains significant information about the transformation behavior. In general for isothermal crystallization of an amorphous alloy, a mean value of the Avrami exponent is used. However, it has been also proposed to use the differential value of the Avrami exponent n(x) [93-95] which reflects the change in Avrami exponent with respect to the crystallized volume fraction X. This is given as:

$$n(X) = \frac{\partial \ln[-\ln(1 - X)]}{\partial \ln(t - t_0)} \qquad \text{Equation 13}$$

Rapid Solidification Techniques

Rapid solidification techniques include melt-atomization, melt-spinning, splat-quenching, surface remelting, and planar flow-casting, as well as derivatives of these main

methods [96-98]. The two RSP techniques employed in this study are high pressure gas atomization (HPGA) and chill block melt spinning. Gas atomization is a melt atomization method where a molten alloy is broken into small droplets by a stream of high pressure gas. These droplets cool by radiation and forced convection of heat from their surface and solidify during the free fall inside the spray chamber. Although the solidification process is chaotic for the gas atomization process, the amount of undercooling is approximately the same for the particles with similar diameters. The smallest size particles tend to undercool deeply so that they solidify more rapidly as compared to larger size particles [11, 99]. This can be understood because a melt that is broken up into many fine droplets can have the number of droplets may exceed the number of active nucleation sites, or motes, present in the melt. This effect, known as mote isolation [100], is enhanced with extreme reduction of particle size, making gas atomized powder ideal for solidification studies at extreme undercoolings regardless of the imposed cooling rate [101,102].

In the melt-spinning technique, the molten alloy is ejected as a stream onto a rotating surface such as a (usually copper) wheel that has a relatively high circumferential speed (max 40 m/s in this study). In some cases multiple melt streams can be used to make composite ribbons. In order to increase the cooling rate and create a homogeneous structure throughout the cross-section of the ribbon, twin chill roll surfaces are used. The product of this process is a ribbon that is typically 10 to 100 μm thick and a few millimeter wide [96].

Although thermal undercooling is the main mechanism in fine powders with a reduced number of catalyst, kinetic undercooling is more prevalent in melt spinning techniques [8].

Literature Review

Rapid Solidification of Al-Si and Al-Sm Binary Alloys

The high Al content (Al > 80 at%) Al-Si and Al-Sm binary alloy systems represent two different types of non-equilibrium solidification paths based on the constructions of their respective T_0 lines. The Al-Si system has slightly depressed T_0 lines near the eutectic composition, which makes Al-Si a good candidate for partitionless solidification. On the contrary, in the Al-Sm system T_0 lines plunge to very low temperatures near the eutectic composition, which promotes glass formation within this system. Amorphous phase formation has been reported in many Al-RE and Al-RE-TM (RE: Rare-earth, TM: transition metals) [88]. Glass formation in Al-RE based alloys is observed between Al- RE eutectic points and $Al_{11}RE_3$ or Al_3RE intermetallics [51]. Among the Al-RE binary alloys, the Al-Sm system has the widest glass formation range, from 8 to 16 at %Sm (34 – 52 wt %Sm), as shown in Fig. 6.

The tendency for glass formation in Al-RE systems has been discussed by several researchers in terms of the large atomic size difference that exists between Al and Sm [49] and the relatively large enthalpy of mixing [51]. It is interesting to note that glass forming Al-RE systems have high temperature metastable compounds (973 – 1217K) in the form of $Al_{11}RE_3$ or Al_3RE in the phase diagrams, which shows strong attractive interactions between Al and RE [103]. Although Al-Sm has the widest glass formation range, its phase diagram is not completely understood. However, several experimental and theoretical studies have been conducted to model the thermodynamics and kinetics considerations of non-equilibrium solidification in the Al-Sm system [104-106]. Table 3 shows several stable and metastable phases observed in Al-Sm system. Further information on the Al-Sm system will be given in the following sections.

Significant studies on the correlation between undercooling and resultant microstructure were performed by Levi and Mehrabian [117, 118] for the Al-Si binary system. They produced submicron aluminum alloy powders (including Al-Si) via vacuum electro-hydrodynamic atomization (EHD) and investigated them using TEM. Most of the submicron particles showed the basic segregation pattern shown in Fig. 7 (a).

In terms of the effect of particle size, as the powder diameter decreases the cellular structure becomes less defined and eventually disappears, leaving only a few segregated Si particles. At the lower end of the size distribution the particles appeared almost featureless, showing only a supersaturated region, denoted as "A" in Fig. 7 (a). A small portion of the powders (<5%) exhibit a different type of segregated microstructure where large, faceted silicon phases appear distributed along the particle surface, Fig. 7 (b). It was concluded that powders showing the faceted silicon were unlikely to have reached substantial undercooling prior to nucleation, and, hence, were extensively segregated. The lack of cellular morphology was explained as evidence of interface morphological stability due to surface tension effects [117].

Following these studies, Boettinger, Bendersky and Early [119] investigated the microstructure of rapidly solidified Al-Fe powders. Their results have many key observations that appear applicable to Al-Si rapid solidification microstructures. According to their TEM studies, powders less than 10 μm in diameter yield a two-zone microcellular-cellular structure. However, larger particles do not exhibit a two-zone structure but cellular, eutectic, or primary intermetallic structures. In a later study Bendersky and coworkers [120] obtained very similar results with a gas atomized Al-5Mn-5Fe-2Si(wt%) alloy. One of their remarkable results is the observation of microcellular structures in powders with less than a 10 μm particle size.

Laser resolidification experiments of compositions varying from Al-15.5 to 20 wt% Si were conducted by Pierantoni and coworkers [121]. The microstructure of a laser treated

sample with composition higher than 20wt% Si consists of fine equiaxed silicon crystals surrounded by α-Al cells distributed in an equiaxed eutectic matrix. According to their SEM micrographs, the mean eutectic spacing was affected only by the solidification rate and not by silicon content. They used an Al-17wt% Si alloy to measure the eutectic spacing and to calculate the corresponding growth rates. This study also found the Al-rich boundary of the coupled zone, and this limit is shown superimposed upon an equilibrium phase diagram. It should be noted that this construction is only concerned with growth; in a real system nucleation effects also impact the final microstructure and must be considered. In accordance with this, Allen, Gremaud and Perepezko [122] performed an analysis of microstructural transitions based upon the limiting solidification interface temperature at the transition using a heterogeneous volume nucleation model. This nucleation analysis indicated that primary Si restricted the coupled eutectic zone for silicon compositions greater than 18wt%, Fig. 8.

Birol [123] investigated ribbon of an Al-12wt% Si alloy produced by quenching from the melt at a cooling rate of 10^6 $K.s^{-1}$. XRD analysis of as-quenched ribbons revealed the following phases: (i) a supersaturated aluminum solid solution and (ii) Si crystals. TEM analysis showed that the Al solid solution forms a cellular structure between which nanosize Si crystals are distributed along cell boundaries. Birol also claimed that a featureless zone (called this due to a lack of response to etching) was created along the wheel side. However, whether this corresponds to the same featureless zone observed by Levi and Mehrabian [117, 118] has not been verified. Other experiments and data (for example SAD of this region) is required to characterize the nature of this featureless zone.

Wang et al. [124] used a different technique and produced Al-18wt%Si alloys via a drop tube method. Droplets ranging from 60 to 1000 μm in diameter were obtained. They calculated the cooling rate using a Newtonian cooling model and found it to be 3.8×10^5 K/s and 3.9×10^3 K/s for the smallest droplets, respectively. According to microstructural analysis, in particles larger than 500 μm polygonal primary Si crystals were present

surrounded by eutectic distributed homogeneously in an α-Al matrix. In smaller particles, star-shaped primary silicon formed along with spherical eutectic grains, which were composed of anomalous eutectic at the core with lamellar eutectic radiating outward.

The microstructural details of rapidly solidified Al-20wt%Si alloy powders produced by gas atomization were examined by Kim and co-workers [125] using TEM. Due to the high convective cooling rate during gas atomization, powder samples showed a fine distribution of primary Si embedded in an Al matrix. Alloy powders of 10 μm in diameter consisted of Si particles that formed within Al grains of 1 μm. The two phases were found to have a semicoherent boundary between Al {111} and Si {111}.

Recently, Trivedi, Anderson, Jin and Genau [33, 126, 127] investigated the dynamical evolution of the microstructure in eutectic and hypereutectic Al-Si powders. According to their studies, all solidified droplets showed the presence of more than one microstructural feature and generally exhibited eutectic, dendritic and cellular morphologies. As the droplet size becomes smaller, the predominant morphology changed from eutectic to dendritic to microcellular. The variations of the eutectic and cellular spacings inside the droplets as a function of droplet diameter were measured as well. For both eutectic [126] and hypereutectic compositions (15-18wt%Si) [128] the average spacing found to be decreased for smaller powders due to higher interface velocity.

A microstructure map that described the range of droplet undercooling as related to droplet diameter and alloy composition was first suggested by Trivedi et al [126]. The effect of atomization gas was also investigated using hypereutectic Al-Si alloy powders. Two different gases were compared, nitrogen and helium. Helium seemed to provide noticeably smaller powder, along with generally higher undercooling and faster interface velocities. However, for particles with size about 11 μm or below, the gas choice was found to be irrelevant in determining the solidification morphology due to complete adiabatic solidification of these particles [128].

Devitrification Studies

One of the first studies performed to identify the crystallization behavior of Al-Sm amorphous alloys was carried out by Battezzati and coworkers [129]. They prepared $Al_{(100-x)}Sm_x$ (x=8,10,12,and 14) by arc-melting the pure elements in a chamber evacuated and back-filled with Ar. Samples of each alloy were melt spun with a wheel speed of 150 m s^{-1}. The resulting ribbons were 1-2 mm wide and 20-30 μm thick. Both fully and partially amorphous phases were obtained and the crystallization processes of the amorphous phases were followed using TEM, XRD and DSC. No glass transition was seen in conventional DSC experiments; such a transition is often absent in systems showing a tendency toward marginal glass formation. In a narrow composition range of 8 to 14 at% Sm they found several types of devitrification processes: primary crystallization of α-Al in $Al_{92}Sm_8$; polymorphic crystallization to a metastable phase in $Al_{90}Sm_{10}$; eutectic crystallization again involving unidentified metastable phases, in $Al_{88}Sm_{12}$ and $Al_{86}Sm_{14}$. The other details are given in Table 4 and Table 5.

Further devitrification studies by Guo and co-workers [130] involved $Al_{(100-x)}Sm_x$ (x=8,10,12,and 14) alloys produced initially by arc-melting and subsequently rapidly solidified into ribbons via melt spinning with thicknesses in the range of 20-30μm. The decomposition behavior of the ribbons was examined by XRD, TEM and DSC. Three kinds of new phases, designated as G2, G3, and G4 were identified. G2 is an orthorhombic phase with lattice parameters a = 13.781 Å, b = 11.019 Å and c = 7.303 Å, G3 is a metastable hexagonal phase with lattice parameters a = 4.597 Å and c = 6.358 Å, and G4 is a metastable cubic phase with lattice parameter a = 19.154 Å.

Recently, Rizzi and coworkers [131] in a follow-on study to previous work [132] investigated the devitrification process for $Al_{92}Sm_8$ and $Al_{90}Sm_{10}$ melt spun alloys. One interesting result that they found for $Al_{90}Sm_{10}$ is that ribbons containing a fraction of a cubic

phase (corresponding to G4 discovered by Guo and co-workers [130]) after quenching transformed according to the following sequence:

Amorphous + α-Al + G4 → Amorphous + α-Al + G4 (higher fraction) → α-Al+R5→ α-Al+R4

They concluded that the cubic phase (G4) forms during undercooling and does not nucleate from the glass. Rather, it simply grows as if it were already present. Their experimental results, as well as the findings reported from similar studies, are summarized in Table 4 and Table 5.

Examination of the tables shows no clear consensus exists concerning the exact devitrification path and existing intermediate phases for $Al_{(100-x)}Sm_x$ (x=8,10,12,and 14) alloys. There is a possibility that the existence of various nucleating phases indicates a "confusion principle" is operative in the alloy that aids in glass formation [131]. However, it is more likely true that the exact nature of the starting materials used in the various studies differed from one another. It is certainly true that all of the previous studies examined different material using different equipment and methodologies, and while slight, these differences in may have produced significant changes in observed results.

If further experiments are to be conducted in order to more clearly identify the devitrification path, it would appear that extensive characterization of the starting material followed by in-situ experiments (for example, time resolved high temperature studies) using powerful X-ray sources (e.g., synchrotron radiation) capable of identifying initial crystallization events as they occur hold the best chance of resolving discrepancies in the literature. At present the only time resolved in-situ study for Al-Sm alloys is the work by Antonowicz [133], who sought to identify the primary crystallization event and quantify the crystalline phase volume fractions and mean crystal sizes for five different binary Al-rare earth glassy alloys including $Al_{92}Sm_8$.

High Density Nanocrystalline Formation and Applications

Devitrification of certain types of amorphous alloys, particularly marginal glass forming alloys, results in formation of very high number of densities of primary crystals with sizes of less than 25 nm. Among these types of metallic glasses, Fe and Al based systems have attracted much attention due to their unique properties [134]. Fe-based alloys are used both as magnetically soft and hard materials, according to the size and volume percentages of the nanocrystals formed in the amorphous matrix. For hard magnetic applications almost full crystallization is required whereas for soft magnetic applications partial crystallization of 70-75% is enough. Finemet® ($Fe_{73.5}Cu_1Nb_3Si_{13.5}B_9$) and Nanoperm® ($Fe_{84}Zr_{3.5}Nb_{3.5}B_8Cu_1$) are well known alloy systems for magnetically soft materials and Fe-RE-B systems are good candidates for hard magnet applications [134].

Al-based nanocrystalline alloys are particularly interesting due to their unique structural properties. GIGAS®, a commercial Al-nanocrystalline alloy, was reported to have a tensile strength of more than 1 GPa. Al-based nanocrystalline alloys are usually in form of Al-RE, or Al-RE-TM (RE=Y, La, Ce, Nd, Sm; TM=Ni, Co, Fe, Cu). A very high number of density of primary fcc-Al nanoparticles on the order of 10^{21} to 10^{23} m^{-3} are formed during partial or complete crystallization of the amorphous alloy as a result of annealing. Despite many previous investigations the origin of the high nucleation density after crystallization of certain amorphous alloys has not been thoroughly understood.

The isothermal crystallization of $Zr_{41}Ti_{14}Cu_{12}Ni_{10}Be_{23}$ was investigated by J. Schroers and coworkers [135]. The number density of nuclei formed during primary crystallization was estimated from measurements made using electron microscopy and small-angle neutron scattering experiments. For comparison, the nucleation density was also calculated from classical nucleation theory, where the steady-state nucleation rate I_{ss} is given as:

$$I_{ss} = \frac{kTN_0}{3\eta(T)a^3}\exp(-\frac{\Delta G^*}{kT}) \qquad \text{Equation 14}$$

where k is Boltzmann's constant, T is the absolute temperature, N_0 is the number of active nucleation sites, η is viscosity, a is interatomic spacing, and ΔG^* is the activation energy to form a critical nucleus. As it is shown in Fig. 9 the solid curve calculated from Eq. 14 is in good agreement with experimental data for temperatures higher than 850 °C, but for lower temperatures experimental data deviates drastically from calculated values. For example, at temperatures close to 600 °C the experimental data is 21 orders of magnitude larger than the calculated value.

The results of [135] show clearly that classical steady-state nucleation theory fails to predict the observed nucleation density. One of the first models that was suggested to explain this unusual behavior proposed the existence of "quenched-in" nuclei in the amorphous state [41, 87, 136-144]. In this model the initial amorphization reaction is under the control of two different mechanisms, namely, nucleation control and growth control. Schematics illustrating the basic differences behind these mechanisms are illustrated in Fig. 10.

With nucleation control, the undercooling achieved during rapid cooling by-passes the nucleation reaction, so no nuclei form. Perhaps more importantly, the cluster size distribution, C(n), retained by the quench does not have a significant density at the critical size, n^* at T_x. As a result, there is no precursor reaction to influence the evolution of crystalline clusters during subsequent thermal treatment. In this way, a clear separation in temperature between the T_g and T_x signals can be observed during reheating.

Under growth control some small fraction of crystallites may form initially during cooling. However, the rapidly rising viscosity that occurs with continued cooling near T_g prevents their development. Another possibility is that the cluster distribution that is retained upon cooling has a significant density at the critical nucleation size at T_g. In either case, upon reheating a sample with preexisting crystallites, rapid crystallization ensues at T_g, which will essentially coincide with T_x [137, 145].

Perepezko and co-workers investigated these mechanisms on rapidly quenched melt-spun and on cold-rolled $Al_{92}Sm_8$ alloys. According to their calorimetry and microstructural analyses, cold-rolled $Al_{92}Sm_8$ samples that have not been exposed to high temperatures in the liquid state before vitrification exhibit a clear T_g signal.

The formation of a high number density of Al-nanocrystals, as observed during heating of melt-spun ribbon samples, does not occur in the cold rolled samples (Fig. 11). Therefore, nucleation at a temperature at or below T_g in melt-spun ribbons does not cause primary crystallization, but results in the growth of "quenched-in" nuclei.

Following these studies, fluctuation electron microcopy (FEM) of amorphous $Al_{92}Sm_8$ identified Al-like medium range order clusters for the as-quenched melt-spun alloy produced at high wheel speeds (150 m/s) but not for the cold-rolled sample, where a different nanoscale ordering was observed [56]. The size of these clusters is on the order of between 1 and 2 nm, which make them difficult to detect using conventional TEM and XRD in the as-quenched state. Upon heating, these sub-size nuclei showed a restricted growth and the glass transition temperature was obscured, i.e., blended with the first crystallization peak, for as-quenched amorphous alloys. However, the hypothesis of these "quenched-in" nuclei has been questioned by several researchers [146]. The main objection to the idea of quenched-in nuclei is the observation of an unrealistically large apparent nucleation density in this Al-Sm and several other Al-based marginal glass forming alloys (ex. Al-Ni-Gd and Al-Y systems). In other words, continuous heating seemed to promote a continuous process of nucleation and growth of fcc-Al crystals.

Another hypothesis is based on phase separation of the amorphous phase into Al-rich and solute-rich regions prior to crystallization. One of the first observations of phase separation was in the $Al_{88}Gd_6La_2Ni_4$ alloy system, in Fig. 12 [147]. Kelton explained the origin of the phase separation by developing a time-dependent homogeneous nucleation theory called coupled-flux nucleation [148 149]. In this theory the nucleation kinetics are a

function of both the number of atoms in the cluster, n, and the number of atoms in the cluster neighborhood, ρ. Cluster growth is determined by the relative rates of exchange of atoms with the parent phase and the cluster. Similar types of phase separations were also reported in other systems such Fe and Zr systems [76, 150-153]. Fig. 13 shows one such observation using simultaneous in-situ X-ray diffraction and small angle X-ray scattering (SAXS) of $Zr_{52.5}Cu_{17.9}Ni_{14.6}Al_{10}Ti_5$ also known as BAM-11 during isothermal heating [154]. The results of this study showed a delay between SAXS and diffraction signals, which was interpreted as phase separation prior to crystallization. However, such phase separations are strongly dependent upon composition of the as-quenched alloy. For example, although a phase separation was reported within the $Al_{88}Gd_6La_2Ni_4$ alloy [147], no phase separation was observed for an $Al_{88}Gd_6ErNi_4$ alloy [155]. Instead, a surface crystallization was seen prior to fcc-Al crystallization.

It should also be pointed out that the evidence offered for phase separation in [147] is less than conclusive. Specimen preparation artifacts from either electropolishing or ion-milling for TEM investigation can produce contrast similar to phase separation in conventional BF images. Therefore, special care must be taken before giving any conclusion about phase separation based solely on TEM BF imaging.

Another hypothesis to describe the observed high nucleation densities of nanocrystals is the possibility of an extremely large number of heterogeneous nucleation occurring on impurity sites such as nano-scale oxides [156]. This hypothesis was observed in a few amorphous systems such as $Zr_{52.5}Cu_{17.9}Ni_{14.6}Al_{10}Ti_5$, but it is still in question since the density of the impurities are usually orders of magnitudes lower than the number of nanocrystals formed in partially crystalline amorphous matrix.

In summary, there is still no agreement on the mechanism of high density nanocluster formation. A detailed analysis of the as-quenched and liquid structures is crucial to develop a

better understanding of the unusual behavior of amorphous alloys forming a high density of nanocrystals after the initial crystallization.

Experimental procedure

Sample Production

As rapidly solidified samples were produced using high pressure gas atomization and copper chill block melt spinning techniques.

Powder samples were produced using the high pressure vertical gas atomizer (Fig. 14) in Ames Laboratory of DOE. The melt chamber was charged with high purity (99.95%) Al, Si (99.99%) and Sm (99.9%) in lump form for each experiment to a total weight of about 1.5 kg. N_2 and He were used as the atomization gas for Al-Si and Al-Sm, respectively. The applied gas pressure was 6.6 MPa for N_2 and 5.5 MPa for He gases. A cyclone separator was incorporated into the system to collect the particles while allowing the atomization process gas to escape and be vented out of the system.

The powder collected from both experiments was screened using an ASTM standard sieve with a vibratory shaker to obtain particles of 45 μm in diameter or less of Al-Si and particles of 106 μm in diameter or less of Al-Sm samples. Air classification was used to obtain 5-10 μm and <5 μm diameter powder. For further classification (<3 μm) sedimentation technique in Hexane (C_6H_{14}) was employed. The complete size classification of the experimental powders is given in Table 6.

Al-Sm ribbon samples were produced using the copper chill block melt spinner (Fig. 15) in Ames Laboratory. Ingots of $Al_{100-x}Sm_x$ (x=8, 10 and 12 at%) were prepared initially from highly pure Al (99.99%) and Sm (99.9%) by arc melting under an Argon atmosphere. The pre-alloyed ingot was then remelted and rapidly solidified into ribbon form at circumferential speeds of 10, 20, 30 and 40 m/s in a He atmosphere. The thickness of these ribbons was in the range of 20 - 70 μm for high and low circumferential speeds, respectively.

The overall chemical compositions of the ribbons were determined using a JEOL® JXA-8200 Superprobe for comparison to the initially determined compositions.

Specimen Preparation

The Al-Si and Al-Sm samples produced through gas atomization and/or melt spinning techniques were subjected to a series of sample preparation steps in order to be ready for characterization using various techniques.

The SEM work was done using JSM 6060 LV and JSM 5910 LV microscopes equipped with energy dispersive X-ray spectrometers (EDS). Samples selected for SEM analysis were mounted in epoxy resin for cross sectional studies. The mounted samples were ground with 800 and 1200 grit SiC papers under water and polished with aqueous slurries of 0.3 and 0.05 μm alumina. Each polished mount was then etched with Keller's reagent for approximately 10 seconds. To facilitate electron microscopy, the mounts were carbon painted around the sides and sputter coated with gold.

TEM investigations were conducted either using a Philips® CM30 S/TEM equipped with EDS or an FEI Tecnai® G^2 F20 S/TEM equipped with EDS, electron energy loss spectroscopy (EELS), energy filtered transmission electron microscopy (EFTEM) and high angle annular dark field (HAADF) capabilities. Due to the strong interaction between electrons and matter, the specimens have to be rather thin (<< 1000 nm for conventional TEM and << 30 nm for HRTEM) for TEM investigation. Thus, bulk materials have to be thinned to make them electron transparent. This is done either by simply crushing them and subsequently depositing some fragments onto a carbon foil or by mechanical grinding and ion milling. If produced directly, nanoparticles are thin enough for direct observation.

In general, all specimens to be prepared for transmission electron microscopy can be divided in two broad categories: self supporting specimens, where the whole specimen

consists of one material, and specimens supported on a grid or washers containing a small hole or slot.

In the case of powder samples a supporting grid or matrix is most often needed as the powders are too small to support themselves. However, melt spun ribbons can usually support themselves, although a double sided copper grid or Cu (Be) washer is used to secure the sample and prevent movement in the TEM holder.

Sample preparation of Al-Sm ribbon samples is a straightforward process. Ribbons were first punched to create three millimeters discs. These discs were mechanically thinned with a Dimpler® initially and final thinning was performed using electropolishing with a chemical composition of 25 ml HCl, 500 ml H_2O, and 300 ml methanol. Electropolishing was performed at -25°C using a double jet electropolisher at a fixed voltage. In some cases the alternative chemical solution of 333 ml nitric acid and 667 ml methanol at -40°C was used. (N.B. Ion milling was also attempted, however, damage due to the ions was noted on numerous samples. Particularly for amorphous specimens it was seen that ion milling induced surface patterns on the amorphous matrix, and in some cases it triggered crystallization. Therefore, ion milling was avoided for as-quenched amorphous specimens.)

Many different methods were proposed in the literature for obtaining thin sections from powder specimens, such as dispersion in a volatile liquid [157], embedding between metal powders or sheets [158, 159], microtomy [160, 161], electronic deposition, focus ion beam milling [162, 163] and miscellaneous other methods (such as using dental amalgam [164]. Of these techniques two were used for preparation of Al-Si and Al-Sm powders, the first being dispersion in a volatile liquid.

Larger particles (1μm<Powder diameter<5μm) are too thick for electron transmission, therefore, a thinning process was performed. Samples were prepared from an epoxy-hardener-sample mix (EPOTEK 353 ND), hardened at room temperature. Conventional

mechanical thinning and dimpling, followed by ion milling (Gatan® Dual Ion Mill Model 600) utilizing a LN_2 cold stage to perforation, was applied.

A small number of conventional (Cu-K_α) XRD studies were conducted using a Scintag® XPS 2000 X-ray diffractometer employing the Bragg-Brentano focusing geometry and a horizontal goniometer axis. The sample holder used in this geometry is a specially cut quartz sample holder with a rectangular cavity etched into the surface to accommodate the powder. The cavity was filled with powder and the excess was removed from the surface of the sample holder by scraping with a razor blade. Amorphous ribbon specimens were fixed onto no-background glass holders with Vaseline. This type of glass holder is particularly useful to distinguish low intensity amorphous humps at lower angles. Both free and wheel sides of the as-rapidly solidified ribbons were examined for angles in the range $10° \leq 2\theta \leq 120°$ with a step size of 0.02°.

Most of the X-ray diffraction studies were conducted using synchrotron radiation at the 6ID-D beamline of the Advanced Photon Source (APS) in Argonne National Laboratory (ANL), U.S. Department of Energy (DOE), in collaboration with the Midwest Universities Collaborative Access Team (MUCAT). Synchrotron radiation has many benefits over conventional laboratory sources [62, 64, 65], the most important being short wavelength, high brilliance, high collimation with small angular divergence of the beam, and high level of polarization. The diffraction data was collected using either a MAR345 image plate detector or a charge coupled detector (CCD) in Debye-Scherrer (transmission X-ray diffraction) geometry from the entire sample over a wide angular range. These detectors both have high spatial resolution (4096 x 4096) and high count rates. The devitrification experiments were conducted *in-situ* during isothermal and isochronal heating. The crystal specimens were rotated for improved powder averaging. The schematic of the experimental set-up and the furnace used in this study are shown in Fig. 16 (a) and (b).

The powder specimens were inserted into 2 mm diameter quartz capillary tubes. For each experimental condition a minimum of three sets of tubes were prepared. For room temperature experiments the sample tubes were sealed with an epoxy mixture to ensure that the powders did not escape the tube.

Ribbon samples were cut into small pieces (1cm long) and stacked (at least 20 pieces per tube) into glass capillary tubes. The thicknesses of the tube walls are 10μm, which is thin enough to transmit X-rays at the applied energy. The quartz capillary tubes used for high temperature time resolved experiments were backfilled with Argon gas then sealed to prevent oxidation. Care was taken to prevent unwanted annealing of powders during sealing by inserting glass fibers between the ribbons and the region of the capillary that was sealed. Sealing of the capillaries was accomplished by inserting a glass rod into the end, followed by flash heating at the point of closure.

For liquid structure analysis, samples were cast initially into rods of 15 mm length. The rods were then fractured and rod pieces were inserted into 2 mm quartz tube that first C-deposited on the inside surface to prevent reaction of the melt with the quartz. These samples were then sealed under an Ar atmosphere using the method described above. Diffraction patterns from empty quartz capillaries were always collected and subtracted from the liquid data sets to provide background corrections. The diffraction data from amorphous ribbon samples were collected at room temperature without the use of a sample holder.

Differential scanning calorimetry (DSC) and differential thermal analysis (DTA) were carried out using a Perkin Elmer® DSC Pyris-1 and DTA 7 instruments, respectively. For DSC experiments, the Al sample pan was filled with an average sample weight of 10 mg of powders or ribbon fragments and sealed with an Al cover. Temperature and heat flow calibrations were conducted using In and Zn standard samples. For DTA measurements powder and ribbon samples were inserted into small alumina crucibles with an average sample weight of 40 mg. After each isothermal and/or isochronal thermal scan, a subsequent

run was performed to calculate the baseline. A protective gas atmosphere of pure Ni was employed for each thermal analysis experiments.

Chemical distributions in the as-solidified ribbons was investigated using 3D APT microscopy (LEAP 3000X) in collaboration with the University of North Texas. Sharp needle-shaped samples for atom probe tomography analysis were prepared using a focused ion beam (FIB) instrument with Ga ion milling.

Thesis organization

This dissertation is written in the alternate paper format and is composed of five original manuscripts. The references are cited after each chapter. The first chapter is a general "Overview", including introduction, literature review, and experimental procedure.

The second chapter, entitled "Characterization of hypereutectic Al-Si powders solidified under far-from equilibrium conditions," was published in *Metallurgical and Materials Transactions A* in 2007. The authors were Y. Eren Kalay (graduate student and teaching assistant at the Materials Science and Engineering Department of Iowa State University and research assistant at the Ames Laboratory of the U.S. Department of Energy, L. Scott Chumbley (professor and graduate advisor in the Materials Science and Engineering Department of Iowa State University and primary investigator at the Ames Laboratory of the U.S. Department of Energy), Iver E. Anderson (adjunct professor and graduate advisor in the Materials Science and Engineering Department of Iowa State University and primary investigator at the Ames Laboratory of the U.S. Department of Energy), and Ralph E. Napolitano (associate professor in the Materials Science and Engineering Department of Iowa State University and primary investigator at the Ames Laboratory of the U.S. Department of Energy). This manuscript presents the morphological transitions with respect to interface velocity and undercooling observed in Al-Si gas-atomized powders, including a

direct comparison of experimental results with theoretical predictions based on the Jackson-Hunt (JH) and Trivedi-Magnin-Kurz (TMK) solidification models.

The third chapter, entitled "Characterization of a marginal glass former alloy solidified in gas atomized powders," was published in *Materials Science and Engineering A* in 2008. The authors were Y. Eren Kalay, L. Scott Chumbley, and Iver E. Anderson. This manuscript reveals the metastable phase hierarchy and glass formation during vitrification of the marginal glass former $Al_{90}Sm_{10}$ rapidly solidified using high pressure He gas atomization (HPGA).

The fourth chapter, entitled "Crystallization behavior in a highly driven marginal glass forming alloy," was published in *Journal of Non-Crystalline Solids* in 2008. The authors were Y. Eren Kalay, L. Scott Chumbley, and Iver E. Anderson. This manuscript focuses on the devitrification path of the marginal glass former $Al_{90}Sm_{10}$ and discusses the appearance of a pre-peak on high energy X-ray diffraction pattern.

The fifth chapter, entitled "Local structure of the marginal glass forming Al-Sm alloy," will be submitted to *Philosophical Magazine A* in 2009. The authors are Y. Eren Kalay, L. Scott Chumbley, Matthew J. Kramer (adjunct professor in the Materials Science and Engineering Department of Iowa State University and primary investigator at the Ames Laboratory of the U.S. Department of Energy) and Iver E. Anderson. This manuscript discusses the local structure in quenched $Al_{(100-x)}Sm_x$ (x=8, 10, and 12) investigated using a combination of high resolution electron microscopy (HRTEM) and high energy synchrotron X-ray diffraction (HEXRD). It presents atomic structure models constructed using Reverse Monte Carlo (RMC) simulations coupled with Voronoi Tesellation analysis. A model based on structural rearrangements in the melt is proposed to explain the high number of density nanocrystal formation.

The sixth chapter, entitled "Initial crystallization in a nanostructured Al-Sm rare earth alloy," will be submitted to *Journal of Non-Crystalline Solids* in 2009. The authors are Y.

Eren Kalay, C. Yeager (undergraduate student in the Materials Science and Engineering Department at Missouri University of Science and Technology), L. Scott Chumbley, Matthew J. Kramer, and Iver E. Anderson. This manuscript highlights the transformation kinetics and microstructural evolution that occur during initial stages of crystallization in a highly driven $Al_{90}Sm_{10}$ alloy containing pre-existing fcc-Al nanocrystals. The effect of local structure on crystallization kinetics is discussed.

The seventh chapter is the "General Conclusions" which summarizes the important results of the dissertation and gives recommendations for future studies.

Reference

1. Duwez P., Willens R.H., and Klemnet W., Journal of Applied Physics, 1960. **31**: p. 1136-1137.
2. Giessen B.C., 1969: Metallurgical Society of AIME.
3. Kurz W. and Fisher D.J., 1992, Trans Tech Publications. p. 63-89.
4. White C.W., et al., 1983: p. 81.
5. Picraux S.T. and Follstaedt D.M., 1983: p. 287.
6. Baker J.C. and C. J.W., ASM, Metals Park, 1971: p. 23-58.
7. Boettinger W.J. and Corriell S.R., Sahm P.R, Jones H., and A. C.M., Editors. 1986.
8. Boettinger W.J. and Perepezko J.H., L. H.H., Editor. 1993. p. 17-78.
9. Cahn J.W., Coriell S.R., and Boettinger W.J. 1980.
10. Szade, J., G. Skorek, and A. Winiarski, Journal of Crystal Growth, 1999. **205**: p. 289 - 293.
11. Turnbull D., Journal of Applied Physics, 1950. **21**: p. 1022.
12. Turnbull D., Journal of Chemical Physics, 1952. **20**: p. 411.

13. Turnbull D., Contemporary Physics, 1969. **10**: p. 473.

14. Porter D.A. and Easterling K.E., 1992: Nelson Thornes Ltd.

15. www.wikipedia.com.

16. Aziz M.J., Journal of Applied Physics, 1982. **53**: p. 1158-1168.

17. Aziz M.J. and K. T., Acta Metallurgica, 1988. **36**: p. 2335-2347.

18. Jackson K.A., Gilmer G.H., and Leamy H.J., White C.W. and Peercy P.S., Editors. 1980, Academic Press: New York.

19. Jones H. and Kurz W., Z. Metallkde, 1981. **72**: p. 792.

20. Jackson K.A. and Hunt J.D., Transactions of the Metallurgical Society of AIME, 1966. **236**: p. 843-852.

21. Hillert M., Jernkontorests Ann., 1957. **141**: p. 757-782.

22. Zener C., Transactions of the Metallurgical Society of AIME, 1946. **167**: p. 550-565.

23. Trivedi R. and Kurz W., Metallurgical Transactions A, 1991. **22A**: p. 3051-3057.

24. Trivedi R., Magnin P., and Kurz W., Acta Metallurgica, 1987. **35**: p. 971-980.

25. Boettinger W.J., Coriell S.R., and Trivedi R.,, Mehrabian R. and P. P.A., Editors. 1988. p. 13.

26. Bolling G.F. and Tiller W.A., Journal of Applied Physics, 1961. **32**: p. 2587.

27. Papapetrou Z., Fur Kristallographie, 1935. **92**: p. 89.

28. Ivantsov, G.P., 1947.

29. Mullins W.W. and Sekerka R.F., Journal of Applied Physics, 1963. **34**: p. 323.

30. Mullins W.W. and Sekerka R.F., Journal of Applied Physics, 1964. **35**: p. 444.

31. Langer J.S. and Müller-Krumbhaar H., Acta Metallurgica, 1978. **26**: p. 1681-1697.

32. Langer J.S., Science, 1989. **243**: p. 1150.

33. Jin F., 1995, Iowa State University: Ames.

34. Bendersky L.A. and Boettinger W.J., Rapid quenched metals, 1985(edited by Steeb S. and Warlimont H.,): p. 887.

35. Boettinger W.J., et al., 1987. **80**: p. 17.

36. Van Aken D.C. and Fraser H.L., Acta Metallurgica, 1985. **33**: p. 963.

37. Inoue A. and Hashimoto K., ed. Kawazoe Y. 2001: Springer.

38. Zallen R., 1983, Blacksburg, Virginia: John Wiley & Sons, Inc.

39. Ossi P.M., 2003, Berlin: Springer.

40. Chiang Y., Birnie D., and Kingery W.D., 1997, New York: John Wiley and Sons.

41. Wilde G., Sieber H., and Perepezko J.H., Scripta Materialia, 1999. **40**: p. 779-783.

42. Turnbull D. and Fisher J.C., Journal of Chemical Physics, 1949. **17**: p. 71-73.

43. Greer A.L., Science, 1995. **267**: p. 1947.

44. Johnson W.L., MRS Bulletin, 1999. **24**: p. 42-55.

45. Loffler J.,Intermetallics, 2003. **11**: p. 529.

46. Schneider S., Intermetallics, 2001. **11**: p. 529.

47. Frank F.C., Proceedings of the Royal Society of London Series A Mathematical and Physical Sciences, 1952. **215**: p. 43.

48. Inoue A., Zhang T., and Masumoto T., Journal of Non-Crystalline Solids, 1993. **156-158**: p. 598-602.

49. Egami T. and Waseda Y., Journal of Non-Crystalline Solids, 1984. **64**: p. 113-134.

50. Inoue A., Acta Materialia, 2000. **48**: p. 279-306.

51. Inoue A., Progress in Materials Science, 1998. **43**: p. 365-520.

52. Egami T., Liebermann H.H., Editor. 1993, Marcel Dekker: Parsippany, New Jersey.

53. Gibson J.M., 2007: Lecture at Neutron and X-Ray School at Argonne National Laboratory.

54. Stratton W.G. and Voyles P.M., Journal of Physics: Condensed Materials, 2007. **19**.

55. Stratton W.G., et al., Intermetallics, 2006. **14**: p. 1061-1065.

56. Stratton W.G., et al., Applied Physical Letters, 2005. **86**: p. 141910.

57. Voyles P.M., Gibson J.M., and Treacy M.M., Journal of Electron Microscopy, 2000. **49**: p. 259-266.

58. Voyles P.M. and Muller D.A., Ultramicroscopy, 2002. **93**: p. 147-159.

59. Treacy M.M., Ultramicroscopy, 2007. **107**.

60. Waseda Y., 1980: Mc-Graw-Hill, Inc.

61. Aur S., et al., Journal of Non-Crystalline Solids, 1984. **61-62**: p. 331-336.

62. Gerson A.R., et al., 1999, New york: Wiley-VCH.

63. Schaefer R.J., et al., Journal de Physique. IV, 1994. **4**: p. 415-421.

64. Kramer M.J and Sordelet D.J., Journal of Non-Crystalline Solids, 2005. **351**(19-20): p. 1586-1593.

65. Sordelet J.S., et al., Journal of Non-crystalline Solids, 2001. **290**: p. 163-172.

66. Lytle F.W., Journal of Synchrotron Radiation 1999. **6**: p. 123-134.

67. Sayers D.E., Stren E.A., and Lytle F.W., Physical Review Letters, 1971. **27**: p. 1204-1207.

68. Meneghini C., Gualtieri A.F., and Siligardi C., Journal of Applied Crystallography, 1999. **32**: p. 1090-1099.

69. Fukunaga T., Suzuki K., and Mizutani U., Journal of Non-Crystalline Solids, 1992. **150**(1-3): p. 15-20.

70. Itoh K., et al., Journal of Non-Crystalline Solids, 2007. **353**(32-40): p. 3049-3052.

71. Itoh K., et al., Journal of Alloys and Compounds, 2007. **434-435**: p. 180-182.

72. Itoh K., et al., Journal of Non-Crystalline Solids, 2007. **353**(18-21): p. 1975-1978.

73. McGreevy R.L., International Jornal of Modern Physics B, 1993. **7**: p. 2965.

74. McBride W.E., Cockayne D.J.H., and Goringe C.M., Ultramicroscopy, 1999. **76**: p. 115.

75. Ohkubo T., et al., Materials Science and Engineering A, 2001. **312**(1-2): p. 274-283.

76. Hirata A., et al., Physical Review B, 2006. **74**: p. 184204.

77. McGreevy R.L., Journal of Non-Crystalline Solids, 1993. **156-158**: p. 949.

78. McGreevy R.L. and Howe M.A., Annual Review of Materials Science, 1992. **22**: p. 217-242.

79. McGreevy R.L. and Pusztai L., Molecular Simulation, 1988. **1**: p. 359-367.

80. Keen D.A. and McGreevy R.L., Nature, 1990. **344**: p. 423-442.

81. Pusztai L. and Scvib E., Journal of Non-Crystalline Solids, 1993. **156-158**: p. 973.

82. Evans R.A., Molecular Simulation, 1990. **4**: p. 409.

83. Gurman S.J. and McGreevy R.L., Journal of Physics: Condensed Materials, 1990. **2**: p. 9463-9474.

84. Roik S., Kazimirov V.P., and Sokolskii V.E., Journal of Structural Chemistry, 2004. **45**: p. 648-656.

85. Fukunaga T., et al., Intermetallics, 2006. **14**: p. 893-897.

86. Medvedev N.N., Journal of Computational Physics, 1986. **67**: p. 223.

87. Wu R.I., Wilde G., and Perepezko J.H., Materials Science and Engineering A, 2001. **301**: p. 12-17.

88. Battezati L., Pozzovivo S., and Rizzi P., N. H.S., Editor. 2004. p. 341-364.

89. Koster U. and Schunemann U., L. H.H., Editor. 1993, Marcel Dekker, Inc.: Parsippany, New Jersey.

90. Avrami M., Journal of Chemical Physics, 1939. **7**: p. 1103.

91. Avrami M., Journal of Chemical Physics, 1940. **8**: p. 212.

92. Avrami M., Journal of Chemical Physics, 1941. **9**: p. 177.

93. Christian J.W., 1975, Oxford: Pergamon Press.

94. Calka A. and Radlinski P.A. in MRS. 1987. Warrendale, PA.

95. Venkataraman S., et al., Physical Review B, 2007. **75**: p. 104206.

96. Otooni M.A., Materials Science, ed. Gonser U. 1998: Springer.

97. Jones H., Suryanarayana C., Editor. 1999, Pergamon: Glden, Colorado.

98. Jones H., Mehrabian R., Kear B.H., and Cohen M., Editors. 1978.

99. Perepezko J.H., Mehrabian R., Kear B.H., and Cohen M., Editors. 1980. p. 56.

100. Anderson I.E. and K. M.P., TMS-AIME, 1986(Undercooled Alloy Phases edited by Coolings E.W., and Koch C.C.): p. 269-285.

101. Grant N.J., Jones H., and Lavernia E.J., O. M.A., Editor. 1998.

102. Ogushi M., et al., Mater. Trans. JIM 1990. **31**: p. 1005-1010.

103. Massalski T.B., 1986, Metals Park, OH: American Society for Metals.

104. Zhou S.H. and Napolitano R.E., Metallurgical and Materials Transactions A, 2008. **39A**: p. 502-512.

105. Zhou S.H. and Napolitano R.E., Metallurgical and Materials Transactions A, 2007. **38A**: p. 1145-1151.

106. Zhou S.H. and Napolitano R.E., Physical Review B, 2008. **in press**.

107. Buschow K.H.J., Journal of the Less-Common Metals, 1965. **8**: p. 209-212.

108. Bècle C. and Lemaire R., Acta Crystallograhica, 1967. **23**: p. 840-845.

109. Runnals O.J.C and Lorimer G.W., Journal of the Less-Common Metals, 1965. **8**: p. 75-77.

110. Buschow K.H.J. and Van Vucht J.H.N., Philips Research Reports, 1967. **22**: p. 233-245.

111. Iandelli A., National Physical Laboratory, U.K., Symposium, 1959. **1** (9).

112. Wernick J.H. and Geller S., Transactions of the Metallurgical Society of AIME, 1960. **218**: p. 866-868.

113. Cannon J.F. and Hall H.T., Journal of the Less-Common Metals, 1975. **40**: p. 313-328.

114. Casteels F., Journal of the Less-Common Metals, 1967. **12**: p. 210-220.

115. Van Vucht J.H.N. and Buschow K.H.J., Philips Research Reports, 1964. **19**: p. 319-322.

116. Pearson's Handbook of Crystallographic Data for Intermetallic Phases. 1991: ASM International, Materials Park.

117. Levi C.G. and Mehrabian R., Metallurgical Transactions A, 1982. **13A**: p. 221-234.

118. Levi C.G. and Mehrabian R., Metallurgical Transactions A, 1982. **13A**: p. 13-23.

119. Boettinger W.J., Bendersky L., and Early J.G., Metallurgical Transactions A 1986. **17A**: p. 781-790.

120. Bendersky L.A, et al., Materials Science and Engineering A 1991. **134**: p. 1098-1102.

121. Pierantoni M., et al., Acta Metallurgica Materialia, 1992. **40**: p. 1637-1644.

122. Allen D.R., Gremaud M., and P. J.H., Materials Science and Engineering A, 1997. **A226-228**: p. 173-177.

123. Birol Y., Journal of Materials Science, 1996. **31**: p. 2139-2143.

124. Wang Z., et al., Trans. Nonferrous Met. Soc. China, 2000. **10**: p. 699-701.

125. Kim T., et al., Materials Science and Engineering A, 2001. **304-306**: p. 617-620.

126. Trivedi R., Jin F., and Anderson I.E., Acta Materialia, 2003. **51**: p. 289-300.

127. Genau A.L., 2004, Iowa State University: Ames.

128. Genau A.L., Anderson I.E., and Trivedi R., TMS-AIME, 2004.

129. Battezati L., et al., Materials Science and Engineering A, 1994. **179-180**: p. 600-604.

130. Guo J.Q., et al., Materials Letter, 1995. **24**: p. 133-138.

131. Rizzi P., et al.,. Materials Science and Engineering A, 2001. **304-306**: p. 574-578.

132. Rizzi P., et al., Nanostructured materials 1998. **10**: p. 767-776.

133. Antonowicz J., Journal of Non-Crystalline Solids, 2005. **351**: p. 2383-2387.

134. Kulik T., Journal of Non-Crystalline Solids, 2001. **287**: p. 145-161.

135. Schroers J., et al., Applied Physical Letters, 1999. **74**: p. 2806-2808.

136. Wilde G., Sieber H., and Perepezko J.H., Journal of Non-Crystalline Solids, 1999. **250-252**: p. 621-625.

137. Perepezko J.H., et al., Journal of Non-Crystalline Solids, 2003. **317**: p. 52-61.

138. Perepezko J.H., Hebert R.J., and Tong W.S., Intermetallics, 2002. **10**: p. 1079-1088.

139. Perepezko J.H., et al., Materials Science and Engineering A, 2007. **449-451**: p. 84-89.

140. Foley J.C., AllenD.R., and Perepezko J.H., Scripta Materialia, 1996. **35**: p. 660-665.

141. Hebert R.J. and Perepezko J.H., Materials Science and Engineering A, 2004. **375-377**: p. 728-732.

142. Foley J.C., Allen D.R., and Perepezko J.H., Scripta Materialia, 1996. **35**: p. 655-660.

143. Boucharat N., et al., Materials Science and Engineering A, 2004. **375-377**: p. 713-717.

144. Allen D.R., Foley J.C., and P. J.H., Acta Metallurgica, 1998. **46**(No.2): p. 431-440.

145. Das S.K., et al., Materials Science and Engineering A, 2001. **304-306**: p. 159-165.

146. Gao M.C., et al., Materials Science and Engineering A, 2008. **485**: p. 532-543.

147. Kelton K.F., et al., Journal of Non-Crystalline Solids, 2003. **317**: p. 71-77.

148. Kelton K.F., Acta Materialia, 2000. **48**: p. 1967-1980.

149. Kelton K.F., Journal of Non-Crystalline Solids, 2000. **274**: p. 147-154.

150. Hirata A., Hirotsu Y., and Matsubara E., Materials Transaction, 2005. **46**: p. 2781-2784.

151. Schroers J., et al., Applied Physical Letters, 1999. **74**: p. 2806.

152. Schneider S., Thiyagarajan P., and Johnson W.L,. Applied Physical Letters, 1995. **68**: p. 493-495.

153. Hirata A., et al., Journal of Microscopy, 2006. **223**(3): p. 191-194.

154. Wang X.L., et al., Physical Review Letters, 2003. **91**: p. 265501.

155. Tian N., et al., Mater. Trans. JIM, 2005. **46**: p. 2880–2885.

156. Kajiwara K., et al., Materials Science and Engineering A, 2004. **375-377**: p. 738-743.

157. Anderson, R., Materials Research Society Symposium Proceedings, 1990. **199**.

158. Schechtman D. and Gutmanas E., Praktishe Metall., , 1981. **18**: p. 578-593.

159. Montone A. and Antisari M.V., Micron, 2003. **34**: p. 79-83.

160. Ulan J.G., Schooley C., and Gronsky R., Mat. Res. Soc. Symp. Proc., 1990. **19**.

161. Chowdhury J.S., Freundlich A., and Sheppard T., Mat. Res. Soc. Symp. Proc. , 1990. **199**.

162. Giannuzzi L.A. and Stevie F.A., Micron, 1999. **30**: p. 197-204.

163. Cairney J.M and Munroe P.R., Materials Characterization, 2001. **46**: p. 297-304.

164. Chumbley L.S., Laabs F.C., and Sanders S.C., Mat. Res. Soc. Symp. Proc., 1990. **199**.

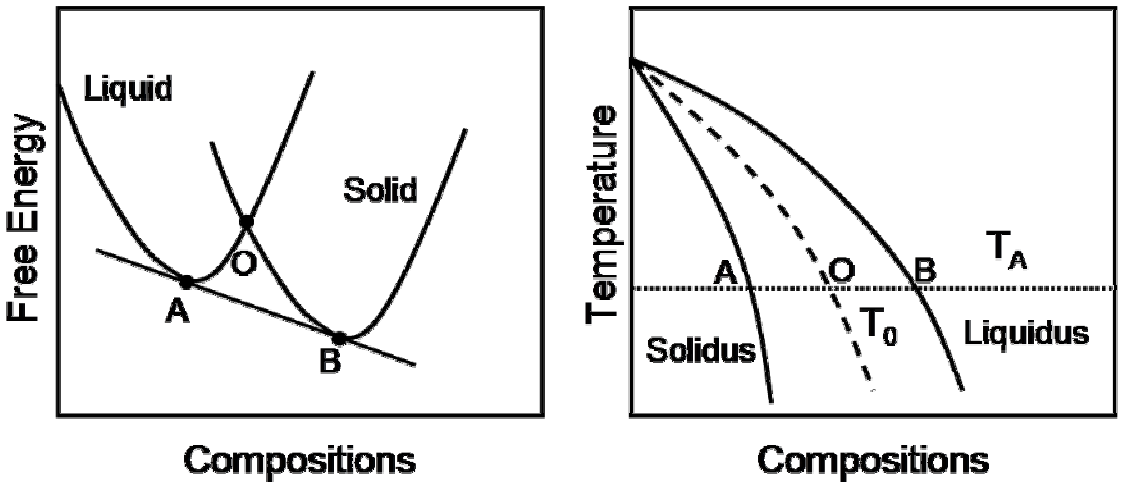

Figure 1. Schematic free energy curves and phase diagram showing T_0 curve.

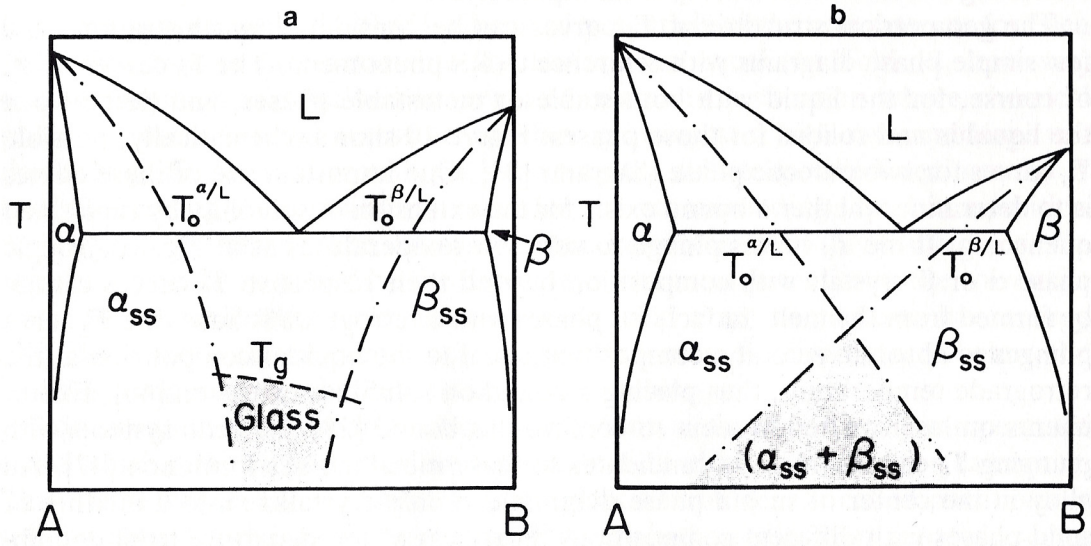

Figure 2. Schematic representation of T_0 curves of different eutectic systems, (a) Plunging T_0 curves, (b) Intersecting T_0 curves. Figure from [8]

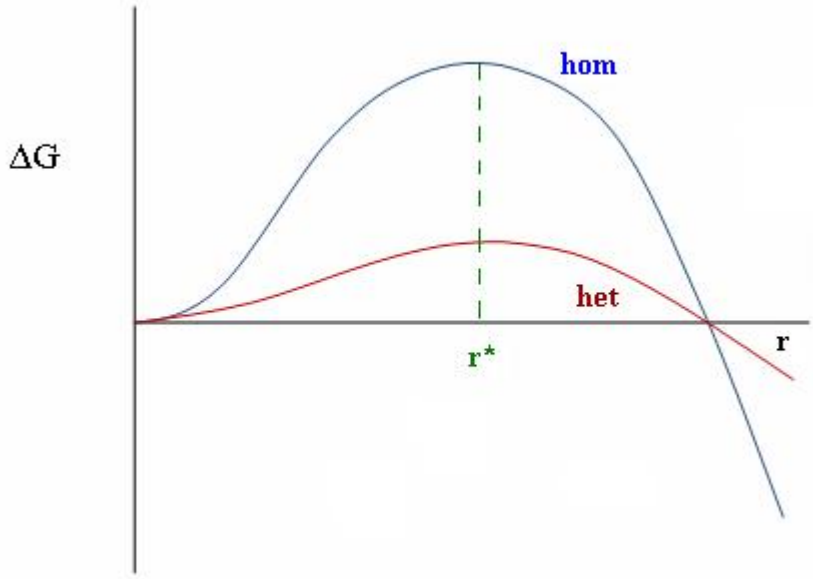

Figure 3. The free energy change related to homogeneous and heterogeneous nucleation. Figure from [15].

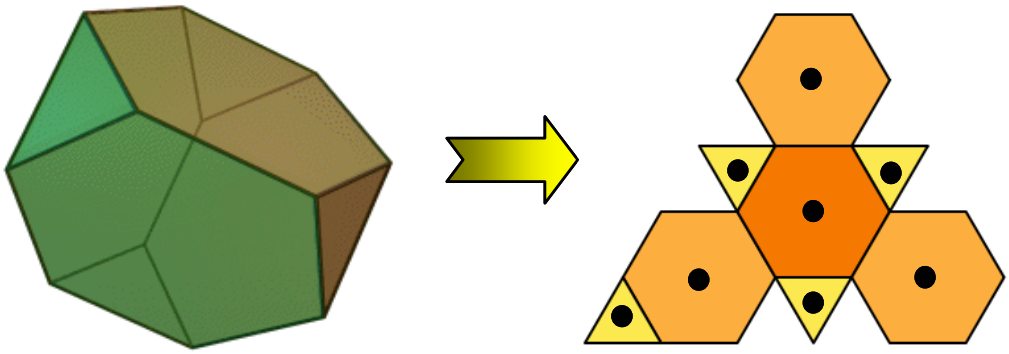

Figure 4. Truncated tetrahedrons in 3-D and 2-D. Black points represent the atoms in the Voronoi polyhedron with <400400> indices. Figure from [15].

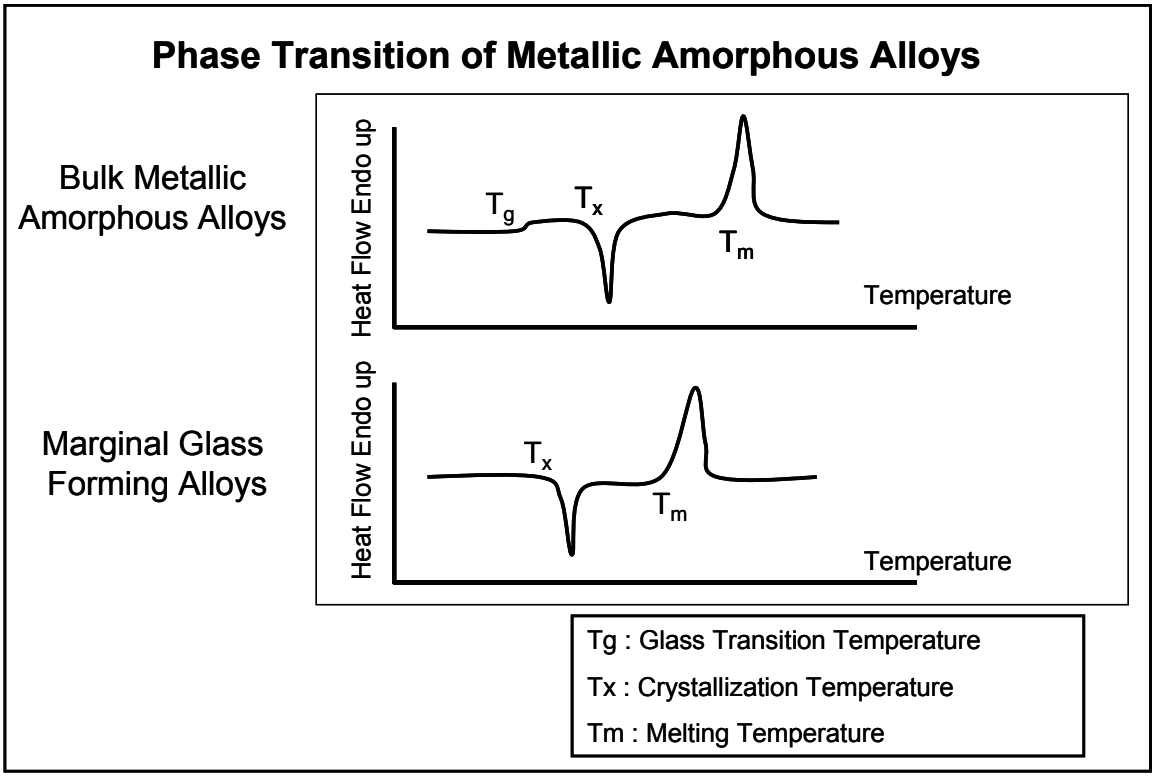

Figure 5. Specific temperatures observed during an isochronal thermal analysis for bulk metallic amorphous and marginal glass forming alloys.

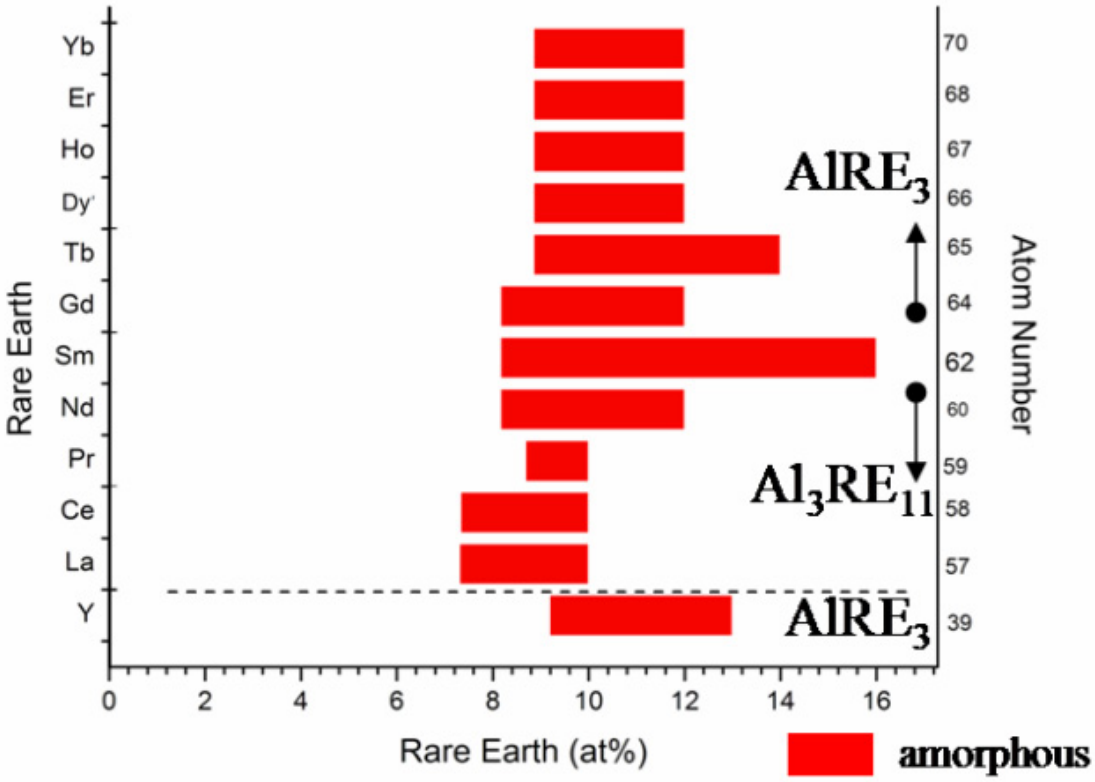

Figure 6. Glass formation composition range for Al-RE binary systems. Figure modified from [51].

Figure 7. (a) TEM bright field image of Al-6wt%Si submicron sample (1µm > $2r_0$ > 0.5µm) A : supersaturated zone, B : precipitate free zone, C : cellular region (1µm > $2r_0$ > 0.5µm) (b) TEM bright field image of the anomalous morphology of a silicon segregate (pro-eutectic phase) observed in some of the Al-Si powders [117]

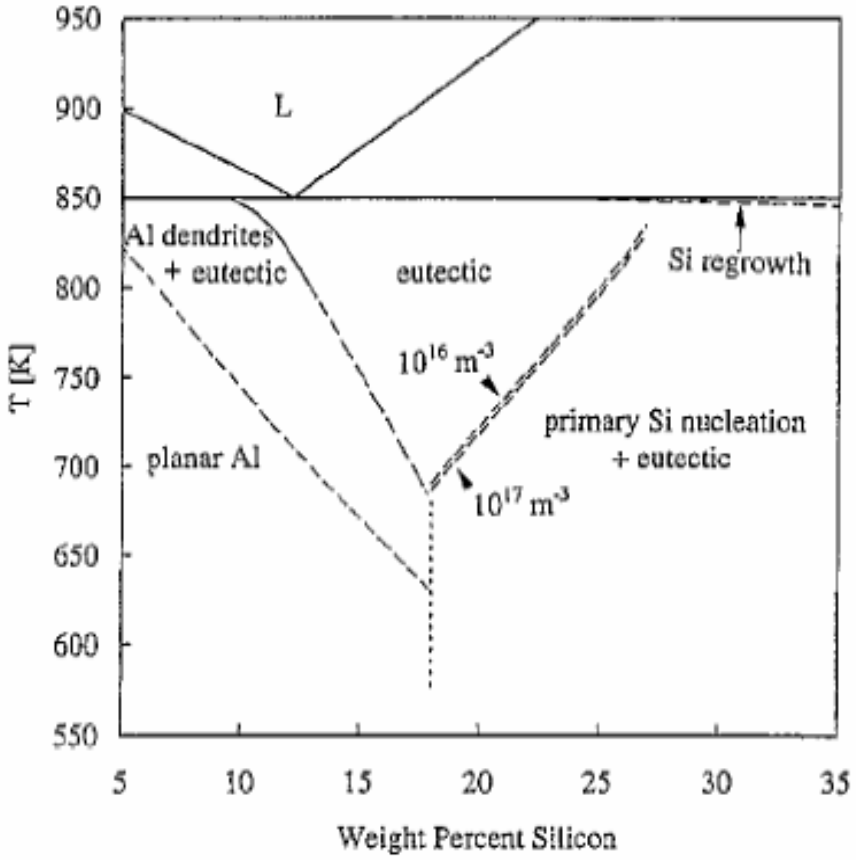

Figure 8. Interface temperature microstructure map for laser-processed Al-Si alloys: (-) equilibrium phase boundaries; (- - -) calculated microstructure transition boundaries; (. . .) boundaries between primary Si and Al re-growth. Figure from [122].

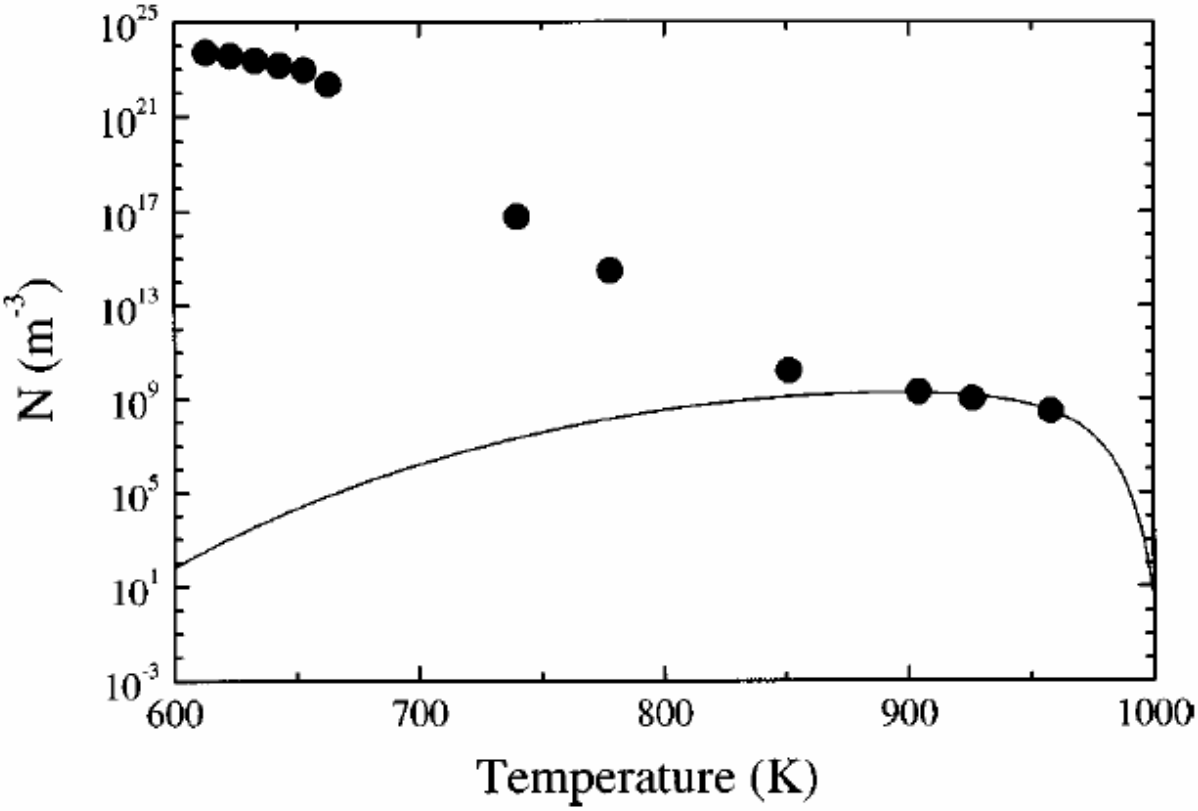

Figure 9. The number densities measured from electron microscope and small angle neutron scattering data (•). The solid line shows the trend of nucleation according to classical nucleation theory. Figure from [135].

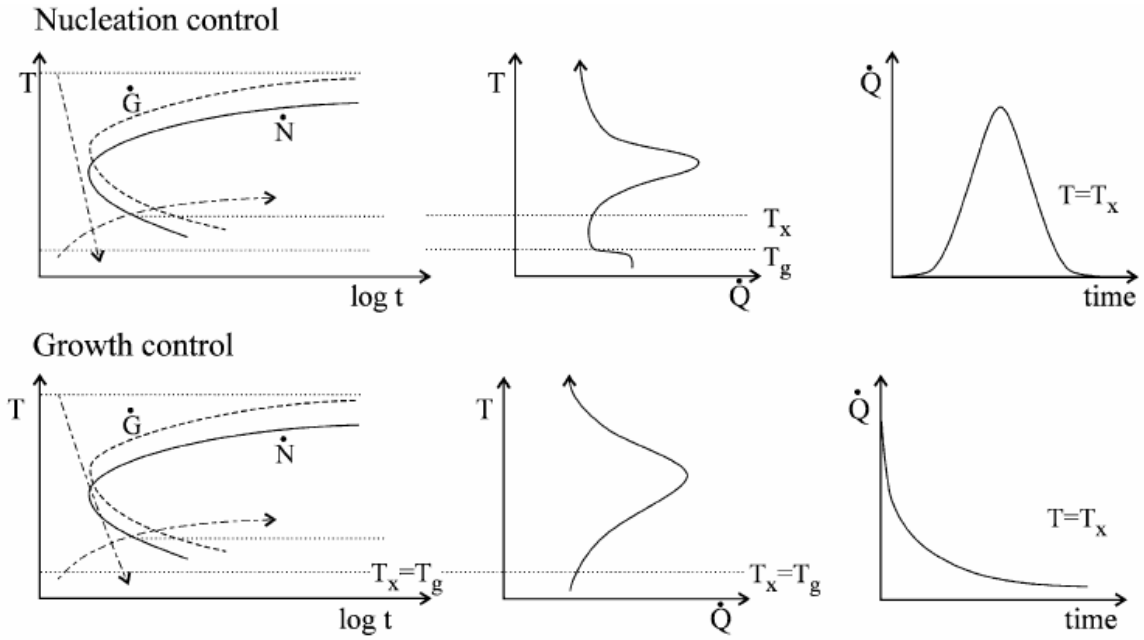

Figure 10. Schematics showing kinetics of metallic glass formation: nucleation control vs. growth control (dQ/dt: Heat evolution rate).Figure from [137].

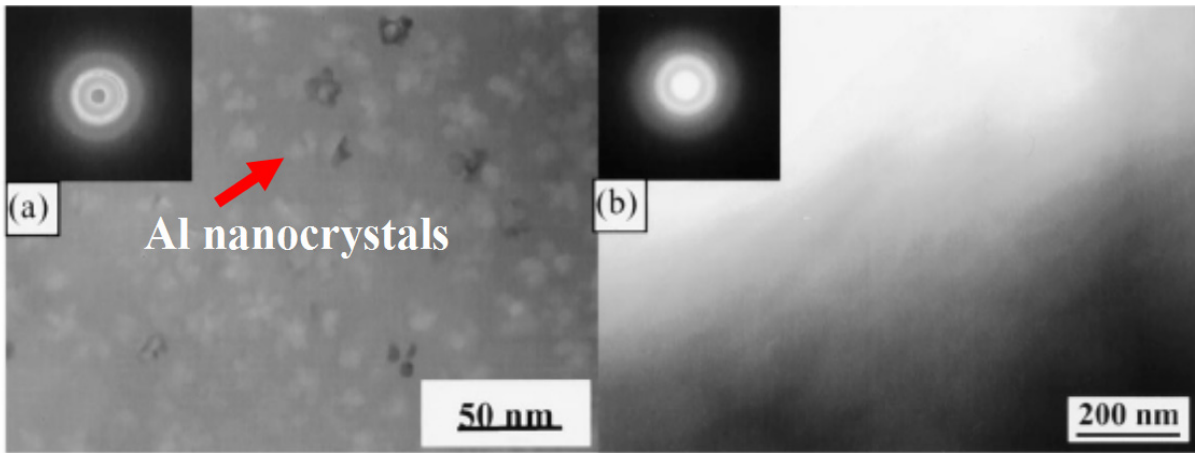

Figure 11. TEM bright field images and SAED patterns (insets) of $Al_{92}Sm_8$ samples. (a) Melt-spun ribbon after annealing at 150°C for 10 min. (b) Cold-rolled sample after annealing at 150°C for 60 min. Figure from [41].

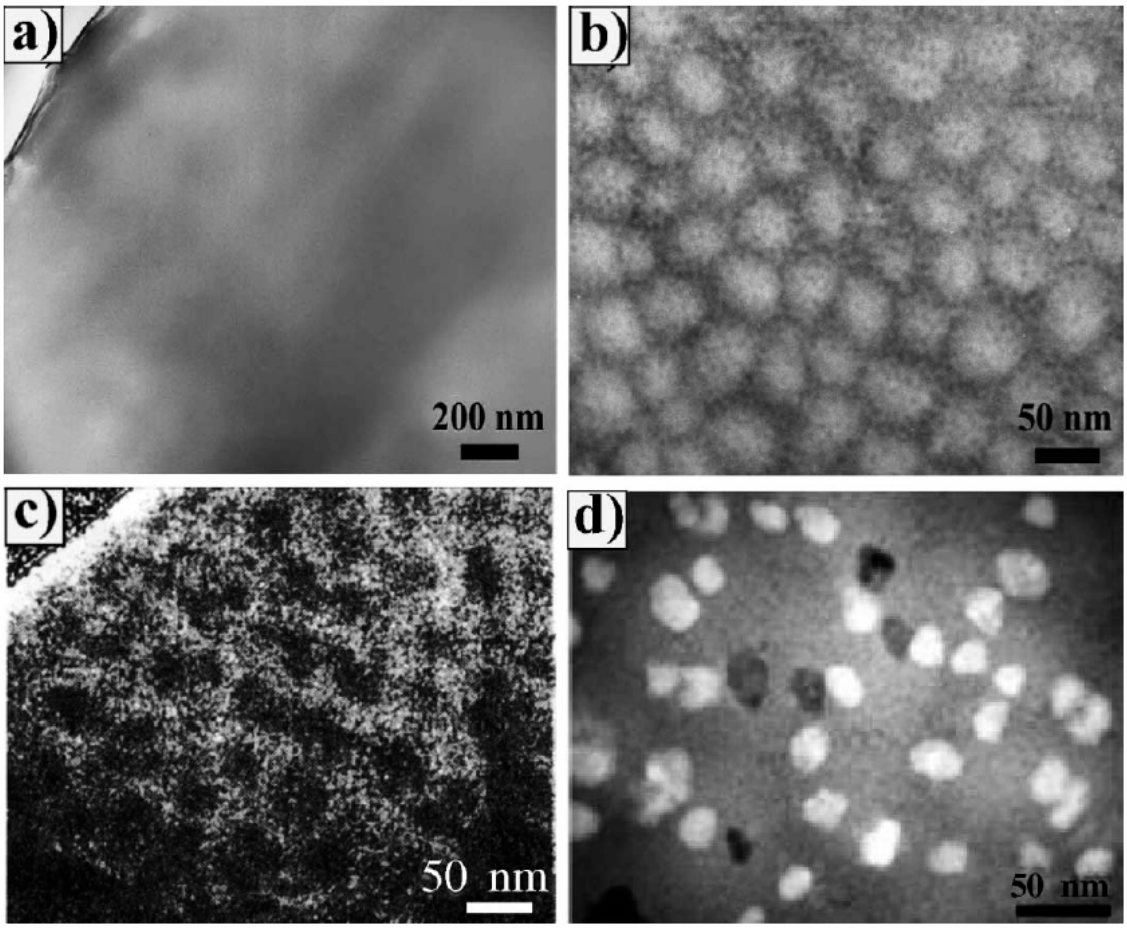

Figure 12. (a) as-quenched amorphous state, (b) after annealing for 223 °C for 1 min. contrast attributed to phase separation, (c) jump ratio image near Ni_{M23} loss edge, (d) after first crystallization. Image from [147].

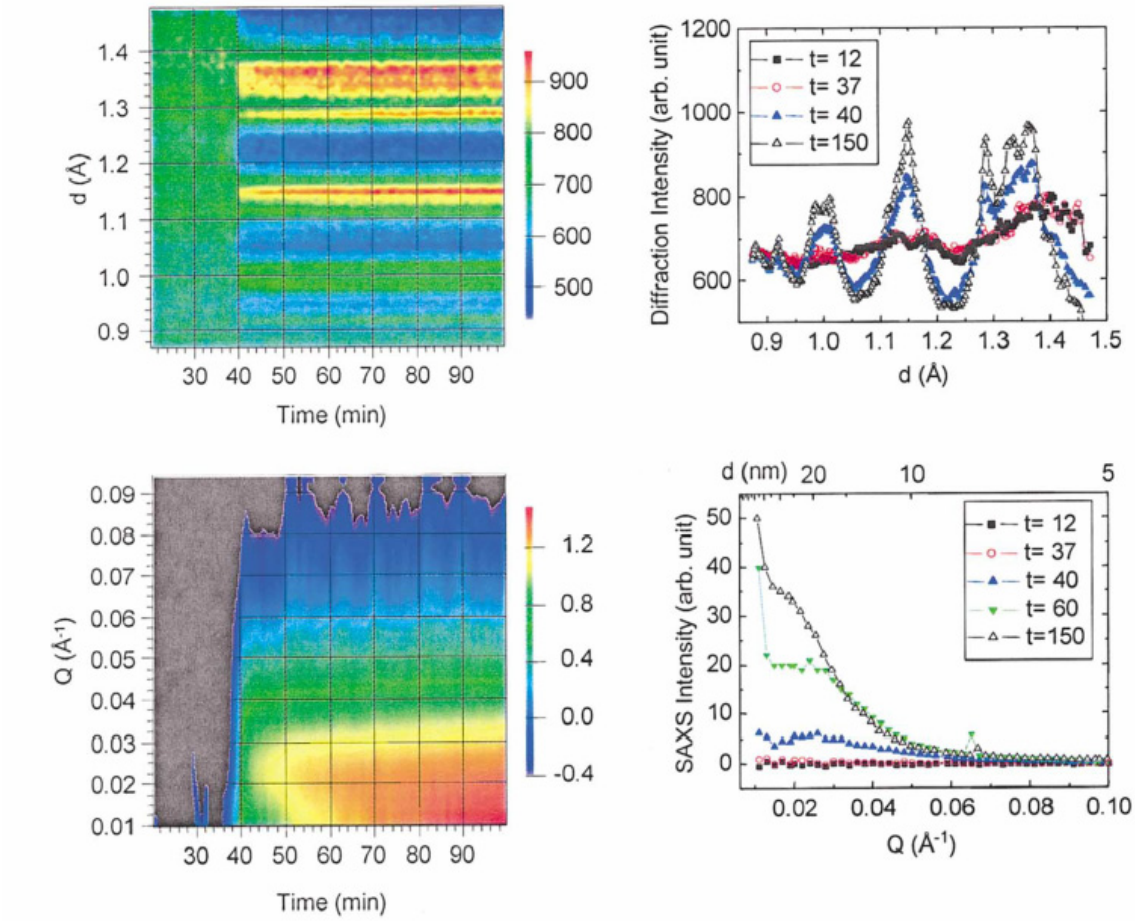

Figure 13. Simultaneous in-situ X-ray diffraction and small angle X-ray scattering results showing phase separation taking place prior to crystallization of a $Zr_{52.5}Cu_{17.9}Ni_{14.6}Al_{10}Ti_5$ amorphous alloy. Figure from [154].

Figure 14. High pressure gas atomizer, Ames Laboratory.

Figure 15. Copper chill block melt spinner, Ames Laboratory.

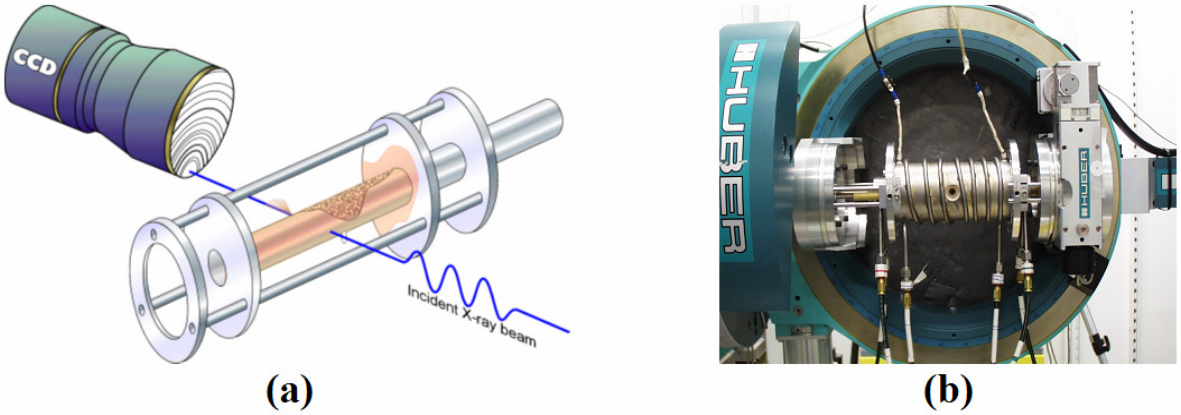

Figure 16. (a) Schematic of the experimental set-up showing the positions of incident X-ray beam, CCD, and the (b) furnace.

Table 1. Effects of solute Péclet number. Table from [8].

Subject	l	Pe<<1	Pe~1	Reference
Eutectic growth	Eutectic spacing	Jackson-Hunt Analysis	$\lambda^2 V \neq$ constant Trivedi – Magnin- Kurz Analysis	[18-24]
Dendritic growth	Dendritic tip radius	Trivedi, Lipton-Glicksman-Kurz Analysis	Boettinger-Coriell, Lipton-Kurz-Trivedi Analysis	[25-32]
Microsegregation	Cell spacing or primary dendrite	Scheil-type analysis	Flat solute profiles	[33-35]
Interface shape stability	Interface perturbation wavelength	Constitutional supercooling	Absolute stability	
Solute trapping	Interatomic distances	Local equilibrium	Partitionless solidification	[14, 15]

Table 2. Examples of bulk metallic glasses and marginal glass formers (RE: rare-earths, TM: Transient metals)

Bulk Metallic Glasses	***Marginal Glass Formers***
Vitreloy ®	Finemet®
($Zr_{41.2}Ti_{13.8}Cu_{12.5}Ni_{10}Be_{22.5}$)	($Fe_{73.5}Cu_1Nb_3Si_{13.5}B_9$)
Vit105®	Nanoperm®
($Zr_{52.5}Ti_5Cu_{17.9}Ni_{14.6}Al_{10}$)	($Fe_{84}Zr_{3.5}Nb_{3.5}B_8Cu_1$)
$Fe_{56}Co_7Ni_7Zr_{10}B_{20}$	Al-RE-TM

Table 3. Crystal Structure Data of the Al-Sm Binary System

Phases	Structure Type	Lattice Constants (Å)			Space Group	Reference
		a	b	c		
α-Sm	Rhombohedral hR9- α-Sm	3.6290		2.6207		[103]
β-Sm	Hexagonal hP2-Mg	3.6630		5.8448 γ:120°		[103]
γ-Sm	Cubic cI2-W	4.1000				[103]
AlSm	Orthorhombic oP16-AlDy	5.8990	11.622	5.6780	Pbcm-57	[107]
AlSm	Orthorhombic oP16-AlDy	5.8990	11.622	5.778	Pbcm-57	[108]
AlSm	Cubic ClCs-cP2	3.7392			$Pm\bar{3}m$-221	[109]
$AlSm_2$	Orthorhombic ?	7.7820	9.3020	11.210	?	[110]
$AlSm_2$	Orthorhombic Co_2Si-oP12	6.6540	5.1930	9.6310	Pnma-62	[110]
$AlSm_3$	Cubic $AuCu_3$-cP4	4.901			$Pm\bar{3}m$-221	[111]
Al_2Sm	Cubic Cu_2Mg-cF24	7.9405			$Fd\bar{3}m$-227	[112]
Al_3Sm	Hexagonal Ni_3Sn-hP8	6.3800		4.5970 γ:120°	$P6_3/mmc$-194	[113]
Al_4Sm ($Al_{11}Sm_3$)	Tetragonal Al_4Ba-tI10	4.2800		9.9000	I4/mmm-139	[114]
Al_4Sm ($Al_{11}Sm_3$)	Tetragonal Al_4Ba-tI10	4.2870		9.9050	I4/mmm-139	[115]
Al_4Sm	Orthorhombic Al_4U-oI20	4.4400	6.3800	13.6200	Imma-74	[114]
$Al_{11}Sm_3$	Orthorhombic $Al_{11}La_3$ -oI28	4.3330	12.8100	9.9700	Immm-71	[110]
Al	Cubic cF4-Cu	4.0495			Fm3m-225	[116]

Table 4. Previous studies on devitrification path of Al-Sm alloy.

	8	**10**	**12**	**14**	
Initial State	PartiallyAmorphous	Amorphous	PartiallyAmorphous	Amorphous	**Reference[129]** Samples produced by single roller melt spinning apparatus and crystal; structure examined by Co-Kα XRD.
1. DSC Peak	197°C α-Al+Amorphous	195°C B1	210°C α-Al+B2+B3+B5	225°C α-Al+B3+B5	
2. DSC Peak	270°C α-Al + B2	290°C α-Al + B2	307°C -	325°C α-Al+B5	
3. DSC Peak	? α-Al + B4	451°C α-Al+B4	451°C α-Al+B4	490°C α-Al+B4	
	8	**10**	**12**	**14**	**Reference[130]** Samples produced by single roller melt spinning apparatus and crystal; structure examined by Cu-Kα XRD.
Initial State	PartiallyAmorphous	PartiallyAmorphous	PartiallyAmorphous	PartiallyAmorphous	
1. DSC Peak	197°C α-Al+Amorphous	234°C α-Al+G1+G3	234°C α-Al+G1+G3	227°C α-Al+G1+G4	
2. DSC Peak	268°C α-Al + G1	307°C -	307°C -	325°C α-Al+G1+G3	
3. DSC Peak	321°C α-Al + G2	451°C α-Al+G2	451°C α-Al+G2	490°C α-Al+G2	
	8	**10**	**12**	**14**	**Reference[131]** Samples produced by single roller melt spinning apparatus and crystal; structure examined by Co-Kα XRD.
Initial State	Amorphous	Amorphous			
1. DSC Peak	Ann. at 200°C α-Al+Amorphous	Ann. at 270°C R1			
2. DSC Peak	Ann. at 320°C α-Al + R5	Ann. at 350°C α-Al + R2 + R3			
3. DSC Peak	Ann. at 600°C α-Al+R4	Ann. at 600°C α-Al+R4			

Table 5. Phases identified during devitrification of $Al_{(100-x)}Sm_x$ (x=8,10,12,and 14).

Phases	Structure	Lattice Constants (Å)		
		a	***b***	***c***
G1	Tetragonal	4.280		9.900
G2	Orthorhombic	13.781	11.019	7.303
G3	Hexagonal	4.597		6.358
G4	Cubic	19.154		
B1	Iso-structure $Al_{20}Cr_2Nd$	?	?	?
B2	Not identified			
B3	Not identified			
B4	Tetragonal	4.440	6.340	13.700
B5	Orthorhombic	4.333	12.810	9.970
R1	Cubic	4.597		
R2	Tetragonal	4.280		9.900
R3	Hexagonal	4.597		6.358
R4	Orthorhombic	4.333	12.810	9.970
R5	Tetragonal	4.280		9.900

Table 6. Powder Classification

Powder Classifications (µm)	Composition Wt%
-90 +75	Al- 38 Sm
-75 +63	Al – 38 Sm
-63 +53	Al – 38 Sm
-53 +45	Al – 38 Sm
-45 +38	Al – 38 Sm
	Al – 12.6 Si
	Al- 15 Si
	Al – 18 Si
	Al – 25 Si
	Al – 50 Si
-38 +32	Same as above
-32 +25	Same as above
-25 +20	Same as above
-20 +15	Al – 38 Sm
	Al – 12.6 Si
	Al- 18 Si
-15 +10	Same as above
-10 +05	Same as above
<03	Al – 38 Sm
	Al – 12.6 Si
	Al- 15 Si
	Al – 18 Si
	Al – 50 Si
<01	Same as above

CHAPTER 2: CHARACTERIZATION OF HYPEREUTECTIC Al-Si POWDERS SOLIDIFIED UNDER FAR-FROM EQUILIBRIUM CONDITIONS

A paper published in *Metallurgical and Materials Transactions A*

Y.E. Kalay[1,2], L.S. Chumbley[1,2], I.E. Anderson[1,2], R.E. Napolitano[1,2]

Abstract

The rapid solidification microstructure of gas-atomized Al-Si powders of 15, 18, 25, and 50 wt pct Si were examined using scanning electron microscopy (SEM) and transmission electron microscopy (TEM). In order of increasing particle size, the powders exhibited microcellular Al, cellular/dendritic Al, eutectic Al, and primary Si growth morphologies. Interface velocity and undercooling were estimated from measured eutectic spacing based on the Trivedi–Magnin–Kurz (TMK) model, permitting a direct comparison with theoretical predictions of solidification morphology. Based on our observations, additional conditions for high-undercooling morphological transitions are proposed as an extension of coupled-zone predictions.

Introduction

Attributed primarily to its ability to achieve high cooling rates in a single process step for large quantities of material, gas atomization is, perhaps, the most industrially significant technique for rapid solidification, with over 50,000 tons of material produced by this method each year [1]. From a scientific standpoint, atomization methods provide experimental access

[1] Ames Laboratory (DOE), Iowa State University, Ames IA 50011-3020, USA

[2] Department of Materials Science and Engineering, Iowa State University, Ames IA 50011-3020 USA

to very high undercoolings in a containerless environment, presenting an opportunity to investigate the fundamentals of nucleation and growth in highly driven systems. In addition, the droplet size itself is a useful metric of the prevailing undercooling or cooling rate, and the atomization of a volume of liquid will typically produce a large range of droplet sizes, corresponding to a wide range of cooling rates. Thus, a quantity of atomized powder will exhibit a spectrum of solidification microstructures. Detracting from the scientific utility of the atomization method, however, is the chaotic nature of the process, which gives rise to considerable variation of microstructure, even for droplets of a particular size. Accordingly, employing gas atomization for the systematic study of solidification can be problematic.

Numerous atomization experiments for fundamental investigation of microstructural evolution during rapid solidification have been reported [2,3,4]. A detailed investigation of the correlation between undercooling and microstructure was performed by Levi and Mehrabian, [2] who used a vacuum-electrohydrodynamic atomization process to produce submicron powders of Al-Si and Al-Cu alloys. The typical microstructure exhibited by their powders revealed that solidification occurred primarily in two stages, beginning with the planar growth of a supersaturated solid solution followed by a transition to a cellular morphology and the concomitant segregation pattern. This two-stage freezing behavior has been observed by others [5] and indicates a transition from the rapid cooling associated with the absorption of latent heat by the droplet itself to the slower cooling associated with the transfer of heat to the particle's surroundings (i.e., Newtonian cooling). Atomized particles often exhibit a clear microstructural transition associated with the change in cooling rate that accompanies the onset of Newtonian dominated cooling. Indeed, while microstructures were observed to vary within any given particle size range, the results of Levi and Mehrabian clearly indicate that decreasing particle size can be generally correlated with increasing undercooling and a departure from Newtonian cooling conditions. Thus, for smaller particles, solidification during recalescence becomes dominant and the transition to external heat-

transfer control is suppressed. In the adiabatic limit, undercooling is sufficiently high that all of the latent heat liberated by the freezing droplet can be accommodated within the droplet itself and no external heat extraction is required for solidification. These general features have been well evidenced by microstructural observations [2] where smaller particle sizes have been associated with an increasing degree of planar growth of the supersaturated solid solution and a suppression of the segregation-induced transition from planar to cellular growth morphologies.

In the current study, we employ high-pressure gas atomization to investigate microstructural selection in hypereutectic Al-Si alloys. In particular, we examine microstructural selection at high undercoolings and compare our observations with the selection map reported by Trivedi et al[4]. In addition, we consider the implications of our observations with respect to the onset of nonequilibrium solidification phenomena and non-Newtonian cooling conditions.

Experimental Procedure

Hypereutectic alloy powders of Al-15Si, Al-18Si, Al-25Si, and Al-50Si (wt pct) were produced using high-pressure gas atomization. For each experiment, the melt chamber of the gas atomizer was charged with high-purity (99.95 pct) Al and (99.99 pct) Si to a total weight of about 1.5 kg. Each charge was induction melted to 400 °C above the relevant liquidus temperature in a hard-fired bottom-pouring crucible made from high-purity (99.7 pct) Al2O3. Atomization was accomplished using ultrahigh purity (99.995 pct) nitrogen with a supply pressure of 6.6 MPa. The powder collected from each experiment was screened using ASTM standard vibratory sieves to obtain particles with diameters of #45 μm. Air classification and sedimentation methods were then used to isolate particles in size classes of 0 to 5 μm and 5 to 10 μm. Samples selected for scanning electron microscopy (SEM) analysis were mounted in epoxy resin, ground, polished, and etched (in aqueous solution of 3 pct HCl, 2 pct HNO3,

and 1 pct HF, by volume) for cross-sectional analysis. In any given specimen, the largest particle cross sections were selected for examination to best ensure near-diametral sections. In addition, the particle diameter was measured on cross-sectional planes, which include at least three particles in contact, again ensuring a true diametral measurement. For transmission electron microscopy (TEM) investigation, selected powders were dispersed in epoxy, and the mixture was cured, thinned, and argon-ion milled (4 kVacceleration voltage and 20 deg incident angle) to perforation. For both SEM and TEM analyses, only the most spherical particles were considered for quantitative investigation because they are the ones that most likely solidified during free fall in the chamber. The relative dominance of the different growth morphologies was measured as a function of powder size and composition using a linear-intercept analysis on selected powder cross sections. A total of 80 particles were examined, ranging from 0.5 to 45 μm in diameter and from 15 to 50 wt pct in Si content. For each particle, a total line length equal to 3 times the particle diameter was used for the analysis. Measurements of eutectic spacing were also performed using a line-intercept method, where the eutectic spacing was simply taken as the reciprocal of one-half the measured linear density of phase boundary intersections. A total of 21 particles, all with a composition of 18 wt pct Si but ranging from 2 to 45 μm in diameter, were used for this analysis.

Results

The range of morphologies observed in the powder samples includes primary silicon, eutectic, dendritic/cellular primary aluminum, and a microcellular aluminum structure. This is illustrated in Figure 1, showing the microstructure in ~25-μm-diameter powders over a range of compositions, and in Figure 2, showing the microstructure in 18 wt pct Si powders over a range of particle sizes. For the larger powders, growth morphology was easily

ascertained using SEM analysis, but finer particles (i.e. <5 μm diameter) required TEM imaging.

The influence of composition on growth morphology is summarized in Figure 1 for large (~25 μm) diameter powders. These exhibit dominant morphologies of primary Si (Figure 1(a)), eutectic (Figure 1(b)), or primary aluminum (Figure 1(d)), for compositions of 50, 25, and 15 wt pct Si, respectively. Similarly, the morphology varies with particle size, as shown in Figure 2, for powders of 18 wt pct Si. Here, the dominant morphology varies from eutectic at 30 μm (diameter) to cellular plus eutectic at 20 μm, cellular at 4 to 10 μm, and microcellular at 0.4 μm. For our purposes, we differentiate the microcellular morphology from the cellular morphology on the basis of the intercellular structure. Thus, the cellular structure contains a resolvable two-phase intercellular constituent (Figure 2(d)), where the microcellular morphology exhibits a distinguishable cellular segregation pattern, but no clearly distinguishable twophase intercellular microstructure (Figure 2(f)). Rather, selected area diffraction reveals nanocrystalline Si and Al in the intercellular region.

The relative amount of each type of microstructure measured for two powder size classes (2 to 4 μm and 20 to 24 μm diameter) is plotted in Figure 3 as a function of alloy composition. This figure shows that, for the 20- to 24-μm size class, as the alloy composition is decreased from 50 wt pct Si to 18 wt pct Si, the dominant microstructure shifts from primary silicon to a eutectic morphology. The interpolated curves suggest that such a transition occurs at approximately 41 mm.

As a means for the estimation of undercooling, powders of 18 wt pct silicon, which were generally observed to be dominated by the eutectic morphology, were selected for the measurement of eutectic spacing. The results are shown in Figure 4, where measured eutectic spacings are plotted as a function of powder diameter and are compared with results from a previous study, [6] where helium, rather than nitrogen, was used as the atomization gas.

Discussion

The variation of eutectic spacing with particle diameter, plotted in Figure 4, indicates that the atomization gas has a measurable effect on undercooling for large particles. This is not particularly surprising, given that the heat capacity and thermal conductivity for helium gas are much greater than those for nitrogen gas. The plot indicates, however, that for particles less than ~10 m, the undercooling may not be measurably dependent on these factors, perhaps indicating the threshold diameter below which the solidification rate is primarily governed by the heat absorption that occurs during recalescence, as discussed by Mehrabian et al.[2,3]

The values of undercooling (ΔT) and interface velocity (v), corresponding to the various particle sizes, are plotted in Figures 5(a) and (b). These values were obtained from the eutectic spacing (λ) measurements for the 18 wt pct alloy, using the Trivedi–Magnin–Kurz (TMK) model [7] for eutectic growth at high velocity, and are based on the equations

$$\Delta T = \frac{m a^L}{\lambda}(1+q) \tag{1}$$

$$v = \frac{a^L q}{\lambda^2 Q^L} \tag{2}$$

where m, aL, and QL are defined by Eq. [16] in Reference 8, q is defined here as

$$q \equiv \frac{P}{P + \lambda\left(\frac{\partial P}{\partial \lambda}\right)} \tag{3}$$

and P is a function of phase fraction, solute partition coefficient, and Péclet number, as described in Reference 7. Note that the value of P approaches a constant for low Péclet numbers (λv/2D), and q approaches unity, where Eqs. [1] and [2] reduce to the Jackson–Hunt (JH) equations, $\lambda\Delta T = 2ma^L$ and $\lambda^2 v = a^L/Q^L$ [7]. The material parameters used for the

undercooling and velocity estimates are given in Table I. For the low Péclet number (i.e., $p < 0.2$) regime, corresponding to $d > 10$ μm and $v > 20$ μm/s, the JH and TMK models are in good agreement (Figure 6). Above this velocity (smaller particle diameter and higher Péclet number), there is a substantial difference between the models, indicating that nonequilibrium partitioning and temperature dependent diffusivity are important considerations. Figure 5(c) shows that this $d > 10$ μm threshold corresponds to a Péclet number of approximately 0.2. It is interesting to note that this threshold in the Péclet number, where rapid solidification effects become important, coincides with the observed transition to recalescence-controlled growth rate, indicated by Figure 4.

Given the estimated undercooling values of Figure 5(b), the implications of the observed microstructure measurements can be considered in light of the morphology selection map previously proposed by Trivedi et al [4]. This map, along with the current experimental observations, is shown in Figure 7. The dashed vertical lines indicate the alloy compositions used for this study, and each symbol represents the indicated microstructural observation. It should be noted that these data indicate the dominant microstructure and do not imply that only a single morphology was observed. It should also be recognized that the analytical predictions shown [4] indicate transitions in the favored growth morphology, where boundaries are defined by equal velocity at the given temperature. Such a calculation does not include any consideration of the time scale of competition dynamics and is not meant to imply that a single morphology would be observed in the microstructure. Rather, it is expected that several competing morphologies would be observed under many conditions. Finally, we point out that the prediction does not include any consideration of nucleation phenomena, which may play an important role in overall selection dynamics.

Focusing on the predicted transitions in growth morphology, observed microstructures are in good agreement with previously calculated microstructure regions. For example, the largest size particles of all compositions show primary Si formation being dominant. As particle size decreases, eutectic growth morphology becomes dominant for all compositions, although this transition occurs at a Si content that decreases with increas powder diameter. Thus, the eutectic morphology is seen in powders of diameter 40 μm for 15 wt pct Si, 30 μm for 18 wt pct, and 25 μm for 25 wt pct, corresponding to temperatures of 840, 810, and 780 K respectively, in good agreement with the map. Examination of the 50 wt pct Si powders shows that the primary Si region extends to powders of size > 3 to 4 μm, at which point the microcellular structure becomes dominant. Similarly, the calculated transition from eutectic to primary Al growth at low Si compositions and smaller powder sizes is also well supported by experimental observations, being seen in 15, 18, and 25 wt pct alloys.

In powders dominated by primary Al formation, a fairly continuous transition appears from dendritic to cellular to microcellular. The transition from cellular, where clearly identifiable lamellar eutectic formation is observable, to the refined microcellular structure begins approximately at a powder diameter of 10 μm (p ~0.2) for 15 to 25 wt pct Si alloys. While no sharp morphological transition was observed in any single particle, the existence of the microcellular structure shows a reasonable correlation with the convergent region in Figure 4, where recalescence appears to be controlling the growth rate. As we have noted, this transition is observed at a Péclet number that is coincident with the divergence of the TMK and JH models.

Conclusion

Eutectic spacing measurements indicate that, for particle diameters less than 10 μm, the solidification rate may be unaffected by the type of gas used during atomization, suggesting that growth rate is governed by recalescence in this regime. Moreover, this diameter is consistent with the appearance of the microcellular growth morphology and with the divergence of the JH and TMK models for eutectic growth at Péclet numbers greater than ~0.2.

Microstructure observations of large powders for alloys in the composition range from 15 to 50 wt pct Si agree well with the microstructure map proposed by Trivedi et al [4]. The SEM and TEM observations of 18 wt pct Si indicate a continuous dendritic-cellular microcellular transition that occurs with decreasing particle size. While the lamellar eutectic structure is easily discernable at large and midrange powder sizes, the intercellular constituents of the smallest size powders appear to consist of a nanocrystalline mixture of Si and Al.

Acknowledgment

Appreciation is expressed to R. Trivedi for valuable discussions and his comments. This work was supported by the United States Department of Energy, Office of Basic Energy Sciences, Contract No. W-7405-ENG-82.

Reference

1. H. Jones: Non Equilibrium Processing of Materials, 1st ed., C. Suryanarayana, ed., Elsevier Science Ltd., Amsterdam, The Netherlands, 1999, pp. 23-45.

2. C.G. Levi and R. Mehrabian: Metall. Trans. A, 1982, vol. 13, pp. 13-23.

3. C.G. Levi and R. Mehrabian: Metall. Trans. A, 1982, vol. 13, pp. 221-34.

4. R. Trivedi, F. Jin, and I.E. Anderson: Acta Mater., 2003, vol. 51, pp. 289-300.

5. L.A. Bendersky, F.S. Biancaniello, S.D. Ridder, and A.J. Shapiro: Mater. Sci. Eng., A, 1991, vol. 134, pp. 1098-102.

6. A.L. Genau: Master's Thesis, Iowa State University, Ames, IA, 2004.

7. R. Trivedi, P. Magnin, and W. Kurz: Acta Metall., 1986, vol. 35, pp. 971-80.

8. K.A. Jackson and J.D. Hunt: Trans. TMS-AIME, 1966, vol. 236, pp. 1129-42.

9. H. Jones and W. Kurz: Z. Metallkd., 1981, vol. 72, p. 792.

10. Y.E. Kalay, I.E. Anderson, L.S. Chumbley: International Conference on Powder Metallurgy and Particulate, MPIF/AIME, June 18-21, San Diego, CA, 2006, pp. 95-105.

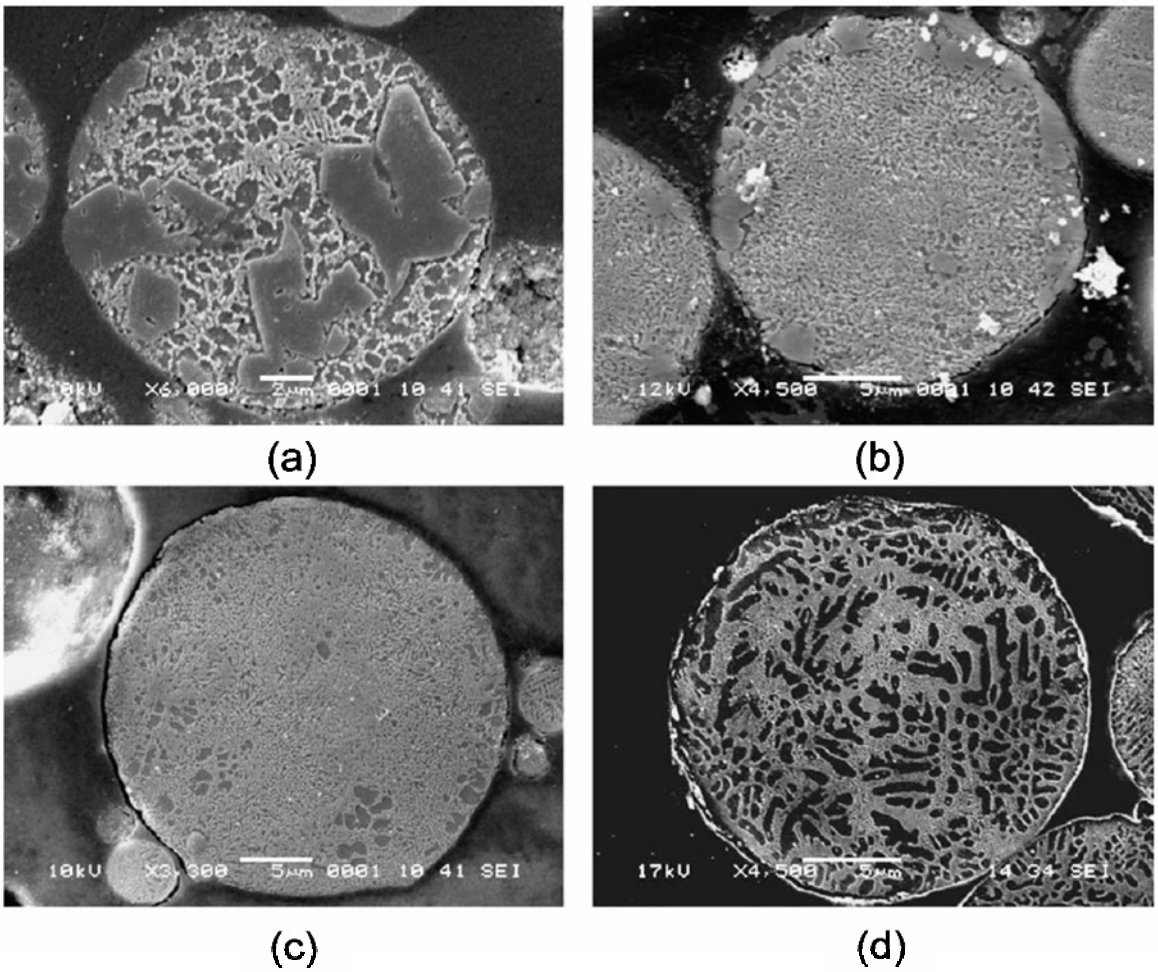

Figure 1. Representative microstructures of rapidly solidified powders (25-µm diameter): (a) Al-50 wt pct Si, showing faceted primary Si, eutectic, and dendritic structures; (b) Al-25 wt pct Si, showing a large amount of eutectic; (c) Al-18 wt pct Si, showing primary Al and eutectic; and (d) 15 wt pct Si, [6] showing primary Al and eutectic.

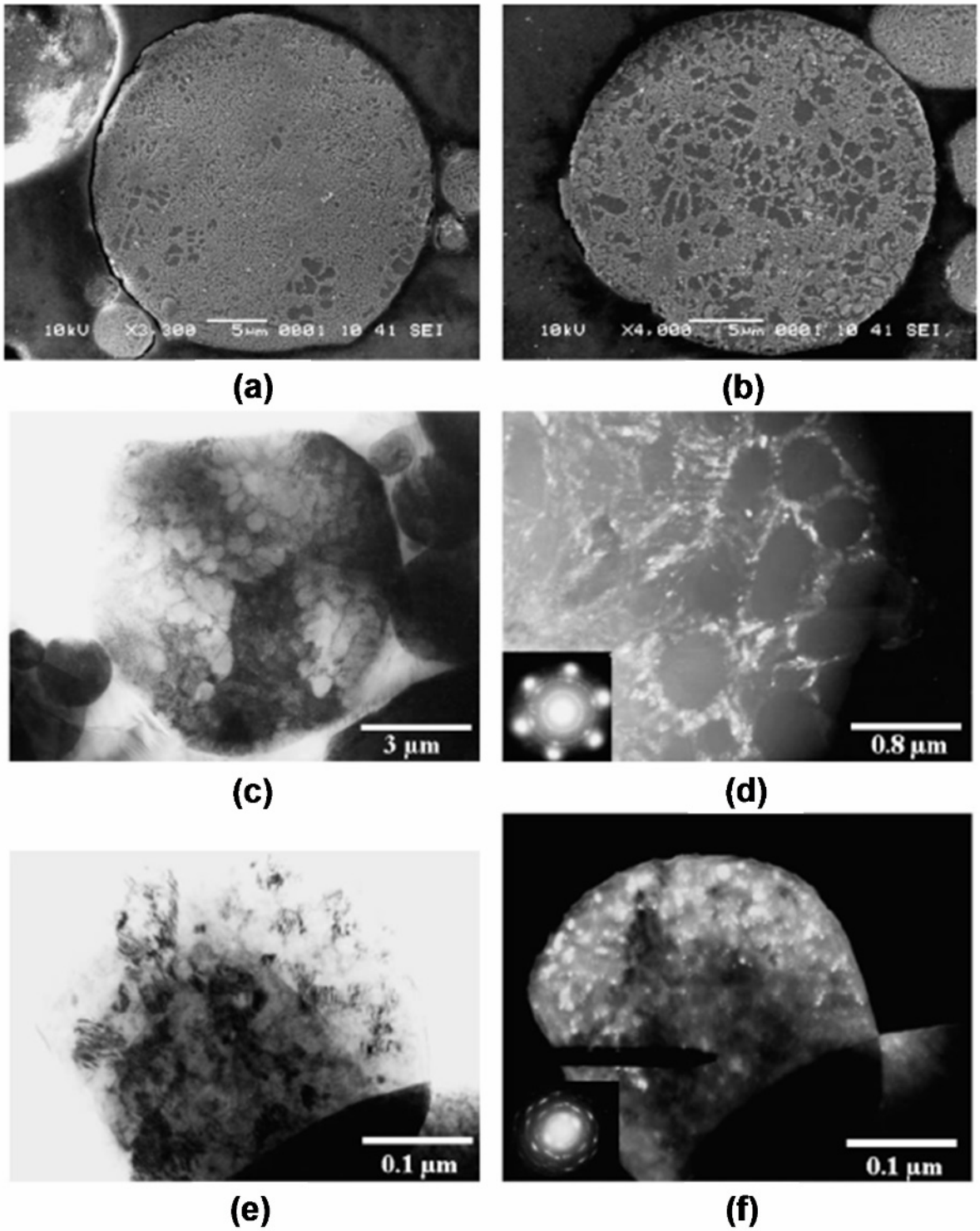

Figure 2. Al-18 wt pct Si microstructures in powder particles of various diameter: (a) 30 µm, (b) 20 µm, (c) 10 µm, (d) 4 µm, and (e) and (f) 0.4 µm. Imaging: (a) and (b) secondary electron SEM, (c) and (e) bright-field TEM, and (d) and (f) dark-field TEM.

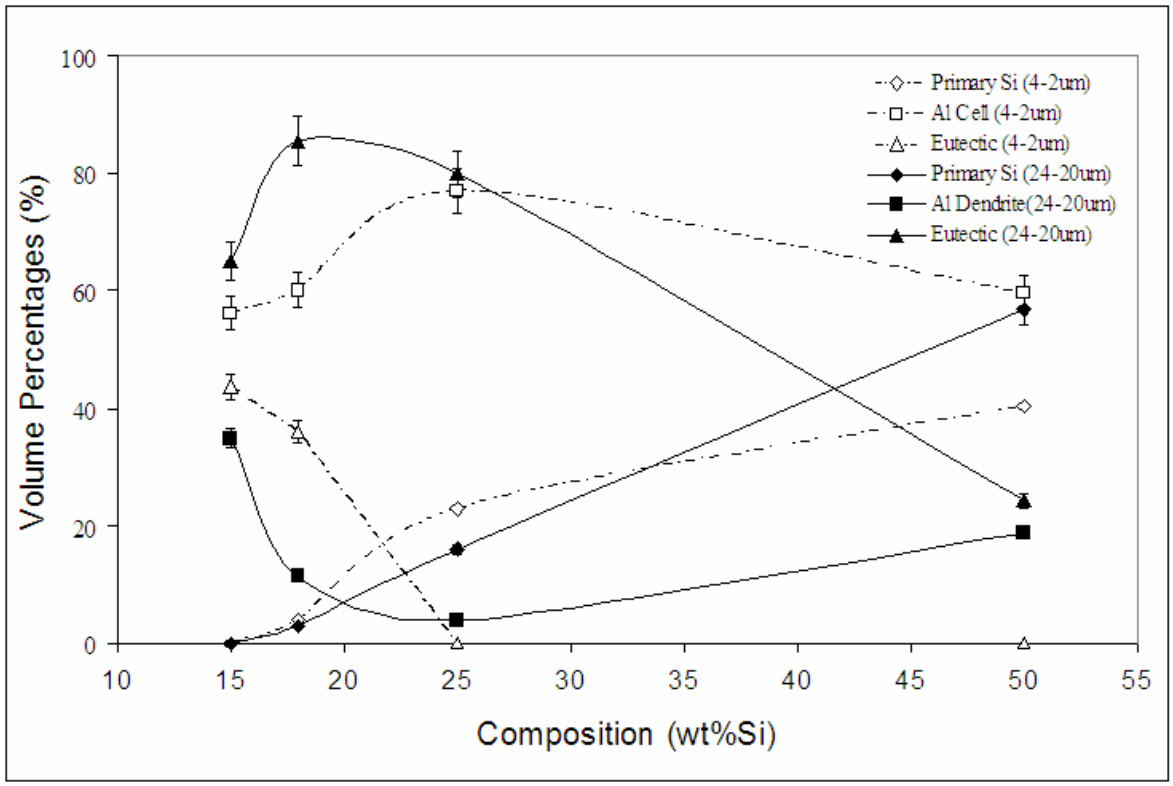

Figure 3. The relative amount of each observed microstructure type, as a function of composition and powder size.

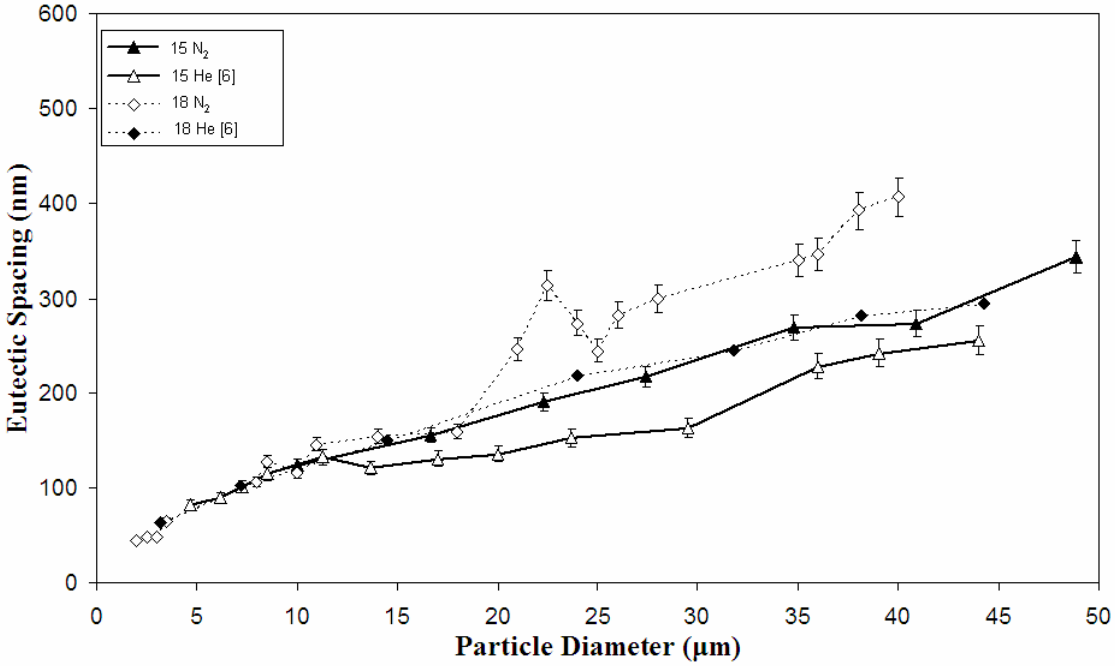

Figure 4. Measured eutectic spacing vs powder diameter in 18 wt pct Si compared to results from [6].

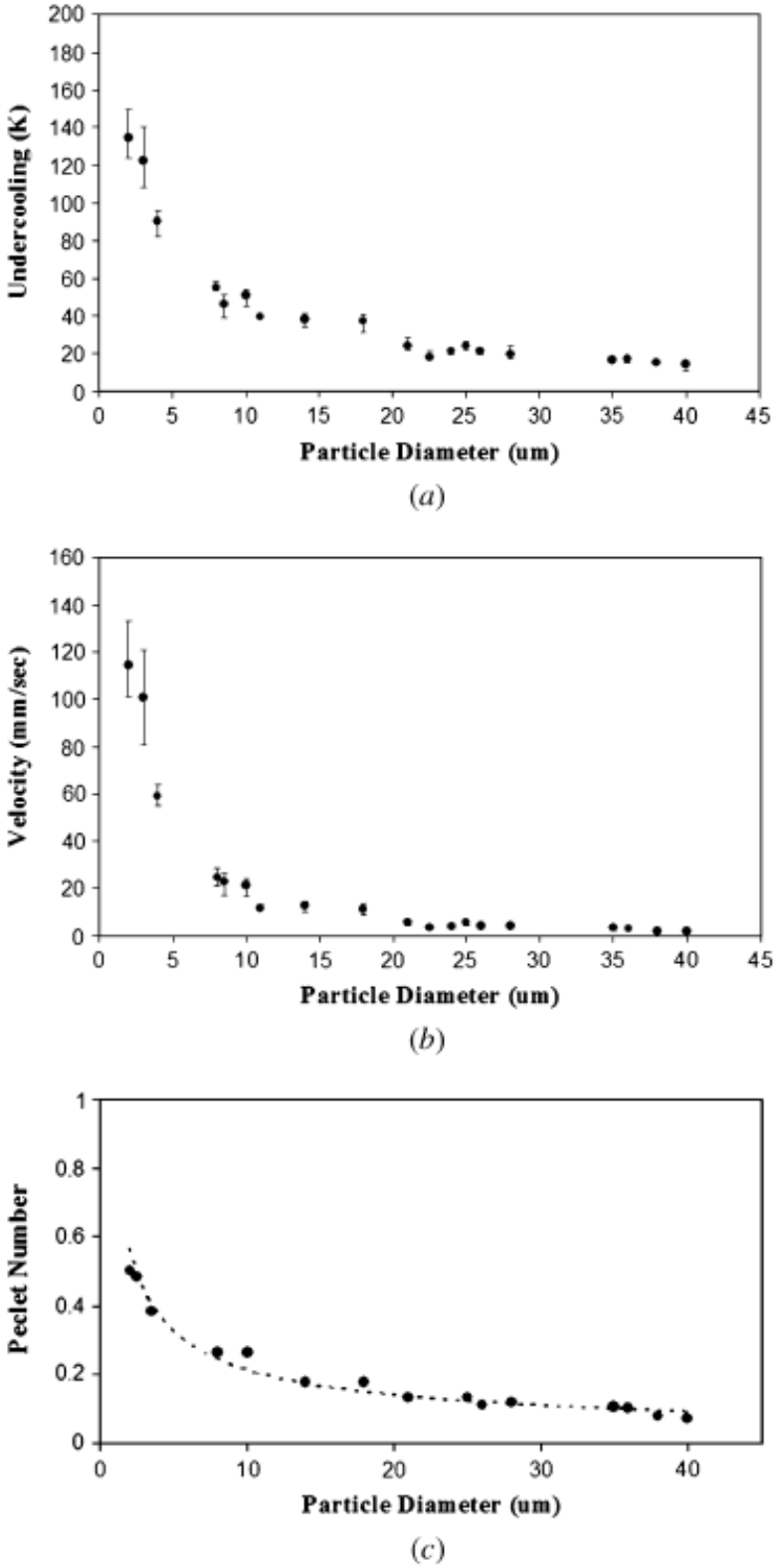

Figure 5. (a) Growth velocity, (b) undercooling, and (c) Péclet number for eutectic growth, all estimated from eutectic spacing measurements in the 18 wt pct Si powders.

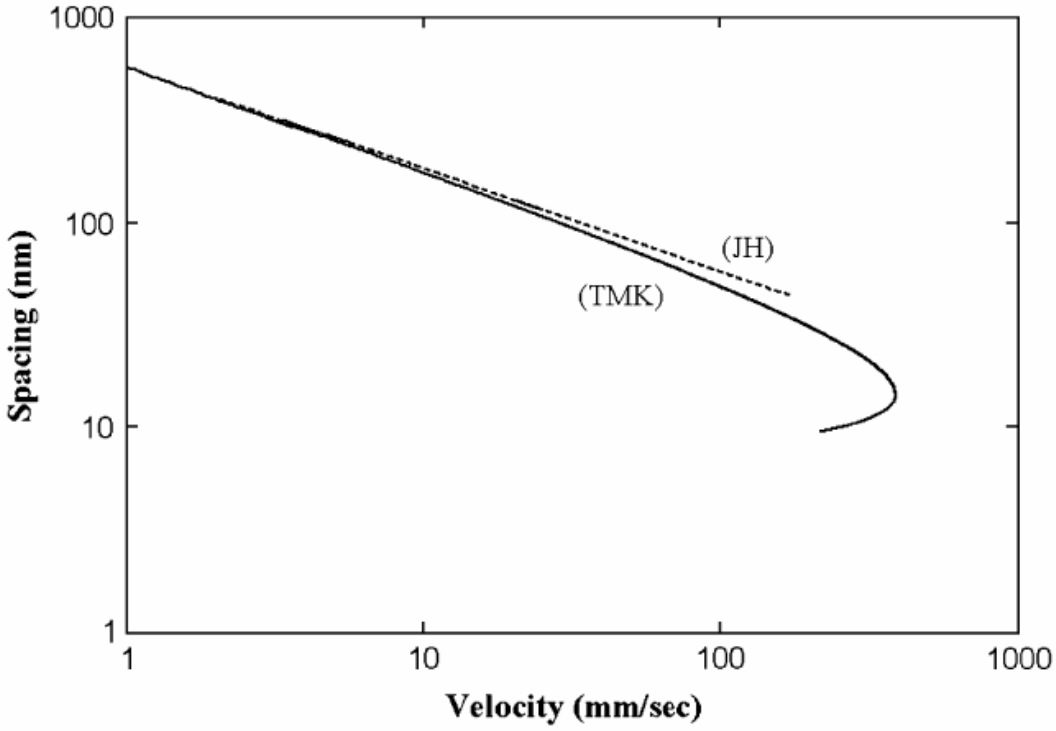

Figure 6. The spacing-velocity relationship predicted by JH and TMK eutectic growth models for Al-18 wt pct Si, computed using the parameters in Table I.

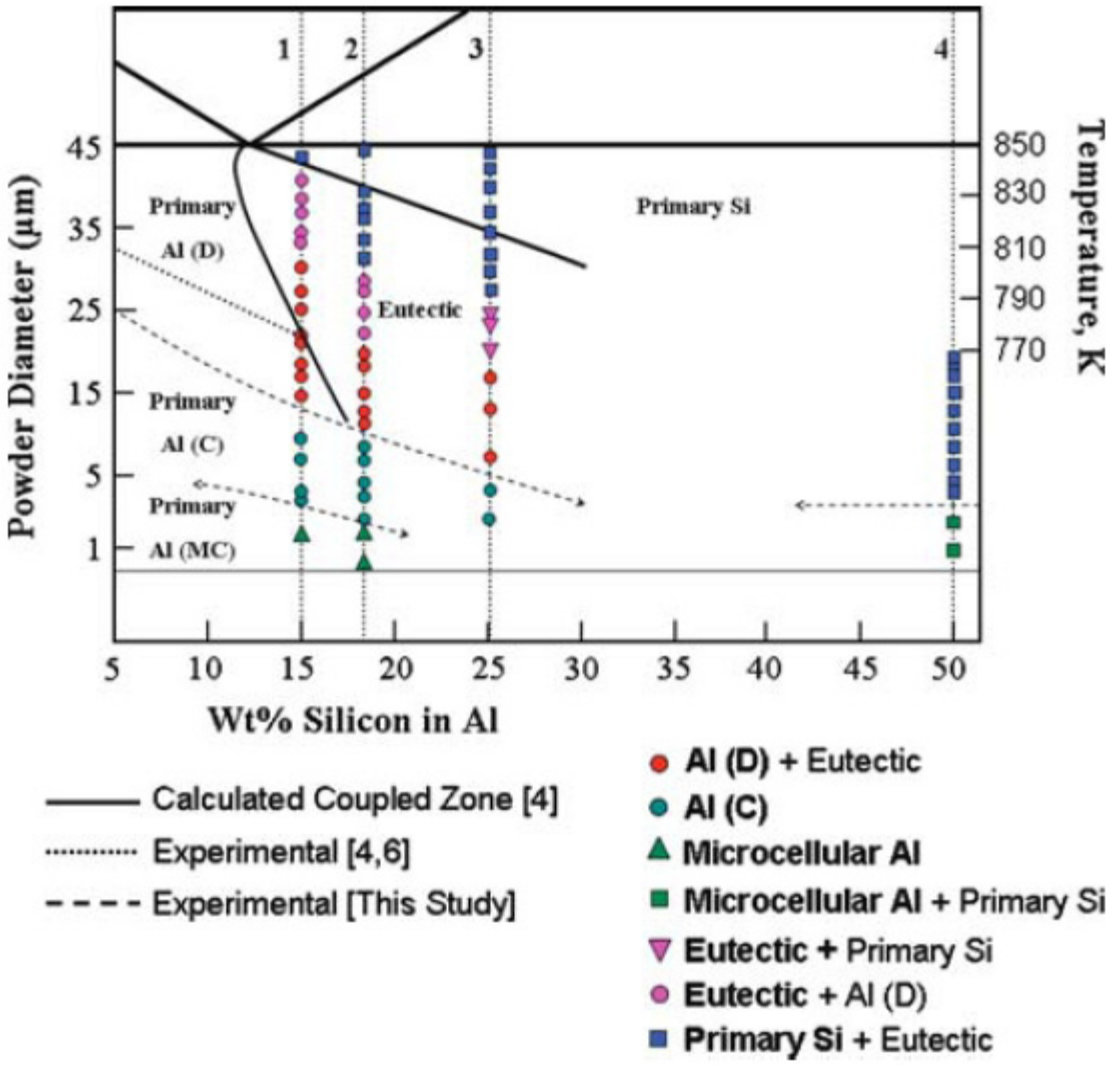

Figure 7. Microstructure map [10] for the Al-Si system extended from the previously calculated map [4]. Lines 1 through 4 correspond to undercooling paths for Al-15 wt pct to 50 wt pct Si droplets.

Table 1. Parameters used in undercooling and velocity estimates.

Parameter Symbol	*Parameter Value*	*Unit*	*Parameter Name*
D	5×10^{-9}	m^2/s	Diffusion coefficient
C	98.2	wt%	Length of eutectic tie-line
m_α	7.5	K/wt%	α phase liquidus slope
m_β	17.5	K/wt%	β phase liquidus slope
Γ_α	1.96×10^{-7}	Km	Gibbs-Thomson Coefficient (α phase)
Γ_β	1.7×10^{-7}	Km	Gibbs-Thomson Coefficient (β phase)
θ_α	30°	deg	Angle of α phase
	0.524	rads	
θ_β	65°	deg	Angle of β phase
	1.134	rads	
T_{eut}	577.2	°C	Eutectic temperature
C_{eut}	0.126	-	Eutectic composition
ρ_α	2.50×10^6	g/m^3	Density (α phase)
ρ_β	2.33×10^6	g/m^3	Density (β phase)
Φ	3.2	-	Extremum condition parameter

CHAPTER 3: CHARACTERIZATION OF A MARGINAL GLASS FORMER ALLOY SOLIDIFIED IN GAS ATOMIZATION POWDERS

A paper published in Materials Science and Engineering A

Y.E. Kalay[1,2], L.S. Chumbley[1,2], I.E. Anderson[1,2]

Abstract

$Al_{90}Sm_{10}$, a marginal glass former, was rapidly solidified using high pressure gas atomization (HPGA). Rapid solidification is a non-equilibrium process, with different degrees of departure from full equilibrium constituting a microstructural hierarchy that correlates with increasing solidification rate. In accordance with this the resultant HPGA powders show a variety of microstructures according to their particle diameters, corresponding to degree of undercooling, with an amorphous structure appearing at high cooling rates. Five distinct phases and microstructures have been identified at different undercoolings; Al solid solution, tetragonal $Al_{11}Sm_3$, two different orthorhombic phases, and an amorphous phase which exists in company with a high number density of Al nanocrystals. The product phases of the rapid solidification were identified and analyzed using high energy transmission X-ray diffraction (HEXRD), high resolution transmission electron microscopy (HRTEM), scanning electron microscopy (SEM), Energy Dispersive X-ray Spectroscopy (EDS) and thermal analysis (DSC). The results of the study will be helpful in identifying metastable phase hierarchy and glass formation during vitrification of marginal glass formers.

---

[1] Department of Materials Science and Engineering, Iowa State University, Ames IA 50011-3020 USA

[2] Ames Laboratory (DOE), Iowa State University, Ames IA 50011-3020, USA

Introduction

Al–rare earth (RE)-based alloys are known to be marginal glass formers, where amorphization is often accompanied by nano-crystalline phases due to kinetically related growth limitations [1] and [2]. The as-quenched phases formed in Al–RE binary systems show a diversity of crystal structures in the composition range where glass formation is observed, which typically lies in the range between the Al–RE eutectic point and $Al_{11}RE_3$ (for $Z_{RE} \leq 62$) or Al_3RE ($Z_{RE} \geq 63$, except yttrium) intermetallics [3] and [4]. Among the Al–RE binary alloys, the Al–Sm system has the widest glass formation range, from 8 to 16 at.% Sm (33–52 wt% Sm) [4].

Amorphization and nano-crystalline phase formation in Al–Sm binary alloys has been extensively investigated using both melt spinning and mechanical mixing methods [5], [6], [7] and [8]. The common belief [5] for this binary system under non-equilibrium conditions is that the formation of an amorphous matrix accompanied with nano-crystalline phases is due to the growth of quenched-in nuclei, if the initial state is liquid before vitrification. Amorphous phase formation without any nanocrystals was reported for an Al–Sm binary alloy which underwent extensive mechanical deformation [10]. This shows that solid state mixing is one possible route for complete vitrification of this alloy system. Recent experiments that involved melt spinning of identical compositions using similar processing conditions has resulted in both partially, and completely, amorphous structures [7], [8] and [9]. Thus, studies to date have yet to provide a complete description and understanding of the vitrification process. Similarly, a complex phase selection sequence has been observed in devitrification within the same composition of glass [6], [7], [8] and [9].

In this study, the vitrification path of Al–Sm (38 wt% Sm) binary alloy was investigated using powders produced by a gas atomization technique. Among rapid solidification processes, gas atomization presents an opportunity to investigate the fundamentals of nucleation and growth in a containerless environment where a high amount

of undercooling can be reached. Droplets with different diameters that solidified at different undercooling values provide an opportunity to explore metastable phases and novel microstructures [10], [11], [12], [13] and [14] over a wide range of conditions within a single sample. Powders at different diameters were investigated systematically to characterize the microstructures, to determine the potential for metastable phase formation, and to examine whether nanocrystal formation can be suppressed at high undercoolings in this marginal glass former.

Experimental Procedure

Powders of an Al–38Sm (wt%) alloy were generated at Ames Laboratory using high pressure gas atomization (HPGA). High purity (99.99 wt%) Al and (99.9 wt%) Sm was used, with He atomization gas employed at a supply pressure of 5.5 MPa. The charge was induction melted at 1200 °C, 300 °C above the relevant liquidus temperature, in a hard-fired bottom-pouring crucible made from high purity (99.7 wt%) Al_2O_3. The collected powders were screened using a series of ASTM standard sieves with a vibratory shaker to obtain particles of 75 μm in diameter or less. Air classification was used to obtain 5–10 μm and <5 μm diameter powders. In order to obtain precise particle size for TEM investigation, powders ranging in size from submicron to 3 μm were separated using a sedimentation technique in Hexane (C_6H_{14}). The microstructural changes during vitrification were investigated using scanning electron microscopy (SEM) and scanning/transmission electron microscopy (S/TEM). Chemical compositions were measured using EDS. Powder specimens for SEM were mounted in epoxy resin and their surfaces were cut using a serial micro-cutter. This new cross-section method, which eliminates grinding and polishing steps, was found to be very effective. Samples were etched in a 2.5 ml nitric acid, 1.5 ml HCl, 1 ml HF, 95 ml H_2O solution at room temperature. S/TEM specimens were dispersed in epoxy, the mixture cured, thinned, and argon-ion milled (4 kV acceleration voltage and 20° incident angle) to

perforation using a liquid nitrogen cooled stage. In order to remove any suspicion that sample heating during TEM preparation was occurring, powders smaller than 1 μm were dispersed on carbon-coated copper grids and directly examined using high resolution imaging (HRTEM).

The solidification product phases, including crystal structures and vitrification results were investigated using HEXRD at the Advanced Photon Source at Argonne National Laboratory in collaboration with the Midwest Universities Collaborative Access Team (MUCAT). The as-atomized powders were sealed in silica capillaries and exposed to 100 keV X-rays of wavelength 0.012347 nm at ambient temperature. The thermal stabilities of phases in as-rapidly solidified powders were determined by differential scanning calorimetry (DSC).

Results

Scanning electron microscopy

A previous study of gas atomized Al–Si powders showed that particle size refinement through gas atomization has a measurable effect on increasing the undercooling at a constant alloy composition [11], [12], [13], [14] and [15]. In light of this observation as-atomized Al–Sm powders were screened and classified for systematic characterization (Table 1). Particles with set numbers from 1 to 8 were investigated with SEM using electron back scattered imaging (BSE). The transition in solidification morphology from larger to smaller particle diameter is illustrated in Fig. 1. Note that for this study only spherical particles were considered for investigation as they are the ones that most likely solidified during free fall in the chamber.

A dendritic morphology is seen for larger powders (>45 μm) where the undercooling is relatively low, Fig. 1a and b. Starting with powders 45–38 μm in size, the highly branched

primary dendrites are replaced with primary faceted flakes without significant secondary arm branching, Fig. 1c and d. According to EDS, both dendrites and faceted flakes are rich in Sm content compared to the matrix, which is consistent with the contrast observed using BSE, since the atomic number of Sm (62) is far bigger than Al [13]. No difference in contrast is observed between dendrites. However, EDS in SEM resolved slightly different compositions for the dendritic structures showing a compositional variation between dendrites having similar morphologies. Two distinct compositions, one having an average of 21 ± 1 at.% Sm and the second 16 ± 1 at.% Sm, were observed from similar size dendrites using EDS in SEM. Some of these larger powders showed peripheral featureless rims (as arrowed in Fig. 1c), in agreement with previous observations by other investigators [16]. The smallest size particle groups observed using SEM (<25 μm), corresponding to high undercooling, show small faceted grains within a featureless matrix, Fig. 1e and f.

High energy transmission X-ray diffraction (HEXRD)

Fig. 2a shows a digitally processed image plate scan for powders at different diameters. This figure visually displays the changes in structure detectable using X-rays from large to small powder size. The lines indicate the location of Bragg peaks, with the contrast level being proportional to diffracted beam intensities. The intensity of crystalline peaks is seen to decrease as particle size decreases, and a partially amorphous hump is observed for the smallest size powder group of <5 μm. Fig. 2b shows XRD patterns integrated from the image plate scan for selected ranges of powder diameters. For the largest powder size group (63–75 μm), fcc-Al and peaks consistent with tetragonal Al–Sm phases can be resolved. According to Refs. [17] and [18], Al_4Sm and $Al_{11}Sm_3$ are two different representations of the same high temperature metastable tetragonal phase [19], with common diffraction peaks and lattice parameters. These are isostructural with the Al_4Ba compound with Al deficiency due to vacancies, resulting in a discrepancy in chemical composition. The atomic percentage of

Sm is 0.2 and 0.214 in Al_4Sm and $Al_{11}Sm_3$, respectively. A Rietveld refinement of the selected powder groups yielded an atomic percentage of 0.214% Sm in the tetragonal phase (Table 2), which indicates an Al deficiency. Thus, this phase will be described as tetragonal $Al_{11}Sm_3$, and is associated with the highly dendritic microstructure observed in the SEM studies. The tetragonal $Al_{11}Sm_3$ phase has lattice parameters of $a = 0.428$ nm and $c = 0.992$ nm.

There is only one unidentified Bragg peak at ($2\theta = 2.86$) in largest powder size group. As the particle size decreases, additional Bragg reflections became visible (Fig. 2b). A body centered orthorhombic structure, corresponding to the Al_4Sm [20] phase with lattice parameters of $a = 0.444$ nm, $b = 0.638$ nm, and $c = 1.362$ nm and isostructural with the Al_4U, can be identified. A second phase, also determined on the basis of X-ray diffraction to be orthorhombic with lattice parameters with $a = 0.416$ nm, $b = 0.634$ nm, and $c = 1.328$ nm was also identified. This phase, designated ER, has a similar Bravais structure and lattice parameters to Al_4Sm. However, ER and Al_4Sm have different atom arrangements as deduced by the presence of extra reflections for the ER structure that are forbidden for Al_4Sm.

The Bragg peaks of all observed crystal structures become weak as the average particle size becomes smaller (Fig. 2b). However, even at the smallest powder sizes (<5 μm) crystalline peaks are still observed, although they are superimposed on a large amorphous hump. Fig. 3 shows the diffraction pattern of smallest powder size in detail. Two points should be noted here. First, the initial amorphous hump seen in Fig. 3 and located below 2° 2θ is due to the quartz capillary used as a sample holder during the experiments, while the second amorphous hump indicates actual amorphous phase formation in this system. Secondly, it must be kept in mind that the X-ray samples consist of a large number of powders of different sizes. Thus, crystalline peaks superimposed on an amorphous hump in the XRD pattern for smaller size powder do not mean that crystalline and amorphous phases coexist in every particle. For example, the sample may consist of fully or partially amorphous

powders, and entirely crystalline powders. In other words, the XRD data gives phase information as an average for the sample, not individually for each powder.

In order to investigate the stability of the observed phases, powders of size 63–75 μm (containing $Al_{11}Sm_3$ and fcc-Al) were annealed at 873 K for 86.4 ks. As shown by the X-ray scans in Fig. 4, the $Al_{11}Sm_3$ completely transforms to Al_4Sm, with a few peaks from the low temperature stable hexagonal Al_3Sm phase also being observed. The types of crystalline phases observed in this study, in addition to amorphous materials, are summarized in Table3.

Transmission electron microscopy (TEM)

Powders in the smallest size group (<5 μm) were investigated using TEM. Fig. 5a shows a bright field (BF) image of a crystalline powder in this size group. The powder possesses what appears to be a primary solidification phase (Fig. 6) and an eutectic structure. EDS results in TEM reveal that the white contrast phase is almost pure Al (average atomic composition of ≈1 at.% Sm) and the dark contrast phase is rich in Sm (average atomic composition of 19 at.% Sm). The inset in Fig. 5a shows the SAD of taken from the circled area. Measured d-spacings for the most intense reflections, designated by g1 and g2, as well as the closest planar spacing corresponding to Al and $Al_{11}Sm_3$, are shown in Table 4. Comparison of these values indicates the likely candidate for the phase showing the most diffracted intensity (i.e. the dark phase of Fig. 5a) is $Al_{11}Sm_3$. Fig. 5b shows a simulated [0 0 1] diffraction pattern for tetragonal $Al_{11}Sm_3$ phase (*I*4/*mmm*) which is in good agreement with the observed major reflections, and also agrees with the EDS results. The remaining weaker reflections of Fig. 5a (inset), attributed to the Al-rich, light contrast, weakly diffracting phase of Fig. 5a, match a number of Al d-spacings oriented at different zone axis, and are assumed to be a combination of allowed fcc Al reflections and double diffraction.

Fig. 6a shows the BF image of the primary solidification phase and Fig. 6b illustrates observed and simulated SAD patterns of o-Al_4Sm (*Imma*) taken at different zone axes. The observed and simulated patterns are in good agreement.

Fig. 7 shows a powder approximately 5 μm in diameter. This particular powder consists of equiaxed grains and an amorphous matrix detected by SAD. EDS in TEM gave an approximate average atomic composition of 16 at.% Sm. The interplanar spacings obtained at different zone axis through tilting experiments are in good agreement with the ones obtained for ER phase by using HEXRD analysis (Table 5).

Fig. 8 shows a region of a powder classified by the sedimentation method as being less than 3 μm in diameter. (N.B. Since the entire particle was not visible there is always the possibility that the region shown had fractured from a powder with a diameter larger than 3 μm. The dominant amorphous microstructure, appearing jointly with the presence of nanocrystals, makes this possibility unlikely.) A high nucleation density (1.25×10^{23} m^{-3}) of Al nanocrystals detected by SAD was observed in Region A (Fig. 8). Fig. 9a shows a high angle annular dark field image (HAADF image) and EDS line scan across a nanocrystal with approximate size of 25 nm diameter. EDS shows (Fig. 9b) relatively high Sm content in the amorphous matrix near the nanocrystal as compared to the crystal itself. Fig. 10 shows a representative HRTEM micrograph of a submicron-sized powder. The as-solidified structure consists of large number of clusters, roughly ellipsoidal in shape and randomly distributed, within an amorphous matrix. The sizes of these clusters are much smaller than the nanocrystals shown in Fig. 8, and lattice fringes can be seen using HRTEM imaging. Using fast Fourier transform (FFT) analysis (Fig. 10a, inset) the distance and the small intersecting angle between adjacent planes was found to be 0.240 ± 0.002 nm and 70.80°, respectively, which agrees well with the planar spacings and interplanar angles for (1 1 1) planes in fcc-Al when viewed along ⟨1 1 0⟩. For comparison, the distance between the (1 1 1) planes of pure Al was measured as 0.237 ± 0.002 nm using HRTEM under the similar conditions. Using this

indexing scheme the lattice parameters were calculated as 0.416 nm, which varies slightly from those of measured and calculated pure fcc-Al where the lattice parameters are 0.410 and 0.405 nm, respectively. The EDS profiles taken from amorphous and cluster regions show no appreciable difference in the intensities of Al and Sm peaks.

Thermal analysis (DSC)

Fig. 11 shows the results of isochronal DSC scans conducted on powders in six different size ranges at a heating rate of 40 K/s. Starting with powders in the 20–25 μm size range, a series of clear broad exothermic peaks is detected, Fig. 11. This size range corresponds to the point at which a featureless region was seen in some of powders using SEM. These peaks become more defined and of higher intensity as powder size decreases. The three peak temperatures for the powders of <5 μm are found to be 488, 576 and 714 K. No evidence of a second order phase transition at lower temperatures was seen, which might indicate the existence of a glass transition temperature (Tg), if observed.

Discussion

While a binary phase diagram for the Al–Sm is shown in Fig. 12a, it should be noted that the equilibrium phase diagram of the Al–Sm binary system is not completely known. In a previous study [7], it was speculated that orthorhombic $Al_{11}Sm_3$ with the *Immm* space group is the low-temperature stable phase in the Al-rich region of the phase diagram. However, according to Refs. [17] and [18] orthorhombic $Al_{11}Sm_3$ decomposes, producing hexagonal Al_3Sm (h-Al_3Sm) with $P6_3/mmc$ space group. Neither orthorhombic $Al_{11}Sm_3$ with *Immm* space group, nor hexagonal Al_3Sm with $P6_3/mmc$ space group, were observed in as-solidified powders. This is not surprising considering the non-equilibrium solidification conditions that exist as a result of gas atomization. Heat treatment of powders in the 63–75 μm size range did result in the presence of hexagonal Al_3Sm peaks, which agrees with what is predicted in Refs. [17] and [18].

The predominant intermetallic found in all powder sizes in the present study is tetragonal $Al_{11}Sm_3$, in a matrix of fcc-Al. According to Ref. [21], $Al_{11}Sm_3$ is a high temperature metastable phase that appears between 1339 and 1723 K. The existence of $Al_{11}Sm_3$ at room temperature can be explained by extension of the metastable liquidus curves as shown on the schematic phase diagram of Fig. 12b. Solidification under metastable equilibrium conditions, present due to rapid solidification, probably results in a bypassing of the equilibrium hexagonal Al_3Sm to retain the metastable $Al_{11}Sm_3$ at low temperatures. Thus, the eutectic structure consists of fcc-Al and $Al_{11}Sm_3$ as shown by BF and SAD analyses in Fig. 5a, rather than stable Al_3Sm. The dendritic nature of the microstructure seen in large powders may also contribute to the formation of $Al_{11}Sm_3$. As the formation of primary and secondary arms proceeds, an increase in the interfacial area between the intermetallic and matrix phases occurs. As interfacial area increases, a concomitant increase in vacancy sites at these interfaces can occur, causing a deficiency in Al, which tends to favor $Al_{11}Sm_3$ formation.

Orthorhombic Al_4Sm starts to appear in powders within the 45–53 μm size range. It is expected that $Al_{11}Sm_3$ and Al_4Sm are competing phases and the change from tetragonal to orthorhombic with increasing undercooling is due to Al_4Sm nucleation being more kinetically favored. However, the presence of Al_4Sm and $Al_{11}Sm_3$ within a single powder (Fig. 5a) might also indicate a solid–solid phase transformation of $Al_{11}Sm_3$ to Al_4Sm due to recalescence after solidification. Al_4Sm is only seen to exist in conjunction with the crystalline eutectic structure and it is possible that the latent heat released due to solidification drives the phase transformation. This is somewhat supported by studies [6] and [8] where a similar decomposition has been seen upon devitrification of Al–Sm during heating. However, the amount of heat available due to recalescence is much less than what is necessary for devitrification. Thus, external heating in addition to recalescence effects within

a single powder would appear to be required to cause such a solid–solid transformation to occur.

Peaks corresponding to a metastable phase, designated ER, were observed in all powder sizes using XRD. Only one Bragg peak was distinguishable in the 65–73 μm range but several peaks become apparent as powder size decreased below 32 μm. This phase has not been previously reported in studies of Al–Sm, but ER's presence at all powder sizes (and, therefore, undercoolings) suggests that it forms upon solidification rather than as a result of a solid–solid phase transformation, with increasing amounts seen as a function of increased undercooling. XRD and TEM results indicated existence of a second orthorhombic phase (ER) in this highly driven binary system. EDS in TEM showed that ER has an approximate average atomic composition of 16 at.% Sm. No information has been reported about the formation of this phase during devitrification of Al–Sm system at any other composition. This may indicate that ER is competitive with $Al_{11}Sm_3$ and forms during solidification due to the diffusion limited solidification conditions.

Complete glass formation was not observed in any powder particle. HRTEM revealed a large number of clusters (<10 nm) and nanocrystals even in the smallest powders. The number and distribution of nanocrystals varied with powder diameter. It is believed that the nanocrystals observed resulted from growth of that clusters and the variation in distributions seen within a powder (e.g. Fig. 8), and from powder to powder is due to the chaotic nature of gas atomization. Powders that undergo collisions during solidification may exhibit a different morphology than powders that remain isolated in the gas stream. In the latter case powders might be expected to show restricted growth of clusters due to recalescence or reduced temperature during quenching. The appearance of a high number of Al nanocrystals within a confined region of a powder particle, such as seen in Fig. 8, may be an example of evidence that the particle underwent a collision during solidification, resulting in a burst of growth of clusters in one area of the powder near the point of collision. As the Al nanocrystals grow,

rapid rejection of solute atoms into the amorphous matrix could result in diffusion field impingement that interrupts growth. Such a condition would exist in a region where a large number of nanocrystals nucleate and grow within nanometers of each other, and this hypothesis has been proposed by others [5]. The STEM EDS results of this study clearly show an elevated Sm content in regions adjacent to Al nanocrystals (≥10 nm), and it is reasonable to assume that if a high density of nanocrystals do exist within a restricted volume (as in the case of Fig. 8), diffusion field impingement could result.

From isochronal DSC scans, a glass transition temperature (T_g) was not resolved. The absence of a distinct glass transition temperature (T_g) upon reheating during the isochronal calorimetry experiments supports the hypothesis that the observed clusters act as nucleation sites for subsequent nano-crystalline formation. This lack of T_g has been previously reported in marginal glass formers quenched from the liquid state [22]. One should note, however, that calorimetric data, like XRD data, is an average over a range of powder sizes in any given sample. Therefore, a uniform and fully amorphous state could exist in powders of the smallest size. A more detailed study of as-solidified submicron powders using HRTEM is needed before any definite conclusions can be drawn.

Conclusion

Rapid solidification of Al–38Sm (wt%) alloy by gas (He) atomization resulted in the formation of metastable and amorphous phases. Droplets with different diameters solidified at different undercooling values and resulted in formation of fcc-Al, tetragonal $Al_{11}Sm_3$, orthorhombic Al_4Sm, and a new orthorhombic phase designated as ER. The room temperature stable phases are not observed in any of the powder size groups. It is believed that $Al_{11}Sm_3$ and ER are competing metastable phases at different levels of undercooling. The crystallization path of orthorhombic Al_4Sm is not clear. It may possibly be formed by decomposition of solid $Al_{11}Sm_3$ or by solidification of highly undercooled melt.

Decrease of particle size in powders tends to decrease the internal nucleant concentration which promotes larger undercoolings. This results in formation of amorphous phases with a high density of supersaturated fcc-Al nanoclusters. In the smallest observed powders some of these clusters showed a restricted growth by rejecting solute into the amorphous matrix that, in turn, yields a diffusion field impingement. Clusters with a critical diameter of less than 10 nm did not show any obvious partitioning according to EDS. The formation of Al nanocrystals was not suppressed at any powder size, but vitrification was always accompanied by crystal cluster formation during gas atomization.

Acknowledgment

Appreciation is expressed to M.J. Kramer for valuable help in HEXRD. The work at Ames Laboratory and at the MUCAT sector at the APS, Argonne National Laboratory, was supported by the United States Department of Energy (USDOE), Office of Science (OS), Office of Basic Energy Science (BES), and Iowa State Materials Science and Engineering Department, Contract No. DE-AC02-07CH11358. The assistance of the Materials Preparation Center of the Ames Laboratory [23] is acknowledged for supplying our samples.

Reference

1. R.I.Wu, G. Wilde, and J.H. Perepezko, Materials Science and Engineering A, 301, (2001), 12-17.
2. J.C. Foley, D.R. Allen, and J.H. Perepezko, Scripta Materialia, 35, (1996), 665-660.
3. L. Battezatti, S. Pozzovivo, and P. Rizzi, Encyclopedia of Nanoscience and Nanotechnology, Edited by H.S Nalwa, (2004), 341-364.
4. A. Inoue, Progress in Materials Science, 43, (1998), 365-520.
5. J.H. Perepezko, R.J. Hebert, R.I. Wu, and G. Wilde, J. Non-Cryst. Solids, 317, (2003), 52-61.

6. J.Q. Guo, K.Ohtera, K. Kita, J. Nagahora, and N.S. Kazama, Materials Letters, 24, (1995), 133-138.
7. A. Saccone, G. Cacciamani, D. Maccio, G. Borzone, and R. Ferro, Intermetallics, 6, (1998), 201-215.
8. P. Rizzi, C. Antonione, M. Baricco, L. Battezzati, L. Armelao, E. Tandello, M. Fabrizio, and S. Daolio, Nanostructured Materials, 10, (1998), 767-776.
9. P. Rizzi, M. Baricco, S. Borace, and L. Battezatti, Materials Science and Engineering A, 304-306, (2001), 574-578.
10. G. Wilde, H. Sieber, and J.H. Perepezko, Scripta Materialia, 40, (1999), 779-783.
11. Y. E. Kalay, L.S. Chumbley, I.E. Anderson, and R.E. Napolitano, Metallurgical and Materials Transactions A, 38A, (2007), 1452-1457.
12. Y.E. Kalay, I.E. Anderson, and L.S. Chumbley, International Conference on Powder Metallurgy and Particulate, *MPIF/AIME*, June 18-21, San Diego- California, (2006), 95-105.
13. R. Trivedi, F. Jin, and I.E. Anderson, Acta Materialia, 51, (2003), 289-300.
14. C.G. Levi, and R. Mehrabian, Metall. Trans. A, 13, (1982), 13-23.
15. C.G. Levi, and R. Mehrabian, Metall. Trans. A, 13, (1982), 221-234.
16. E. Vasilyeva, and V. Vystavkina, J. Mag. and Mag. Mat., 267, (2003), 267-273.
17. F. Casteels, J. Less-Common Metals, 12, (1967), 210-220.
18. K.H.J. Buschow, and J.H.N van Vucht, Philips Res. Repts., 22, (1967), 233-245.
19. T.B. Massalski, Binary Alloy Phase Diagrams, 1, (1987), 166-167.
20. F. Casteels, P. Diels, and A. Cools, J. Nuclear Materials, 24, (1967), 87-94
21. J.H.N van Vucht, and K.H.J. Buschow, Philips Res. Repts., 19, (1964), 319-322.
22. J.H. Perepezko, and G.Wilde, , J. Non-Cryst. Solids, 274, (2000), 271-281.
23. Materials Preparation Center, Ames Laboratory, US DOE Basic Energy Sciences, Ames, IA, USA, available from: www.mpc.ameslab.gov.

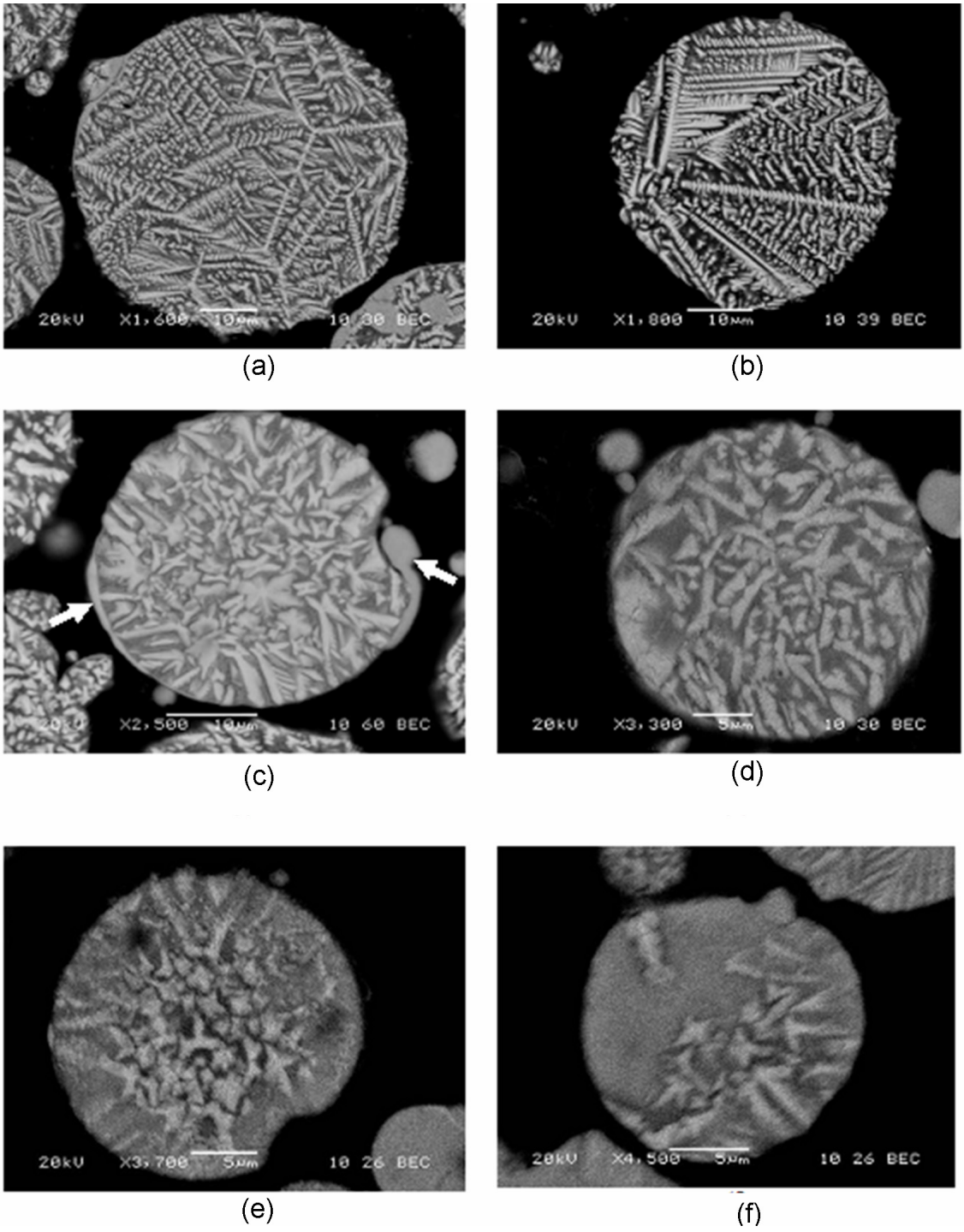

Figure 1. Representative cross-sectional BSE micrographs of Al–Sm alloy at different particle sizes: (a) 58 µm, (b) 50µm, (c) 35 µm, (d) 28 µm, (e) 23 µm, and (f) 18 µm size in average diameter.

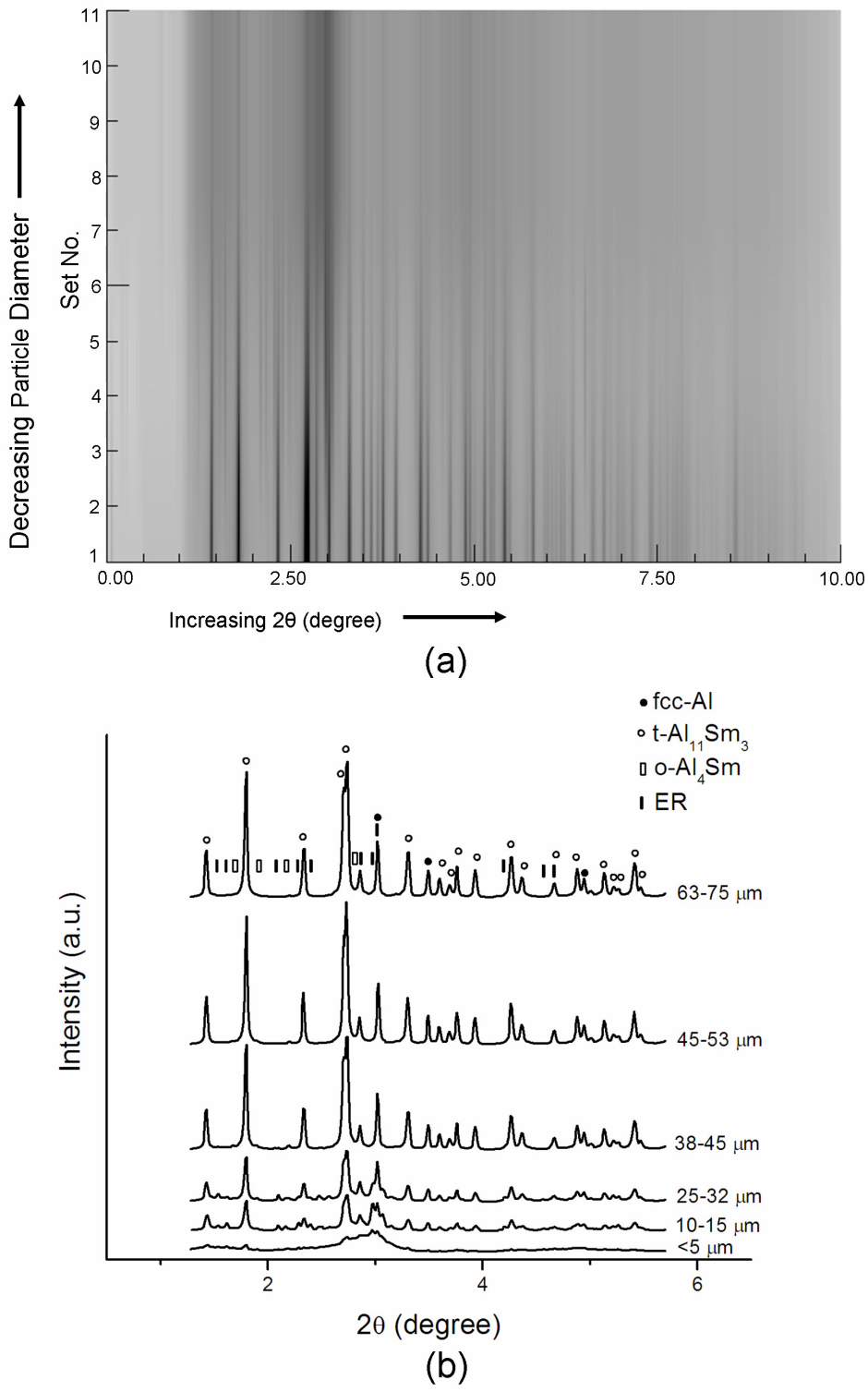

Figure 2. (a) Image plate scan of powders at different diameters. (b) X-ray diffraction patterns extracted from image plate scan (a) for selected powder diameters.

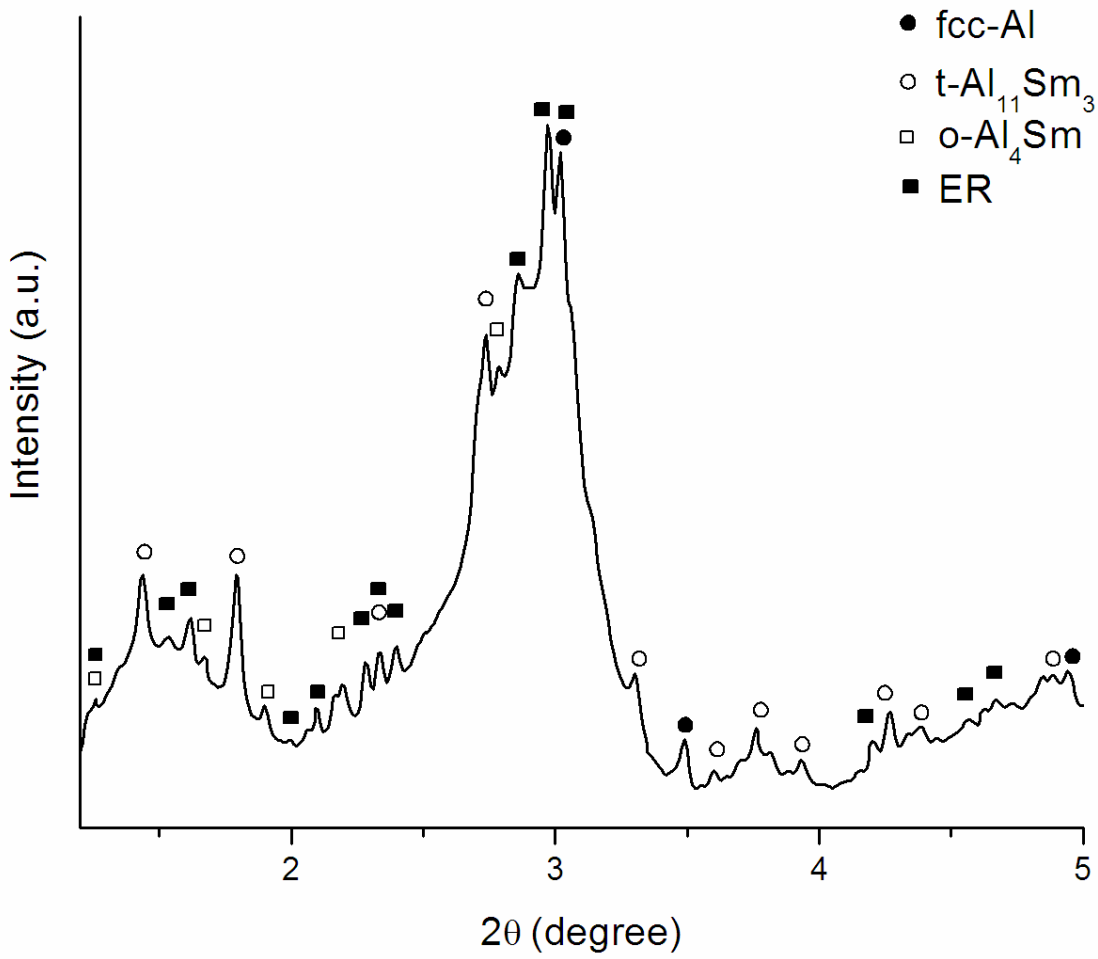

Figure 3. X-ray diffraction patterns of below 5 µm average diameter particles.

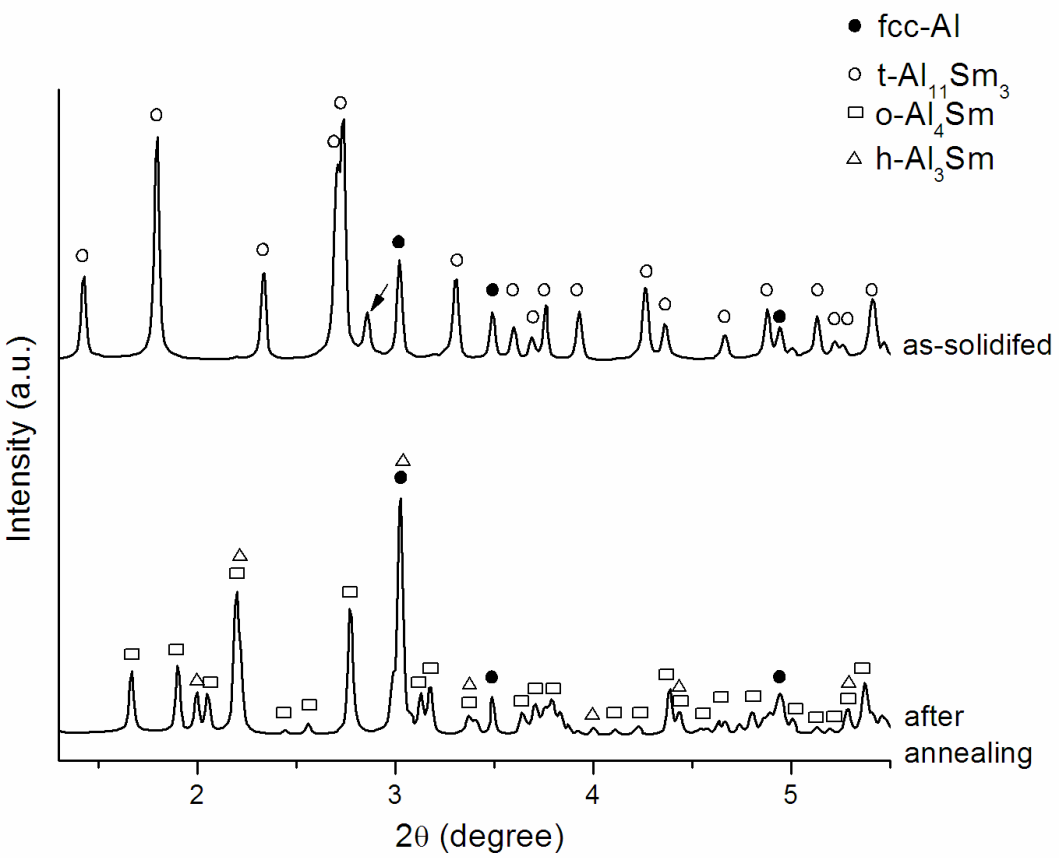

Figure 4. X-ray diffraction patterns of as-solidified and annealed powders with 75–63 µm size diameter.

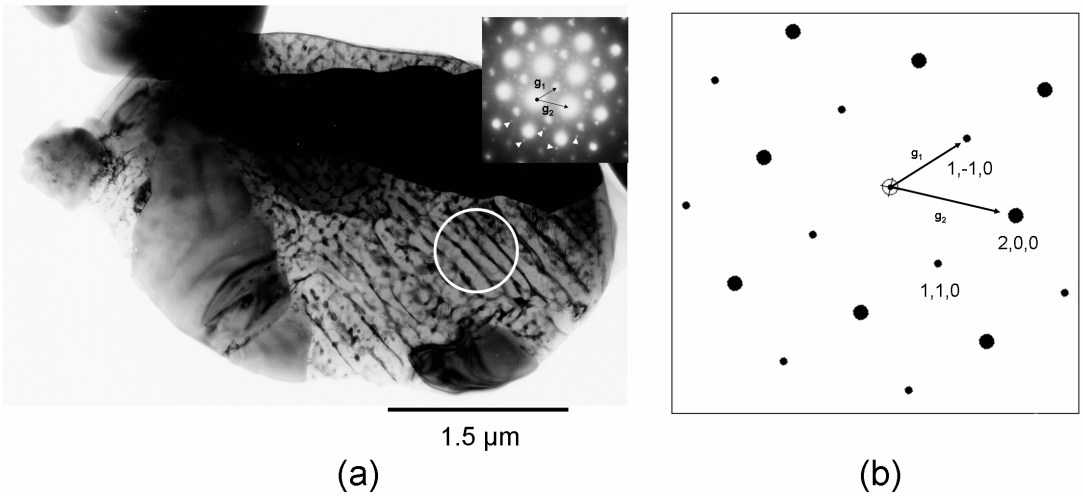

Figure 5. (a) BF image of an Al–Sm powder showing a primary phase and a eutectic matrix, inset shows SAD taken from the area circled. Arrows show the possible fcc-Al reflections. (b) Simulated [0 0 1] diffraction pattern for tetragonal $Al_{11}Sm_3$. Note that possible Al reflections overlap the brightest $Al_{11}Sm_3$ reflections.

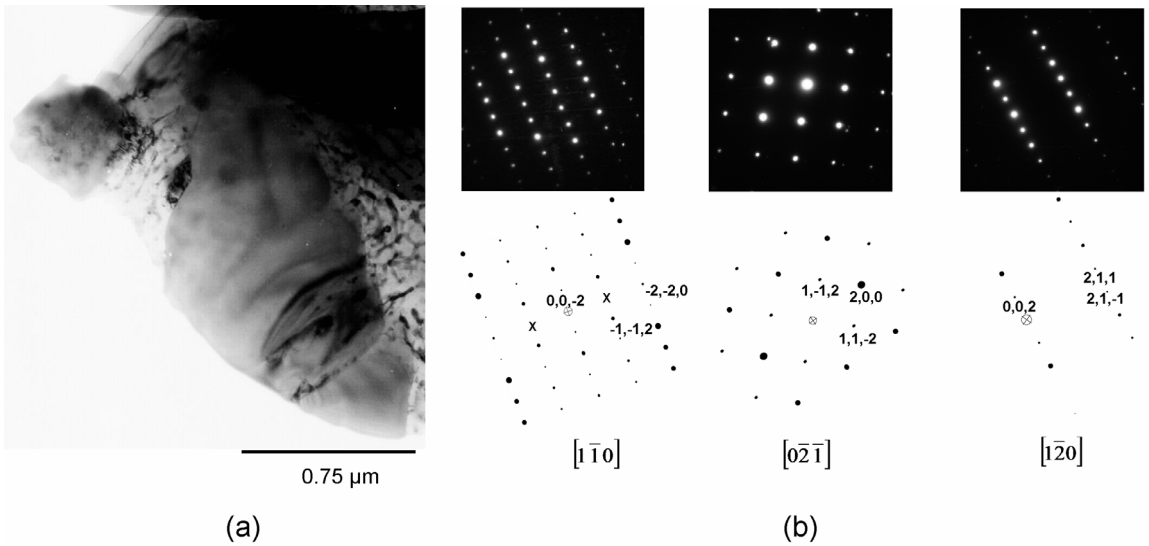

Figure 6. (a) BF image of the grain in Fig. 5(a), and (b) corresponding SAD and simulations at different zone axes. The (x) denotes double diffraction.

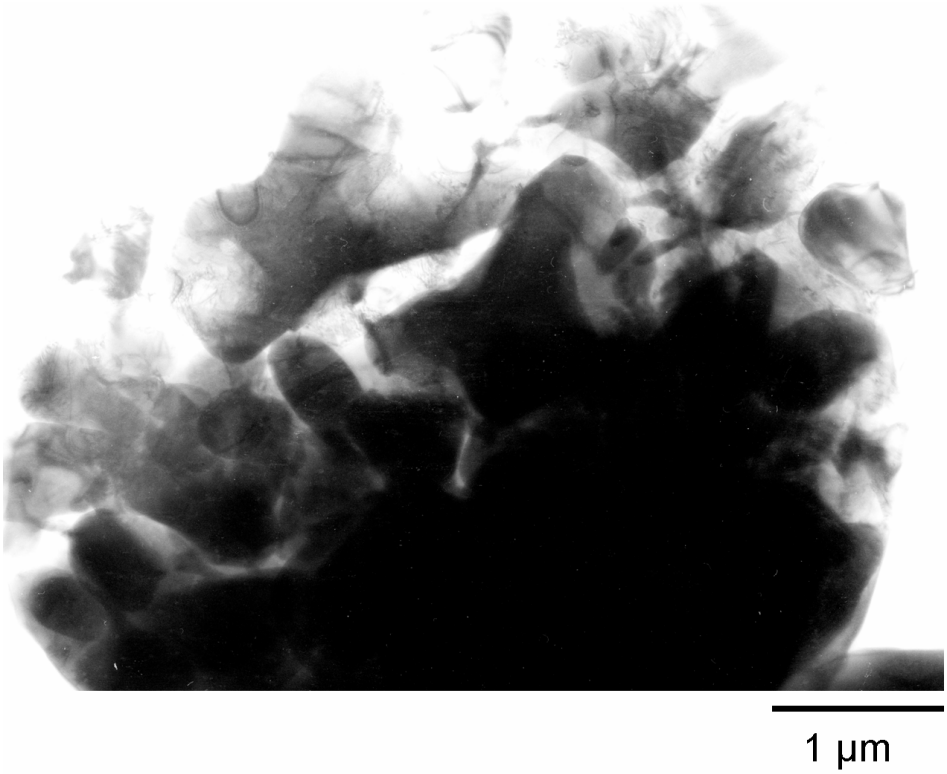

Figure 7. BF image of an Al–Sm powder showing equiaxed grains.

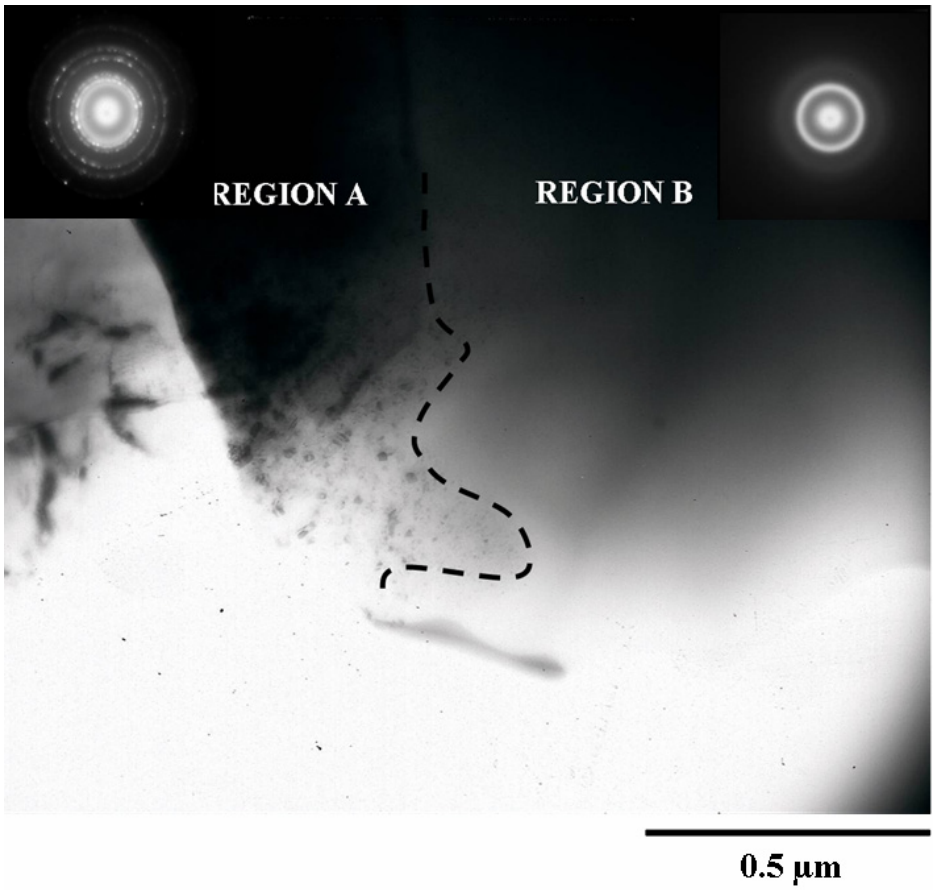

Figure 8. Al–Sm powder (diameter ≤3 µm) exhibiting nano-crystalline (Region A) and amorphous regions (Region B). The insets show the SAD patterns of Regions A and B.

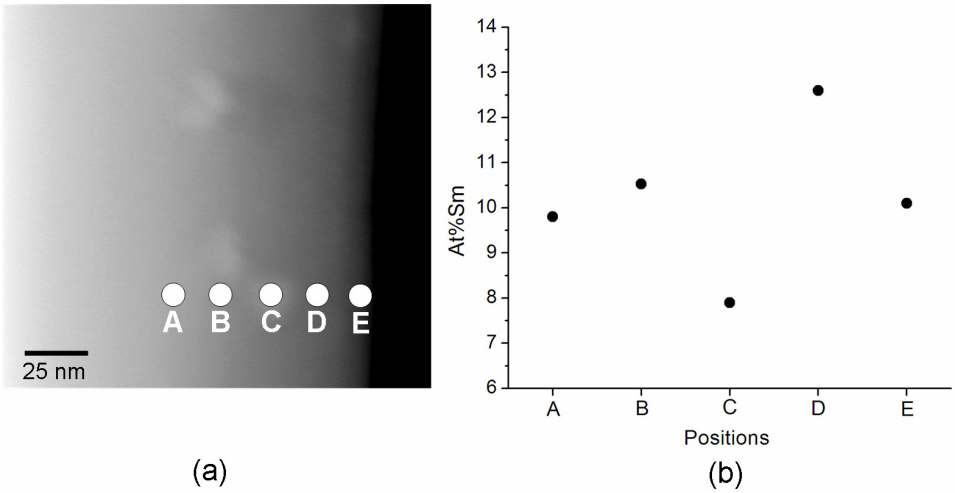

Figure 9. (a) HAADF image of nanoparticles and (b) EDS line scan across a nanoparticle.

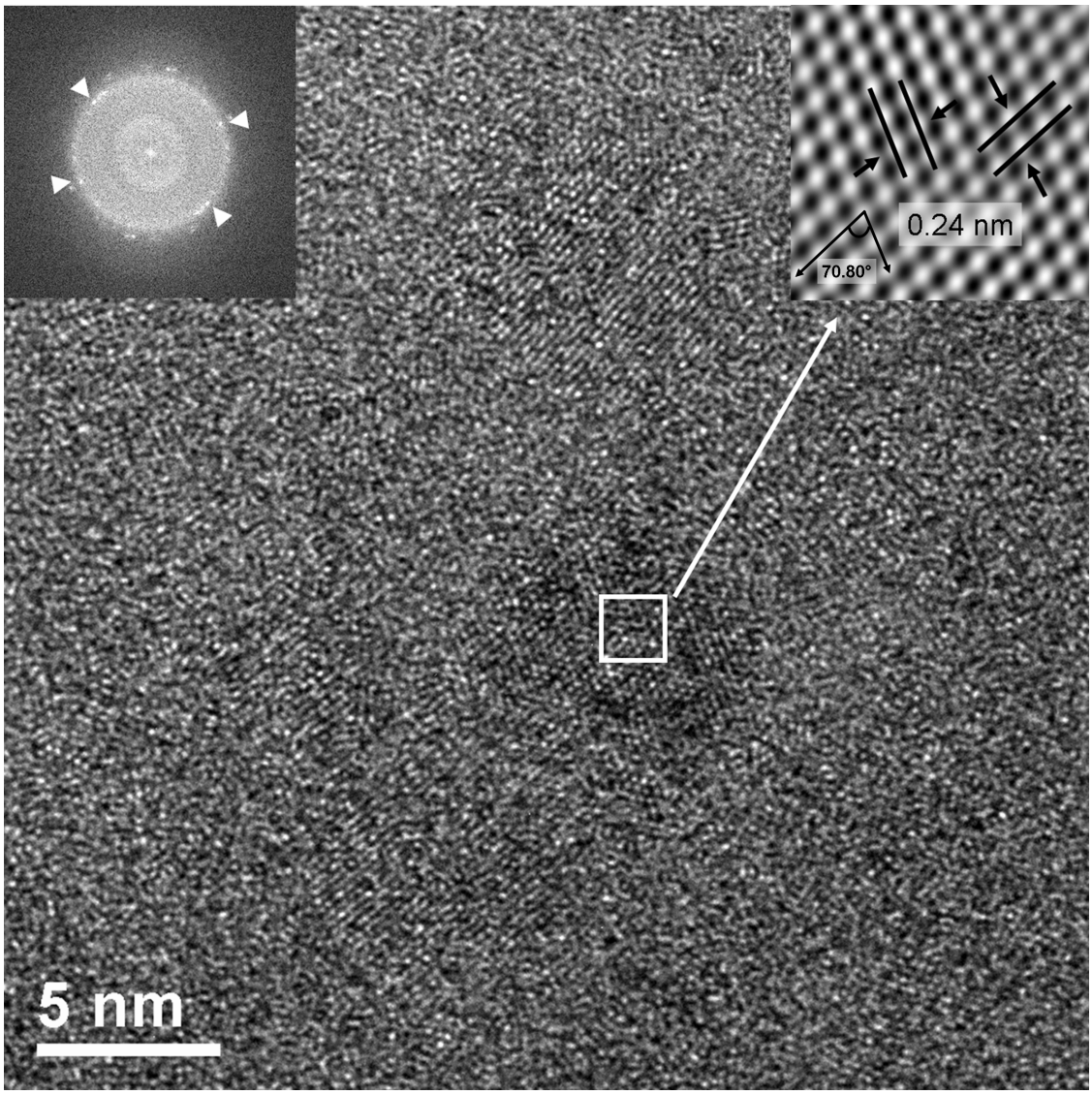

Figure 10. (a) High resolution TEM image taken from a submicron size Al–Sm powder. Insets show fast Fourier transform of the full area (left) and inverse Fourier transformed image (right) of the area denoted by the square. The image was calculated using only the reflections denoted by arrows in the FFT. An isolated Al nanocrystal is shown in the as-solidified powder. Lattice fringes corresponding to (1 1 1) spacing of fcc-Al are indicated.

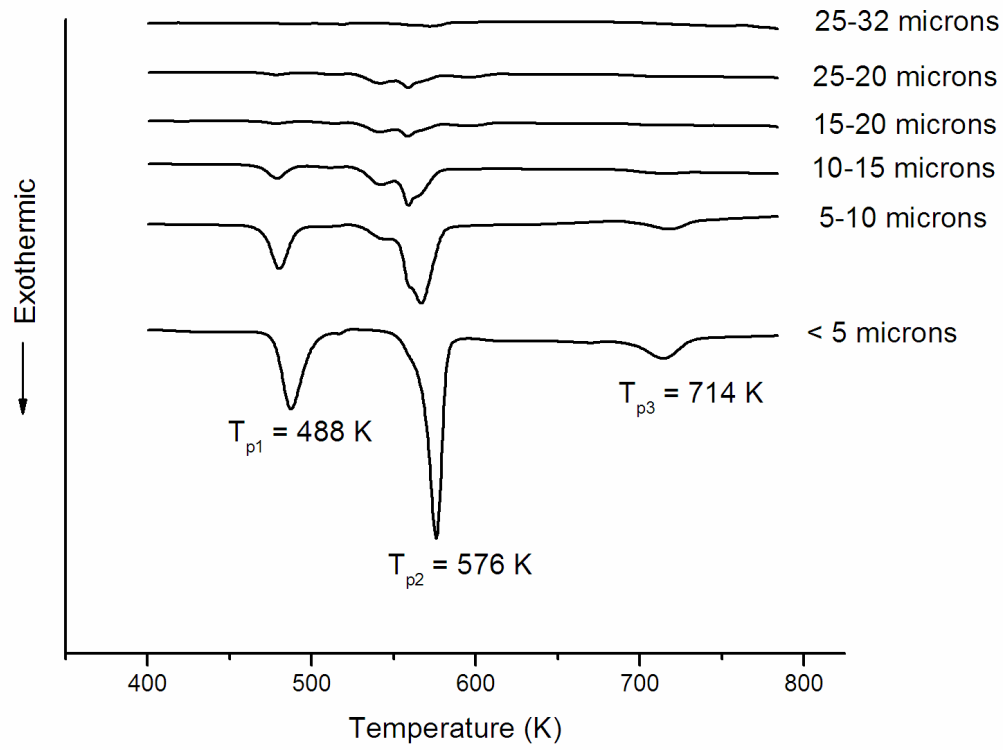

Figure 11. Isochronal DSC scans of powders from different size groups at a heating rate of 40 K/s. Peak temperatures of three crystallization events are shown for below 5 µm average diameter particles.

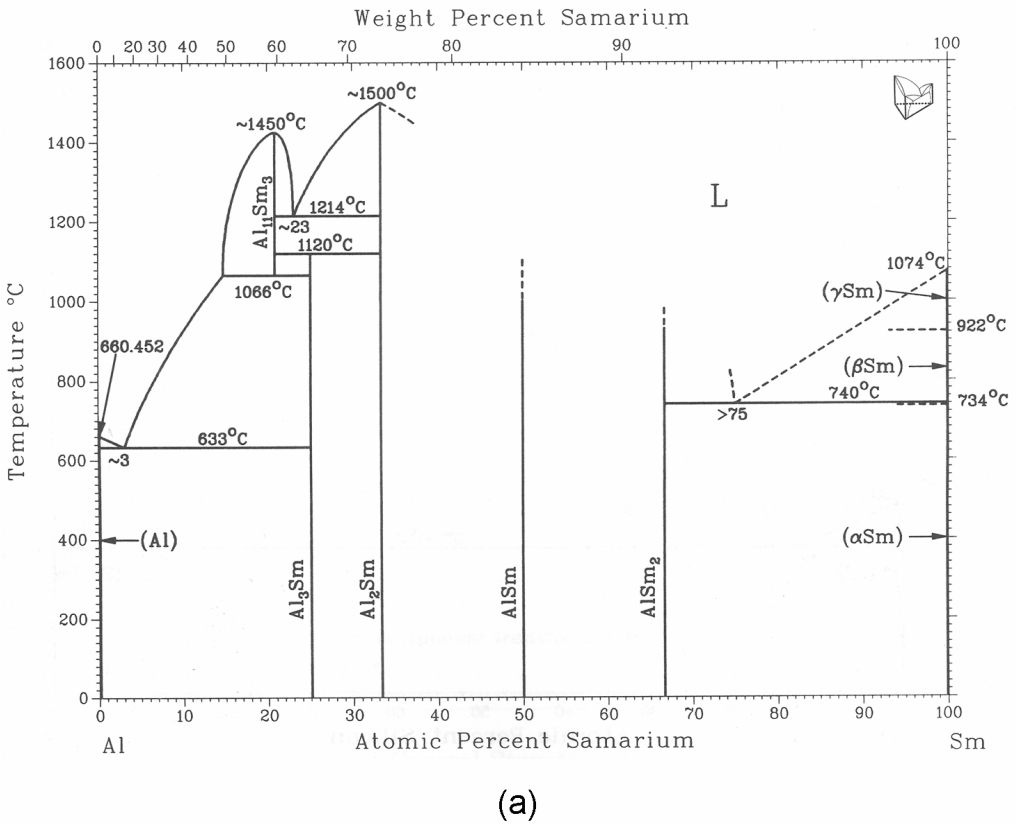

(a)

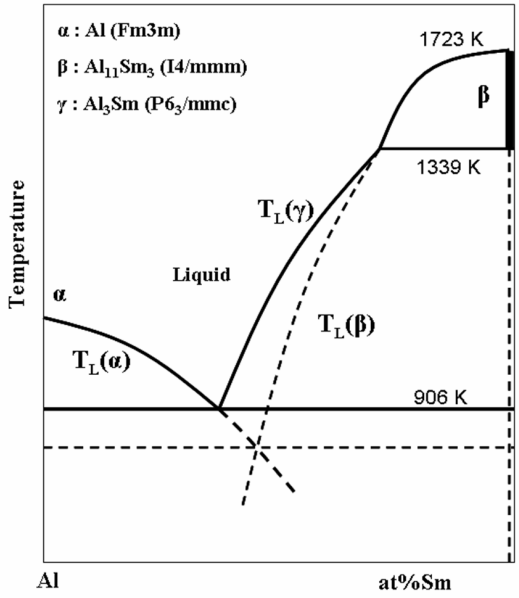

(b)

Figure 12. (a) Phase diagram of Al–Sm binary system [19]. (b) Schematic illustration of Al-rich portion of Al–Sm phase diagram (not to scale) under a different level of hierarchy of equilibrium. Metastable liquidus and eutectic are shown as dashed lines.

Table 1. Classification of a rapidly solidified gas atomized Al-Sm powders

Set No		**1**	**2**	**3**	**4**	**5**	**6**	**7**	**8**	**9**	**10**	**11**[†]
Diameter	***max***	75	63	53	45	38	32	25	20	15	10	<05
(μm)	***min***	63	53	45	38	32	25	20	15	10	05	

[†] Please note that below 5 μm diameter particle size was further classified using sedimentation method for TEM analyses.

Table 2. Rietveld refinement results for selected powder groups showing the atomic percentages (at %) of Sm in tetragonal phase.

Names of the Atomic Sites	Multiplicity (m)	Occupancies (Occ)		
		75 – 63 µm	**63 – 53 µm**	**53 – 45 µm**
Aluminum(1)	2	1.0000	1.0000	1.000
Aluminum (2)	4	0.6180	0.6148	0.6171
Samarium (1)	2	0.6025	0.6078	0.6106
At% Sm		**0.213**	**0.214**	**0.214**

Table 3. Phases observed in gas atomized Al-Sm powders

Component	Structure (HEXRD)	Space Group	Lattice Parameter (nm)	Reference
Amorphous				[6, 9]
Al Solid Solution	FCC	F m 3 m	a = 0.405 -0.420	
t-$Al_{11}Sm_3$	Tetragonal	I4 / m m m	a = 0.428 c = 0.992	[17, 18]
o-Al_4Sm	Orthorhombic	I m m a	a = 0.444 b = 0.638 c = 1.362	[20]
ER	Orthorhombic		a = 0.416 b = 0.634 c = 1.328	This study

Table 4. The measured (Fig5a (inset) and calculated interplanar spacings for fcc-Al and t-$Al_{11}Sm_3$ for allowed reflections. (*double diffraction)

Interplanar Spacings (nm)		
Measured	**Calculated**	
	t-$Al_{11}Sm_3$	**fcc-Al**
0.301 (g_1)	0.4950	0.2338
0.234	0.3929	0.2024
0.207	0.3026	0.1431
0.211 (g_2)	0.2613	0.1221
0.163*	0.2582	0.1169
0.132*	0.2140	0.1012
0.115	0.1964	0.9290
0.106	0.1879	0.9050
0.101	0.1656	0.8260

Table 5. Interplanar spacings for ER measured by HEXRD and TEM

Interplanar Spacings (nm)	
HEXRD	TEM
0.633	
0.573	0.571
0.461	
0.357	0.358
0.337	0.331
0.309	
0.303	
0.295	
0.286	
0.274	
0.259	0.254
0.248	0.247
0.234	0.232
0.224	0.222

CHAPTER 4: CRYSTALLIZATION BEHAVIOR IN A HIGHLY DRIVEN MARGINAL GLASS FORMING ALLOY

A paper published in Journal of Non-Crystalline Solids

Y.E. Kalay[1,2], L.S. Chumbley[1,2], I.E. Anderson[1,2]

Abstract

$Al_{90}Sm_{10}$, a marginal glass former, was rapidly solidified using Cu-block single roller melt spinning at wheel speeds of 30 and 40 m/s. The product phases of rapid solidification were identified and analyzed using high energy synchrotron X-ray diffraction (HEXRD), high resolution transmission electron microscopy, and atom probe tomography. The as-quenched structure consists of a saturated amorphous phase and nanocrystalline Al with typical length scale of about 5 nm. The appearance of a pre-peak on HEXRD diffraction patterns and a low activation energy for first crystallization as determined using the Kissinger and Ozawa methods indicate some local ordering in the amorphous phase. The devitrification phase transformation path was determined using in-situ high energy synchrotron radiation. Three phases, MS1, H1, and Al_4Sm, were identified during decomposition of the amorphous phase. MS1, H1 and Al_4Sm are cubic, hexagonal and orthorhombic metastable phases, respectively.

Introduction

In marginal glass formers amorphization is often accompanied by the presence of nanocrystals after quenching from the liquid [1], [2] and [3]. The presence of nano-sized crystalline precursors in the amorphous matrix can result in several important improvements

[1] Department of Materials Science and Engineering, Iowa State University, Ames IA 50011-3020 USA

[2] Ames Laboratory (DOE), Iowa State University, Ames IA 50011-3020, USA

such as a remarkable increase in strength and ductility, compared to single phase amorphous structures in lightweight Al alloys [3], [4] and [5].

Al–Rare Earth (RE) based alloys constitute an important part of the marginal glass forming alloy family, where glass formation is observed between the Al–RE eutectic point and $Al_{11}RE_3$ or Al_3RE intermetallics [3] and [6]. Among the Al–RE binary alloys the Al–Sm system has recently attracted considerable interest due to its wide glass formation range, being from 8 to 16 at.% Sm [3].

Studies have shown that vitrification of Al–Sm alloys within the glass formation composition range is a complicated process. Even when using the same processing route, such as melt spinning of identical compositions with similar processing conditions to produce amorphous phase, various studies have identified different product phases [7], [8] and [9]. Similarly, the devitrification of amorphous Al–Sm is not understood clearly since crystallization from the same amorphous phase has resulted in different decomposition paths [9], [10] and [11]. Examples of the various decomposition paths identified for $Al_{90}Sm_{10}$ are given in Table 1, with information concerning the identified phases summarized in Table 2. The phases shown in Table 2 were identified using conventional X-ray diffraction (XRD) instruments with either Cu [10] or Co [9] and [11] targets.

In the present study the devitrification path of melt-spun $Al_{90}Sm_{10}$ alloy was investigated in-situ using high energy synchrotron X-ray diffraction (HEXRD). Synchrotron radiation has many benefits over conventional laboratory X-ray sources. For example, the shorter wavelength of synchrotron X-ray radiation, coupled with high coherency and highly sensitive photon detection system, helps to detect smaller features such as nanocrystals during devitrification. Since a Debye–Scherrer (transmission X-ray diffraction) geometry is employed, data can be collected from the entire sample over a wider angular range [12]. Moreover, collection of X-ray diffraction data in-situ can avoid many of the problems

associated with using samples that have been quenched to room temperatures to facilitate X-ray diffraction analysis.

The structure and chemistry of as-quenched samples prior to devitrification was investigated using high resolution electron microscopy (HRTEM), and atom probe tomography (APT). The crystallization kinetics of amorphous $Al_{90}Sm_{10}$ was studied by using differential scanning calorimetry (DSC) under isochronal heating conditions.

Experimental Procedure

Ingots of $Al_{90}Sm_{10}$ were prepared by arc melting under an Ar atmosphere from highly pure Al (99.99 wt%.) and Sm (99.9 wt%.) elements. Rapidly-solidified ribbons with a thickness of 20–30 μm were produced by Cu-block melt spinning techniques under an Ar atmosphere at tangential wheel speeds of 30 and 40 m/s.

Isochronal analysis of as-rapidly-solidified ribbons was performed using a Perkin Elmer Pyris 7 DSC at scanning rates of 5–60 K/min to assess the crystallization kinetics.

The as-solidified and devitrification product phases were investigated in-situ using HEXRD at the Advanced Photon Source at Argonne National Laboratory in collaboration with the Midwest Universities Collaborative Access Team (MUCAT). The as-solidified ribbons were cut to around 10 mm lengths and inserted into 2 mm diameter thin-walled quartz tubes that were evacuated and sealed in Ar for high temperature experiments. The sealed capillary tubes were exposed to 100 keV X-rays of wavelength 0.012347 nm during in-situ devitrification experiments. The diffraction data were collected with Debye–Scherrer geometry by a CCD camera every 20 s. The onset (T_x) and peak temperatures (T_p) measured using DSC and in-situ HEXRD contain an error of ±1°.

The as-solidified ribbons were investigated using a Tecnai G^2 F20 scanning/transmission electron microscope (S/TEM) before the devitrification process.

Samples for HRTEM were thinned using electropolishing at −25 °C with a solution of 3 vol.% HCl, 36 vol.% methanol and distilled water.

Chemical distributions in the as-solidified ribbons was investigated using 3D APT microscopy (LEAP 3000X) in collaboration with the University of North Texas. Sharp needle-shaped samples for atom probe tomography analysis were prepared using a focused ion beam (FIB) instrument with Ga ion milling

Results

Thermal analysis

Heating amorphous $Al_{90}Sm_{10}$ from room temperature at selected heating rates of 5, 10, 20, 30, 40 and 60 K/min resulted in three exothermic events corresponding to crystallization processes, as shown in Fig. 1. No obvious endothermic event, indicative of a glass transition, was seen at any heating rate. As the heating rate increased from 5 to 60 K/min, the crystallization temperatures of all three exothermic events shift towards higher temperatures. The onset (T_x) and peak (T_p) temperatures of crystallization events are shown in Table 3.

The activation energies for these crystallization events were determined by the Kissinger [13] and Ozawa [14] equations, given as Eqs. (1) and (2), respectively:

$$\ln\left(\frac{T^2}{\beta}\right) = \left(\frac{E}{RT}\right) + \text{constant} \tag{1}$$

$$\log(\beta) = -0.4567\left(\frac{E}{RT}\right) + \text{constant} \tag{2}$$

where β is the heating rate, T is the specific temperature, R is the gas constant and E is the activation energy for a specific reaction. Fig. 2(a) and (b) shows Kissinger and Ozawa plots of the different crystallization events, respectively. Based upon the slopes of the plotted data, the activation energies were calculated and are shown in Table 4. The activation energies

found by using both methods are in excellent agreement. When comparing the different crystallization events, the activation energy of the third event is the highest, while the second crystallization has the lowest values, based on the peak temperature calculations.

In-situ high energy XRD experiments

X-ray diffraction experiments were conducted in-situ, while heating the Al–Sm ribbons at 5 K/min. Fig. 3(a) shows the change in maximum diffraction intensity at one fixed peak position with respect to temperature in the range of 468–510 K. The temperature corresponding to the onset of initial devitrification as measured by high temperature X-ray diffraction is in good agreement with the onset temperature (472 K) measured by DSC at a heating rate of 5 K/min (Fig. 3).

Fig. 4, Fig. 5 and Fig. 6show the image surface plots and three dimensional surface plots of first, second and thirds crystallization events, respectively. These plots show crystallization events in-situ during isochronal heating with a rate of 5 K/min. The plots are created by collecting diffraction patterns every 20 s with a CCD camera. These patterns (in the form of Debye–Scherrer images) are stored and subsequently integrated to produce an intensity vs. Q (or 2θ) plot for each temperature, where the lines on the images indicate the location of Bragg peaks, with the contrast level being proportional to diffracted beam intensities. All of the individual plots are then assembled to produce the displayed 3D image. Thus, the 2D image surface plots which show the amorphous diffracted intensity as a broad line in Fig. 4(a) and sharper lines corresponding to crystalline peaks visible in Fig. 4, Fig. 5 and Fig. 6(a) can be displayed as a 3D surface plot which is easier to interpret. In addition to X and Y axes which show the 2θ and temperature, the Z axis shows the absolute diffracted intensity.

The three different crystallization events seen in HEXRD are in good agreement with DSC results that show three exothermic reactions below the melting point. Fig. 4 shows the

initial crystallization with the major broad peak of the amorphous phase located at 2.94° 2θ. This peak decomposes to crystalline phase(s) at approximately 472 K for a heating rate of 5 K/s. An interesting observation is the existence of a minor broad peak located at 1.42° 2θ, well below the position of the amorphous hump. Possible implications of this peak will be discussed later.

Fig. 5 and Fig. 6 show the solid–solid phase transformations corresponding to the last two exothermic events detected by DSC. According to HEXRD, each transformation occurs by nucleation and growth of a new phase at the expense of the previous phase. Thus, the initial phase is replaced by a second phase, which in turn is replaced by the third phase. The peak temperatures corresponding to the point where approximately 50% of the phase transformation is complete are 542 and 667 K, respectively, at a heating rate of 5 K/min. These values also are in good agreement with the DSC data.

Identification of the devitrification product phases were determined from intensity versus 2θ scans at specific temperatures extracted from the three dimensional surface plots. Temperatures were chosen where the exothermic reaction for each transformation as measured by DSC is fully completed and a local equilibrium apparently is established. These temperatures were 503, 604 and 773 K. The first crystalline phase after devitrification was found to be a cubic phase with a lattice parameter of a = 0.9831 nm. This phase decomposes and is replaced by an hexagonal phase with lattice parameters of a = 0.4619 and c = 1.2772 nm. This hexagonal phase subsequently decomposes and is replaced by an orthorhombic phase with lattice parameters of a = 1.3872, b = 0.6441 and c = 0.4494 nm

Peaks from what appears to be fcc-Al could also be identified at all temperatures after initial devitrification has occurred at 503 K. The peaks were small initially, but grew in intensity as temperature increased. It should be noted that the Bragg peaks coming from fcc-Al phase would overlap many of the peaks associated with the primary crystallization of the identified cubic phase. Thus, it is possible that fcc-Al nucleation occurs early in the

transformation sequence. Fig. 7 summarizes all the phases identified at different temperatures.

HRTEM and APT

The as-solidified microstructure of melt-spun ribbons was investigated using HRTEM. Fig. 8 shows a HRTEM image of a ribbon produced at a wheel speed of 40 m/s. While nanocrystal formation is not easily recognized from the original HRTEM image at room temperature, the Fourier transform of the image (Fig. 8(a), inset) shows slight diffracted intensity superimposed on the amorphous halo, indicative of the existence of crystalline material within the amorphous matrix. Fig. 8(b) shows the inverse-Fourier-transform image of the full area shown in Fig. 8(a) by masking all but the outer ring of the Fourier transformed image. The inverse-Fourier-transform image clearly demonstrates that nanocrystals with an approximate size of less than 5 nm are formed during melt quenching.

The formation of nanocrystals is more clearly seen in ribbons produced at a wheel speed of 30 m/s. As shown in Fig. 9, both the HRTEM and filtered inverse Fourier images reveal clusters of nanocrystals in the amorphous matrix. Their sizes are on the order of 5 nm, larger in diameter than those observed in ribbons produced at 40 m/s wheel speed. The lattice spacings between two adjacent planes (0.24 nm) in the clusters observed in Fig. 9(b) are in good agreement with the distance between (1 1 1) planes in fcc-Al.

Atom probe tomography (APT) was also used to study ribbons solidified at a wheel speed of 30 m/s. Since APT samples were thinned by FIB, a thin damaged layer enriched in Ga ions was formed in the thinnest region. Thus, only the region beneath the line (shown by arrows in Fig. 10) was taken under consideration. As shown in Fig. 10, images obtained show clusters of Al atoms on the order of 5 nm, which is in good agreement with HRTEM observations. Since two different sample preparation techniques (electropolishing and FIB, for HRTEM and APT, respectively) show similar structures, the local heating and structural

damage caused by FIB is apparently minor. The local nano-sized structures seen in amorphous $Al_{90}Sm_{10}$ alloy are therefore believed to be an accurate representation of atomic structure. The Sm atoms appear to form a network surrounding the Al clusters, with a small amount of Sm trapped inside the clusters. The Sm-rich regions between the nanocrystalline fcc-Al phases represent the amorphous regions seen in HRTEM images.

Discussion

Before a discussion of the crystallization of the amorphous phase can take place it is imperative that the as-solidified structure is well-defined. Under the kinetic constraints of a rapid solidification process such as melt spinning, the nucleation of equilibrium phases can be suppressed [15]. According to the current Al–Sm binary phase diagram [16], the predicted phases forming upon equilibrium solidification of $Al_{90}Sm_{10}$ alloy are hexagonal Al_3Sm and fcc-Al, with the microstructure consisting of proeutectic Al_3Sm and fcc-Al/Al_3Sm eutectic. HRTEM images show that fcc-Al solid solution nanocrystals form within an amorphous phase, and this is supported by APT data where Al atom clusters of similar size are clearly identifiable. Similarly sized nanocrystals were observed in powders of the same composition that were solidified having high undercoolings produced using high pressure gas atomization (HPGA) [17]. Both of these observations indicate that solidification of $Al_{90}Sm_{10}$ under metastable conditions results in bypassing of the equilibrium hexagonal Al_3Sm and eutectic structures to retain the fcc-Al structure in an amorphous matrix. The size of fcc crystallites in melt-spun ribbons is on the order of 2–5 nm for 30 and 40 m/s wheel speeds. Previous [17] and current results show a high density of nanocrystalline formation in the amorphous matrix (within the range of 10^{22}–10^{23} m^{-3}) as estimated from HRTEM. Similar results in different alloy systems including $Al_{92}Sm_8$ are reported in the literature [18], [19], [20] and [21]. The mechanism of formation of such a high density of crystallites in amorphous alloys is not fully understood [18]. Classical nucleation theory predicts a much smaller number for the number

of nuclei [21] and [22], and different crystallization mechanisms alternative to classical theory have been developed to explain unusual high-density nanocrystallization in certain amorphous alloys [18], [19], [20], [21], [22], [23], [24] and [25]. One hypothesis for the existence of such high nanocrystalline densities is the growth of "quenched-in" nuclei formed by growth kinetic limitations [19] and [20]. During rapid solidification of $Al_{90}Sm_{10}$ ribbons, a relatively high fraction of crystallites may nucleate initially in the liquid state, but show a restricted growth in the amorphous matrix. Reasons for this restricted growth have been attributed to the effects of increased viscosity [19] and diffusion field impingement [20] during continuous cooling in the melt spinning process.

Room temperature HEXRD pattern of as-rapidly-solidified $Al_{90}Sm_{10}$ ribbons showed no crystalline peaks (Fig. 7). It is interesting that the fcc-Al nanocrystals easily seen in HRTEM are not detectable using synchrotron radiation. One possible reason for this may be the broadening of the Bragg peaks due to the small size (2–3 nm) of the nanoclusters (Fig. 8). As noted earlier, a small pre-peak is observed well below the major amorphous peak position (Fig. 4 and Fig. 7 (Room Temp) at 1.42° 2θ). Fig. 11 shows the positions of the pre-peak and major amorphous peak positions in reciprocal space (Q, nm^{-1}). The pre-peak (Fig. 11 at 12.6 nm^{-1} Q) evolved into strong Bragg diffraction of cubic MS1 phase at the first crystallization temperature. Thus, the appearance of the pre-peak may be an indication of local ordering in the amorphous phase. According to HRTEM, APT and HEXRD results the as-solidified structure consists of nano-sized Al crystallites dispersed in the amorphous matrix. Previous studies on devitrification of $Al_{90}Sm_{10}$ melt-spun ribbons [9], [10] and [11] employed conventional Cu or Co Kα radiation rather than in-situ diffraction using synchrotron radiation, which has a far shorter wavelength and higher signal to noise ratio. Therefore, the presence of nanosized, pre-existing clusters in the amorphous matrix would have been extremely difficult to detect.

DSC scans do not show any obvious endothermic event indicative of a glass transition at any heating rate (Fig. 1). A previous study showed that an amorphous $Al_{92}Sm_8$ alloy, presumably free of any quench-in nuclei produced by solid-state processing, exhibited a clear separation between a glass transition and the crystallization temperatures upon reheating of the sample in the DSC [28]. Thus, the pre-existing Al nanocrystals seen in HRTEM are believed to not only catalyze nucleation of the first crystalline phase, but also to cause T_g to coincide with T_x, obscuring a clear separation between these two temperatures [19] and [20]. It should be noted that the absence of a T_g upon reheating in the DSC is a general observation for samples of marginal glass formers [3] that were quenched from a liquid alloy. Also, the possible role in the catalysis reaction of MS1 phase in a pre-cluster form within the glass is not known.

The activation energies of the first crystallization event calculated by Kissinger and Ozawa plots (Fig. 2) were found to be relatively low compared to many other bulk amorphous alloys [26] and [27], which indicates a low thermal stability against crystallization. This statement is in good agreement with the observed HRTEM and APT data, which show the amorphous phase existing with a high density of Al nanocrystals. The nanocrystals presumably act as heterogeneous nucleation sites, decreasing the energy required for crystallization of the cubic crystalline phase (MS1) identified as being the first phase to form in the amorphous matrix. The preliminary evidence of MS1 pre-clusters in the glass may also help to lower the barrier for crystallization of MS1 phase.

The crystallization temperatures obtained by in-situ synchrotron experiments and DSC analyses are in good agreement. The first crystallization resulted in formation of a cubic phase with $a = 0.9831$ (lattice parameter measured for $T = 503$ K). A similar cubic phase was seen in [9] with a smaller lattice parameter (Table 2). However, it should be noted that the lattice parameters analyzed in this study came from the in-situ diffraction patterns, which were obtained at high temperatures. Therefore, it is reasonable that the higher values for

lattice parameters of the cubic phase observed in this study are the same as for MS1 in [9]. At higher temperatures MS1 decomposes and a hexagonal phase (designated H1) forms with lattice parameters of a = 0.4619 and c = 1.2772 nm (lattice parameter measured for T = 603 K). Finally, hexagonal H1 decomposes to orthorhombic Al_4Sm with lattice parameters of a = 1.3872, b = 0.6441, and c = 0.4494 nm, as analyzed for T = 773 K.

As discussed previously, fcc-Al does not appear to nucleate but already exists as nanoclusters in the amorphous matrix and grows with increasing annealing temperature. Peak position overlap between fcc-Al and cubic MS1 most likely prevents the presence of the fcc-Al nanocrystals from being discernable using X-ray diffraction at the lower temperatures. A more detailed study including high resolution and energy filtered transmission electron microscopy at different stages of devitrification is in progress. Such a study will be helpful in elucidating phase transformation mechanisms and solute concentration distribution at different stages of devitrification.

Conclusion

Rapid solidification of $Al_{90}Sm_{10}$ by Cu-block melt spinning with wheel speeds of 30 and 40 m/s resulted in formation of an amorphous phase accompanied by nanocrystalline fcc-Al. The results of the current work show that HRTEM and/or APT are very important tools when examining the amorphization level of as-quenched samples. HRTEM and APT data showed that fcc-Al nanocrystals in size range of 2–5 nm are present in melt-spun material obtained using 40 and 30 m/s wheel speeds. The high nucleation density indicates that these fcc-Al nanocrystals may have originated from “quenched-in” nuclei that formed during rapid solidification. The existence of nanocrystalline fcc-Al influences both the composition and kinetics of the first bulk phase crystallization. Isochronal analyses using the Kissinger and Ozawa method indicate that the as-quenched material has a relatively low thermal stability against crystallization. High energy synchrotron X-ray diffraction shows a major amorphous

peak with a pre-peak formation in as-solidified ribbons. While fcc-Al nanocrystalline material is seen using HRTEM it can not be discerned in the HEXRD of as-solidified material due to broadening of the Bragg peaks. Devitrification of the as-quenched structure over the temperature range 298–773 K at a heating rate of 5 K/min was investigated in-situ using high energy synchrotron X-ray radiation and can be summarized as follows:

Amorphous → MS1 (cubic) → H1 (hexagonal) → Al_4Sm (orthorhombic).

The temperatures corresponding to 50% completing of each transformation during devitrification are 483, 542 and 667 K, respectively, at a heating rate of 5 K/min.

The results of HEXRD experiments indicate that local chemical ordering is occurring to a certain degree in the amorphous phase. Further studies are in progress to identify the glass structure in detail in the Al–Sm system.

Acknowledgment

Appreciation is expressed to M.J. Kramer and M. Kaufman (University of North Texas) for valuable help in HEXRD and APT, respectively. The work at Ames Laboratory and at the Midwest Universities Collaborative Access Team (MUCAT) sector at the APS, Argonne National Laboratory was supported by the United States Department of Energy (USDOE), Office of Science (OS), Office of Basic Energy Science (BES), under Ames Laboratory Contract No. DE-AC02-07CH11358, and Iowa State Materials Science and Engineering Department. The assistance of the Materials Preparation Center [29] of the Ames Laboratory is acknowledged for supplying our samples.

Reference

1. R.I. Wu, G. Wilde and J.H. Perepezko, Mater. Sci. Eng. A 301 (2001), pp. 12–17.
2. J.C. Foley, D.R. Allen and J.H. Perepezko, Scripta Mater. 35 (1996), pp. 660–665.
3. A. Inoue, Prog. Mater. Sci. 43 (1998), pp. 365–520.

4. A. Inoue, K. Ohtera, A. Tsai and T. Masumoto, Jpn. J. Appl. Phys. 27 (1988), p. L479.

5. Y. He, G.M. Dougherty, G.J. Shiflet and S.J. Poon, Acta Metall. Mater. 41 (1993), p. 337.

6. L. Battezatti, S. Pozzovivo, P. Rizzi, in: H.S. Nalwa, (Ed.), Encyclopedia of Nanoscience and Nanotechnology, 2004, pp. 341–364.

7. A. Saccone, G. Cacciamani, D. Maccio, G. Borzone and R. Ferro, Intermetallics 6 (1998), pp. 201–215.

8. P. Rizzi, C. Antonione, M. Baricco, L. Battezzati, L. Armelao, E. Tandello, M. Fabrizio and S. Daolio, Nanostruct. Mater. 10 (1998), pp. 767–776.

9. P. Rizzi, M. Baricco, S. Borace and L. Battezatti, Mater. Sci. Eng. A 304–306 (2001), pp. 574–578.

10. J.Q. Guo, K. Ohtera, K. Kita, J. Nagahora and N.S. Kazama, Mater. Lett. 24 (1995), pp. 133–138.

11. L. Battezati, M. Baricco, P. Schumacher, W.C. Shih and A. L Greer, Mater. Sci. Eng. A 179&180 (1994), pp. 600–604.

12. M.J. Kramer, M.F. Besser, N. Yang, E. Rozhkova, D.J. Sordelet, Y. Zhang and P.L. Lee, J. Non-Cryst. Solids 317 (2003), pp. 62–70.

13. H.E. Kissinger, Anal. Chem. 29 (1957), pp. 1702–1706.

14. T. Ozawa, Polymer 12 (1971), p. 150.

15. Y.E. Kalay, L.S. Chumbley, I.E. Anderson and R.E. Napolitano, Metall. Mater. Trans. A 38A (2007), pp. 1452–1457.

16. T.B. Massalski, Binary Alloy Phase Diag. 1 (1987), pp. 166–167.

17. Y.E. Kalay, L.S. Chumbley, I.E. Anderson, Mater. Sci. Eng. A, 490, (2007), pp.72-80.

18. M.C. Gao and G.J. Shiflet, Intermetallics 10 (2002), pp. 1131–1139.

19. J.H. Perepezko and G. Wilde, J. Non-Cryst. Solids 274 (2000), pp. 271–281.

20. J.H. Perepezko, R.J. Hebert, R.I. Wu and G. Wilde, J. Non-Cryst. Solids 317 (2003), pp. 52–61.

21. A. Hirata, Y. Hirotsu, E. Matsubara, T. Ohkubo and K. Hono, Phys. Rev. B 74 (2006), p. 184204.

22. J. Schroers, R. Busch, A. Masuhr and W.L. Johnson, Appl. Phys. Lett. 74 (1999), p. 2806.

23. X.L. Wang, J. Almer, C.T. Liu, Y.D. Wang, J.K. Zhao, A.D. Stoica, D.R. Haeffner and W.H. Wang, Phys. Rev. Lett. 91 (2003), p. 265501.

24. K. Hono, D.H. Ping, M. Ohnuma and H. Onodera, Acta Mater. 47 (1999), p. 997.

25. K.F. Kelton, J. Non-Cryst. Solids 274 (2000), pp. 147–154.

26. Z.J. Yan, S.R. He, J.R. Li and Y.H. Zhou, J. Alloy Comp. 368 (2004), pp. 175–179.

27. T.W. Wilson, H. Choo, W.D. Porter, S.A. Speakman, C. Fan and P.K. Liaw, J. Non-Cryst. Solids 352 (2006), pp. 4024–4029.

28. G. Wilde, H. Sieber and J.H. Perepezko, Scripta Mater. 40 (1999), pp. 779–783.

29. Materials Preparation Center, Ames Laboratory, US DOE Basic Energy Sciences, Ames, IA, USA. Available from: <www.mpc.ameslab.gov>.

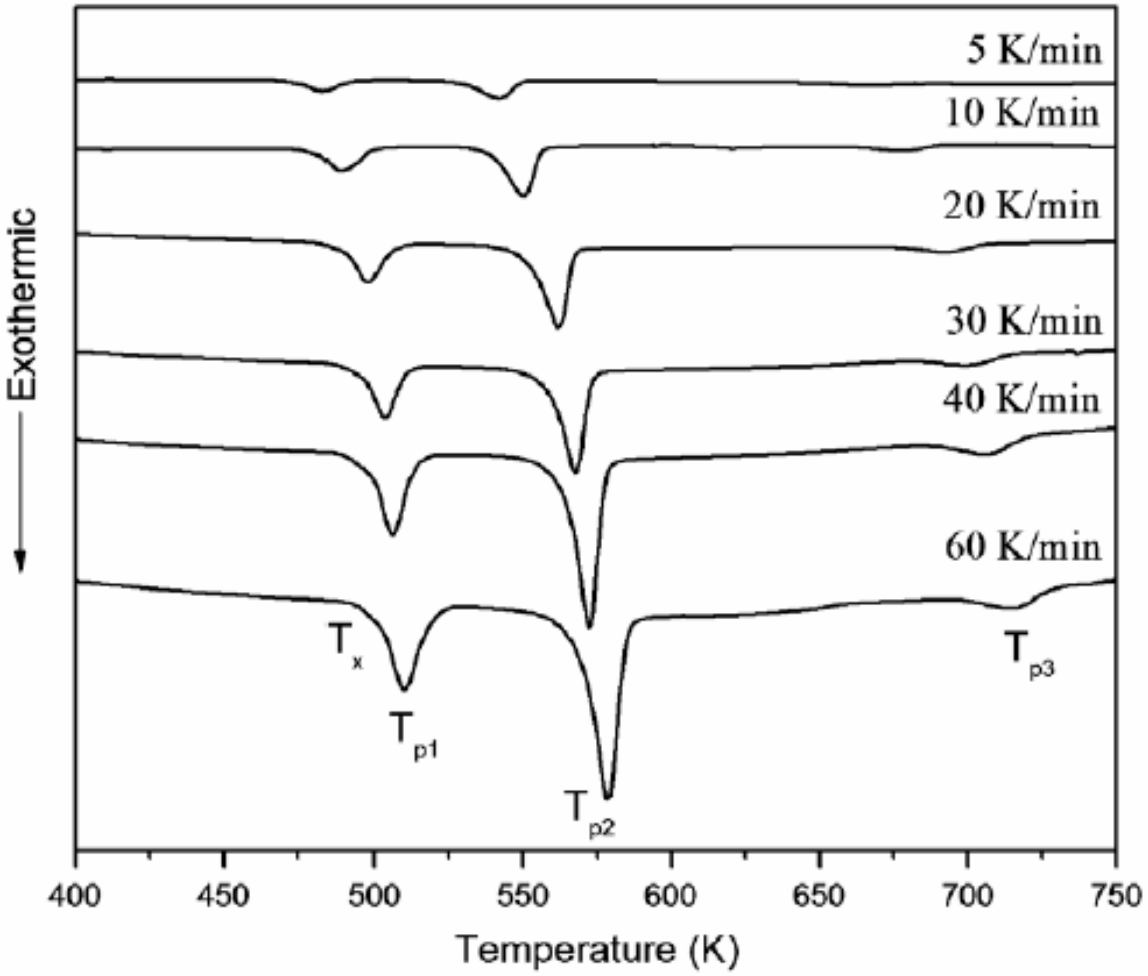

Figure 1. Isochronal DSC traces of $Al_{90}Sm_{10}$ amorphous alloy at heating rates of 5–60 K/min. The positions of T_x and T_p temperatures are shown as an example for 60 K/min heating rate.

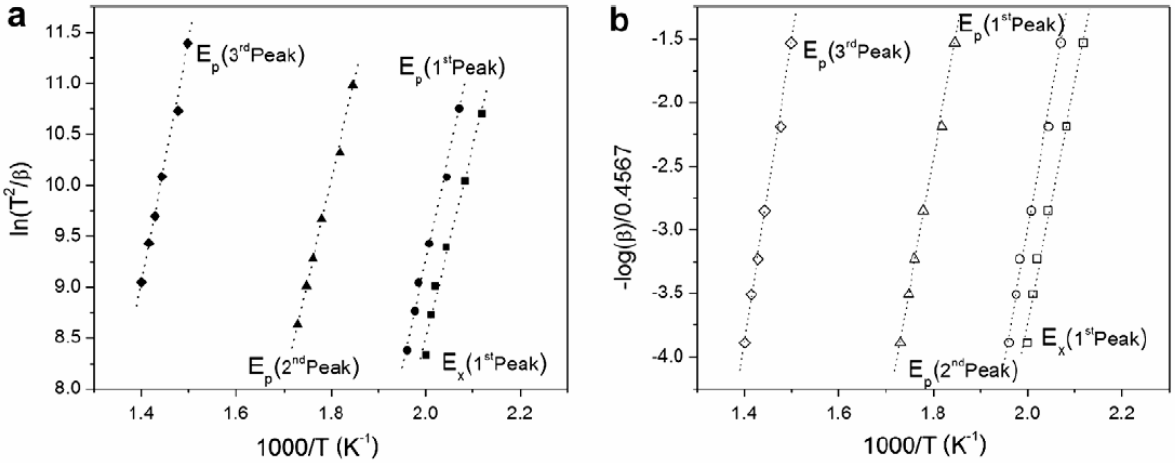

Figure 2. The Kissinger (a) and Ozawa (b) plots of $Al_{90}Sm_{10}$ amorphous alloy.

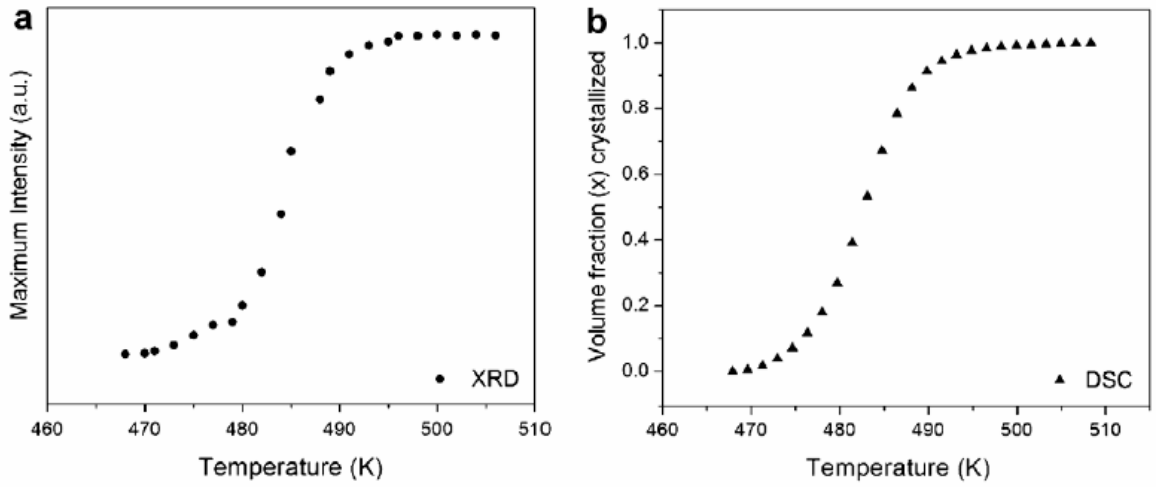

Figure 3. (a) Maximum diffraction intensity (at 2.96 2θ) as a function of temperature for a heating rate of 5 K/min. (b) Change in the crystallized volume fraction during first crystallization as a function of temperature as measured by DSC for a heating rate of 5 K/min.

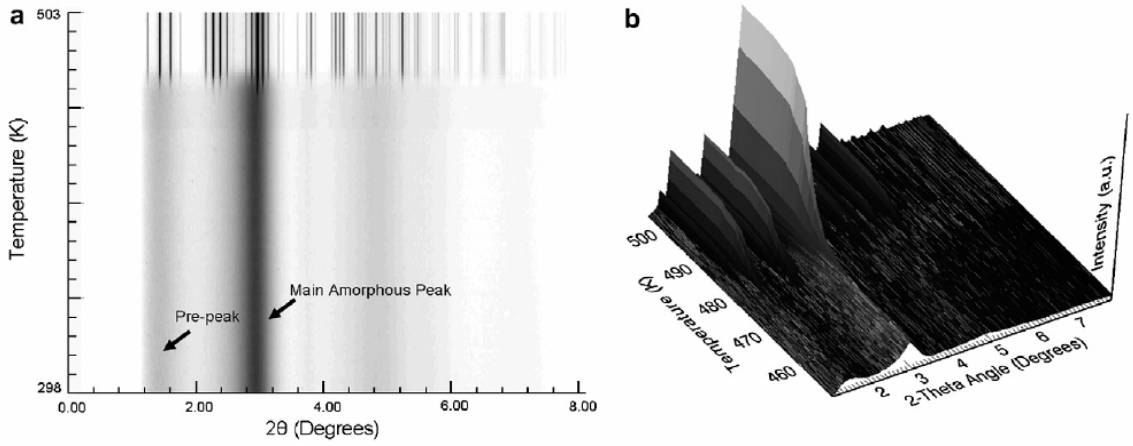

Figure 4. (a) Image plate scan and (b) surface plot of diffraction for first crystallization event.

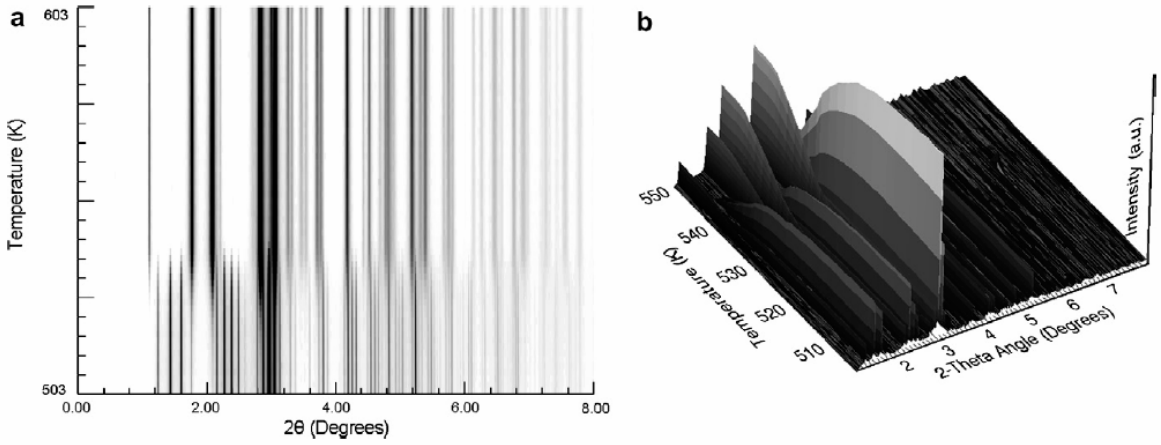

Figure 5. (a) Image plate scan and (b) surface plot of diffraction for second crystallization event.

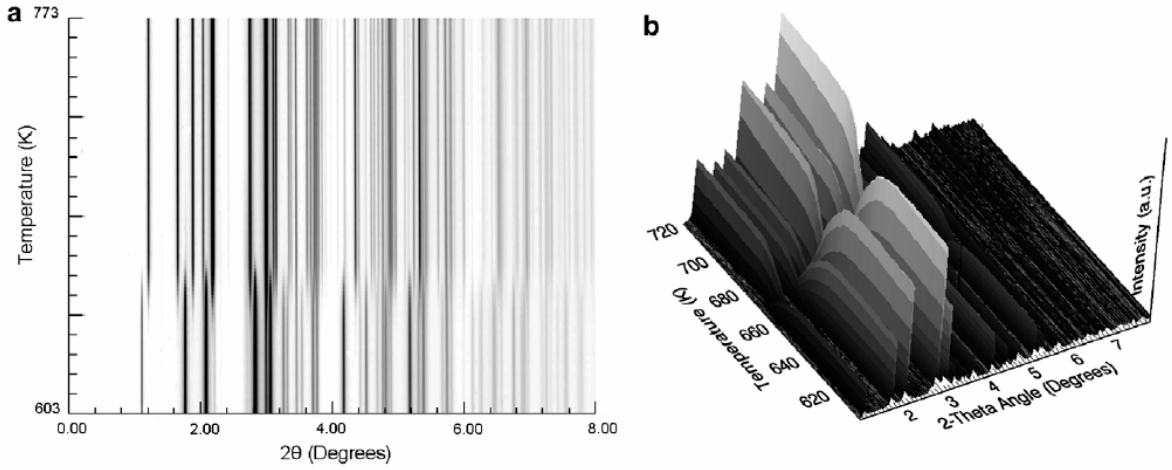

Figure 6. (a) Image plate scan and (b) surface plot of diffraction for second crystallization event.

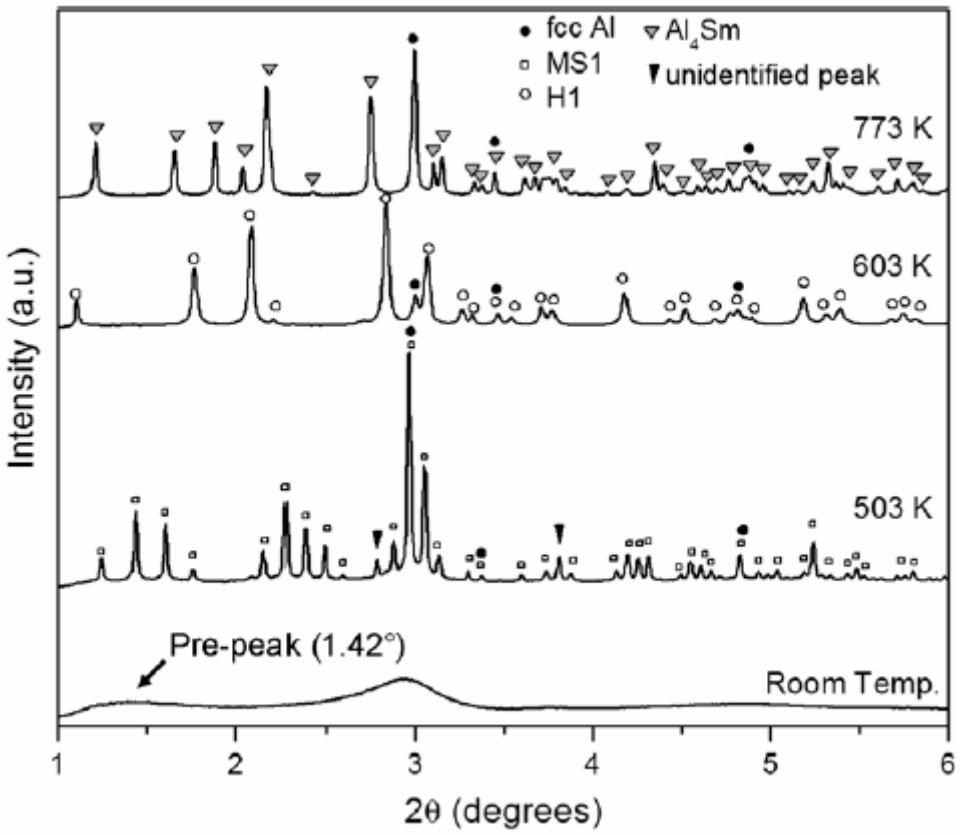

Figure 7. HEXRD patterns of rapidly-solidified Al90Sm10 ribbons (40 m/s wheel speed) in as-quenched condition and, after first (503 K), after second (603 K), and after third (773 K) crystallization events (heating rate is 5 K/min).

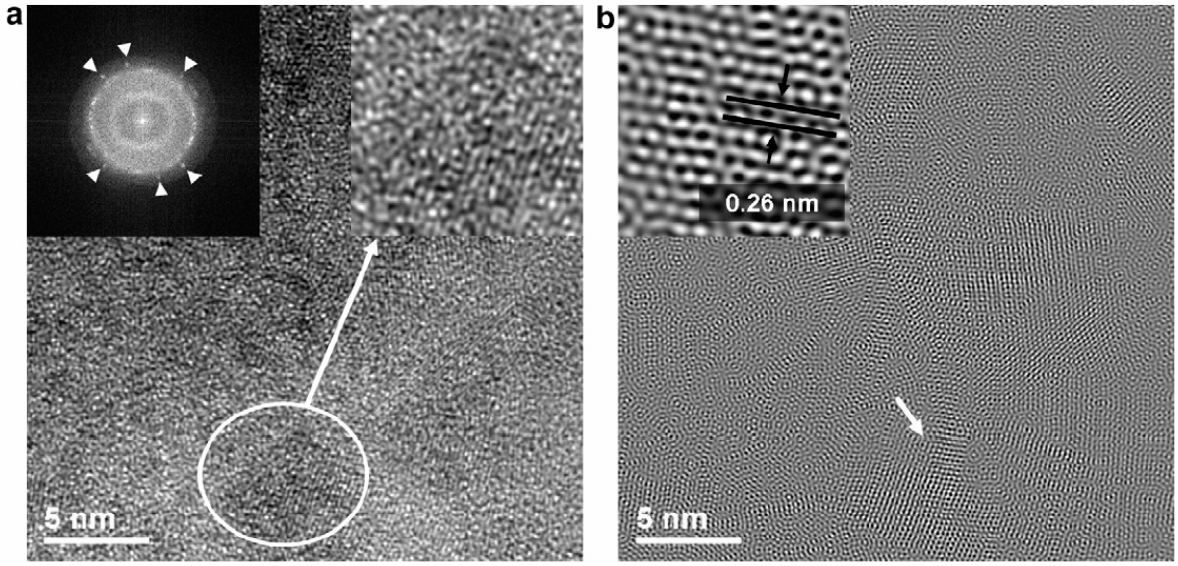

Figure 8. (a) HRTEM image of as-solidified $Al_{90}Sm_{10}$ (40 m/s wheel speed), insets show the Fourier transformed image of the full area (left), and a magnified view of the circled area (right). (b) The inverse Fourier transformed image shown in (a). The image was created by masking all but the outer ring in Fourier transformed image ((a) inset). Inset shows a magnified view of a nanocrystal shown by an arrow ((b) inset).

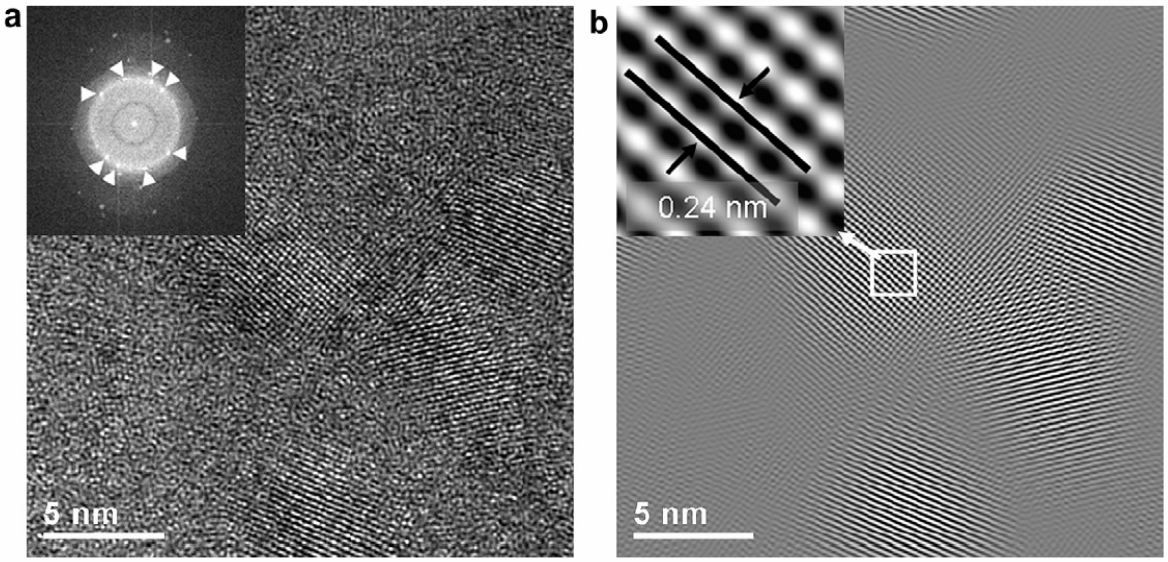

Figure 9. (a) HRTEM image of as-solidified $Al_{90}Sm_{10}$ (30 m/s wheel speed), inset shows the Fourier transformed image of the full area. (b) The inverse Fourier transformed image of the full area. The image was created by masking all but the spots shown by arrows in the outer ring in Fourier transformed image ((a) inset).

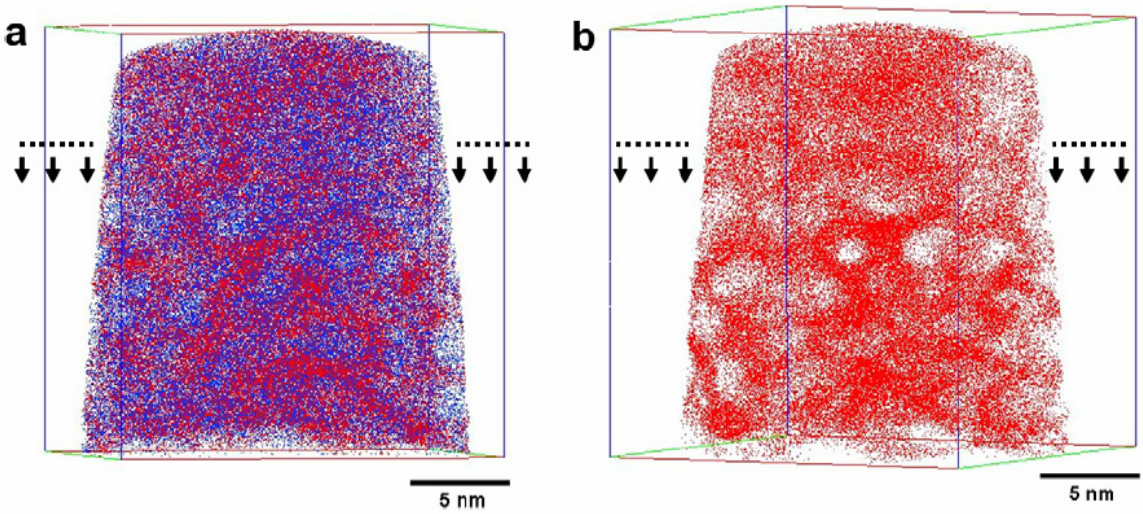

Figure 10. (a) HRTEM image of as-solidified Al90Sm10 (30 m/s wheel speed), inset shows the Fourier transformed image of the full area. (b) The inverse Fourier transformed image of the full area. The image was created by masking all but the spots shown by arrows in the outer ring in Fourier transformed image ((a) inset).

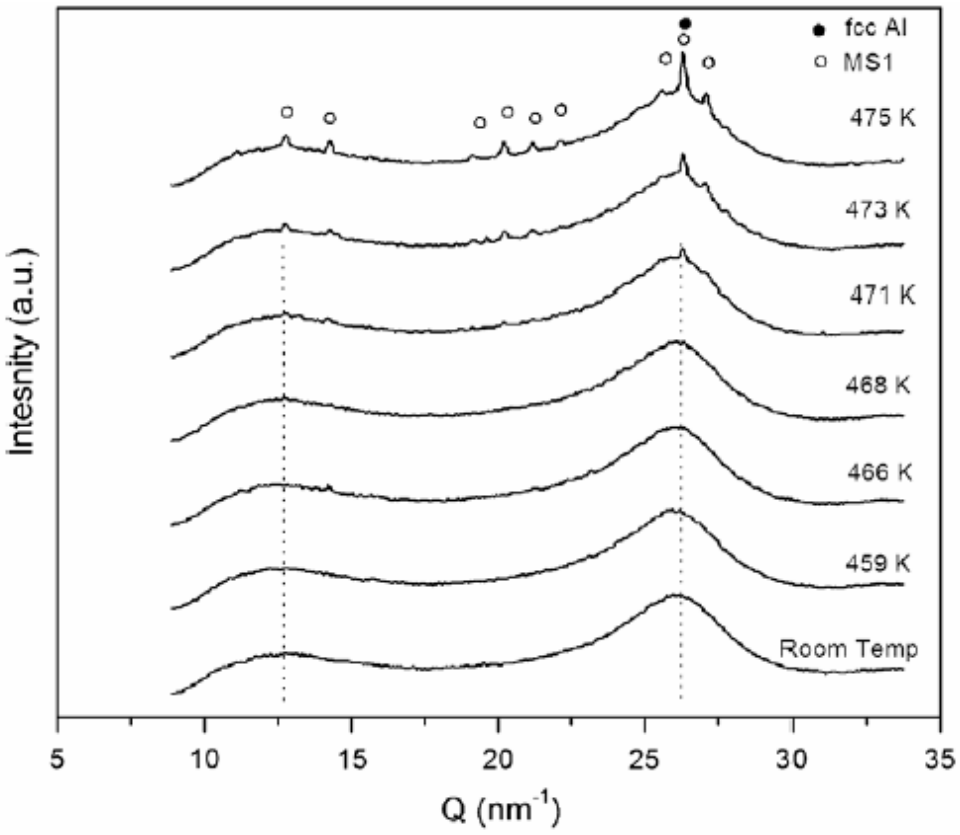

Figure 11. Isochronal diffraction spectra evolution for initial crystallization. First and second lines show the positions of the pre-peak and main amorphous peak, respectively.

Table 1. Summary of crystallization processes of rapidly solidified $Al_{90}Sm_{10}$ alloy

Initial Stage	*First Crystallization*	*Second Crystallization*	*Third Cystallization*	
Am.	MS1	α-Al +$Al_{11}Sm_3$ + M1	α-Al + Al_4Sm	[9]
Am. + α-Al + M2	Am + α-Al + M2	α-Al +$Al_{11}Sm_3$	α-Al + Al_4Sm	
Am.	α-Al + Al_4Sm + M1	α-Al + S3		[10]
Am.	MS1	α-Al + MS2	α-Al + Al_4Sm	[11]

Table 2. Phases observed during crystallization of rapidly solidified $Al_{90}Sm_{10}$ alloy

	Crystal Structure	*Lattice Parameters (nm)*
Am.	Amorphous	
M1	Hexagonal	a = 0.4597, c = 0.6358
S3	Orthorhombic	a = 1.3781, b = 1.1019, c = 0.7303
MS1	Cubic	a = 0.976
M2	Cubic	a = 1.9154

Table 3. The isochronal DSC data of $Al_{90}Sm_{10}$

β (K.min-1)	*1st Peak*	*1st Peak*	*2nd Peak*	*3rd Peak*
	T_x *(K)*	T_p *(K)*	T_p *(K)*	T_p *(K)*
5	472	483	542	667
20	489	498	562	693
30	495	504	568	700
40	497	506	572	707
60	500	510	578	714

Table 4. Activation Energies calculated according to Kissinger and Ozawa plots

Crystallization Event	**Kissinger**		**Ozawa**	
	E_c (kJ/mol)	|r|	E_c (kJ/mol)	|r|
1^{st} Event (T_x)	158 ± 2	0.9862	157 ± 2	0.9874
1^{st} Event (T_p)	171 ± 3	0.9950	171 ± 2	0.9954
2^{nd} Event (T_p)	168 ± 2	0.9970	169 ± 1	0.9970
3^{rd} Event (T_p)	195 ± 2	0.9991	195 ± 2	0.9992

CHAPTER 5: LOCAL STRUCTURE OF THE MARGINAL GLASS FORMING Al-Sm ALLOYS: LIQUID AND AMORPHOUS STATES

A paper to be submitted to *Philosophical Magazine A*

Y.E. Kalay[1,2], L.S. Chumbley[1,2], M.J. Kramer[1,2], I.E. Anderson[1,2]

Abstract

The local structure in rapidly quenched $Al_{(100-x)}Sm_x$ (x = 8, 10, and 12) and liquid $Al_{90}Sm_{10}$ has been investigated using a combination of high resolution electron microscopy (HRTEM) and high energy synchrotron X-ray diffraction (HEXRD). The as-quenched alloys possess crystalline clusters of fcc-Al on the order of 2-5 nm which are embedded in a non-crystalline matrix. Total structure factor analysis of the liquid and as-quenched alloys showed a distinct pre-peak located well below the main amorphous peak. The same pre-peak was also resolved in rotationally averaged Fourier transformed (FT) diffractograms of the as-quenched HRTEM images. The structural unit size corresponding to the pre-peak remains constant for both the liquid and as-quenched states, but the correlation length is increased after quenching. The presence of the pre-peak is related to the formation of medium-range order (MRO) in the liquid that is retained in the as-quenched alloys. The structural unit size corresponding to the MRO is similar to the (002) interplanar distances of the high temperature metastable $Al_{11}Sm_3$ tetragonal phase. Atomic structure models constructed using Reverse Monte Carlo (RMC) simulations from experimentally determined total structure factors and coupled with Voronoi Tesselation analysis indicated icosahedral and deformed bcc-like clusters surrounding Al and primarily Sm atoms, respectively. The existence of the MRO clusters in the as-quenched state is believed to promote the high nucleation density of

---

[1] Department of Materials Science and Engineering, Iowa State University, Ames IA 50011-3020 USA

[2] Ames Laboratory (DOE), Iowa State University, Ames IA 50011-3020, USA

fcc-Al nanocrystals that form when the material is devitrified by acting as catalyst sites. These sites promote heterogeneous nucleation of the fcc-Al, while blocking long range diffusion and preventing formation of the thermodynamically stable phases.

Introduction

In marginal glass forming amorphous alloys, the first crystallization to occur is often related to ease of nucleation of metastable phases rather than enhanced driving force for the thermodynamically favored phases. This results in the formation of a very high nucleation density of nanocrystals, on the order of 10^{20} to 10^{23} m^{-3}, in the amorphous matrix [1-4]. An exact mechanism to explain the presence of such a high nanocrystal density after complete or partial devitrification has not been identified to date. Classical nucleation theory fails to predict the observed number density of nanocrystals [5]. Several mechanisms have been proposed, including heterogeneous nucleation with a high density of insoluble impurities [6]; a high density of quenched-in nuclei [3,7]; phase separation in the amorphous state [8, 9]; and time-dependent homogeneous nucleation [10, 11]. However, there is still no agreement on the mechanism of high-density nanocrystal or nano-cluster formation. Thus, a detailed analysis of the as-quenched and liquid structures is crucial in developing a better understanding of the unusual behavior of such marginal glass formers.

Among the marginal glass forming alloys, Al based alloys have recently attracted much attention due to their high fracture strengths, exceeding 1 GPa [12] and their low densities. In these alloys, an amorphous structure is often observed for Al rich (between 80 and 92 at% Al) Al-RE and Al-TM-RE (TM: transition metals; RE: rare earth elements) by either mechanical deformation or rapid quenching [1,13]. The Al-Sm binary alloy has the widest glass formation range (from 8 to 16 at. % Sm) of all similar Al-RE systems [1]. In accordance with this, the binary Al-Sm system has been chosen as a model to investigate the liquid and the amorphous structures.

In a previous study [14] it has been shown that amorphous samples of cold-rolled (transformed in the solid state) $Al_{92}Sm_8$ exhibit a calorimetric signal of glass transition (T_g) that is separated from the first crystallization peak. However, alloys of the same composition quenched from the liquid state using melt spinning do not show any distinct T_g [14]. Fluctuation electron microcopy (FEM) studies identified fcc-Al-like medium range order structures for the as-quenched melt-spun alloy but not for the cold-rolled sample, where a different nanoscale ordering was observed [15]. The size of the clusters in the as-quenched melt-spun state is between 1 and 2 nm, which makes it difficult to detect them using conventional TEM and XRD. Upon heating, these sub-size nuclei showed a restricted growth and no distinct glass transition temperature was measured for as-quenched amorphous alloys. Further studies using atom probe tomography (APT) of as-quenched $Al_{90}Sm_{10}$ revealed clusters of Al atoms in a size range of 2-5 nm [16], indicative of compositional fluctuations in the amorphous state. The APT results also indicated that amorphous Al-Sm forms a skeleton-like structure, similar to cross-linking in a polymer, and that fcc-Al nucleates between the links of this structure. Partial devitrification of as-quenched melt-spun ribbons [16], as well as high pressure gas atomized [17] powders, yields a high nucleation density (population) of fcc-Al, similar to $Al_{92}Sm_8$ as-quenched samples [14].

An interesting observation noted in $Al_{90}Sm_{10}$ as-quenched melt-spun samples [16] is the presence of a pre-peak located well below the primary diffuse scattering peak in HEXRD patterns. Similar types of pre-peaks have previously been observed in other systems [18-20], often being interpreted as topological or chemical ordering occurring to a certain degree in the amorphous phase. However, the structural origin of this pre-peak has not been understood or fully described, yet.

In this study, as-quenched samples of $Al_{100-x}Sm_x$ (x=8, 10, and 12) and the liquid structure of $Al_{90}Sm_{10}$ alloy were analyzed using a combination of HEXRD and transmission electron microscopy. Three-dimensional atomic configurations of amorphous structures were

modeled using the Reverse Monte Carlo (RMC) technique [21], coupled with Voronoi Tesselation analyses [22], based on the HEXRD experiments. The existence of the pre-peak and possible implications that may apply to the observed fcc-Al nanocrystallization with extremely high nucleation density seen in Al-Sm alloys are discussed.

Experimental Procedure

Ingots of $Al_{(100-x)}Sm_x$ (x = 8,10, and 12) were prepared by electric arc melting under Ar atmosphere from highly pure Al (99.99 wt%) and Sm (99.9 wt%) elements [23]. Amorphous ribbons with a thickness of 20-30 μm and a width of 1.0 – 1.2 mm were produced from bulk alloy by Cu block single melt spinning technique under Ar atmosphere at a tangential speed of 30 m/s [23].

X-ray diffraction studies were carried out using high-energy transmission synchrotron X-ray diffraction (HEXRD) at the Advanced Photon Source at Argonne National Laboratory in collaboration with the Midwest Universities Collaborative Access Team (MUCAT). For liquid structure analysis, samples were cast into rods initially then pieces of the rod were inserted into 2 mm diameter, carbon-lined quartz capillaries and sealed in Ar. The sealed quartz capillaries were exposed to 99.586 keV of x-rays corresponding to a wavelength of 0.012450 nm. The diffraction data were collected in a Debye-Scherrer geometry by a MAR charge coupled device (CCD), with up to 60 seconds of exposure time. No reaction between the liquid melt and the carbon-lined quartz capillary was observed within the experimental time duration. A diffraction pattern from a similar carbon-lined empty quartz capillary was collected and subtracted from the liquid data sets for the background corrections. The diffraction data from the solid amorphous samples were collected without using any sample holder at room temperature.

The raw HEXRD data were corrected for the background and converted to the total structure factor function, S(Q), according to [24,25]

$$S(Q) = 1 + \frac{I^c(Q) - \sum_{i=1}^{n} a_i \left| f_i(Q) \right|^2}{\left| \sum_{i=1}^{n} a_i f_i(Q) \right|^2} \quad (1)$$

where $I^c(Q)$ is the coherent scattering intensity normalized to the atomic concentrations, a, and f(Q) is the atomic structure factors for each component in the system as corrected for polarization, absorption, multiple and Compton scattering [26].

In order to construct 3D structural models of amorphous structures, reverse-Monte-Carlo (RMC) simulations [27,28] were carried out with an RMC analysis program using the S(Q) data derived from the HEXRD experiments. In these simulations random configurations of 10,000 atoms were distributed in a cubic cell with periodic boundary conditions. The random configurations for each amorphous composition contain the proper stoichiometry, density and nearest neighbor distances, as determined from the data. The densities for the model configurations were estimated to be on the order of 3.07 – 3.13 g/cm^3 from density measurements of as-quenched ribbon samples using a pycnometer with He gas. The cut-off distances of the interatomic distances in the RMC calculations were chosen from direct Fourier transforms and ab-initio calculations as 0.22, 0.24, and 0.27 nm for Al-Al, Al-Sm and Sm-Sm, respectively [29]. The difference between the measured S(Q) from HEXRD experiments and the calculated $S^C(Q)$ from each RMC modeled configuration is determined by χ^2.

$$\chi_o^2 = \sum_{i=1}^{n} \frac{[S_0(Q_i) - S_0^C(Q_i)]^2}{\sigma(Q_i)^2} \quad (2)$$

In order to minimize the χ^2, approximately 10^6 iterations were performed for a constant σ(Q) value of 0.001. The local atomic environment was investigated by applying Voronoi Tessellation analyses [30]. In this analysis, different types of polyhedrons are defined with 6 digit indices in the form of N_i (i = 3-8) where N represents the number of

faces having "i" edges around the central atom (Al or Sm). The summation of N ($\sum_i N$) gives the coordination number around a specific atom.

Conventional transmission and high-resolution transmission electron microscopy (TEM, HRTEM) analyses were performed using an FEI Inc. Tecnai G^2 F20 scanning/transmission electron microscope. Samples for electron microscopy were thinned using double jet polishing at 248 K with a solution of 3 vol% HCl, 36 vol% Methanol, and distilled water.

Results

As-Quenched and Liquid Structures

The rapidly solidified microstructures of melt-spun ribbons as revealed using TEM are shown in Fig. 1. Bright field (BF) images and selected area electron diffraction (SAED) patterns (inset) of each as-quenched $Al_{(100-x)}Sm_x$ (x = 8, 10, and 12) alloy ribbon show a featureless microstructure, while SAED patterns indicate a diffuse ring, typical for an amorphous phase.

Although no indication of crystallinity was observed for each of these three different compositions, within the limitations of conventional TEM, existence of nano-sized crystals was detected using HRTEM. Fig.2 shows HRTEM images of as-quenched ribbons produced at a wheel speed of 30 m/s. Fourier transformed images (Fig.2 insets) resolve individual diffracted spots on the diffuse halo, indicative of crystallization in the amorphous matrix, and nanocrystal formation can be recognized easily in the HRTEM images.

The size of the nanocrystals observed in the as-quenched state is on the order of 5 nm. The lattice spacings observed within these nanocrystals are in good agreement with fcc-Al. During the HRTEM investigations, care was taken to avoid radiation damage by minimizing exposure to the beam.

Fig.3 shows HEXRD patterns of as-rapidly-solidified ribbons of different compositions. Note that HEXRD does not show any sharp crystalline peaks in the diffraction patterns. However, two broad peaks appear at scattering vector magnitudes of 12.6 nm^{-1}, and 33.4 nm^{-1} where $Q = \frac{4\pi \sin(\theta)}{\lambda}$. Since this data was collected without using any sample holder, these extra peaks should be an intrinsic feature of the Al-Sm system. Comparison of the peaks to the positions expected for fcc-Al diffraction (dashed lines of Fig.3) reveals that this broad scattering is not due to any Al-Al correlations expected for fcc-Al.

Fig.4 shows the HEXRD pattern of liquid $Al_{90}Sm_{10}$ alloy at a temperature of 1273 K in comparison with that obtained from the amorphous solid. The most interesting observation is that the pre-peak in the liquid after the alloy is melted appears in a similar position to that seen for the solid amorphous alloy. Thus, the appearance of the two broad scattering peaks seen in the amorphous solid may be an indication of an ordered structure other than fcc-Al in rapidly-solidified ribbon, of particular interest is the pre-peak (Q = 12.6 nm^{-1}), located well below the major amorphous peak (Q = 26.1 nm^{-1}), that is also present in the liquid.

Another intriguing observation is the detection of a similar type of pre-peak in HRTEM analyses. Fig.5 (a) shows the rotationally averaged FFT patterns collected at different defocus (Δf) values for $Al_{90}Sm_{10}$ alloys. Although no indication of any ordered structure other than fcc-Al was detected in HRTEM, a broad peak is observed in the FFT patterns. A similar peak is also detected for $Al_{92}Sm_8$ and $Al_{88}Sm_{12}$, as shown in the data in Fig. 5 (b) and in the broad halo seen in the inset. The position of the first broad halo measured from the rotationally averaged FFT is independent of the defocus value and is in good agreement with the position of the pre-peak calculated from HEXRD.

Calculations of the Total Structure Factor

Fig.6 and Fig.7 show the total structure factor (S(Q)), calculated for amorphous and liquid alloys. The amorphous structure factors were calculated for three different

compositions, whereas the liquid structure factor was calculated for $Al_{90}Sm_{10}$ at 1273 K. The negative values of the S(Q) in the low-Q region are due to a large difference in Al and Sm atomic scattering factors [26]. The existence of a pre-peak can also be seen in these calculated values. An expression similar to the Scherrer equation used for crystalline materials is often applied for disordered materials in order to estimate the size of any short or medium range ordered structure. This expression is given as $D \approx 2\pi/\Delta Q_{pre\text{-}peak}$, where D is the correlation length and ΔQ is the half-width of the pre-peak on the S(Q)-Q graph. The structural unit size (R) corresponding to the pre-peak can be estimated using the relationship $R \approx 2\pi/Q_{pre\text{-}peak}$ [31]. In order to identify the position and the width of the pre-peak, a Lorentzian function was fit to the low-Q part of the S(Q)-Q data [32]. In doing this, the intensity of the pre-peak is seen to decrease but its position remains almost constant for the liquid structure, as compared to the amorphous material. Table 2 summarizes peak positions, structural unit sizes, and correlation lengths determined for the pre-peaks observed in amorphous and liquid samples.

Reverse Monte Carlo Simulations (RMC)

Figure 8 shows comparisons of the total structure factor measured from HEXRD experiments to results obtained when the data is fit using the indirect RMC method for as-quenched $Al_{(100-x)}Sm_x$ (x=8, 10, and 12) alloys to produce the same S(Q). A good fit is obtained in both the low-Q regions (including the pre-peak) and the high-Q regions.

Figure 9 shows the partial structure factors ($S_{Al\text{-}Al}(Q)$, $S_{Al\text{-}Sm}(Q)$, and $S_{Sm\text{-}Sm}(Q)$) determined for as-quenched $Al_{(100-x)}Sm_x$ (x=8, 10, and 12) alloys. In the low-Q region (Q~12.6 nm^{-1}) of the partial structure factors, a pre-peak (arrowed) is seen for both $S_{Al\text{-}Sm}(Q)$, and $S_{Sm\text{-}Sm}(Q)$, being somewhat more intense for $S_{Sm\text{-}Sm}(Q)$. Interestingly, the pre-peak is absent from the $S_{Al\text{-}Al}(Q)$, indicating that the pre-peak seen in the total structure factor arises due to strong Al-Sm and especially Sm-Sm correlations in the as-quenched alloys.

The second broad peak at 33.4 nm^{-1}, noted in Figure 3, can also be seen on the $S_{Al-Sm}(Q)$, and $S_{Sm-Sm}(Q)$ curves, although it is not as strong as the pre-peak. The pair distribution functions and their partials for the as-quenched amorphous alloys were calculated from RMC results and are shown in Figure 10. The nearest neighbor coordination numbers (CN) and bond lengths for Al-Al, Al-Sm, and Sm-Sm atom pairs are summarized in Table 2. The average CN for Sm-Al pairs is higher than Al-Al pairs for all compositions, indicating a more densely packed structure around Sm atoms. The average CN for Al-Al and Sm-Al pairs is seen to decrease as Sm content in the alloy increases.

The distribution of bond-orientation angles are calculated for Al-Al-Al, Al-Sm-Al, and Sm-Al-Sm triplets within their first coordination shell for as-quenched $Al_{(100-x)}Sm_x$ (x=8, 10, and 12) alloys based on the RMC simulations, and are shown in Fig.11. The distributions of the first shell bond angles are centered at 56°, 52°, and 60° for Al-Al-Al, Al-Sm-Al, and Sm-Al-Sm, respectively. While the average bond angles calculated for these three triplets remain fairly constant, the peak frequencies decrease slightly as composition changes from 8 to 12 at% Sm. Angular analysis of bond-orientations shows a broad distribution of angles, indicating irregular polyhedral coordination in the first shell for these three compositions.

Because of the complexity of polyhedron coordination, it is difficult to analyze local structure by using solely bond-orientation angles or coordination number. Therefore, the complex polyhedral structure in the local atomic configurations generated by RMC was further investigated by Voronoi Tesselation analyses, as shown in Fig. 12. Thirteen and fourteen-coordinated polyhedrons with indices <0,3,6,4,0,0>, <0,2,8,4,0,0>, <0,3,6,5,0,0> are dominant for Al-centered structures. Polyhedrons with such indices correspond to deformed bcc structure [33]. It is also found that some icosahedral-like clusters with indices <0,0,12,0,0,0>, <0,1,10,2,0,0), or <0,2,8,2,0,0> and coordination of 12 and 13 atoms are formed around Al. The Sm-centered polyhedrons almost always have higher coordination as compared to Al-centered polyhedrons. The indices <0,2,8,4,0,0>, <0,2,8,5,0,0>,

<0,3,6,5,0,0>, <0,3,6,6,0,0>, and <0,2,8,6,0,0> corresponding to deformed bcc structures, are the most frequent polyhedral forming around Sm atoms. Another interesting observation is the change in the frequency of Sm centered polyhedrons as a function of composition. As shown in Fig. 12, describing the number of Sm centered polyhedrons as a function of composition is difficult. For example, <0,2,8,4,0,0>, <0,2,8,5,0,0>, <0,1,10,4,0,0>, and <0,1,10,3,0,0> type polyhedron are highly populated for $Al_{92}Sm_8$, but for $Al_{90}Sm_{10}$ the most common are <0,2,8,4,0,0>, <0,2,8,5,0,0>, <0,3,6,6,0,0>, and <0,2,8,6,0,0>. This changes yet again for $Al_{88}Sm_{12}$ where <0,3,6,5,0,0>, <0,2,8,5,0,0>, <0,3,6,6,0,0>, and <0,2,8,4,0,0> are the most frequent polyhedra. However, the number of specific polyhedron with respect to composition is quite stable for Al. Fig.13 (a) shows an example of 3D atomic configuration obtained from RMC simulations for $Al_{90}Sm_{10}$ compositions. The spatial distributions of the Sm atoms that form a deformed bcc-like structure with 14 and higher Al coordination is shown in Fig. 13 (b).

Discussion

According to current and previous high resolution electron microscopy studies [16, 17, as-quenched $Al_{(100-x)}Sm_x$ (x=8, 10, and 12) alloys produced by melt-spinning with wheel speeds of 30 and 40 m/s contain clusters of fcc-Al in a size range of 2-5 nm embedded in an amorphous matrix. The average size of fcc-Al clusters is considerably smaller for 40 m/s compared to 30 m/s wheel speed. In another study [15], clusters that are fcc-Al like showing MRO and having sizes in the range of 0.8 – 1.5 nm were resolved using fluctuation electron microscopy (FEM) in melt-spun $Al_{92}Sm_8$ produced at a wheel speed of 55 m/s. These results clearly show that the size of fcc-Al-like clusters decrease with increasing wheel speeds of melt spinner (i.e. increasing cooling rate). The results presented above show that MRO or nanocrystals of an fcc-Al-like structure always exist in $Al_{(100-x)}Sm_x$ (x=8, 10, and 12) alloys that are quenched from the liquid state, at least for the conditions used in this study. These

fcc-Al nanoclusters show a restricted growth upon annealing below their crystallization temperatures (T_x) and a high density of nanocrystals on the order of 10^{21}-10^{23} m^{-3} in the amorphous matrix. The small size of clusters in the as-quenched state makes them difficult to detect in conventional bright field TEM (Fig.1) but they can be detected easily using HRTEM coupled with FFT (Fig.2). While these fcc-Al nanoclusters also are not detectable with HEXRD, as shown in Fig.3, an intriguing observation is the existence of a pre-peak (Q ~ 12.6 nm^{-1}) at a position well below the major diffuse scattering position for all three as-quenched compositions. Similar types of pre-peaks have been reported for other alloy systems [18-20]. The physical origin of such pre-peaks in not clear and their existence is usually attributed to the formation of MRO structures [34,35]. Figures 3 and 4 show the positions of pre-peaks for as-quenched $Al_{(100-x)}Sm_x$ (x=8, 10, and 12) and liquid $Al_{90}Sm_{10}$, respectively. This data was collected at room temperature without using any sample holder, thus eliminating any possible effect due to the quartz capillaries that were used at higher temperatures. Another interesting observation is the detection of a halo located in the small Q region in the FFT diffractograms of HRTEM images for as-quenched $Al_{(100-x)}Sm_x$ (x=8, 10, and 12) as seen in Fig.2. The corresponding HRTEM images and FFT patterns only show fcc-Al nanocrystals; no other crystalline structure can be observed. The rotationally averaged FFT patterns (Fig.5) clearly show two peaks at approximately 13 and 27 nm^{-1}, which are in good agreement with the positions of the pre-peak and the main amorphous peak observed using HEXRD.

In order to clarify the influence of defocus, FFTs were rotationally averaged at different defocus values for as-quenched $Al_{90}Sm_{10}$. As shown in Fig. 5 (a) the positions of the pre-peak and the main peak remain constant with respect to defocus. As shown in Fig. 5b, the existence of the pre-peak is also consistent with the change in composition, with the pre-peak located at around 13 nm^{-1}. These observations indicate that the pre-peak is not an anomaly of the manner in which the HEXRD data was obtained or the HRTEM images. It is

therefore concluded that the as-solidified structures examined in this study all consist of fcc-Al nanoclusters coupled with a MRO structure according to HEXRD and HRTEM analysis.

The MRO structure is further investigated using the total structure factor function, S(Q). As it is shown in Fig. 6, the pre-peak is a distinct feature in the total structure function calculated for as-quenched $Al_{(100-x)}Sm_x$ (x=8, 10, and 12). There is a slight increase in the intensity of the pre-peak with increasing Sm content, which is more pronounced for the second broad peak located approximately at 33.4 nm^{-1}. Another interesting observation is that the partial structure factor analysis (Fig. 8) shows strong Al-Sm and Sm-Sm correlations in their Fourier component of low Q-regions, which is the area of origin of the pre-peak seen in the total structure factor function. The pre-peak in the partial structure factor is absent for Al-Al interactions but stronger for Sm-Sm ones.

From the current observations it appears the origin of the pre-peak in as-quenched alloys is based on the pre-existing liquid structure. Figures 4 and 7 show the raw data and total structure factor function after background corrections for liquid $Al_{90}Sm_{10}$ at 1273 K approximately 300 K above the liquidus temperature. A pre-peak is clearly seen in both graphs and the position is in good agreement with the pre-peaks observed at room temperatures in the as-quenched samples. Thus, it appears evident that the MRO structure survives in the liquid state even at temperatures that far exceed the melting point. The correlation lengths and structural unit sizes calculated from the position of the pre-peak for as-quenched $Al_{(100-x)}Sm_x$ (x=8, 10, and 12) and liquid $Al_{90}Sm_{10}$ are summarized in Table 1. Note that the correlation lengths of the MRO calculated from pre-peak broadening differ for solid and liquid structures. For as-quenched solids the correlation length is on the order of 2.5 nm and is almost constant with respect to composition. However, correlation length is much smaller in the liquid, being on the order of 1.6 nm. This suggests an agglomeration of the clusters corresponding to pre-peak formation upon quenching from liquid structures.

The structural unit sizes calculated from the positions of the pre-peaks for the as-quenched samples are almost constant with respect to compositions, indicating that they all possess a similar type of MRO, similar to that of liquid $Al_{90}Sm_{10}$. This indicates that the MRO structure formed in the liquid state has been retained in the as-quenched state with an increase in correlation length. The positions of the extra peaks observed in liquid and as-quenched states are close to some of the major diffraction peaks in a high temperature metastable body centered tetragonal phase, $Al_{11}Sm_3$. This compound is stable between 1351 and 1733 K. The interplanar spacing for (002) and (211) planes are given as 0.495 and 0.188 nm, respectively. These planar spacings are close in value to those calculated from the positions of the pre-peaks at 12.6 and 33.4 nm^{-1} for as-quenched $Al_{(100-x)}Sm_x$ (x=8, 10, and 12) and liquid $Al_{90}Sm_{10}$. The extra peaks observed in the diffraction patterns of Figure 3 are probably due to broadening caused by the fine size MRO structure.

According to total structure factor and Voronoi analysis, it is hypothesized that the MRO observed in liquid and as-quenched states have structural similarities with the high temperature metastable $Al_{11}Sm_3$ tetragonal phase. Fig.14 shows the atomic configuration of this phase, which has the I4/mmm space group symmetry. If the Sm atom located at the center is considered, this structure consists of Sm atoms surrounded by 8 Al atoms at a distance of 0.325 nm and another 8 Al atoms at a distance of 0.327 nm. Therefore, every Sm atoms in this structure is highly coordinated with Al in their first and second shells and 16 Al atoms exist at a distance of 0.327 nm or less. In a study where the local atomic structure of amorphous $Al_{92}Sm_8$ was investigated using X-ray absorption fine structure (XAFS) [36], the best fit to the experimental XAFS data was obtained by considering a "single shell" structure of 16 Al atoms surrounding Sm atoms with a first coordination shell radius of 0.32 nm. It is interesting that if one takes the literature values for the radii of Al and Sm atoms (0.143 and 0.181 nm, respectively [37]) and assumes metallic bonding, a simple summation of the radii produces an average bond distance of 0.324, close to the experimental XAFS data [31]. This

is also in agreement with the results of the current pair distribution data of Fig. 10 which shows that Sm-Al bonding for the three compositions investigated in this study is on the order of 0.32 nm, with a maximum experimental error of 2.4 %.

The average coordination number (CN) determined for Al atoms surrounding a Sm atom, shown in Table 2, is on the order of 12 to 13, which usually indicates an icosahedral order. However, the bond angles calculated for the three compositions examined (Fig.11) do not match with the first shell bonds in an icosahedral cluster, as the latter are around 60-63°. Also, according to the Voronoi analyses results, which include the Sm atoms in the near-neighbor cell, the average CN for each Sm atom is given as 15.11, 15.18, and 15.36 for $Al_{92}Sm_8$, $Al_{90}Sm_{10}$ and $Al_{88}Sm_{12}$, respectively. Therefore, a high coordination around Sm atoms is detected for the MRO structure that is similar to tetragonal $Al_{11}Sm_3$.

The MRO clustering in liquid is believed to form due to strong interactions between Al and Sm atoms. The MRO clusters essentially act like distinct “superatoms” with a slightly broad size distribution and huge diameters as compared to individual Al and Sm atoms in the matrix. Upon rapid solidification it is hypothesized that these clusters cause a local atomic size effect, similar to that seen in multi-component bulk amorphous alloys in some sense, preventing the complete crystallization of the Al rich matrix. This results in the as-quenched structure being divided into nano-scale regions by a network of MRO clusters. Depending on size of these regions a certain percentage of fcc-Al clusters will reach the critical nucleus size with the remainder staying below this size. This explanation agrees with results obtained for $Al_{90}Sm_{10}$ using three dimensional atom probe tomography (3D APT) [16].

The cooling rate appears to be directly correlated with the percentage of Al that cannot reach the critical nucleation size. However, it should be noted that cooling rate has a minor effect on the presence of MRO in the as-quenched state. MRO was observed in all liquids for all initial melt temperatures used in this study. Therefore, MRO stability in the liquid needs be studied directly with respect to initial melt temperature, rather than assuming

that the quenched structure varies with cooling rate of the melt. New experimental variable may be used to determine a more accurate representation of the liquid structure.

When as-quenched alloys are annealed, the MRO appears to act as a catalyst site for nucleation of fcc-Al. It should be noted that for the assumed hypothesis, long range diffusion between fcc-Al clusters would be blocked by the Sm rich MRO structure in the matrix, resulting in restricted growth of fcc-Al. Al rich regions with size below critical size for homogeneous nucleation can nucleate via a heterogeneous nucleation mechanism in the vicinity of the MRO clusters. A more detailed study that includes atom probe tomography and scanning transmission electron microscopy equipped with a high angle annular dark field detector is in progress. Such a study should be helpful for identifying the spatial distribution of the MRO and fcc-Al in the as-quenched state, to help elucidate the effect of MRO on producing the observed high nucleation density of fcc-Al in these alloys.

Conclusion

Rapid solidification of $Al_{(100-x)}Sm_x$ (x=8, 10, and 12) using a melt-spinning technique at a wheel speed of 30 m/s resulted in formation of fcc-Al nanocrystals embedded in a non-crystalline matrix. Detailed analysis of the as-quenched structure by HRTEM and HEXRD revealed a pre-peak well below the major amorphous peak in the Fourier transform patterns and total structure factor graphs, respectively. Partial structure factor analysis showed that the pre-peak arises due to Al-Sm and particularly Sm-Sm correlations. A similar type of pre-peak was also resolved for the liquid $Al_{90}Sm_{10}$ using HEXRD at 1273 K. The formation of the pre-peak is related to the formation of MRO clusters in the liquid. After a liquid alloy is quenched, the position of the pre-peak remains almost constant, indicating that the MRO in the liquid is retained in the as-quenched structure. While the size of the MRO cluster is larger in the as-quenched alloys, cluster size appears relatively insensitive to an increase in Sm content. The Voronoi analysis of local atomic structures based on RMC simulation

suggests a deformed bcc-like structure surrounding Sm with CN higher than 15 atoms for as-quenched alloys. These experimental results and simulations indicate the MRO in the liquid and as-quenched states is structurally similar to the high temperature metastable $Al_{11}Sm_3$ tetragonal phase. The MRO in liquid seems to act as a "superatom" of huge diameter to prevent complete crystallization of fcc-Al upon rapid solidification. When as-quenched alloys are annealed, the Sm-rich MRO clusters act as catalyst sites promoting heterogeneous nucleation of fcc-Al, while inhibiting long range diffusion processes between fcc-Al clusters.

Acknowledgment

Appreciation is expressed to Shaogang Hao for his valuable help in Voronoi analyses. The work at Ames Laboratory was supported by the United States Department of Energy (USDOE), Office of Science (OS), Office of Basic Energy Science (BES), under Ames Laboratory Contract No. DE-AC02-07CH11358, the high-energy X-ray work at the MUCAT sector of the APS was supported by the US Department of Energy, Office of Science, Basic Energy Sciences under Contract No. DE-AC02-06CH11357. The assistance of Materials Preparation Center of the Ames Laboratory is acknowledge for supplying our samples [23].

Reference

1. A. Inoue, Progress in Materials Science, **43**, 365-520, (1998).
2. J.C. Foley and J.H. Perepezko, Journal of Non-Crystalline Solids, **205-207,** 559-562, (1996).
3. J.C. Foley, D.R. Allen, and J.H. Perepezko, Scripta Materialia, **35**, 655-660, (1996).
4. A. Hirata, Y. Hirotsu, E. Matsubara, T. Ohkubo, and K. Hono, Physical Review B, **74,** 184204, (2006).
5. J. Schroers, R. Busch, A. Masuhr, and W.L. Johnson, Applied Physical Letters, **74,** 2806-2808, (1999).

6. K. Hono, D.H. Ping, M. Ohnuma, and H. Onodera, Acta Materialia, **47**, 997, (1999).

7. D.R. Allen, J.C. Foley, and J.H. Perepezko, Acta Metallurgica, **46**(No.2), 431-440, (1998).

8. X.L. Wang, J. Almer, C.T. Liu, Y.D. Wang, J.K. Zhao, A.D. Stoica, D.R. Haeffner, and W.H. Wang, Physical Review Letters, **91**. 265501, (2003).

9. S. Schneider, P. Thiyagarajan, and W.L. Johnson, Applied Physical Letters, **68,** 493-495, (1995).

10. K.F. Kelton, Acta Materialia, **48**, 1967-1980, (2000).

11. K.F. Kelton, Journal of Non-Crystalline Solids,**274**, 147-154, (2000).

12. T. Kulik, Journal of Non-Crystalline Solids, **287**, 145-161, (2001).

13. Y. He, S.J. Poon, and G.J. Shiflet, Science, **241**, 1640-1642, (1988).

14. G. Wilde, H. Sieber, and J.H. Perepezko, Scripta Materialia, **40**, 779-783, (1999).

15. W.G. Stratton, J. Hamann, J.H. Perepezko, P.M. Voyles, X. Mao, and S.V. Khare, Applied Physical Letters, **86**, 141910, (2005).

16. Y.E. Kalay, L.S. Chumbley, and I.E. Anderson, Journal of Non-Crystalline Solids, **354**, 3040-3048, (2008).

17. Y.E. Kalay, L.S. Chumbley, and I.E. Anderson, Materials Science and Engineering A, **490**, 72-80, (2008).

18. L. Yang, J.Z. Jiang, K. Saksl, and H. Franz, Journal of Physics: Condensed Materials, **19**, 1-6, (2007).

19. Z. Lin, W. Youshi, B. Xiaufang, L. Hui, W. Weimin, L. Jinguo, and L. Ning, Journal of Physics: Condensed Materials, **11**, 7959-7969, (1999).

20. J. Fang, W. Youshi, S. Yuanchang, Z. Chuanjiang, and Z. Zhiqian, Materials Science and Engineering A, **340**, 212-215, (2001).

21. R.L McGreevy and M.A. Howe, Annual Review of Materials Science, **22**, 217, (1992).

22. J.L. Finney, Proceedings of the Royal Society of London Series A Mathematical and Physical Sciences, **319**, 495, (1970).

23. Materials Preparation Center, A.L., US DOE Basic Energy Sciences, Ames, IA, USA. Avaliable from: <www.mpc.ameslab.gov>.

24. X. Qiu, J.W. Thompson, and S.J.L. Billinge, Journal of Applied Crystallography, **37**, 678, (2004).

25. M.J. Kramer and D.J. Sordelet, Journal of Non-Crystalline Solids, **351**(19-20), 1586-1593, (2005).

26. Waseda Y., The Structure of Non-Crystalline Materials. 1980: Mc-Graw-Hill, Inc.

27. R.L. McGreevy and M.A. Howe, Annual Review of Materials Science, **22**, 217-242, (1992).

28. R.L. McGreevy and L. Pusztai, Molecular Simulation, **1**, 359-367, (1998).

29. H. Shaogang, Unpublished Work. 2008: Ames.

30. N.N. Medvedev Journal of Computational Physics, **67**, 223, (1986).

31. E. Vateva and E. Savova, Journal of Non-Crystalline Solids, **145**, 192-193, (1995).

32. A.P. Sokolov, A. Kisliuk, M. Soltwisch, and D. Quitmann, Pysical Review Letters, **69**(10), 1540-1543, (1992).

33. A. Hirata, Y. Hirotsu, T. Ohkubo, T. Hanada, and V.Z. Bengus, Physical Review B, **74**, 214206, (2006).

34. S.R. Elliott, Nature, **354**: p. 445-452, (1991).

35. S.Y. Wang, C.Z. Wang, M.Z. Li, L. Huang, R.T. Ott, M.J. Kramer, D.J. Sordelet, K.M. Ho, Physical Review B, **78**, 184204, (2008).

36. W. Zalewski, J. Antonowicz, R. Bacewicz, and J. Latuch, Journal of Alloys and Compounds, **in press**, (2008).

37. D.B. Miracle, Acta Materialia, **54**, 4317-4336, (2006).

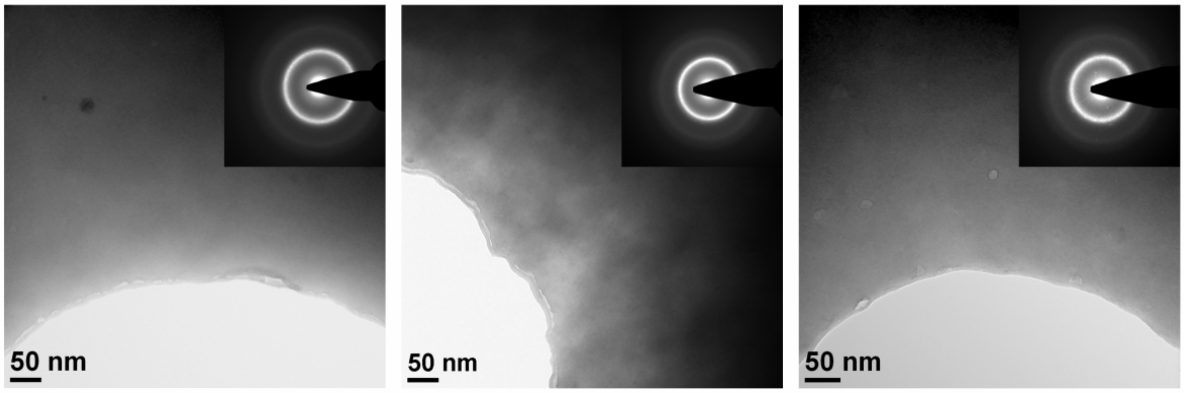

Figure 1. BF images with SAED (inset) showing a featureless matrix and diffuse rings for (a) $Al_{92}Sm_8$, (b) $Al_{90}Sm_{10}$, and (c) $Al_{88}Sm_{12}$ respectively.

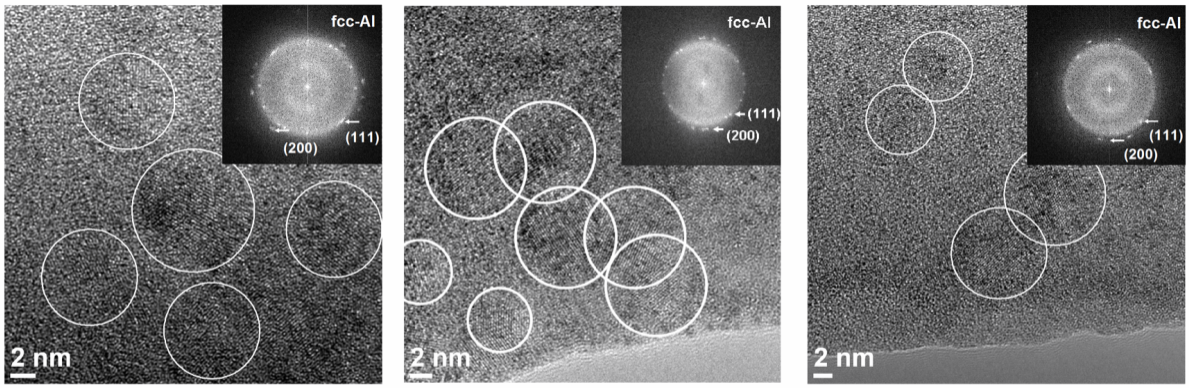

Figure 2. HRTEM images of as-solidified (a) $Al_{92}Sm_8$, (b) $Al_{90}Sm_{10}$, and (c) $Al_{88}Sm_{12}$ respectively. Insets show the Fourier transformed images of the full area. Several fcc-Al nanocrystals are circled.

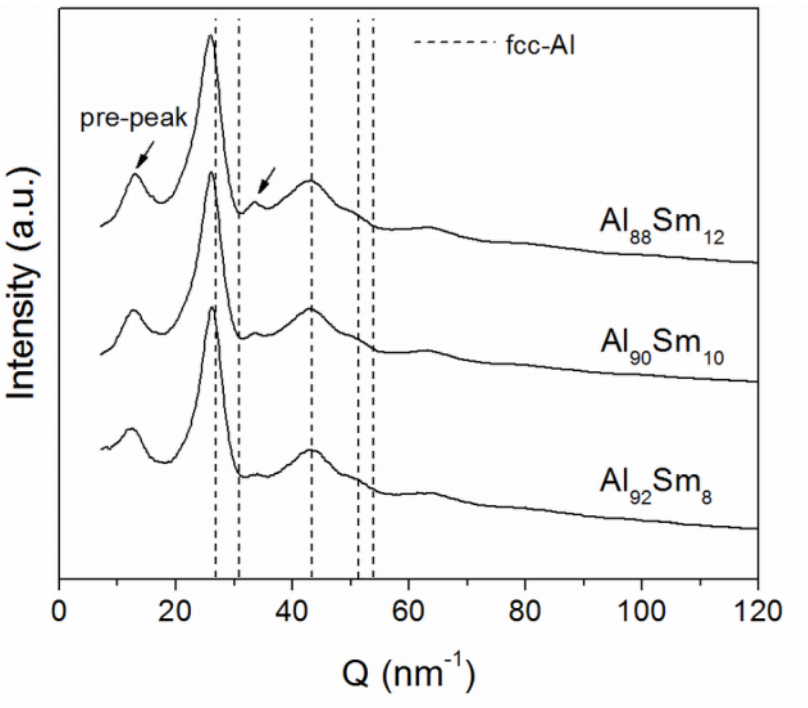

Figure 3. HEXRD patterns of as-rapidly-solidified ribbons. The dash lines show the positions of first five fcc-Al reflections. Two extra reflections are shown with arrows.

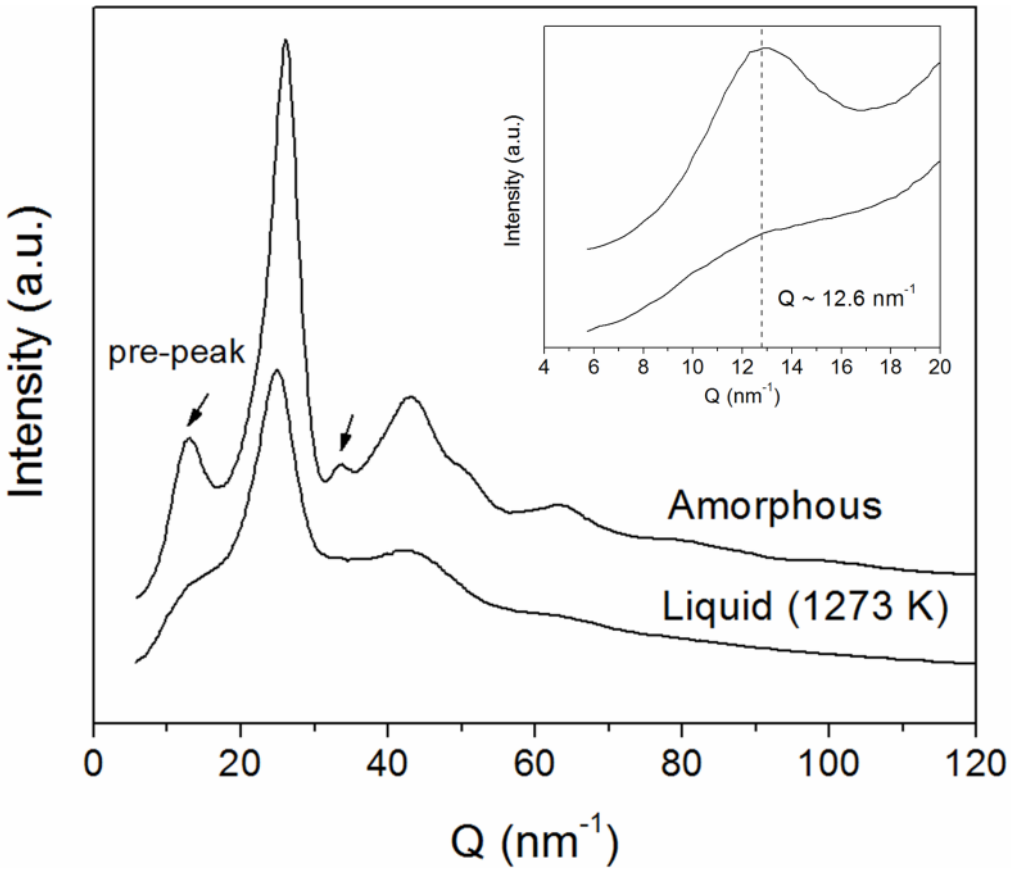

Figure 4. HEXRD pattern of amorphous solid and liquid alloys at 1273 K. Inset shows low Q part of the diffraction pattern.

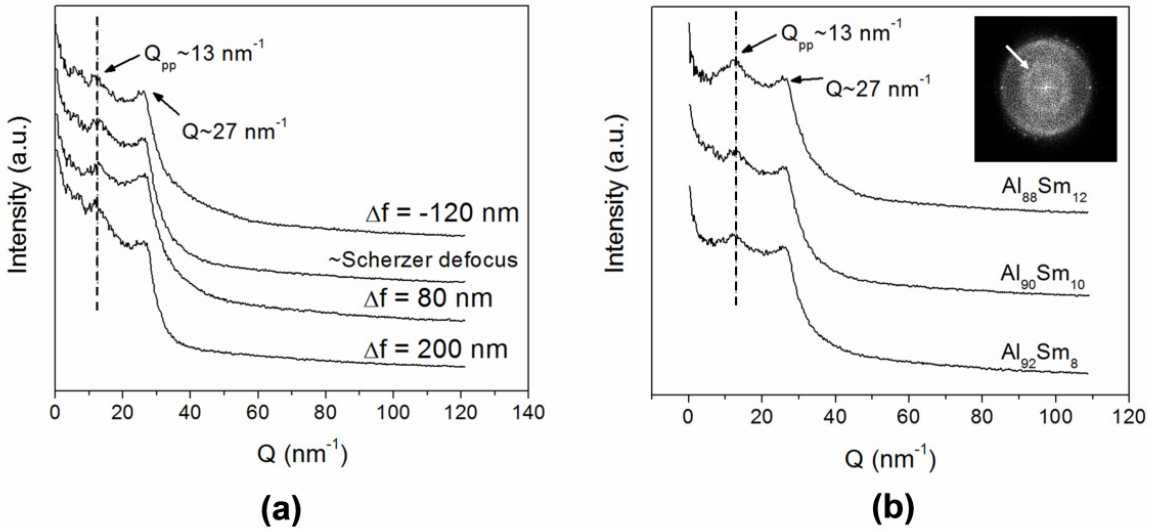

Figure 5. Rotationally averaged FFT at (a) different defocus for $Al_{90}Sm_{10}$ and (b) different compositions for Scherzer defocus. Inset shows example of FFT and the position of Q_{pp} for $Al_{90}Sm_{10}$.

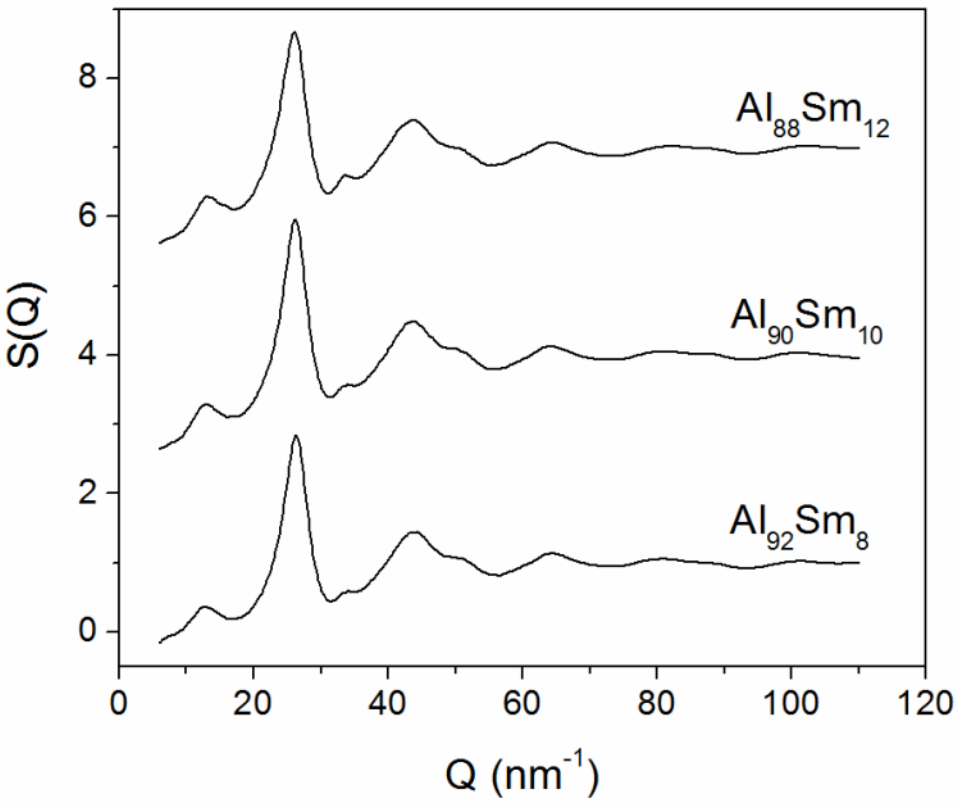

Figure 6. Total structure function data for as-quenched $Al_{(100-x)}Sm_x$ (x=8, 10, and 12).

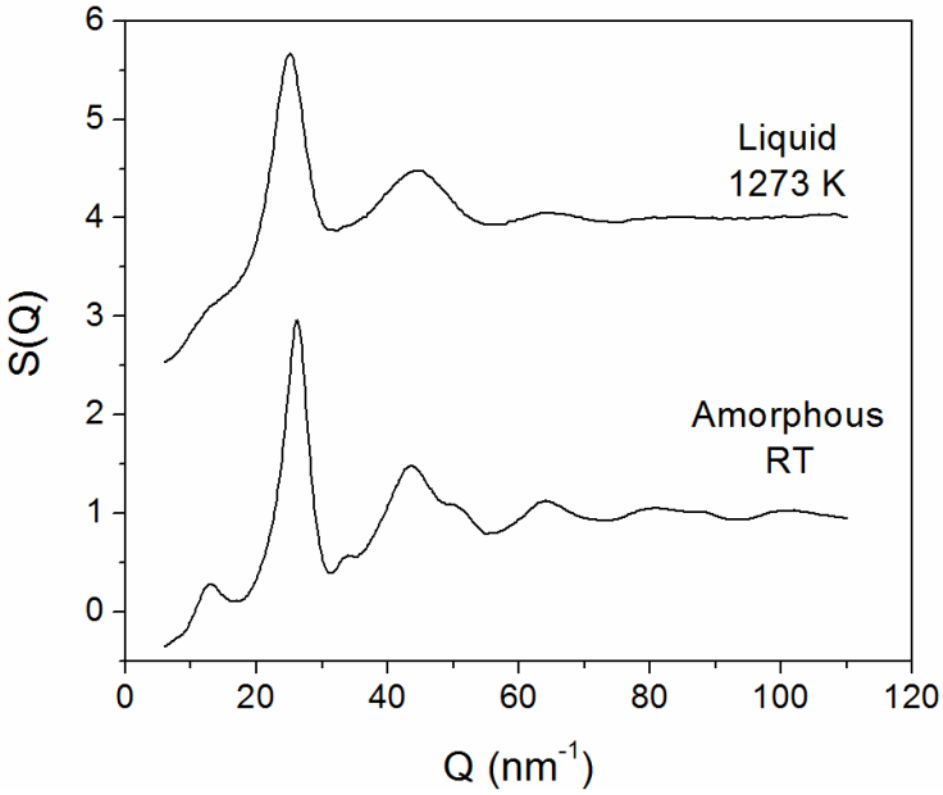

Figure 7. Total structure function data for as-quenched amorphous and liquid $Al_{90}Sm_{10}$ alloy at 1273 K.

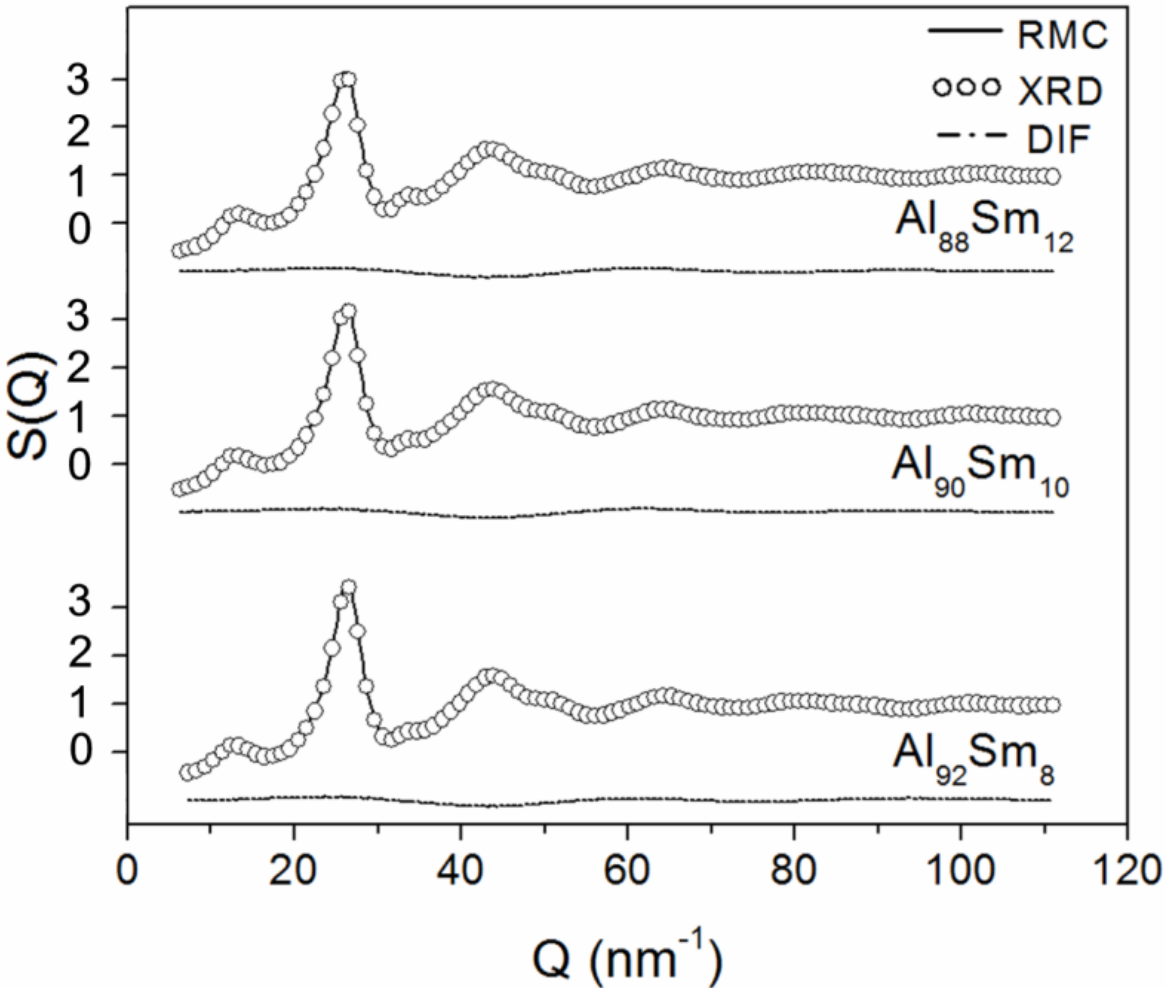

Figure 8. Total structure function data measured (solid line) and calculated using RMC (dot points) for as-quenched $Al_{(100-x)}Sm_x$ (x=8, 10, and 12) alloys. The line at the bottom shows the difference between measured and calculated S(Q).

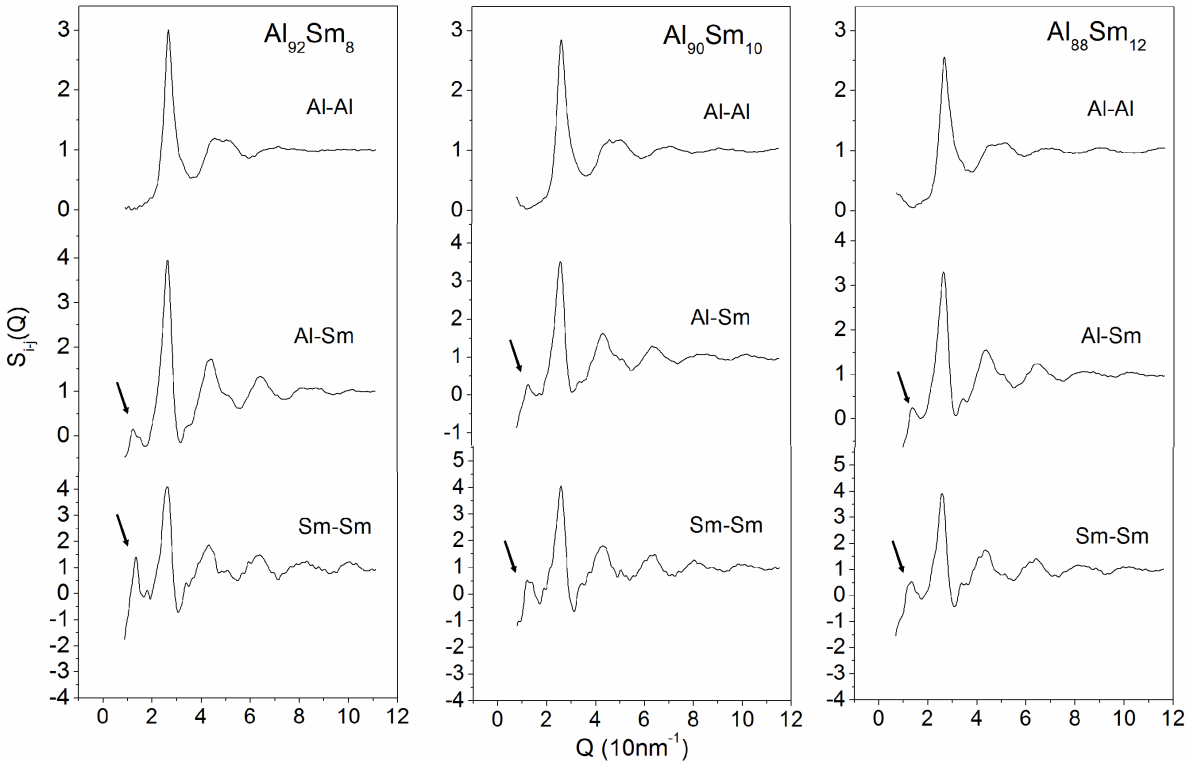

Figure 9. Partial structure factors ($S_{Al-Al}(Q)$, $S_{Al-Sm}(Q)$, and $S_{Sm-Sm}(Q)$) calculated for as-quenched $Al_{(100-x)}Sm_x$ (x=8, 10, and 12) alloys.

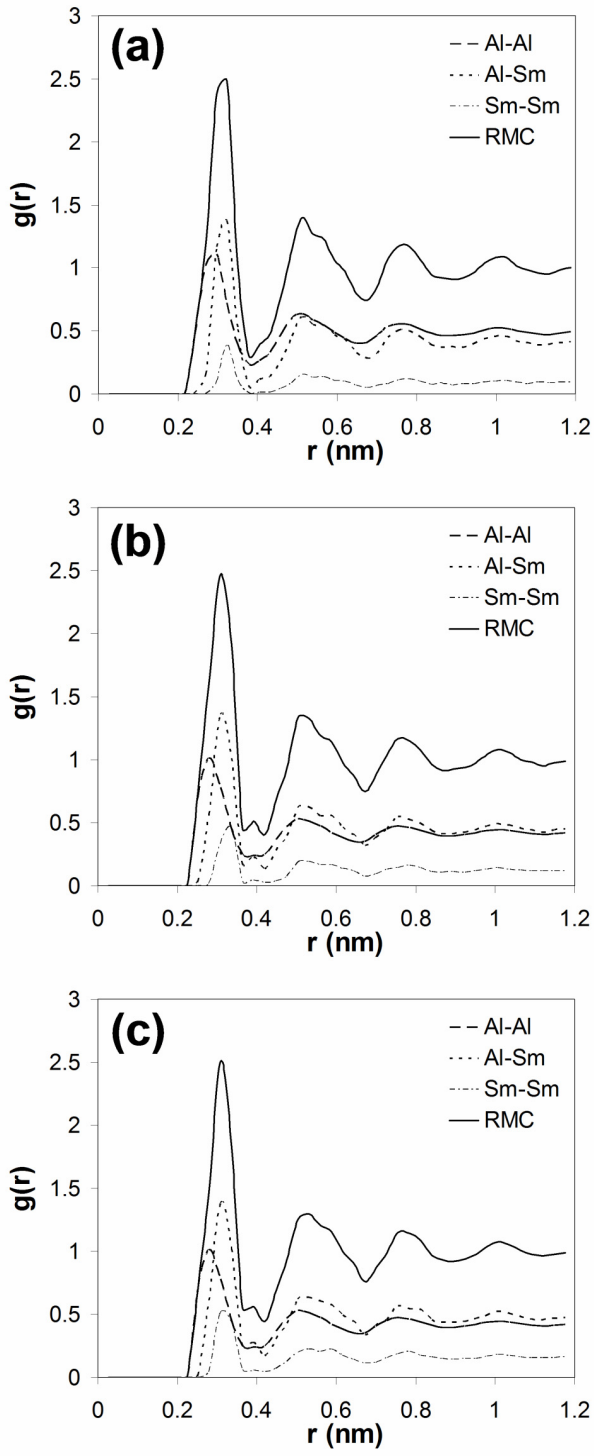

Figure 10. Atomic pair distribution function for as-quenched (a) $Al_{92}Sm_8$, (b) $Al_{90}Sm_{10}$, and (c) $Al_{88}Sm_{12}$ alloys based on RMC simulations and their partial pair distributions (as-indicated on legends).

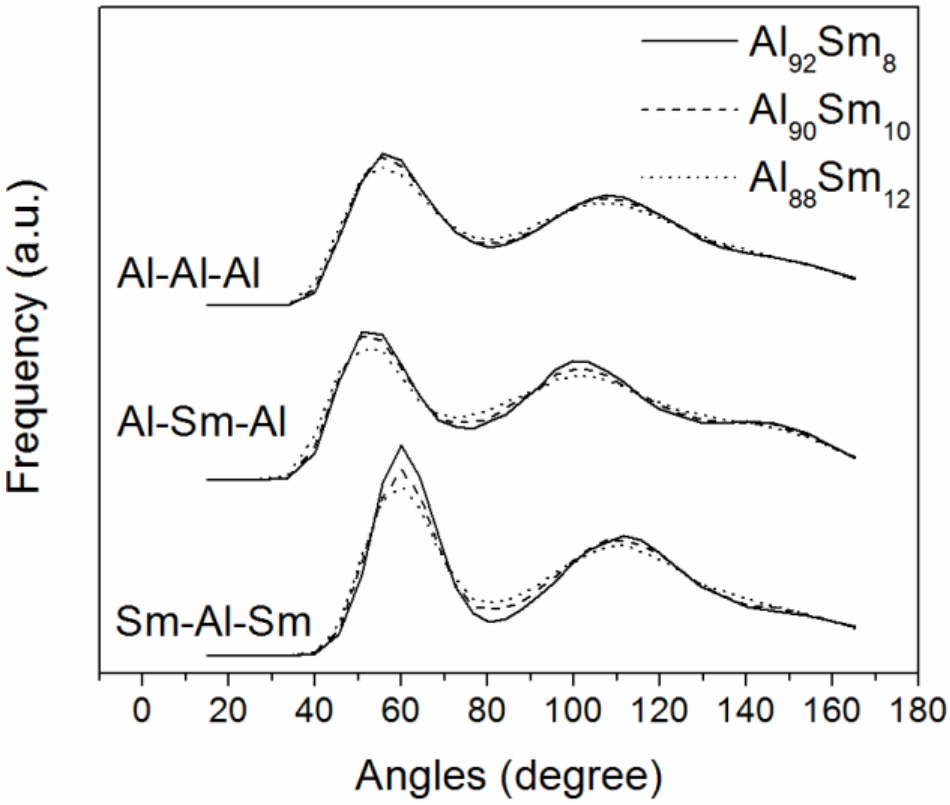

Figure 11. The distribution of bond-orientation angles for as-quenched $Al_{(100-x)}Sm_x$ (x=8, 10, and 12) alloys based on RMC simulations.

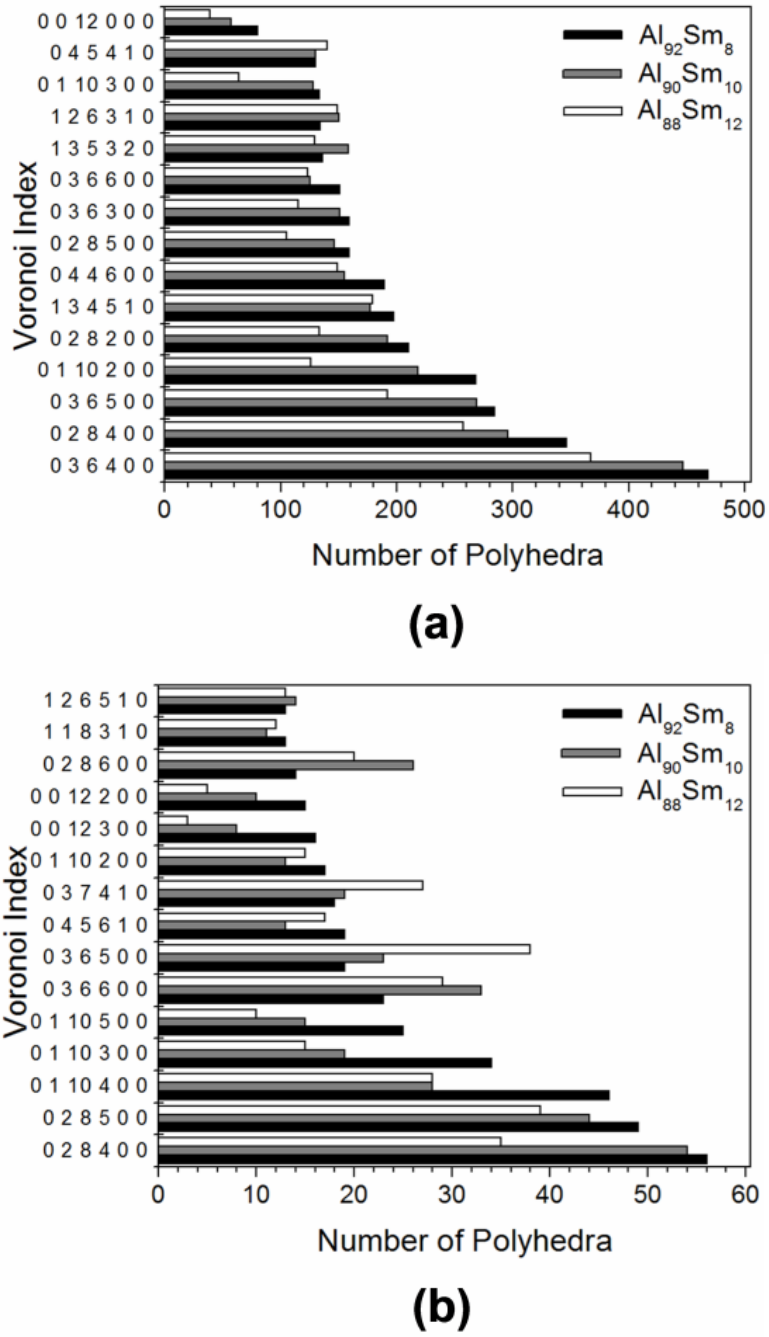

Figure 12. Voronoi polyhedron histograms of (a) Al and (b) Sm centered structure models for as-quenched $Al_{(100-x)}Sm_x$ (x=8, 10, and 12).

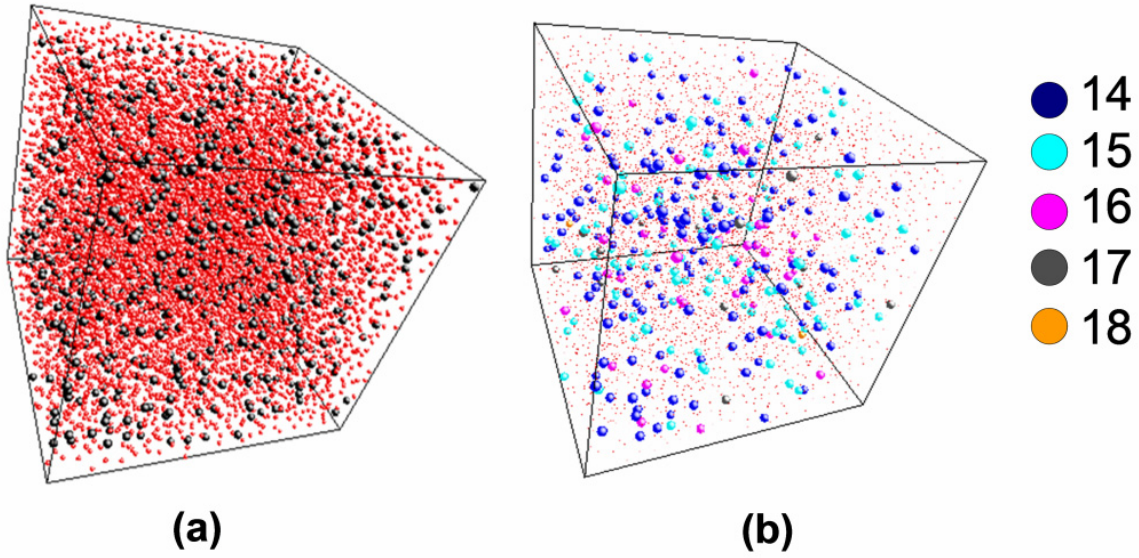

Figure 13. 3-D atomic configurations of as-quenched $Al_{90}Sm_{10}$ calculated from RMC simulations. (a) General view of 3-D configurations. Red and black colors represent Al and Sm atoms respectively. (b) 3-D configuration showing Sm atoms with 14 or higher Al coordination. The red dots represent the Al atoms. Atomic radii are not in scale.

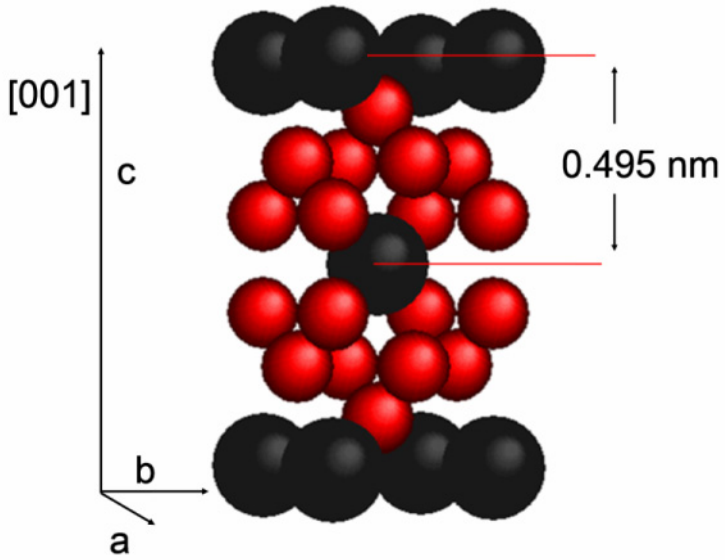

Figure 14. Atomic structure of high temperature metastable tetragonal phase $Al_{11}Sm_3$ with I4/mmm space group symmetry. Red and black colors represent Al and Sm atoms respectively.

Table 1. Peak positions, the structural unit sizes, and the correlation lengths for the pre-peak observed for amorphous and liquid alloys.

Alloy	*Pre-Peak Position ($10nm^{-1}$)*	*Structural Unit Size (nm)*	*Correlation Length (nm)*
Amorphous			
$Al_{92}Sm_8$	1.261	0.498	2.3
$Al_{90}Sm_{10}$	1.263	0.497	2.3
$Al_{88}Sm_{12}$	1.269	0.495	2.4
Liquid			
$Al_{90}Sm_{10}$	1.261	0.498	1.6

Table 2. The average coordination numbers (CN) and bond lengths foras-quenched $Al_{(100-x)}Sm_x$ (x=8, 10, and 12) alloys based on RMC simulations.

	$Al_{92}Sm_8$		$Al_{90}Sm_{10}$		$Al_{88}Sm_{12}$	
	CN	**r (nm)**	**CN**	**r (nm)**	**CN**	**r (nm)**
Al-Al	11.70	0.28(7)	11.44	0.28(6)	11.10	0.28(2)
Sm-Al	13.35	0.32(0)	12.54	0.31(8)	12.33	0.31(6)
Sm-Sm	1.02	0.32(8)	1.39	0.33(2)	1.58	0.32(6)

CHAPTER 6: INITIAL CRYSTALLIZATION IN A NANOSTRUCTURED Al-Sm RARE EARTH ALLOY

A paper to be submitted to *Journal of Non-Crystalline Solids*

Y.E. Kalay[1,2], C. Yeager,[3] L.S. Chumbley[1,2], M.J. Kramer[1,2], I.E. Anderson[1,2]

Abstract

The transformation kinetics and microstructural evolution during initial crystallization in highly driven $Al_{90}Sm_{10}$ was investigated using transmission electron microscopy (TEM), conventional Cu K_α and high energy synchrotron X-ray diffraction (HEXRD) and differential scanning calorimetry (DSC). The as-solidified structures corresponding to different cooling rates showed a variety of metastable structures. The highest cooling rate obtained in this study yielded a high number density of fcc-Al nanocrystals, with sizes on the order of 2-5 nm, embedded in a disordered matrix rich in an Al-Sm medium range order (MRO) structure. Isothermal in-situ HEXRD results indicated a single crystallization of a large primitive cubic phase from the disordered state. Further analysis using DSC showed two crystallization events; a small peak overlapping the peak from the main crystallization event. TEM analysis performed on samples where the crystallization process was interrupted at various temperatures (selected on the basis of DSC curves) resolved pre-existing fcc-Al crystals, further crystallization of fcc-Al, (corresponding to the first small peak) and evolution of the cubic phase, corresponding to the main crystallization event. Fcc-Al nanocrystals showed a restricted growth and stayed at an average size of 16 nm after full crystallization was established. Transformation kinetics were determined after deconvolution of the overlapping

---

[1] Department of Materials Science and Engineering, Iowa State University, Ames IA 50011-3020 USA

[2] Ames Laboratory (DOE), Iowa State University, Ames IA 50011-3020, USA

[3] Missouri University of Science and Technology, Rolla, MO 65401, USA

crystallization peaks using a Gaussian approximation. An Avrami exponent close to 3 suggests a site saturated nucleation for the fcc-Al, forming during solid-state annealing. The long range diffusion of fcc-Al in the matric was prevented by Sm rich clusters. The cubic phase was found to from via a polymorphic crystallization presumably nucleating from Sm-rich clusters that existed in the as-quenched state. The crystallization kinetics were described using an analytical Johnson-Mehl-Avrami (JMA) approach.

Introduction

Al-RE and Al-RE-TM (RE: rare earth element; TM: transition metal) constitute an important class of alloys where a limited glass-forming ability is often observed upon quenching from the liquid state [1, 2]. Partial crystallization of such alloys with high Al content (between 80 and 92 at% Al) has resulted in formation of a very high nucleation density of fcc-Al nanocrystals, on the order of 10^{20} to 10^{23} m^{-3} in the amorphous matrix [3-6]. The resultant composite microstructure of fcc-Al nanocrystals embedded in amorphous matrix has attracted much attention due to the alloy's lightweight structural properties [7, 8]. Several models [4, 9-13] have been proposed to explain the unusual crystallization behavior observed in such systems but there is still no agreement on the mechanism for forming such a high-density of nanocrystals.

The Al-Sm binary system is a simple marginal glass forming alloy which has been reported to form an amorphous phase within a wide range of composition, from 8 to 16 at% Sm [1]. The as-quenched structure of Al-Sm within this range often contains fcc-Al nanocrystals embedded in an amorphous matrix [6, 14]. The size and percentage of these nanocrystals is related to the cooling rate applied to the melt. At high cooling rates, the size of these crystals is so small that conventional TEM and XRD cannot resolve them. However, using new techniques such as fluctuation electron microscopy (FEM), pseudo fcc-Al clusters were identified embedded in an amorphous matrix. These Al clusters appear to show more

coherency in their scattering compared to a glassy alloy yet still lack sharp diffraction, termed medium range order (MRO) [15]. At relatively low cooling rates, fcc-Al can be recognized easily using high resolution electron microscopy (HRTEM) [6]. In a previous study using atom probe tomography (APT) and HRTEM it has been shown that as-solidified $Al_{90}Sm_{10}$ consists of a skeleton-like structure of Al-Sm and fcc-Al preferentially nucleated between the links of the structure [6]. We postutated that the Al-Sm MRO clusters form into a skeleton-like structure that originated because of the strong interactions between Al and Sm in the liquid state [16]. The existence of the Al-Sm MRO structure is evidenced by a pre-peak located well below the main diffuse scattering peak in HEXRD patterns for both liquid and as-quenched alloys and has been described by use of a Reverse Monte Carlo (RMC) technique coupled with Voronoi Tessellation analyses [16]. Upon quenching, the amorphous structure is divided into nano-scale regions by a network of Al-Sm clusters and, depending on the size of these regions, only a certain percentage of fcc-Al clusters reach the critical nucleus size. The remaining Al atoms stay below the critical size, either as amorphous material or fcc-Al MRO [16].

The present study investigates initial crystallization of an amorphous melt-spun $Al_{90}Sm_{10}$ alloy containing pre-existing fcc-Al nanocrystals. Structural characterization of specimens at various stages of crystallization was performed using transmission electron microscopy and X-ray diffraction. The transformation kinetics was studied by use of differential scanning calorimetry (DSC) under isothermal heating conditions.

Experimental Procedure

Ingots of $Al_{90}Sm_{10}$ were prepared by electric arc melting under Ar atmosphere from highly pure Al (99.99 wt%) and Sm (99.9 wt%) elements [17]. Amorphous ribbons with a thickness of 20-30 μm and a width of 1.0 – 1.2 mm were produced from bulk alloy by a Cu

chill block single-roller melt spinning technique under Ar atmosphere at various tangential speeds of 10, 20, and 30 m/s.

High temperature X-ray diffraction studies were carried out using high-energy transmission synchrotron X-ray diffraction (HEXRD) at the Advanced Photon Source at Argonne National Laboratory in collaboration with the Midwest Universities Collaborative Access Team (MUCAT) at sector 6-IDD-D. The as-quenched ribbons were inserted into 2 mm diameter X-ray transparent quartz capillaries and sealed under Ar. The sealed quartz capillaries were exposed to 99.954 keV of X-rays corresponding to a wavelength of 0.012404 nm. As-quenched ribbons were heated and isothermally held at 457 K until fully crystallized. The diffraction data were collected in-situ at Debye-Scherrer geometry by a MAR charge coupled device (CCD) after every 20 seconds of exposure time. A diffraction pattern from a similar empty quartz capillary was collected and subtracted from the high temperature data sets for the background corrections. The room temperature diffraction studies were conducted using a conventional horizontal goniometer axis Cu-K_α X-ray diffractometer in combination with the Bragg-Brentano focusing geometry. The as-quenched ribbon specimens were fixed onto a specially cut zero-background quartz holder with Vaseline® and scanned between $10° \leq 2\theta \leq 90°$ with a step size of 0.02°.

For differential scanning calorimetry (DSC) experiments, the Al sample pans were filled with an average sample weight of 10 mg of ribbon and sealed with an Al cover. Samples were heated-up at 100 K/min heating rate and isothermally held below the crystallization temperature in the temperature range between 451 and 461 K. After each isothermal DSC scan a subsequent run with empty pans was performed to calculate the baseline. A protective gas atmosphere of pure N_2 was employed for each calorimetric experiment.

Transmission and high-resolution electron microscopy (TEM, HRTEM) analyses were performed using an FEI Inc. Tecnai G^2 F20 scanning/transmission electron microscope.

Samples for electron microscopy were thinned using double jet polishing at 248 K with a solution of 3 vol% HCl, 36 vol% methanol, and distilled water. The thickness of each TEM specimens was estimated using electron energy loss spectroscopy (EELS) as described in [18].

Results

As-Quenched Structure

The solidification products of as-quenched $Al_{90}Sm_{10}$, produced at wheel speeds of 10, 20, and 30 m/s, are shown by the XRD patterns in Fig. 1. The as-quenched solidification structures differed according to wheel speeds (or cooling rates). The as-quenched ribbons that were quenched at a wheel speed of 10 m/s consist of several metastable phases, namely tetragonal Al_4Sm, fcc-Al, an orthorhombic phase called ER [14], and a primary diffuse scattering peak indicating an amorphous structure to some degree. Increasing the wheel speed from 10 to 20 m/s, the intensities of the metastable phases decreased. For samples quenched at 30 m/s, formation of any metastable crystalline phases was suppressed according to Cu K_α XRD results. The as-quenched samples of 30 m/s wheel speed were investigated further using transmission HEXRD, and TEM Fig. 2).

The HEXRD pattern (Fig. 2a) shows no crystalline peaks, but two broad peaks at scattering vectors of 12.6 nm^{-1}, and 33.4 nm^{-1}, below and above the major amorphous peak at 26.1 nm^{-1}, respectively. The inset in Fig. 2a showing a bright field (BF) image and the corresponding selected area electron diffraction (SAED) pattern exhibit a featureless microstructure and a diffuse ring typical of an amorphous phase, respectively. Although the crystalline grains are difficult to discern using BF imaging due to their size and small percentage of the total volume resulting, fcc-Al nanocrystals (arrows in Fig. 2b) can be resolved in HRTEM and fast Fourier transform (FFT) of those images. The average size of fcc-Al nanocrystals is on the order of 5 nm.

Crystallization Studies

The melt spun ribbon was next investigated using differential scanning calorimetry (DSC). Fig. 3 shows isothermal DSC traces of $Al_{90}Sm_{10}$ samples produced at 10, 20 and 30 m/s at 451 K. All of the isothermal traces showed an exothermic event after a certain incubation time. While the 10 and 20 m/s samples show a single exothermic event, an interesting observation is the appearance of a small peak overlapping the main exothermic event for the 30 m/s sample, identified with an arrow in Fig. 3.

Fig. 4a shows isothermal DSC traces obtained between 451 and 461 K for the 30 m/s material in greater detail. All of the isothermal curves showed two exothermic events after a certain incubation time (τ). The first exothermic event is subtle and overlaps the second, more dominant exothermic event. These two events are better separated for lower annealing temperatures. Fig. 4b shows the crystallized volume fractions with respect to annealing times, calculated by integrating isothermal DSC traces. The incubation times at different annealing temperatures were found to decrease with increasing annealing temperature, as expected

The Cu K_α XRD patterns of melt-spun ribbons indicate that the sample is fully crystallized after a hold of 451 K for 80 min (Fig. 5). The patterns of $Al_{90}Sm_{10}$ melt-spun at 10 and 20 m/s contain reflections of t-Al_4Sm and ER phases (noted in Fig. 1), which form during solidification, in addition to MS1 that forms after crystallization.

The melt-spun sample produced at 30 m/s contains only reflections of MS1 after the first crystallization as noted by DSC, indicating that the formation of t-Al_4Sm and ER crystal phases are suppressed at this wheel speed. It is difficult to distinguish fcc-Al reflections for the 30 m/s sample because peak overlaping with cubic MS1. However, fcc-Al nanocrystals were resolved before and after the first DSC crystallization event using TEM. Thus, conventional x-ray diffraction does not have the necessary sensitivity to fully resolve all

phases present. The phases observed during rapid solidification and after first crystallization of $Al_{90}Sm_{10}$ are listed in Table 1.

In an attempt to overcome the poor sensitivity of conventional XRD, in-situ HEXRD data was taken. Fig. 6a shows the HEXRD image plate scans of $Al_{90}Sm_{10}$ melt spun (30m/s) material isothermally held at 457 K until the first crystallization as noted by DSC is established. The image plate scans are stored in the form of Debye-Scherrer images and subsequently integrated to produce an intensity vs. Q (or 2θ) plot every 20 seconds. The lines on Fig. 6a indicate the location of Bragg peaks, with the contrast level being proportional to diffracted beam intensities. Similar to DSC analysis, after a certain amount of incubation time, crystallization occurs and crystalline peaks of MS1 phase appear on the diffraction pattern. Unfortunately, unlike DSC analysis the HEXRD shows only a single crystallization event, similar to conventional XRD. No peaks of fcc-Al are resolved in the as-quenched material or during the initial stage of crystallization. However, what is interesting is that the pre-peak observed in the as-quenched state evolves into the Bragg reflection of MS1.

In order to clarify crystallization in the 30 m/s melt spun material S/TEM analysis was performed from samples isothermally annealed at 451 K then quenched. Critical annealing points were chosen on the basis of the DSC data and are marked as A, B, C and D on Fig. 7. Fig. 8a and b shows BF TEM and High Angle Annular Dark Field (HAADF) STEM images, respectively, of $Al_{90}Sm_{10}$ alloy annealed to point A, just after the onset temperature. SAED patterns exhibit broad rings corresponding to the 200 and 220 reflections of fcc-Al. Nanocrystals of fcc-Al in the range of 5-10 nm can be resolved now on BF images as shown by arrows in Fig. 8a.

The nanocrystals of fcc-Al can also be easily recognized in Fig. 8b as dark contrast spherical clusters separated by Sm rich (white contrast) regions. The size of the clusters at this stage of crystallization is on the order of 7 nm. Fig. 9a shows multiple MS1 cubic crystals, ≈120 nm wide, that appear after 10 minutes at 451 K. The inset shows the SAED

pattern taken from the surrounding matrix region. The MS1 continues to grow (Fig. 9b, c) until the grains impinge on one another, Fig. 9d. An intriguing observation is the existence of a high nucleation density of fcc-Al inside the cubic crystals. This is initially evident in Fig. 9c and is shown more clearly in Fig. 10. The inset in Fig. 10a shows an SAED obtained from the cubic structure with the MS1 reflections indexed, as well as the rings corresponding to fcc-Al. From the rings it can be concluded that fcc-Al nanocrystals are randomly distributed and that no specific epitaxial orientation was observed between the MS1 and fcc-Al phases. Fig.10b shows the DF images of fcc-Al nanocrystals imaged using the (111) fcc-Al diffraction ring. Fig. 11 shows the particle size distribution for fcc-Al in as-quenched and annealed samples. The number of particles was counted within the resolution limit of HRTEM and BF conditions for as-quenched and isothermal annealed specimens, respectively. The particle size distribution analysis showed an increase in size distribution with increasing time. This increase saturates for 36 and 80 min annealed samples. The average particle size and number density of particles estimated from BF images are given in Table 2. The particle number density showed a clear increase after the first crystallization event. The average particle size of fcc-Al increased from 7.5 to 15 nm and remained around 16 nm after 80 min

Discussion

The XRD analysis resolved two metastable phases, namely, t-$Al_{11}Sm_3$ and ER, accompanied by amorphous material and fcc-Al for the $Al_{90}Sm_{10}$ ribbons solidified at wheel speeds of 10 and 20 m/s. A very similar type of solidification path was previously observed for $Al_{90}Sm_{10}$ high pressure He gas atomized powders that were sieved to a size range of less than 5 μm in diameter [14]. In that study t-$Al_{11}Sm_3$ and fcc-Al formed an eutectic structure and ER solidified as dendrites, according to [14]. The ribbons produced at 30 m/s wheel speeds do not possess metastable t-$Al_{11}Sm_3$ or ER phases but contain clusters of fcc-Al on

the order of 5 nm embedded in a disordered matrix (Fig. 2). Previous studies of the same alloy system [6, 14, 16, 22, 23] showed that in the compositional range resulting in amorphous formation [22] nanocrystals of fcc-Al are always present if the alloy is quenched from the liquid state. However, if the glassy state is achieved by changing the processing path from melt-quenching to cold-rolling, formation of fcc-Al nanocrystals is completely avoided, as evidenced by the results of isothermal crystallization experiments [22]. This result was explained by hypothesizing pre-existing "quenched-in" fcc-Al nuclei [22, 24, 25]. However, the origin of these possible "quenched in" nucleation sites was not discussed. In a previous study using $Al_{100-x}Sm_x$ (x=8, 10, and 12) alloys, it was speculated that an Al-Sm MRO structure may survive in the melt, creating clusters of Al-Sm atoms which essentially act like distinct "superatoms" with a slightly broad size distribution and huge diameters as compared to individual Al and Sm atoms in the matrix [16]. It was hypothesized that upon rapid solidification these clusters create a local atomic size effect, similar to that seen in multi-component bulk amorphous alloys, preventing the complete crystallization of the Al rich matrix. Evidence of the Al-Sm ordered structure is suggested by the presence of extra reflections at scattering vectors of 12.6 nm^{-1}, and 33.4 nm^{-1} below and above the major amorphous peak at 26.1 nm^{-1} in the HEXRD diffraction pattern of Fig. 2a. Possible structures for this Al-Sm ordered structure calculated using reverse Monte Carlo and Voronoi Tessellation analysis techniques were discussed in [16].

The persistence of structural rearrangement in the as-quenched structure resulting in formation of a network of Al-Sm clusters was observed by atom probe tomography [6]. These clusters appeared to divide the matrix into nano-scale regions and, depending upon the size of theses regions, some percentage of fcc-Al clusters reach the critical nucleus size and grow within the network while the remainders stay at subcritical size. When these as-quenched samples are annealed the subcritical Al regions act as pre-cursors for fcc-Al crystals.

The percentage of subcritical Al clusters and the number of supercritical size particles after nucleation is determined by the cooling rate. In a previous study it was shown that the average size of supercritical fcc-Al particles in $Al_{90}Sm_{10}$ ribbons produced at 40 m/s wheel speed is considerably smaller than ones produced at 30 m/s [6]. Also, in a study of $Al_{92}Sm_8$ the size of supercritical Al particles in a ribbon specimen produced at 55 m/s was so small that they could only be detected with fluctuation electron microscopy [15].

The effect of cooling rate can also be seen on the isothermal DSC traces of $Al_{90}Sm_{10}$ produced at 10, 20, and 30 m/s shown in Fig. 3. The as-quenched structures of $Al_{90}Sm_{10}$ for these three wheel speeds (cooling rates) resulted in formation of a glassy state up to some degree (Fig. 1). The XRD results after isothermal crystallization showed that the glassy state crystallizes to the same metastable cubic phase independent of the cooling rate applied in this study. However, for the 30 m/s wheel speed samples, DSC shows two exothermic events while for 10 and 20 m/s samples it only shows a single exothermic event (Fig. 3 and Fig. 4). The room temperature (Fig. 5) XRD and high temperature in-situ (Fig. 6) HEXRD analysis indicated that the major crystallization event is the formation of the cubic phase (MS1). TEM analysis of the 30 m/s sample before and after the onset point (Fig. 7) revealed that the initial exothermic event observed in DSC corresponds to crystallization of fcc-Al. The fcc-Al particles are large enough to be resolved with BF in annealed samples (e.g. point "A" in Fig. 7), but are so small that they can only be resolved using HRTEM conditions (Fig. 2). Thus, the trend of ever-decreasing fcc-particle size with cooling rate appears valid.

The average fcc-Al particle size is on the order of 7.5 nm with a standard deviation (STD) of 2.1 nm after an isothermal anneal at 451 K for 5 min (Table 2). The size of the fcc-Al particles reaches an average value of 15.1 nm with further annealing for 36 min. (point "C" in Fig. 7) and saturates around 16 nm for 80 min. (point "D" in Fig. 7) when the amorphous material is fully crystallized. This result shows that fcc-Al nanocrystals demonstrate a restricted growth, with long-range diffusion possibly being blocked by the

observed Sm rich clusters, which will be slow to diffuse. This structure is best seen in the HAADF image in Fig. 8b, where the fcc-Al nanocrystals (dark contrast) surrounded by Sm rich (bright contrast) matrix. Moreover, this is also in good agreement with the idea of having regions containing clusters of super and subcritical Al divided by Al-Sm "superatoms" in the as-quenched state. For 30 m/s wheel speed samples the cooling rate is high enough to retain a sufficient number of subcritical Al clusters in the as-quenched state. When these samples are isothermally annealed supercritical size fcc-Al crystals form (nucleate) from subcritical size Al clusters. Therefore, in the fully crystal samples fcc-Al are present that originated both from supercritical size particles formed during rapid solidification and subcritical size Al clusters from which supercritical-sized particles nucleate during solid-state annealing. The latter event appears as an exothermic peak on DSC scans (Fig. 3 and Fig. 4). Moreover, particle density measurements (Table 2) performed before and after the first crystallization peak indicate an increase of particle density that agrees with an additional nucleation process. High temperature in-situ HEXRD (Fig. 6) does not resolve the fcc-Al observed in TEM BF images (Fig. 8) during the early stages of crystallization simply due to low volume percentage and small size of the fcc-Al crystals, which at best would manifest itself as a slight line broadening.

Detailed analysis of the crystallization kinetics of $Al_{90}Sm_{10}$ melt spun (30m/s) samples carried out by isothermal DSC measurements (Fig. 4) showed two overlapped exothermic peaks, indicating two crystallization reactions after a certain incubation time (τ).This is in good agreement with TEM analysis which indicates crystallization of fcc-Al and MS1 phases after initial crystallization. In order to separate these two exothermic peaks, the DSC trace at 451 K was selected and the peaks were deconvoluted using a Gaussian approximation. Fig. 12a and b shows the deconvoluted and integrated DSC traces, respectively.

The volume fraction x can be described by the well know Johnson-Mehl-Avrami (JMA) equation [26]:

$$x = 1 - \exp\left\{-\left[k(t-\tau)\right]^n\right\} \quad (1)$$

where x is the volume fraction of crystallized phase, t annealing time, τ incubation time, k reaction rate constant, and n is the Avrami exponent which represents the characteristics of nucleation and growth kinetic mechanisms [27]. These values are shown in Figure 12b. The JMA plots of ln[-ln(1-x)] versus ln(t-t_0) over the range of 20-80% transformation at 451 K is shown in Fig.13a. The Avrami exponents derived from the slopes of the lines in Fig.13a are found to be 2.9 and 2.93 for fcc-Al and MS1, respectively. It should be noted that Avrami exponents calculated here give an average values of n for a predetermined crystallization regime. It has been proposed [28, 29] that the first derivative of JMA plots with respect to crystallized volume fraction, which is the change of Avrami exponents (also called the local Avrami exponent, n(x)), gives more detailed information during crystallization. The local Avrami exponents calculated for fcc-Al and MS1 reflect variations in nucleation and growth during crystallization. In both cases the local Avrami exponent starts from a value lower than 2 and increases to approximately 3 for fcc-Al and 3.2 for MS1 after 20% of crystallization is completed. During the main crystallization regime (20<x<90%), it stays around 3 and 3.2 for fcc-Al and MS1, respectively. For the final stage (x>90%), it shows a slight decrease followed by a sharp increase towards a value of 4.

The average value of the Avrami exponent calculated for fcc-Al is 2.9. This number is close to n=3, which indicates a zero nucleation rate with interface controlled growth or an increasing nucleation rate with diffusion controlled growth [27]. As was discussed before, there are two distinct origins for fcc-Al particles that form during full crystallization, supercritical particles that nucleate during rapid solidification and subcritical clusters that grow to supercritical size during solid-state annealing at high temperatures. The latter gives rise to the initial peak in the isothermal DSC trace in Fig. 12. Fig. 12b shows that

crystallization of the secondary fcc-Al peak that occurs during solid-state annealing is much faster than the crystallization of the MS1 cubic phase. These results are in good agreement with TEM observations (Fig. 9). It has also been shown that the average size of fcc-Al clusters saturates at around 16 nm before the crystallization of MS1 is completed, as indicated in Table 2. According to TEM and APT [6] results a realistic model for fcc-Al formation during solid-state annealing can be site saturation and interface controlled growth as predicted with JMA. This might seem to conflict with the findings in Table 2 where the average particle density of fcc-Al was found to increase with isothermal annealing. However, it must be remembered that the first exothermic DSC peak represents the nucleation of fcc-Al forming during solid state annealing from subcritical clusters. The average particle density measurements of fcc-Al as determined using TEM and shown in Table 2 give an average value that includes fcc-Al forming both initially during solidification and secondarily as a result of devitrification, since the two are indistinguishable. Therefore, it is not possible to comment on the nucleation rate of the secondary fcc-Al from TEM analysis.

The Sm rich clusters revealed in HAADF and BF images in Fig. 8 and Fig. 9, respectively, is hypothesized to block long-range diffusion of Al in the matrix. Therefore, the growth process of fcc-Al particles should be mostly controlled by the interplay between them and the Sm rich clusters. It is possible that initially growth of fcc-Al is under interface control; once a particular size is attained further growth is controlled by diffusion within the nanoregions defined by the Sm-rich network. The observed saturation in average particle size may indicate point as which the Sm rich clusters prevent long-range diffusion. If such a mixed growth model is active for fcc-Al formation, a key assumption of JMA is violated and further studies beyond JMA modeling are required to explain this mechanism. The normal definition related to the value of the Avrami exponent calculated for solid-state fcc-Al formation is also not applicable as this number does not represent the whole crystallization of fcc-Al. A great portion of fcc-Al has already nucleated before solid-state annealing.

The MS1 phase is a metastable compound and decomposes to a metastable hexagonal phase upon isochronal heating [6]. In this study no crystallographic relationship was found (Fig. 10) between fcc-Al and the MS1 phase and MS1 is assumed to be randomly nucleate in the matrix. The growth rate of MS1 during isothermal annealing at 451K was estimated to be constant and on the order of 15 nm/min from TEM analysis. The migration of Sm atoms during the growth of Al phase may trigger the nucleation for MS1. However, due to the restriction of long range diffusion in the matrix a polymorphic-type of reaction is more probable for MS1 where the phase crystallizes presumably from the same composition in matrix. The in-situ isothermal HEXRD analysis (Fig. 6) showed that the pre-peak evolves into the Bragg reflection of MS1. Moreover, the activation energy for the formation of MS1 was found to be relatively low as compared to many other amorphous alloys [6] which indicates a low thermal stability against crystallization. All of these results indicate that it is quite possible MS1 nucleates from the Sm-rich clusters (MRO) found in the as-quenched structures [16].

Assuming a polymorphic crystallization with constant growth rate, the Avrami exponent estimated for MS1 is in close vicinity to n=3, similar to that determined for crystallization of fcc-Al. While it has been noted that the Avrami exponent calculated for fcc-Al does not represent the formation of all fcc-Al after crystallization, and therefore is not applicable, this is presumably not the case for formation of MS1. Thus, site-saturation may be occurring as regards MS1 formation.

If the ratio of the fcc-Al nucleated during rapid solidification versus solid-state annealing is changed (such as when the cooling rate is altered) the crystallization mechanism may differ. This is an interesting possibility that still remains to be explored. Such a study could further elucidate the complex devitrification sequence seen in the Al-Sm system.

Conclusion

Cu-block melt-spinning of $Al_{90}Sm_{10}$ at different wheel speeds of 10, 20, and 30 m/s resulted in formation of an amorphous phase with a variety of metastable crystalline compounds and fcc-Al. The formation of metastable compounds was suppressed with increasing wheel speeds. The highest cooling rate achieved in this study (at 30 m/s wheel speed) yielded a high number density of fcc-Al crystals in the size range of 2-5 nm, embedded in a disordered matrix. The isothermal crystallization of samples produced at 30 m/s resulted in two exothermic events while the 10 and 20 m/s samples show only a single exothermic event. Further XRD analyses showed that the major crystallization event is the formation of MS1, which is a metastable cubic phase. TEM analysis showed that the minor crystallization event for 30 m/s is the additional nucleation of fcc-Al. The number of subcritical size Al particles retained during quenching appears to be enough to create an exothermic peak on the isothermal DSC trace for 30 m/s samples. These results are in good agreement with the idea of having Sm rich clusters (MRO) in the as-quenched state, which divide the Al rich matrix into nanoscale regions. The subcritical size Al regions act as pre-cursors for formation of fcc-Al formation upon high temperature heat treatment. The average particle density and size of fcc-Al were found to saturate before complete crystallization is established. This indicates that fcc-Al shows a restricted growth and that long range diffusion of Al was prevented by the presence of Sm rich clusters.

The crystallization mechanism was investigated through a JMA approach using isothermal DSC studies at 451 K. The Avrami exponent estimated for fcc-Al represents only the crystallization during solid-state annealing and suggests a zero nucleation rate with interface-controlled growth. The observed saturation point in average particle size may indicate a change in growth mode from interface to diffusion control. The Avrami exponent calculated in this study represents only a portion of fcc-Al crystallization since some fcc-Al was found to pre-exist in the as quenched structure. Thus, the determined exponent it does

not illustrate the total crystallization event for fcc-Al. A similar Avrami exponent was calculated for MS1 also indicating that the reaction was dominated by a fixed number of nuclei. This suggests that MS1 forms by a polymorphic crystallization. The pre-peak observed in the as-quenched samples may indicate that Sm-rich clusters act as the pre-cursors of MS1. Further experimental and theoretical studies are in progress to identify the possible mechanisms behind the high number density of nanocrystals seen.

Acknowledgment

The work at Ames Laboratory was supported by the United States Department of Energy (USDOE), Office of Science (OS), Office of Basic Energy Science (BES), under Ames Laboratory Contract No. DE-AC02-07CH11358. The high-energy X-ray work at the MUCAT sector of the APS was supported by the US Department of Energy, Office of Science, Basic Energy Sciences under Contract No. DE-AC02-06CH11357. The assistance of Materials Preparation Center of the Ames Laboratory is acknowledged for supplying our samples [17].

Reference

1. Inoue A., Amorphous, nanoquasicrystalline and nanocrystalline alloys in Al-based systems. Progress in Materials Science, 1998. **43**: p. 365-520.
2. He Y., Poon S.J., and Shiflet G.J., Science, 1988. **241**: p. 1640-1642.
3. Chen H., et al., Scripta Metallurgica Mater., 1991. **25**: p. 1421-1424.
4. Allen D.R., Foley J.C., and P. J.H., "Nanocrystal development during primary crystallization of amorphous alloys". Acta Metallurgica, 1998. **46**(No.2): p. 431-440.
5. Foley J.C. and Perepezko J.H., The devitrification of Al-Y-Fe amorphous alloys. Journal of Non-Crystalline Solids, 1996. **205-207**: p. 559-562.
6. Kalay Y.E., Chumbley L.S., and Anderson I.E., Journal of Non-Crystalline Solids, 2008. **354**: p. 3040-3048.

7. Kulik T., Journal of Non-Crystalline Solids, 2001. **287**: p. 145-161.

8. He Y., et al., Acta Metallurgica Materialia, 1993. **41**: p. 337.

9. Hono K., et al., Acta Materialia, 1999. **47**: p. 997.

10. Wang X.L., et al., Physical Review Letters, 2003. **91**: p. 265501.

11. Schneider S., Thiyagarajan P., and Johnson W.L., Formation of nanocrystals basd on decomposition in the amorphous $Zr_{41.2}Ti_{13.8}Ni_{10}Be_{22.5}$ alloy. Applied Physical Letters, 1995. **68**: p. 493-495.

12. Kelton K.F., Acta Materialia, 2000. **48**: p. 1967-1980.

13. Kelton K.F., Journal of Non-Crystalline Solids, 2000. **274**: p. 147-154.

14. Kalay Y.E., Chumbley L.S., and Anderson I.E., Materials Science and Engineering A, 2008. **490**: p. 72-80.

15. Stratton W.G., et al., Aluminum nanoscale order in amorphous $Al_{92}Sm_8$ measured by fluctuation electron microscopy. Applied Physical Letters, 2005. **86**: p. 141910.

16. Kalay Y.E., et al., Local Structure of the Marginal Glass Forming Al-Sm Alloys: Liquid and Amorphous States. Submitted to Phyical Review B, 2009.

17. Materials Preparation Center, A.L., US DOE Basic Energy Sciences, Ames, IA, USA. Avaliable from: <www.mpc.ameslab.gov>.

18. Brydson Rik, Electron Energy Loss Spectroscopy. Royal Microscopical Society Microscopy Handbook, ed. Kohler Angela and Rainforth Mark. Vol. 48. 2001, Leeds, UK: BIOS Scientific Publishers Ltd.

19. Casteels F., The Aluminum-rich parts of the aluminum samarium and aluminum-dysprosium systems. Journal of the Less-Common Metals, 1967. **12**: p. 210-220.

20. Buschow K.H.J. and Van Vucht J.H.N., Systematic arrangement of the binary rare-earth-aluminum systems. Philips Research Reports, 1967. **22**: p. 233-245.

21. Battezati L., et al., Crystallization behavior of Al-Sm amorphous alloys. Materials Science and Engineering A, 1994. **179-180**: p. 600-604.

22. Wilde G., Sieber H., and Perepezko J.H., Glass formation versus Nanocrystallization in an $Al_{92}Sm_8$ alloy. Scripta Materialia, 1999. **40**: p. 779-783.

23. Perepezko J.H., et al., Nanocrystallization Reactions in Amrophous Aluminum Alloys. Materials Transactions, 2003. **44**: p. 1982-1992.

24. Foley J.C., Allen D.R., and Perepezko J.H., Analysis of nanocrystal development in Al-Y-Fe and Al-Sm glasses. Scripta Materialia, 1996. **35**: p. 655-660.

25. Wilde G., et al., Nanocrystallization in Al-rich Metallic Glasses. Advanced Engineering Materials, 2003. **5 No.3**: p. 125-130.

26. Avrami M., Journal of Chemical Physics, 1941. **9**: p. 177.

27. Christian J.W., The Theory of Transformation in Metals and Alloys. 1975, Oxford: Pergamon Press.

28. Calka A. and Radinski A. P., Journal of Materials Research, 1985. **3**: p. 59.

29. Ranganathan S. and Heimendahl M.V., Journal of Materials Science, 1980. **15**: p. 1131.

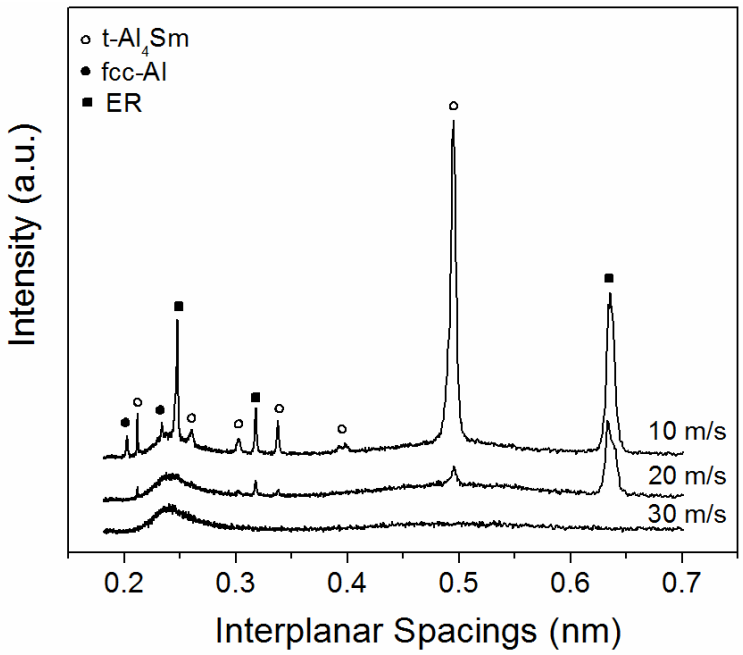

Figure 1. Cu K_α XRD patterns of as-quenched $Al_{90}Sm_{10}$ samples produced at wheel speeds of 10, 20 and 30 m/s.

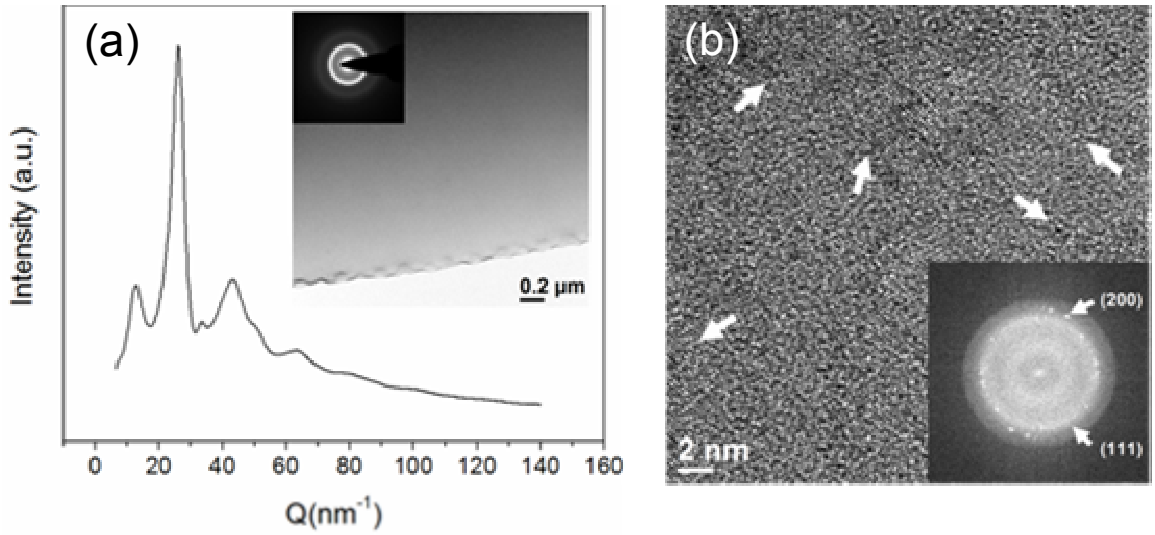

Figure 2. (a) HEXRD pattern and (b) HRTEM image of as-quenched $Al_{90}Sm_{10}$ produced at a wheel speed of 30 m/s. Insets shows BF image and SAD patterns (a) and a fast Fourier transformed (FFT) version of the HRTEM image of the square shown in (b). Arrows show the fcc-Al nanocrystals.

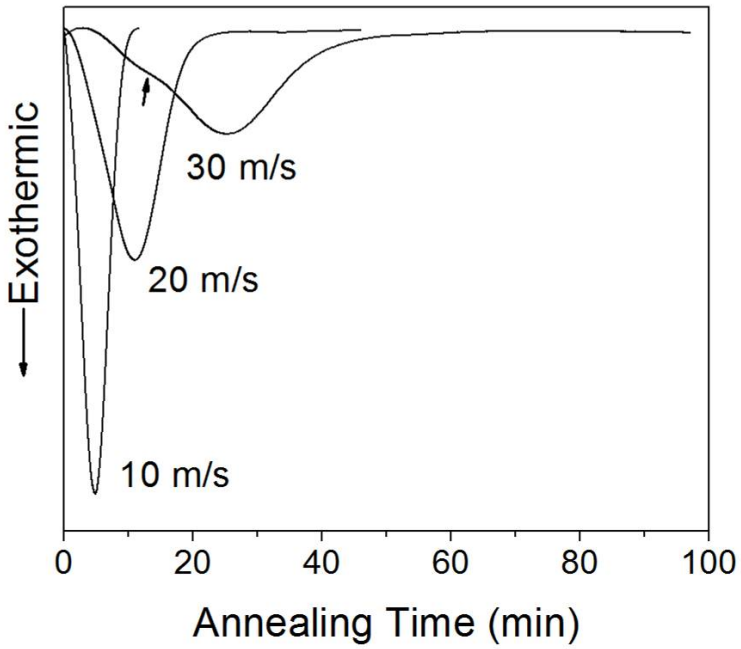

Figure 3. Isothermal DSC traces of $Al_{90}Sm_{10}$ samples produced at 10, 20 and 30 m/s at 451 K.

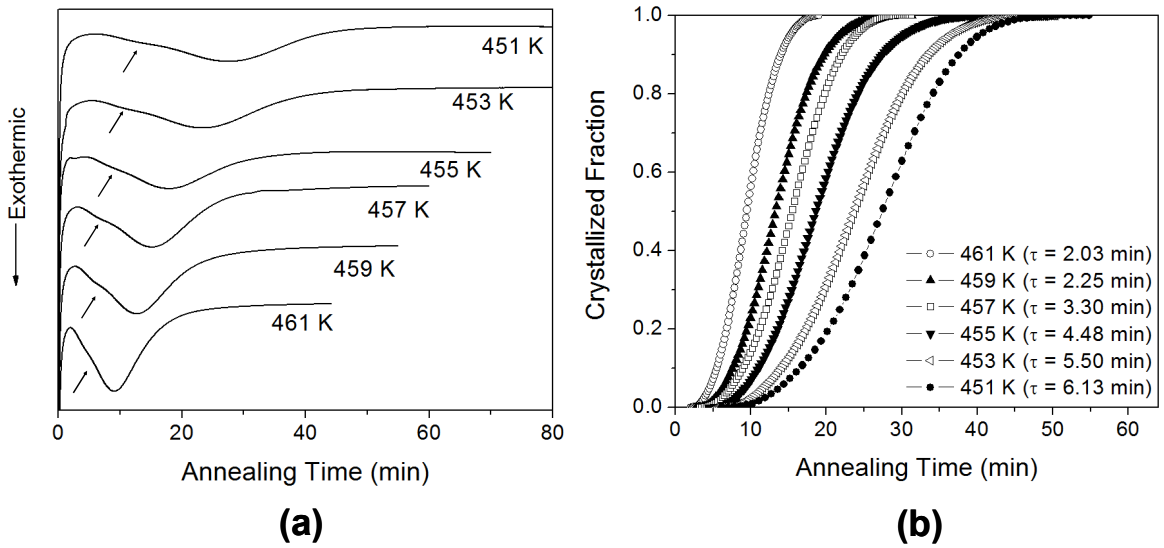

Figure 4. (a) Isothermal DSC traces of $Al_{90}Sm_{10}$ samples produced at 30 m/s between 451 and 461 K. (b) Crystallized volume fractions and incubation times with respect to annealing temperatures.

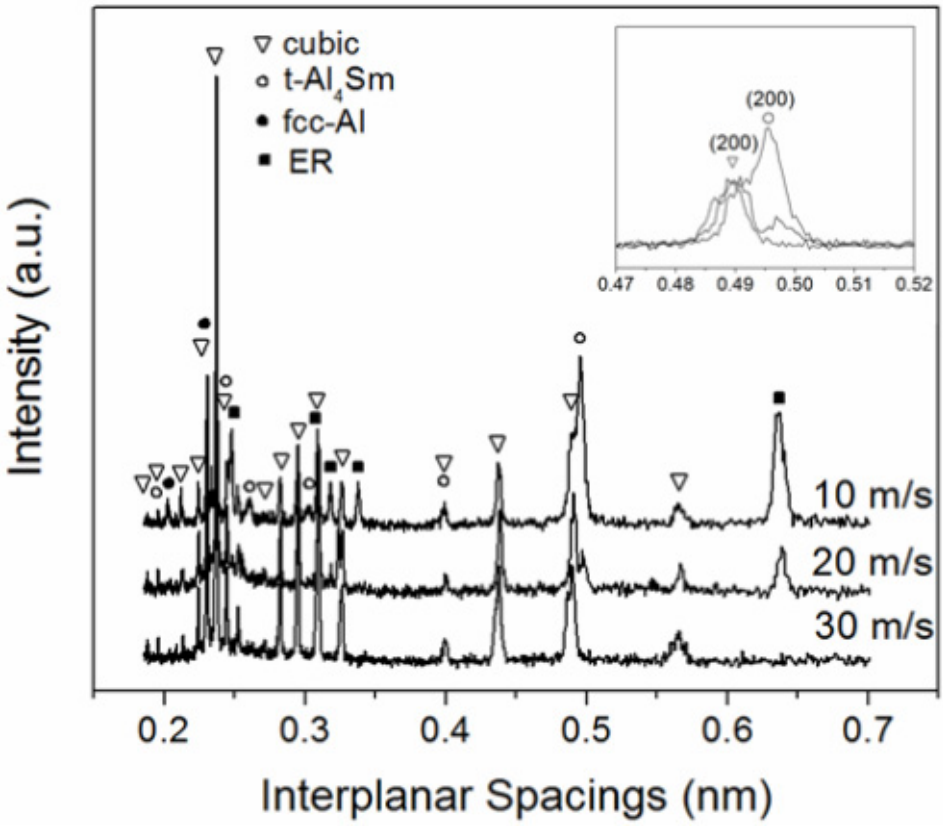

Figure 5. XRD patterns of $Al_{90}Sm_{10}$ samples produced at 10, 20 and 30 m/s after full crystallization at 451 K. Inset shows the position of (200) Bragg reflection for MS1 and t-Al_4Sm phases.

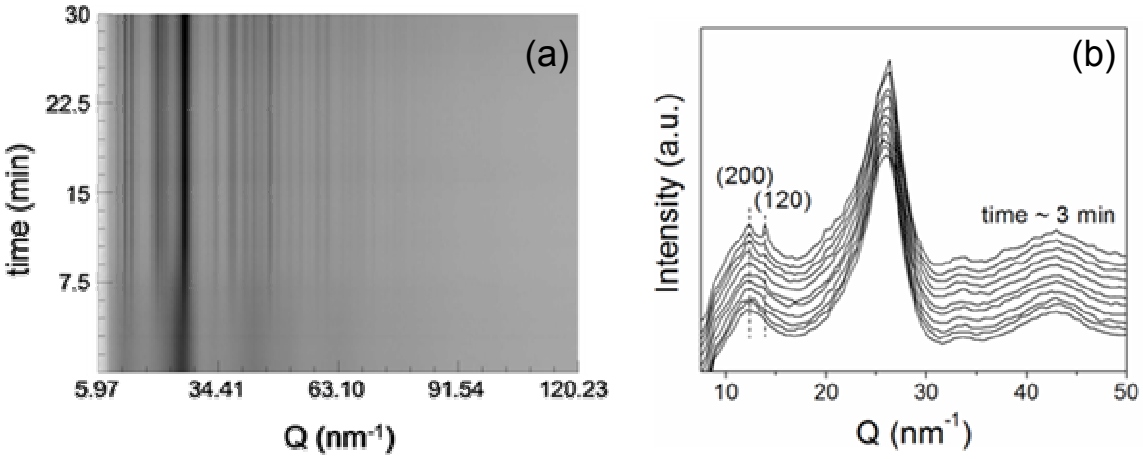

Figure 6. (a) HEXRD image plate scans and (b) integrated XRD pattern series with respect to annealing time at 457 K for melt-spun $Al_{90}Sm_{10}$ at a wheel speed of 30 m/s.

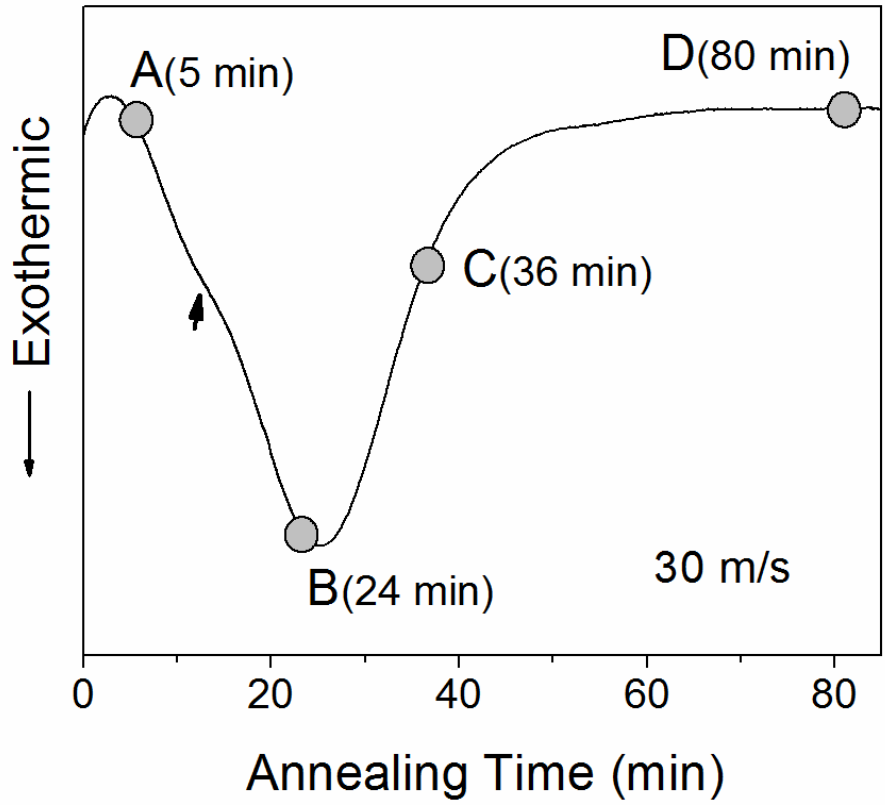

Figure 7. Isothermal DSC trace at 451 K showing the critical annealing points for $Al_{90}Sm_{10}$ produced at 30 m/s wheel speeds for S/TEM analysis.

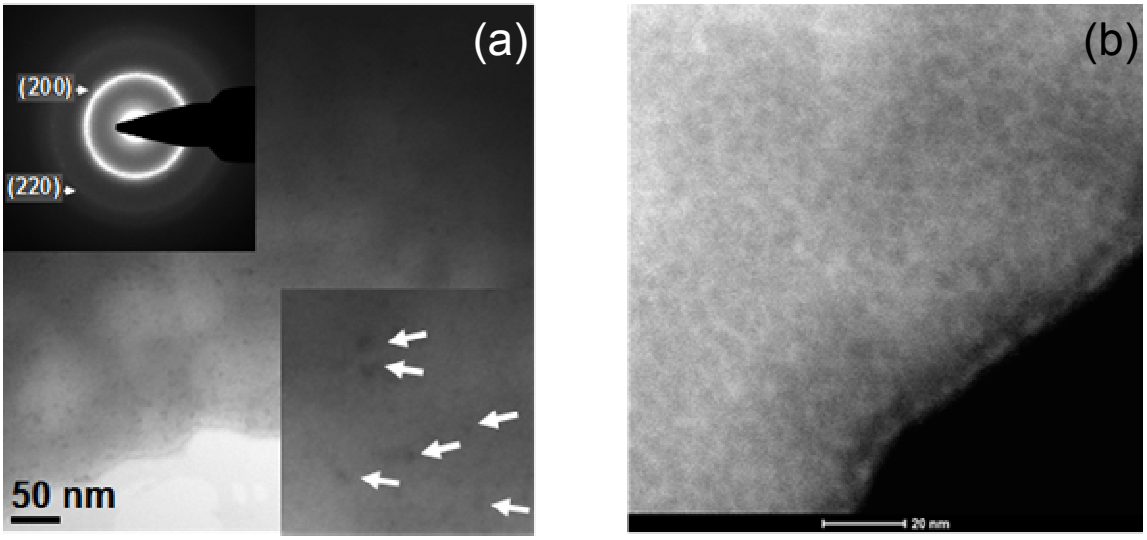

Figure 8. (a) BF image showing the fcc-Al nanocrystals formed after isothermally holding the as-quenched sample up to point A in Fig. 7. Insets represent the fcc-Al nanocrystals (right corner) and corresponding SAED pattern (left corner). (b) HAADF image showing fcc-Al nanocrystals (dark) surrounded by Sm rich matrix (bright).

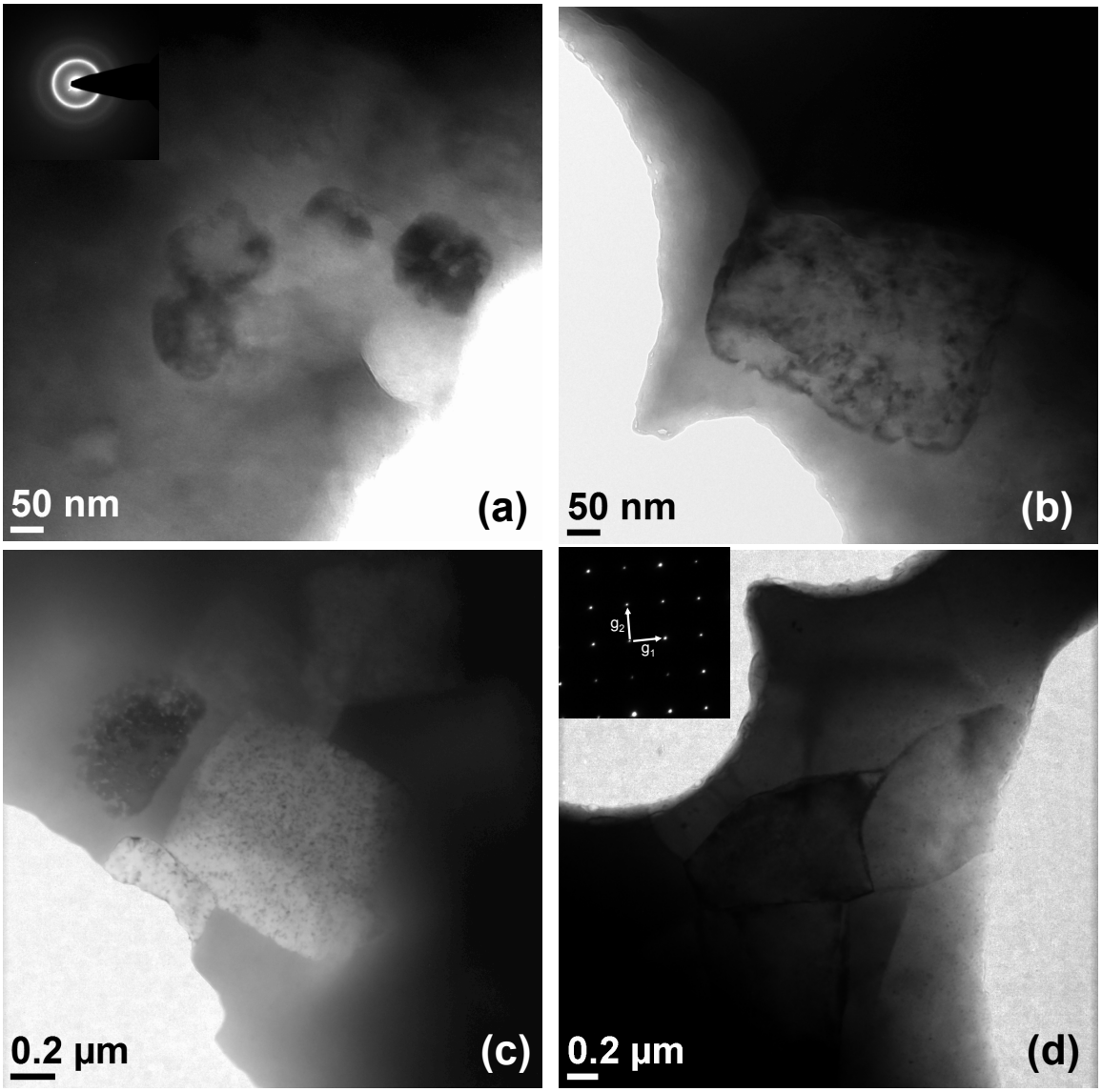

Figure 9. BF images of $Al_{90}Sm_{10}$ alloy (produced at 30 m/s wheel speed) and quenched at 451 K for (a) 24 min. inset shows the SAD for the amorphous like region, (b) and (c) 36 min., and (d) 80 min, inset shows the SAD for the MS1 phase at (001) zone axis.

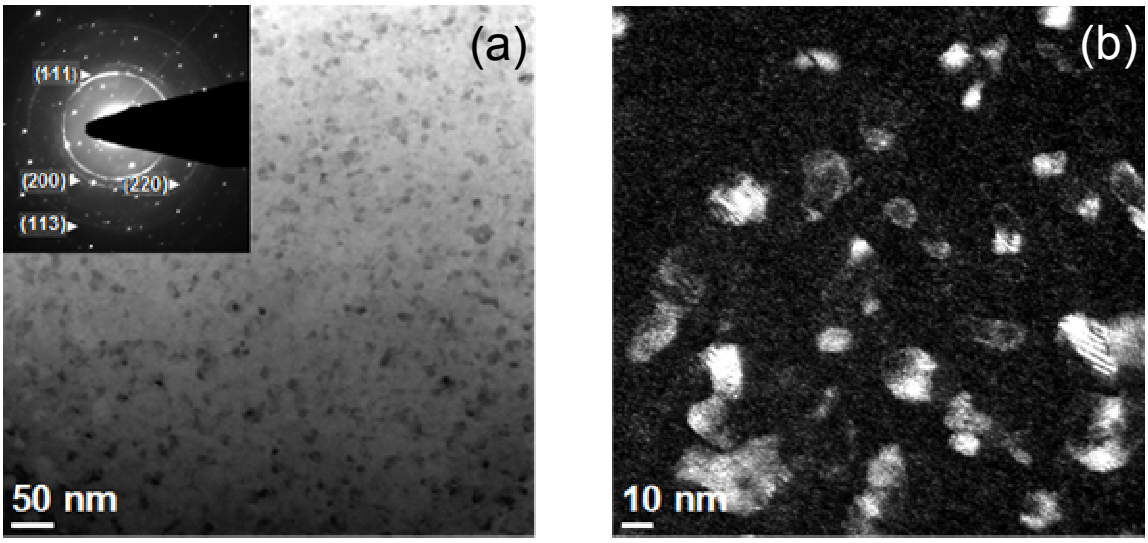

Figure 10. (a) BF image and SAED pattern (inset) of fcc-Al nanocrystals located in MS1. (b) DF image of fcc-Al nanocrystals from (111) reflections.

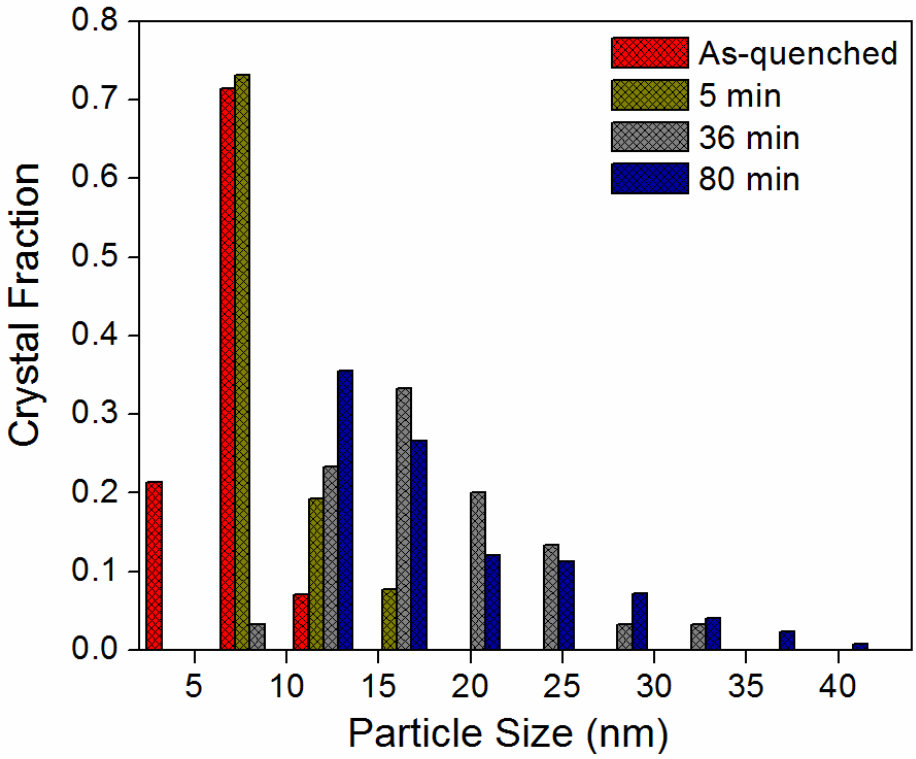

Figure 11. The fcc-Al particle size distributions for as-quenched and isothermally annealed $Al_{90}Sm_{10}$ specimens at 451 K for 5, 36, and 80 min.

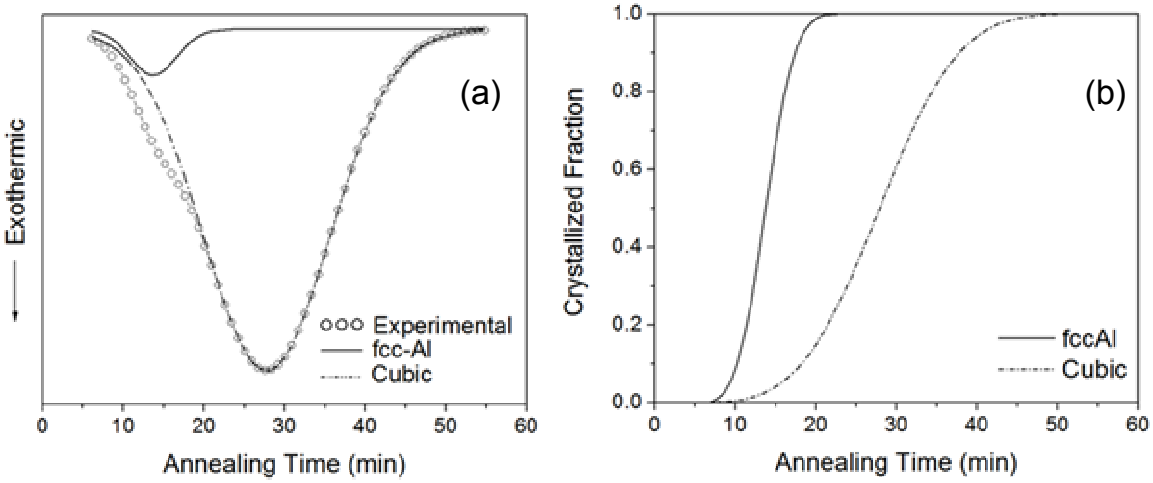

Figure 12. (a) Deconvoluted fcc-Al and cubic events and the raw DSC trace at 451 K (b) The crystallized fraction vs annealing time curve separated fcc-Al and cubic events.

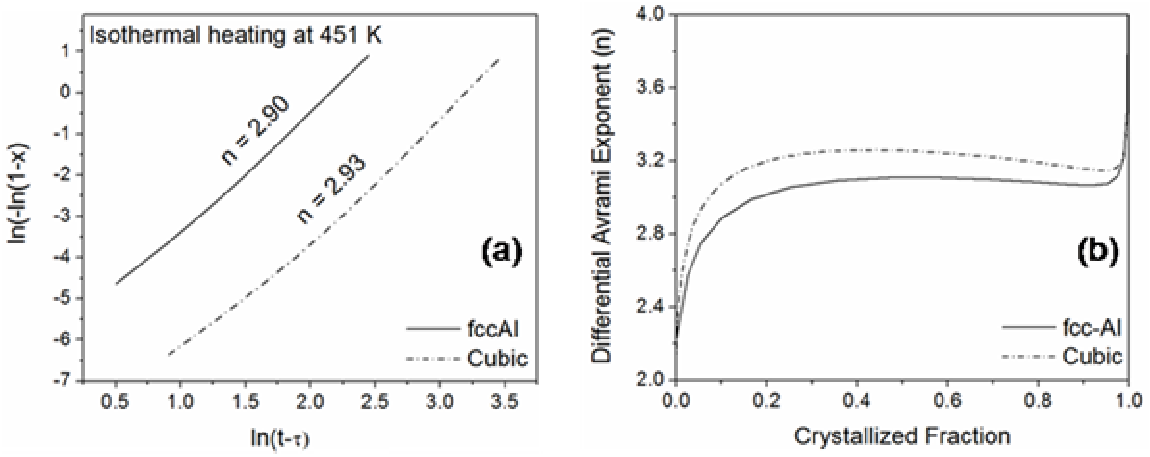

Figure 13. (a) The JMA plots of ln[-ln(1-x)] versus ln(t-t_0) for crystallization of fcc-Al and MS1 phases (b) The derivatives of JMA plots with respect to crystallized fractions.

Table 1. Phases observed in melt-spun $Al_{90}Sm_{10}$

Component	*Structure*	*Space Group*	*Lattice Parameters (nm)*	*Reference*
Amorphous				
fcc-Al	cubic	Fm3m	a=0.405	
t-$Al_{11}Sm_3$	tetragonal	I4/mmm	a=0.428; c=0.992	[14, 19, 20]
ER	orthorhombic		a=0.416; b=0.634; c=1.328	[14]
MS1	cubic		a=0.9831	[6, 21]

Table 2. Particle density (N_v) and average particle size with standard deviation (d) for fcc-Al nanocrystals after isothermally annealed at 451 K.

Isothermal at 451 K	**5min**	**36 min**	**80 min**
N_v (m^{-3})	$1.31x10^{22}$	3.7×10^{22}	$3.9x10^{22}$
d (nm)	7.5 (2.1)	15.1 (5.2)	16.0 (6.8)

CHAPTER 7: GENERAL CONCLUSION

Summary

The research effort detailed in this study couples experimental investigations with computational and analytical methods to investigate the structural dynamics in highly driven metallic systems. The research was mainly focused on two different Al based alloys, Al-Si and Al-Sm, each possessing favorable yet different characteristics to be explored under far-from equilibrium conditions. The methodology of this study was to examine the effects of non-equilibrium solidification on Al-Si and Al-Sm alloys at different compositions. The effects are considered in terms of (i) change in solidification morphology, (ii) amorphous vs nanocrystal formation, (iii) liquid-glass, glass-crystal, crystal-crystal transitions with respect to degree of undercooling, type of solute atom (Si or Sm), and composition, as well as processing methods (gas atomization or melt spinning). Analytical models such as TMK, JMA and simulation techniques such as RMC and Voronoi Tessellation analysis were performed and coupled with experimental observations. The following conclusions can be summarized as the major findings achieved in this study.

The relationship of solidification microstructure and growth morphology to alloy liquid undercooling was investigated in a range of Al-Si alloys. Five alloy powder batches of Al-Si xwt% (x = 12.6, 15, 18, 25, and 50) were generated by using high pressure gas atomization with N_2 and He atomization gas [1]. Al-50wt% atomized particles showed a large number of primary Si crystals surrounded by aluminum rich matrix which may take the form of cells or dendrites. The sizes of the individual primary Si crystals decrease with particle size. Al-25wt%Si atomized particles with relatively large diameters showed primary Si, Al dendrites and a coarse eutectic microstructure. In all microstructures, Si crystals are surrounded by Al dendrites, indicating that Si acts as a catalytic site for Al dendrites in the interior of the powder rather than at the surfaces. The eutectic percentage increases with

decreasing Si content and reaches its maximum value at 18 wt%Si. In very fine droplets of Al-18, 15 and 12.6 wt% Si observed using TEM, most bulk catalytic sites (like primary Si) are removed. In these particles, nucleation often occurs at the surface of the droplets and solidification proceeds with the formation of microcells surrounded by a fine eutectic structure. The relationship between the particle size and eutectic spacing were also investigated and the results were combined with a previous study [2]. SEM and TEM micrographs were used to measure the coupled eutectic spacing for different compositions and particle sizes. Both the atomization gas and particle diameter have an effect on average eutectic spacing in the particles. Increasing the solute composition, or changing the atomization gas from He to N_2, causes an increase in eutectic spacing. It is expected that a lighter gas such as He will produce faster cooling as it has a greater heat capacity and thermal conductivity. However, the type of atomization gas (He or N_2) has no major effect when considering powders below 10 microns in diameter. Extremely fine eutectic structures were resolved with TEM.

The relationship between interface velocity and interface undercooling with eutectic spacing was calculated using the eutectic growth model developed by Jackson-Hunt (JH) [3] for Al-18wt%Si. The results are consistent with the fact that small diameter droplets will have a larger undercooling for nucleation. It is also seen that the change in interface temperature is large for small droplets since they are more subject to the effect of recalesence. The change in velocity and undercooling becomes small after particle size becomes larger than 30 μm, indicating that the effect of recalesence decreases. The JH model was developed under the condition that the diffusion distance in the liquid is much larger than the eutectic spacing, which is justified for eutectic growth at low velocities but not under rapid solidification conditions. A eutectic growth model under rapid solidification conditions developed by Trivedi, Magnin and Kurz (TMK) [4] was also employed. A numerical program in MathCAD was used to relate the eutectic spacing to the eutectic front velocity in

different size particles subjected to high cooling rate solidification. At low Péclet numbers TMK and JH are in good agreement, however, at high Péclet numbers TMK deviates from JH prediction. It is interesting that this divergence point corresponds to the particle diameters where the type of gas used during atomization ceases to affect the microstructure, suggesting that growth rate is governed by recalesence in this regime. Moreover, this diameter is consistent with the appearance of the microcellular growth morphology and with the divergence of the JH and TMK models for eutectic growth at Péclet numbers greater than ~0.2.

The Al-Si powders exhibiting different "classes" of microstructures (eutectic, dendritic and microcellular) were collected and extruded at 300°C to compare their mechanical strengths [5]. The results of the tensile test measurements indicate that yield strength (YS) and ultimate tensile strength (UTS) of microcellular Al-12.6 wt% Si is as high as that for eutectic Al-18 wt%, with a large increase in ductility. Microcellular Al-Si alloys may be an alternative structure to a fine eutectic in structural designs where high strength and ductility is required.

The Al-Sm system is an Al-RE marginal glass former system with complex devitrification and solidification behaviors. Rapid solidification of Al-Sm alloys was obtained by He gas atomization (for $Al_{90}Sm_{10}$) and Cu block free-jet melt spinning for $Al_{(100-x)}Sm_x$ (x=8, 10, and 12). For a given atomization process, droplet diameter can be directly correlated to undercooling, and decreasing particle size was shown to give rise to the formation of fcc-Al, tetragonal $Al_{11}Sm_3$, orthorhombic Al_4Sm, and a new orthorhombic phase called ER. Decreasing particle size tends to decrease the internal nucleant concentration, which promotes larger undercoolings. This results in formation of amorphous phases with a high density of fcc-Al nanoclusters. Fcc-Al nanocrystals (2-5 nm) were also observed after melt-spinning (30 and 40 m/s wheel speeds). Interestingly these nanocrystals cannot be detected in HEXRD, but atom probe tomography APT data clearly shows

nanoscale chemical partitioning within a network of homogeneous matrix. The existence of nanocrystalline fcc-Al influences the kinetics of crystallization, and isochronal heating experiments indicate that the melt-spun material has a relatively low thermal stability against crystallization. Devitrification of the as-quenched structure over the temperature range 298-773 K at a heating rate of 5 K/min was investigated in-situ using high energy synchrotron X-ray radiation and the devitrification sequence was revealed as Amorphous → MS1 (cubic) → H1(hexagonal) → Al_4Sm (orthorhombic) [6]. It should be noted that fcc-Al nanocrystals exist with amorphous phase as confirmed with ATP and HRTEM.

Detailed analysis of the as-quenched $Al_{(100-x)}Sm_x$ (x=8, 10, and 12) structures by HEXRD and HRTEM revealed a pre-peak well below the major amorphous peak in total structure factor and rotationally averaged Fourier transform patterns, respectively. A very similar type of a pre-peak was also resolved in $Al_{90}Sm_{10}$ approximately 300 K above the liquidus temperature. This result shows that the local chemical or topological ordering present in the liquid persists in the amorphous solid. Simple calculations based on the position and width of the pre-peak indicate clustering on the order of 1.5 nm for liquid and 2.5 nm for the amorphous phase with a structural unit dimension of 0.495 nm. The Voronoi tessellation analysis of the local atomic structures based on RMC simulation suggests a deformed bcc-like structure surrounding Sm with coordination of higher than 15 atoms for as-quenched alloys. The “d” spacing of the high temperature metastable tetragonal phase and the first cubic phase observed in the devitrification sequence match the structural unit dimension measured for as-solidified structures. These are the d-spacings associated with the Sm-bearing planes, consistent with the RMC results, and indicate that the pre-peak can be attributed to a strong Sm-Sm correlation in the amorphous state. The MRO clustering in the liquid is believed to form due to strong interactions between Al and Sm atoms. The MRO clusters essentially may act like distinct “superatoms” with a slightly broad size distribution and huge diameters as compared to individual Al and Sm atoms in the matrix. Upon rapid

solidification it is hypothesized that these clusters cause a local atomic size effect, similar to that seen in multi-component bulk amorphous alloys, preventing the complete crystallization of the Al rich matrix. This results in the as-quenched structure being divided into nano-scale regions by a network of MRO clusters. Depending upon size of these regions a certain percentage of fcc-Al clusters will reach the critical nucleus size with the remainder staying below this size. This explanation is supported by results obtained for $Al_{90}Sm_{10}$ using three dimensional atom probe tomography (3D APT). The cooling rate appears to be directly correlated with the percentage of Al that cannot reach the critical nucleation size. However, it should be noted that cooling rate has a minor effect on the presence of MRO in the as-quenched state. MRO was observed in all liquids for all initial melt temperatures used in this study. Therefore, MRO stability in the liquid needs be studied directly with respect to initial melt temperature, rather than assuming that the quenched structure varies with cooling rate of the melt.

The hypothesis of having structural arrangements in the as-quenched state in the form of an Al-Sm network which divides the matrix into nano-scale regions is also supported by the crystallization analyses results. If one considers the isothermal DSC traces of $Al_{90}Sm_{10}$ produced at 10, 20, and 30 m/s, the as-quenched structures of $Al_{90}Sm_{10}$ for these three wheel speeds (cooling rates) resulted in formation of a glassy state up to a certain degree; the metastable glass then transforms to the same metastable cubic phase independent of the cooling rate applied in this study. However, for the 30 m/s wheel speed samples DSC shows two exothermic events while for the 10 and 20 m/s samples it only shows a single exothermic event. TEM showed that the extra exothermic event is coming from nucleation and growth of fcc-Al. These results can be explained by positing that for the 30 m/s wheel speed samples the cooling rate is high enough to keep a sufficient number of subcritical Al particles in the as-quenched state. When these samples are isothermally annealed supercritical size fcc-Al crystals form (nucleate) from subcritical size Al. Therefore, in the fully crystalline samples

fcc-Al originates both from supercritical size particles formed during rapid solidification and subcritical size Al that nucleates during solid-state annealing, with the latter causing the exothermic event resolved in DSC.

The crystallization mechanism was investigated through a JMA approach using isothermal DSC experiments conducted at 451 K. The Avrami exponent estimated for fcc-Al represents only the crystallization during solid-state annealing, and it suggests a zero nucleation rate with interface controlled growth. A similar Avrami exponent calculated for MS1 also indicated that the reaction was dominated by a fixed number of nuclei with a polymorphic crystallization. The pre-peak observed in the as-quenched state may indicate that Sm-rich clusters act as the pre-cursors of MS1. The Avrami exponent calculated in this study represents only some portion of the fcc-Al crystallization since some fcc-Al was found to pre-exist in as quenched structure. Thus, it does not illustrate the total crystallization event for fcc-Al.

Recommendation for Future Work

The Al-Sm system is a representative of the Al-RE and Al-RE-TM class marginal glass formers. These types of alloys have attracted much attention due to their fascinating lightweight structural properties. Apart from their possible engineering applications they also constitute an important class of materials that may aid in understanding the long-time mysterious metallic glass structure. Based on prior results discussed in this dissertation, obtaining answers to the following questions can be considered as a possible future direction of study.

Can a fully amorphous state be obtained by rapid quenching of this alloy at any composition?

What is the effect of the structural rearrangement (the pre-peak) in the liquid on amorphous solid formation? Does the rearrangement in the liquid favor amorphous solid formation?

What is the structural origin of the pre-peak, is it related to identifiable cluster populations?

What specific structures give rise to the observed MRO in amorphous Al-Sm, and how it this structure spatially distributed within the amorphous phase?

Is the fcc-Al nucleation in the amorphous matrix homogeneous or heterogeneous and what is the origin of the very high nucleation density observed?

In order to address these questions, rapid solidification techniques with very high-solidification rates and initial liquid temperatures are required. One possible means to obtain these conditions is the new electromagnetic levitation chamber (Figure 1) equipped with supplemental laser/incandescent heating sources, gas cooling ports for enhanced temperature control, and a double-anvil splat quenching apparatus for rapid solidification, now located in Ames Laboratory. This apparatus could be a good choice to investigate the structural origin of the pre-peak observed in low-Q region of total structural factor analysis for Al-Sm liquid/glass alloys for a number of reasons. Electrostatic levitation will allow us to superheat Al-Sm alloys in a non-contact, contamination free environment. The as-quenched ribbons of Al-Sm superheated at predetermined temperatures (specifically within a temperature range of 900 and 1600 ° C) can be characterized using X-ray and electron diffraction methods. At this point FEM is particularly useful to resolve any MRO structures. A decrease in the amount of MRO (intensity of the pre-peak) with respect to increase in quench temperature is an expected result. Any structural ordering should decompose and the liquid alloy is expected to act as a single phase as a result of increasing the liquid temperature. However, its effect on amorphous solid formation and the transformation mechanism is mysterious and is worthy of further study.

Another critical measurement is the distribution of the MRO Al-Sm clusters. One of the important hypotheses of this dissertation is the formation of nano-zones of MRO in liquid which can act as nucleation sites for fcc-Al. Therefore, the size of the nano-zones is a critical parameter to measure. This can be conducted using APT, HRTEM, and HAADF at different compositions, quench temperature and cooling rates. The critical issue here is the size of the nano-zone with respect to the critical nucleus size for the fcc phase. The application of the classical theory to this situatin requires reliable calculations of bulk free and interfacial free energies.

If a fully amorphous Al-Sm alloy phase cannot be produced using levitation melting, other alternatives such as spark erosion processing may be worth attempting. Grams of nanoparticulates of Al-Sm can be produced using this technique. One of the advantages this technique would be that using nanoparticles eases TEM sample preparation. Fully amorphous samples can be devitrified and the devitrification path can be compared to those obtained from samples possessing structural rearrangements. The nucleation density of fcc-Al should be lowered for the fully amorphous case as the MRO, which is hypothesized to act as a catalyst, will be absent. The number densities could be calculated from isothermally heated samples using BF, DF techniques coupled with thickness measurements conducted using EELS. Such a study will be helpful in determining the role of MRO in formation of a high nucleation density of fcc-Al. Chemical fluctuation effects could theoretically be monitored using APT. Unfortunately, nanoparticles can be problematic with APT, but small angle X-ray scattering could be an alternative.

Lastly, Al-Sm is only a representative alloy system. While the results presented in this dissertation are applicable to other Al-RE, and Al-RE-TM marginal glass former alloys, some other Al based or Fe based marginal glass forming alloy should be investigated using a similar concept and experimental procedures to further validate the conclusions and hypotheses raised by the current study on Al-Sm.

Reference

1. Kalay Y.E., et al., Metallurgical and Materials Transactions A, 2007. **38A**: p. 1452-1457.
2. Genau A.L., Microstructural Development in Al-Si Powder during Rapid Solidification. 2004, Iowa State University: Ames.
3. Jackson K.A. and Hunt J.D.,. Transactions of the Metallurgical Society of AIME, 1966. **236**: p. 843-852.
4. Trivedi R., Magnin P., and Kurz W., Acta Metallurgica, 1987. **35**: p. 971-980.
5. Kalay Y.E., Anderson I E., and Chumbley L.S., Conference on Powder Metallurgy and Particulate, MPIF/AIME, 2006: p. 95-105.
6. Kalay Y.E., Chumbley L.S., and Anderson I.E., Journal of Non-Crystalline Solids, 2008. **354**: p. 3040-3048.

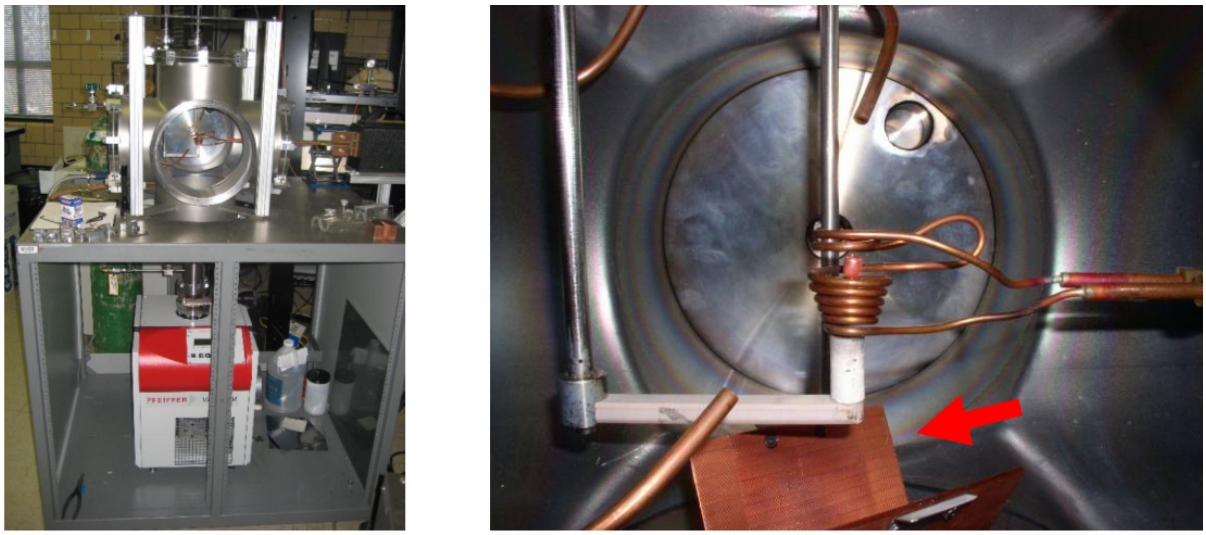

(a) (b)

Figure 1. (a) Levitation melting set-up in Ames Laboratory, (b) levitation melting in operation with an Al test sample, the double anvil splat quench is shown by an arrow.

ACKNOWLEDGEMENTS

Foremost, I would like to express my deep and sincere gratitude to my academic advisors Scott Chumbley and Iver Anderson. I would like to thank them not only for their guidance as an advisor but also for their friendships, too. I've been always impressed by Scott's enthusiasm, motivation, and the sense of humor. He is far most the best teacher I've been ever met. Iver's supports and encouragements have been always inspirational for me. I'll always miss the amazing powder group meetings and the redeye flights.

I am deeply grateful to Matthew Kramer for his helpful discussions and comments. I've been always amazed with his answers to my endless questions. I owe my sincere gratitude to Ralph Napolitano, his wide knowledge and logical way of thinking has always inspired me. I genuinely appreciate the guidance of my other committee members, Rohit Trivedi and Frank Peters. I also would like to thank to Fran Laabs, Yaqiao Wu, Kevin Dennis, and Alfred Kracher, who generously gave me important guidance with the analytical instruments. I also wish to thank many colleagues in Iowa State University, Ames Laboratory, Argonne National Laboratory, University of Wisconsin, and University of North Texas, Missouri University of Science with whom I've been collaborated. I warmly thank to all my friends and officemates (Qian is specially awarded for his wide knowledge on European soccer) for their moral support and remanding me the life beyond research experiments.

Finally, I owe my deepest thanks to my parents Birgül and Mustafa for their encouragement and support since I was born. I owe my lovely thanks to my wonderful wife, İlkay. It would have been impossible to accomplish this without her.

The work at Ames Laboratory was supported by the United States Department of Energy (USDOE), Office of Science (OS), Office of Basic Energy Science (BES), under Ames Laboratory Contract No. DE-AC02-07CH11358, the high-energy X-ray work at the

MUCAT sector of the APS was supported by the US Department of Energy, Office of Science, Basic Energy Sciences under Contract No. DE-AC02-06CH11357. The assistance of Materials Preparation Center of the Ames Laboratory is acknowledged for supplying our samples.